NOTICE

The quality of this microform is heavily dependent upon the quality of the original thesis submitted for microfilming. Every effort has been made to ensure the highest quality of reproduction possible.

If pages are missing, contact the university which granted the degree.

Some pages may have indistinct print especially if the original pages were typed with a poor typewriter ribbon or if the university sent us an inferior photocopy.

Reproduction in full or in part of this microform is governed by the Canadian Copyright Act, R.S.C. 1970, c. C-30, and subsequent amendments.

AVIS

La qualité de cette microforme dépend grandement de la qualité de la thèse soumise au microfilmage. Nous avons tout fait pour assurer une qualité supérieure de reproduction.

S'il manque des pages, veuillez communiquer avec l'université qui a conféré le grade.

La qualité d'impression de certaines pages peut laisser à désirer, surtout si les pages originales ont été dactylographiées à l'aide d'un ruban usé ou si l'université nous a fait parvenir une photocopie de qualité inférieure.

La reproduction, même partielle, de cette microforme est soumise à la Loi canadienne sur le droit d'auteur, SRC 1970, c. C-30, et ses amendements subséquents.

A GLIMPSE OF EPHEMERAL SUBDUCTION ZONE PROCESSES FROM SIMBERI ISLAND, PAPUA NEW GUINEA

by

Brent I. A. McInnes, M.Sc.

A thesis submitted to the School of Graduate Studies in partial fulfillment of the requirements for the degree of Ph.D., Science in Geology

Ottawa-Carleton Geoscience Centre
University of Ottawa

ISBN 0-315-75082-0

Canada

UNIVERSITÉ D'OTTAWA
UNIVERSITY OF OTTAWA

Abstract

Simberi Island is an eroded Pliocene alkaline volcano, the oldest in the Pliocene to Holocene Tabar-Lihir-Tanga-Feni (TLTF) island arc. These islands are derived from partial melting of subduction-modified mantle at >60 km depth along extensional, pull-apart structures. Explosive volcanism has brought samples of the mantle wedge to the surface. Within these samples are sulphate-, carbonate-, hydrous-, alkali-rich aluminosilicate glasses which represent quenched slab-derived magmas (SCHARM). SCHARM reacts with mantle peridotite to create a vertically zoned mantle wedge consisting of phlogopite-clinopyroxenite at P>30 kbar and amphibole-clinopyroxenite at 21 to 30 kbar at 930-1080°C.

Metasomatism of the mantle wedge by SCHARM controls the mineralogical, chemical and isotopic composition of TLTF arc volcanics. The presence of sulphate within SCHARM indicates a high intrinsic oxygen fugacity of FMQ+4. Oxidative metasomatism of the mantle wedge by SCHARM is responsible for high Fe_2O_3/FeO ratios in the lavas, the early appearance of magnetite on the liquidus and the crystallization of a sulphate-bearing feldspathoidal mineral (haüyne) in the TLTF lavas. Titanium depletion in the rocks of the TLTF arc is accounted for by the low initial solubility of Ti in SCHARM, coupled with the strong partitioning of Ti into phlogopite at high fo_2. Enhanced solubility of sulphur in high fO_2 melts, caused destabilization of mantle sulfides and concomitant enrichment of chalcophile Au and Cu in volatile-rich, mantle-derived melts, and may be a significant factor in the development of volcanic-hosted Au-Cu deposits in the arc.

Enrichments of large ion lithophile elements and rare-earth element in basanites and alkali basalts are also due to SCHARM contamination. Negative Ce and positive Eu anomalies in Simberi basalts are produced by partial melting of feldspathic minerals in subducted, seawater altered mid-ocean ridge basalt (MORB), at the basalt-eclogite transition zone in the mantle. Eutectic melting constraints indicate that SCHARM could be derived during the melting of scapolite, produced by prograde metamorphic reactions between MORB plagioclase and low temperature secondary

minerals (calcite, gypsum) in the subducting slab. Metasomatic replacement of forsteritic olivine ($\delta^{18}O = 5‰$) by high $\delta^{18}O$ SCHARM produces ^{18}O-enriched sodian diopside and magnetite ($\delta^{18}O = 6.3\text{-}6.8‰$) in Simberi basanites. Isotopic disequilibrium exists because of the short (< 6 Ma) residence time of SCHARM in the mantle.

RÉSUMÉ

L'île de Simberi est un volcan alcalin Pliocène érodé, il est le plus ancien de l'arc insulaire pliocène à holocène de Tabar-Lihir-Tanga-Feni (TLTF). Ces îles sont dérivées de la fusion partielle d'une source mantellique modifiée par la subduction, à une profondeur de >60 km le long de structures en extension "pull-apart". Un volcanisme explosif a transporté des échantillons du biseau mantellique j'usqu'à la surface. Ces derniers contiennent du verre d'aluminosilicates riche en sulfates, en carbonates, en eau et en alcalins qui est du magma (SCHARM) dérivé d'une plaque et refroidie rapidement. Le SCHARM réagit avec la péridotite du manteau pour créer un biseau mantellique à zonation verticale se divisant en une zone à phlogopite et clinopyroxène (P>30 kbar) et une autre à amphibole et clinopyroxène (21-30 kbar et 930-1080°C).

Le métasomatisme du biseau mantellique causé par le SCHARM contrôle la composition minéralogique, chimique et isotopique des roches volcaniques de l'arc insulaire de TLTF. La présence de sulfate dans le SCHARM indique une forte fugacité de l'oxygène intrinsèque (FMQ+4). Le métasomatisme oxidatif du biseau mantellique par le SCHARM explique le rapport Fe_2O_3/FeO élevé, l'apparation précoce de magnétite à la phase liquide et la cristallisation d'un feldspathoïde sulfaté (haüyne) dans les laves de TLTF. L'appauvrissement en titane dans l'arc de TLTF est dû à la faible solubilité initiale du Ti dans le SCHARM, accompagnée d'un forte fractionnement du Ti dans la phlogopite dans des conditions de fO_2 élevée. La déstabilisation des

sulfures du manteau dans des conditions de forte fO_2 a causé un enrichissement en Au et en Cu des magmas riches en volatiles, dérivés du manteau. Ceci pourrait être un facteur significatif dans la formation des gisements de Au-Cu encaissés dans des volcanite de l'arc insulaire.

L'enrichissement en éléments lithophiles à grand rayon ionique et en terres rares des basanites et des basaltes à feldspathoïde est aussi le résultat de la contamination par le SCHARM. Les anomalies négatives en Ce et positives en Eu dans les basaltes de Simberi résultent de la fusion partielle, dans une zone de subduction, des minéraux feldspathiques d'un basalte de dorsale médio-océanique (MORB) altéré par l'eau de mer, dans la zone de transition à basaltes et éclogites du manteau. Les contraintes de fusion eutectique indiquent que le SCHARM pourrait être formé pendant la fusion de la scapolite, résultant des réactions métamorphiques prograde entre le plagioclase du MORB et les minéraux secondaires de basse température (calcite, gypse) dans la plaque en subduction. Le remplacement métasomatique de l'olivine (forstérite, $\delta^{18}O = 5‰$) par le SCHARM à forte $\delta^{18}O$ produit du diopside sodique et de la magnétite riches en $\delta^{18}O$ ($\delta^{18}O = 6.3$-$6.8‰$) dans les basanites de Simberi. L'existence d'un déséquilibre isotopique est due à la courte (<6Ma) période de résidence du SCHARM dans le manteau.

Acknowledgements

I gratefully acknowledge receipt of an International Development Research Centre Young Canadian Researcher Award, a Geological Society of America Student Travel Grant, and an Ontario Graduate Scholarship. This work was also supported by an NSERC grant to Eion Cameron. I would also like to express my appreciation to the Royal Canadian Legion and to the Sophia Wood Fund of the Women's Institute of the Mining Association of Canada for their benefaction.

I am grateful to Kennecott Exploration (Australia) Ltd. for logistical, technical and financial support, and in particular to Geoff Ballantyne, John Burgess, William Edwards, Linus Kameko and Steve MacIntosh.

I would also like to thank the people of Simberi Island, and particularly Joe Tokavin, for their hospitality and friendship during my stay.

This research was sponsored in Papua New Guinea by Tom Welsh of the Geological Survey of Papua New Guinea.

I have benefitted from the stimulating, constructive and critical reviews of parts of this dissertation by Keith Bell, Eion Cameron, Ken Currie, Bob Drake, Noreen Evans, Marianne Goodfellow, Jeff Hedenquist, Dick Henley, Bruce Karsjaard, Andre Lalonde and John Thompson. Interpretations made within are solely my responsibility.

Technical assistance was provided by Laura Bradburn, Noreen Evans, Bob Gault, Fereydoun Ghazban, Conrad Gregoire, Ron Hartree, Edward Hearn, John Loop, Margaret McLaren, George Mrazek, George Robinson, Gilles St.-Jean, John Stirling, Jean-Francois Tardif and Dave Walker. Doug Stewart is thanked for lending me his Papua New Guinea publications.

Eion Cameron has provided unencumbering supervision and allowed me considerable latitude during the progress of my research. His diligent and relentless efforts to improve and clarify the message of this thesis are to be commended, and are gratefully appreciated.

Special thanks to my friends Caroline Duchesne, Alex Langshur and Jean Morin for contributing their artistic talents and good company, and again to Alex Langshur for translation of the abstract.

But most of all, Noreen Evans, who, with her tireless efforts and tremendous patience, has made the single greatest contribution to the completion of this dissertation.

Preface

This dissertation consists of three parts. Part A includes 8 chapters in conventional thesis format, which introduce the geology, mineralogy, geochronology and geochemistry of the volcanic rocks on Simberi Island, Papua New Guinea. Part B is a manuscript entitled "The nature of slab melts and their effect on the mantle wedge: Tabar-Lihir-Tanga-Feni Arc, Papua New Guinea" which will be submitted to the journal Nature. Part C is a manuscript entitled "The role of subduction in gold-copper metallogenesis: Evidence from the Tabar-Lihir-Tanga-Feni island arc, Papua New Guinea" which will be submitted to the journal Economic Geology. References cited in Parts A, B and C are combined into one reference list.

For Win McInnes

who gave birth to these ideas

Had we never seen the stars, and the sun, and the heaven,
none of the words which we have spoken
about the universe would ever have been uttered.
But now the sight of day and night, and the months
and the revolutions of the years, have created number,
and have given us a conception of time,
and the power of enquiring about the nature of the universe;
and from this source we have derived philosophy,
than which no greater good ever was
or will be given by the gods to mortal man.

-Plato

after so long nobody's wrong
after so long nobody's right

-blue rodeo

Table of Contents

Table of Contents

Table of Contents

List of Figures

List of Figures

List of Figures

List of Figures

List of Tables

Part A

Chapter 1. Regional Tectonics and the Evolution of the Tabar-Lihir-Tanga-Feni Island arc

Introduction

The physiographic, topographic and cultural diversity of Papua New Guinea is the result of its mobilistic tectonic development and, in particular, to accretionary processes operating since the early Tertiary (Hamilton, 1979). The driving force of accretion has been the convergence of the Indo-Australian plate and the Pacific Plate. Mainland Papua New Guinea (Figure 1) consists of three major geological provinces (D'Addario *et al.* 1976):

(1) A southern continental platform (the northern extension of the Australian continent) comprised of Paleozoic metamorphic and granitic rocks overlain by Mesozoic-Cenozoic shelf carbonates and clastic sediments that are folded to the northeast to form the Papuan Fold Belt (Hamilton, 1979).

(2) A Central Orogenic Belt (also termed the New Guinea Mobile Belt), consisting of a folded and upthrust central cordillera extending to the Papuan peninsula. This province contains an Eocene island arc and its underlying Mesozoic peridotite, obducted during accretion with northern New Guinea in late Miocene - early Pliocene (Davies and Smith, 1971; Johnson, 1979; Davies and Jaques, 1984; Kroenke, 1984).

(3) A northernmost belt of rocks (including the Adelbert-Finisterre coastal range and the Huon peninsula) comprised of a Tertiary island arc terrane that collided with Papua New Guinea in the Pliocene. A suture zone demarcating (2) and (3) is the Ramu-Markham fault (Jaques and Robinson, 1977).

Figure 1. Regional geology and tectonic features of Papua New Guinea. Dark triangles indicate presently active subduction zones, white triangles indicate extinct subduction zones. Region 1: Continental platform (northern extension of the Australian continent. Region 2: Central Orogenic Belt. Region 3: Accreted island arc. (from D'Addario *et al.* 1976)

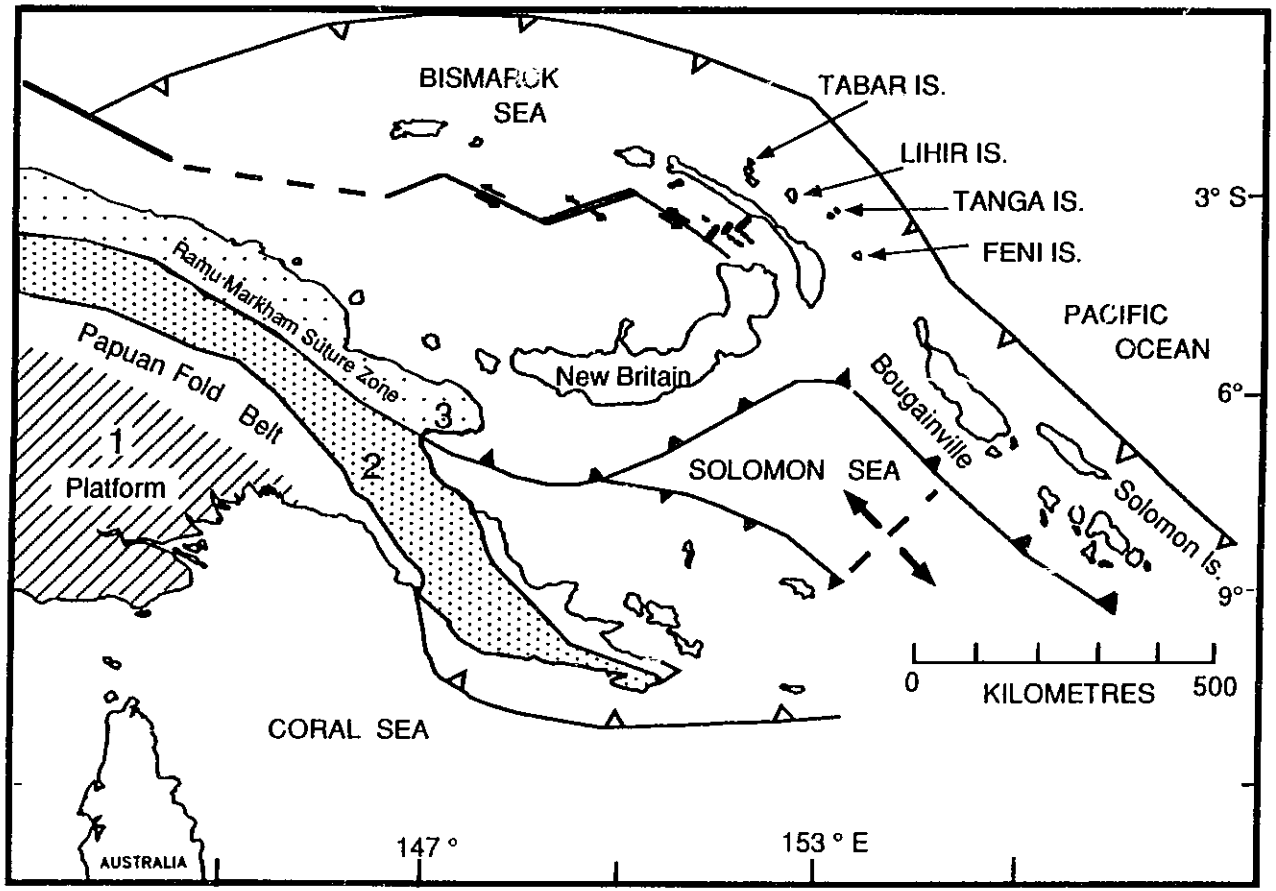
BISMARCK SEA
TABAR IS.
LIHIR IS.
TANGA IS.
FENI IS.
3° S
PACIFIC OCEAN
6°
Ramu-Markham Suture Zone
Papuan Fold Belt
1
Platform
2
3
New Britain
Bougainville
SOLOMON SEA
Solomon Is.
9°
0
KILOMETRES
500
CORAL SEA
AUSTRALIA
147 °
153 ° E

Outboard island arc formation and accretion of volcanic arcs to the Australian continent continues today, and is a modern analogue of the process of continent building. Modern island arcs to the northeast of mainland Papua New Guinea comprise the physiographic region known as the Bismarck Archipelago, which includes the islands of New Britain, New Ireland, Bougainville-Solomon Islands, and the Tabar-Lihir-Tanga-Feni (TLTF) island chain.

Tectonic Development of the Bismarck Archipelago

The Bismarck Archipelago (Figure 2) consists of four volcanic arcs:

(1) Bougainville-Solomon Island Arc (calc-alkaline; presently active)

(2) New Ireland-New Hanover Island Arc (calc-alkaline; extinct)

(3) New Britain or Bismarck Island Arc (calc-alkaline; presently active)

(4) Tabar-Lihir-Tanga-Feni Island Arc (alkaline; recently active (2.3 Ka; Licence *et al.* 1987)

The tectonic development of these island arcs is poorly understood due to relatively rapid, short-term movements within a complex network of microplates, combined with a relative lack of detailed geochronological, field and oceanographic studies. A tectonic synthesis culled from the literature is provided to demonstrate the similarities and differences between the calc-alkaline arcs (1-3) and the alkaline TLTF island arc, and the place of the latter in the tectonic development of the region.

All four island arcs are ensimatic. Volcanic activity on the first three can be correlated directly with subduction events, whereas TLTF volcanism is not directly

Figure 2. Location map and tectonic features of the Bismarck Archipelago.

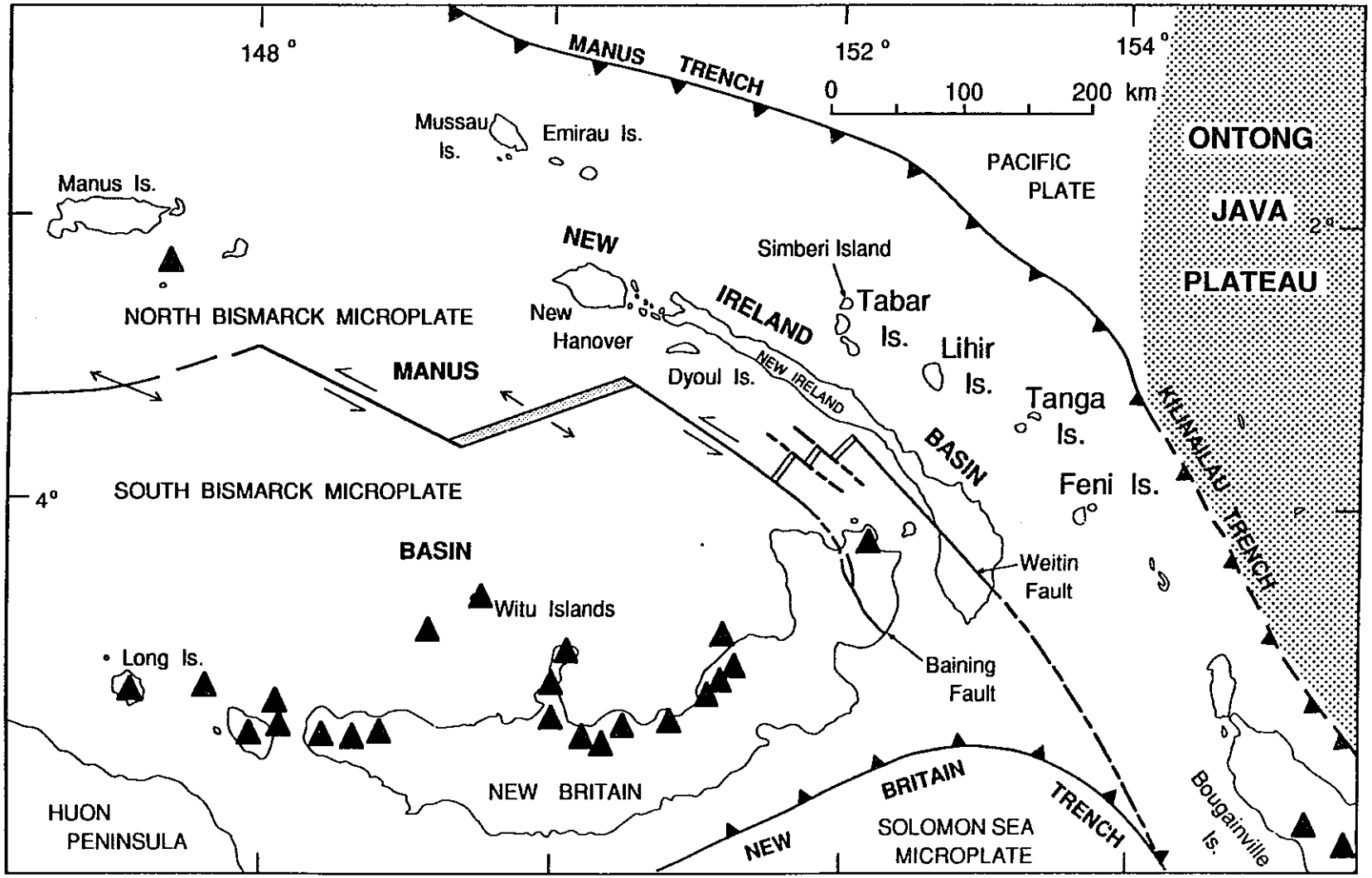
148 °
MANUS TRENCH
152 °
154 °
0
100
200 km
Mussau Is.
Emirau Is.
ONTONG JAVA PLATEAU
PACIFIC PLATE
Manus Is.
NEW IRELAND
Simberi Island
Tabar Is.
Lihir Is.
Tanga Is.
Feni Is.
NORTH BISMARCK MICROPLATE
New Hanover
Dyoul Is.
MANUS BASIN
NEW IRELAND BASIN
KILINAILAU TRENCH
4°
SOUTH BISMARCK MICROPLATE
Weitin Fault
Witu Islands
Long Is.
Baining Fault
NEW BRITAIN
HUON PENINSULA
NEW BRITAIN TRENCH
SOLOMON SEA MICROPLATE
Bougainville Is.
Quaternary Volcanic Centre

related to active subduction. Oblique convergence between the westwardly-moving Pacific Plate and the stable Indo-Australian Plate has occurred since the early Tertiary (Figure 3; Coleman and Packham, 1976), with subduction along the Manus-Kilinailau trench. Oligocene to Miocene volcanism associated with this westwardly-dipping subduction zone generated the Lemau Intrusive complex on New Ireland and New Hanover (Hohnen, 1978; Stewart and Sandy, 1988), the Yirri Intrusive complex on Manus Island (Francis, 1988), the Kieta Volcanics of Bougainville Island (Blake and Miezitis, 1967) and the Suta and Marasa Volcanics of Guadalcanal, Solomon Islands (Dunkley, 1983). These islands may have formed a continuous chain of Tertiary volcanic islands that were the proto- New Britain, New Ireland and Bougainville-Solomon Islands (Curtis, 1973; Johnson, 1979; Weissel *et al.* 1982)(Figure 4).

Kroenke (1972) and Moberly (1972) proposed that subduction in the Manus-Kilinailau trench continued until the anomalously thick Ontong Java Plateau collided with the subduction zone near the Solomon Island proto-arc in the Miocene. The Ontong Java Plateau, with an areal extent of 1600 X 800 km and thickness of between 25 and 40 km (Furumoto *et al.* 1976), is a major oceanic subcontinent formed during prolific basaltic volcanism in the Pacific basin during the Cretaceous. Collision led to the extinction of the westward subduction zone, effectively plugged by the buoyant nature of the oceanic plateau (Coleman and Kroenke, 1981). Continued convergence led to compressional foreshortening of the Ontong Java Plateau, culminating in the creation of the northeastern chain of the Solomon Islands (Kroenke, 1972; Hughes and Turner, 1977), including Malaita Island. The Miocene end to subduction was further characterized by a period of quiescence and

Figure 3. Westward motion of the Pacific Plate since the Tertiary (from Coleman and Packham, 1976), and Miocene collision of the Ontong Java Plateau with the Manus-Kilinailau trench.

NBM = North Bismarck microplate; SBM = South Bismarck microplate; SM = Solomon microplate.

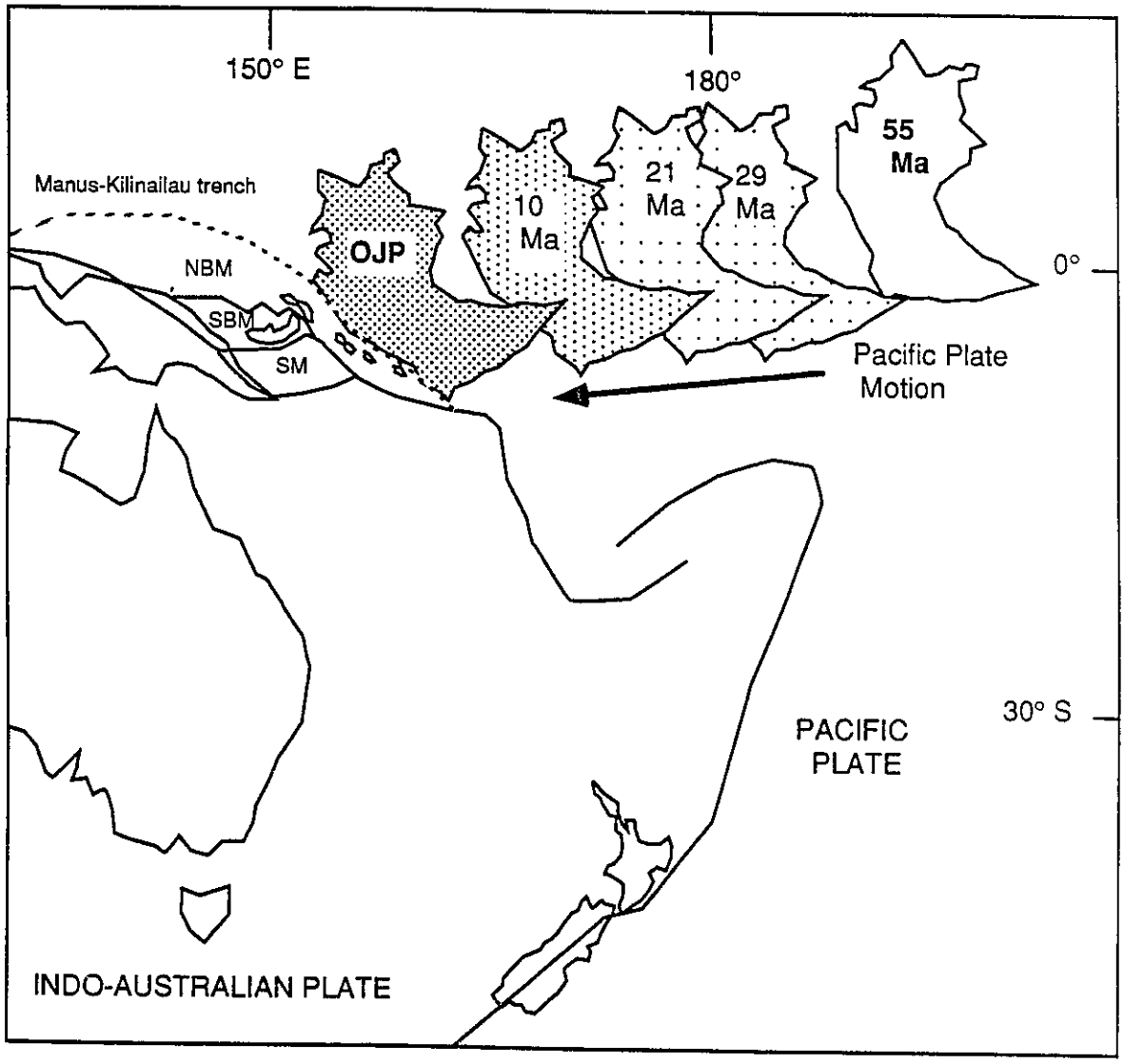
150° E
180°
Manus-Kilinailau trench
NBM
SBM
SM
OJP
10 Ma
21 Ma
29 Ma
55 Ma
0°
Pacific Plate Motion
30° S
PACIFIC PLATE
INDO-AUSTRALIAN PLATE

minimal volcanic activity (Kroenke, 1984). Build-up of stress continued until convergence of the Pacific and Indo-Australian Plates could no longer be accommodated by deformation of the Ontong Java Plateau and a reversal in arc polarity occurred, creating the presently active New Britain trench during the late Miocene (≈10-8 Ma; Figures 1 and 2; Coleman and Kroenke, 1981; Kroenke, 1984).

Renewed calc-alkaline igneous activity in the New Britain-New Ireland-Bougainville-Solomon Island arcs began around 6 Ma (Kroenke, 1984) and still continues today in the New Britain and Bougainville-Solomon Islands. Dynamic restructuring of the aligned island arcs began around 3.5 Ma with the fragmentation of the leading northeast edge of the Indo-Australian Plate and the formation of the Bismarck and Solomon Sea microplates (Figure 4). Backarc spreading in the Manus Basin (Bismarck Sea) began around 3.5 Ma (Connelly, 1976; Taylor, 1979; Weissel, 1981) and has translated the position of New Britain trenchward to the southeast (13.2 cm/yr), causing counter-clockwise rotation of the arc and collision of its western portion with mainland Papua New Guinea (Figure 4).

The movement of New Britain has produced transpressional-transtensional tectonic regimes in the Bismarck Archipelago. Transpressional features are represented by transform fault segments, striking approximately N65°W (Figure 2), which bound the spreading centres. Earthquake focal mechanisms indicate left-lateral strike-slip motion (Taylor, 1979; Johnson, 1979). These transform faults are linked to major structures on New Ireland (Sapom and Weitin Faults; Hohnen, 1978), New Hanover (Brown, 1982) and eastern New Britain (Baining Fault;

Figure 4. Possible configuration (shaded region) of the Oligocene to Miocene proto-island arc consisting of present day New Britain, New Ireland and Bougainville Islands. After arc reversal in the late Miocene (8-10 Ma), backarc spreading at $\approx$3.5 Ma transported New Britain to its present position.

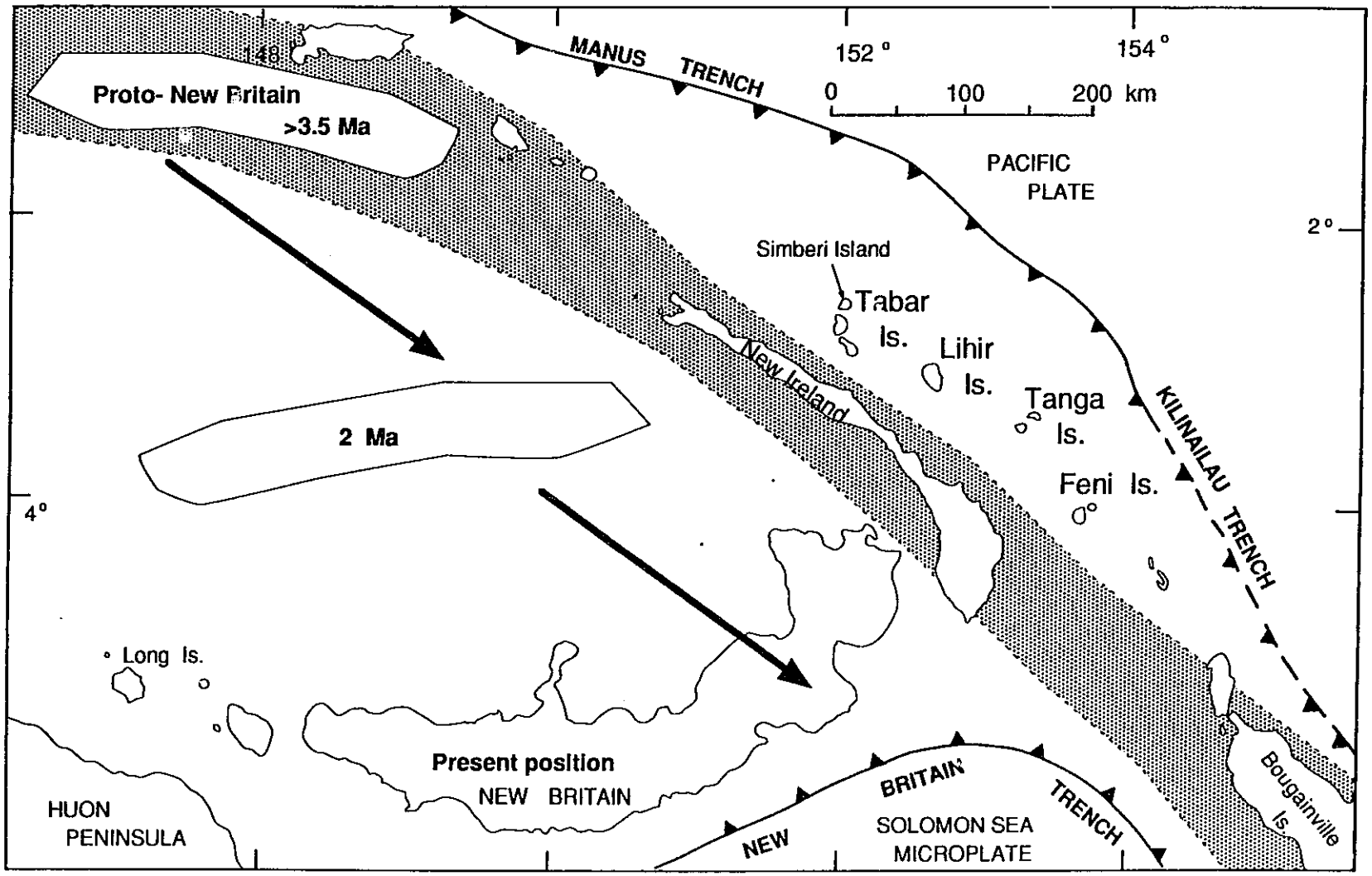
148
MANUS TRENCH
152 °
154 °
0
100
200 km
Proto- New Britain
>3.5 Ma
PACIFIC
PLATE
2 °
Simberi Island
Tabar
Is.
Lihir
Is.
Tanga
Is.
Feni Is.
New Ireland
KILINAILAU TRENCH
2 Ma
4°
Long Is.
Present position
NEW BRITAIN
HUON
PENINSULA
NEW
BRITAIN
TRENCH
SOLOMON SEA
MICROPLATE
Bougainville
Is.

D'Addario *et al.* 1976). A conjugate set of north to northeast high-angle tensional, normal faults on New Ireland (Hohnen, 1978) are transtensional phenomena (Figure 5). The most recent volcanic activity on New Ireland, the early Pliocene to early Pleistocene andesitic to dacitic volcanics of the Rataman Formation are associated with these transtensional features (Hohnen, 1978; Stewart *et al.* 1986; Stewart and Sandy, 1988). Exon *et al.* (1986) contend that the transform and conjugate faults present on New Ireland are relatively recent phenomenon associated with Manus Basin spreading.

Although these combined studies help to shape a general understanding of the complex tectonic development of the Bismarck Archipelago, the origin of the TLTF volcanic arc has remained enigmatic (Johnson *et al.* 1976; Johnson, 1979; Johnson *et al.* 1988). Strong dissimilarities between TLTF volcanic rocks and those of the other island arcs requires the formation of a model employing extensional tectonics in a region dominated by convergence and compression.

Tabar-Lihir-Tanga-Feni Island Arc: Early Tectonic Models

The TLTF arc is comprised of four island groups - Tabar, Lihir, Tanga, and Feni (Figure 5) - located on the leading edge of the Bismarck Plate, parallel to and equidistant ($\approx$ 110 km) from, the Manus-Kilinailau Trench. The island groups are equally spaced about 75 km apart. Each island group is aligned in a north to northeasterly direction, at a highly oblique angle to the arc trend. The Tabar and Lihir Group volcanoes rise 2000 m above the seafloor, while those of the Tanga and Feni Group rise to elevations of 2500-2900 m (Figure 6a).

Figure 5. Regional Tabar-to-Feni map showing transpressional transform faults and conjugate transtensional features. Seismic activity (1964-1985: McCue, 1988), bathymetry cross-sections (Figure 6a) and seismic-reflection survey tracks (NI-18; Figure 6b) are displayed.

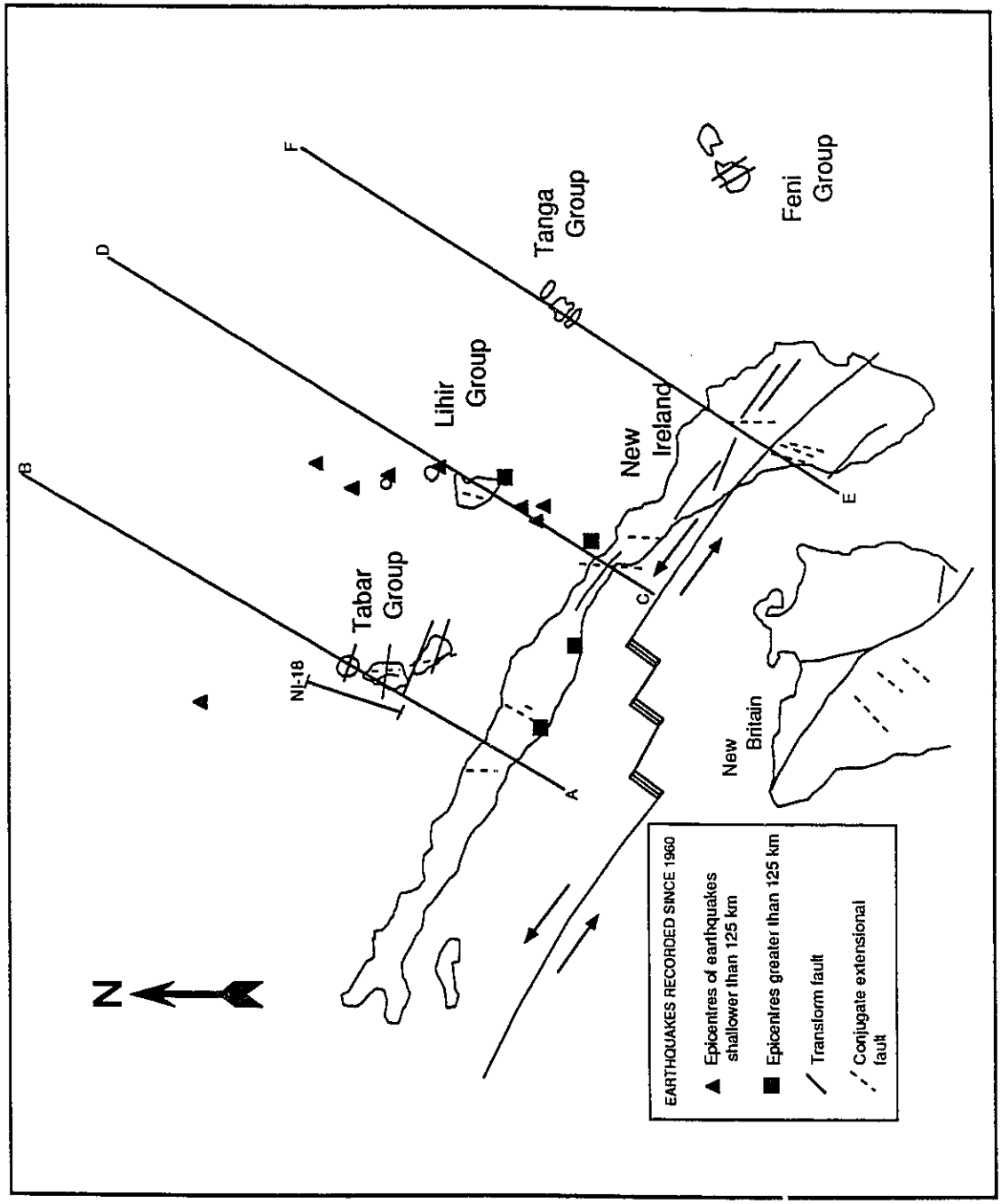
N
Tabar Group
Lihir Group
Tanga Group
Feni Group
New Ireland
New Britain
NI-18
A
B
C
D
E
F
EARTHQUAKES RECORDED SINCE 1960
Epicentres of earthquakes shallower than 125 km
Epicentres greater than 125 km
Transform fault
Conjugate extensional fault

The highly alkaline nature of the TLTF arc is unique among the calc-alkaline dominant arcs of Bismarck Archipelago. It is predominantly comprised of nepheline-normative rocks, including alkali olivine basalt, olivine nephelinite, basanite, tephrite, phonolitic tephrite, trachybasalt and trachyandesite (Johnson, 1979). Late stage quartz trachyte cumulodomes, representing the high silica end member of a strongly developed Daly gap (55 - 65% SiO_2), are the only quartz-normative rocks. Although these rocks are volumetrically insignificant, they represent an unsolved geological problem of long-standing (Daly, 1925, 1927; Yoder, 1973; Bailey, 1987), which further distinguishes the TLTF arc from the others. The surrounding arcs (1-3) contain "typical" calc-alkaline volcanic rocks dominated by andesites, but with a continuous range from tholeiitic basalt to andesite, dacite and rhyolite (Johnson, 1979). Although alkali-rich volcanoes are present in these arcs, they are not located near the fore-arc region as are the TLTF volcanoes, nor do the rocks attain the same degree of alkali enrichment.

Arculus *et al.* (1978) pointed out that volcanic rocks of the TLTF chain have hybrid mineralogical and chemical characteristics shared by both island arc and within-plate volcanic provinces. Early models (Johnson *et al.* 1976) sought to reconcile the island arc characteristics with the absence of evidence for a seismically-active subduction zone. Seismic surveys conducted by Gulf Oil (1973) over the basin between New Ireland and TLTF Islands outlined northerly-trending vertical fault zones, similar to horst and graben structures (Figure 6b). These data, combined with the presence of raised reef limestones and strong gravity anomalies (Finlayson and Cull, 1973), led Johnson *et al.* (1976) to speculate that TLTF volcanism occurred during isostatically-controlled uplift and partial melting of a

Figure 6. Bathymetry and seismic-reflection profiles in the Tabar-Lihir-Tanga-Feni arc region.

(a) Bathymetry profiles from Manus-Kilinailau trench to New Ireland

(b) Seismic-reflection profile (Gulf, 1973), adjacent to the Tabar Group.

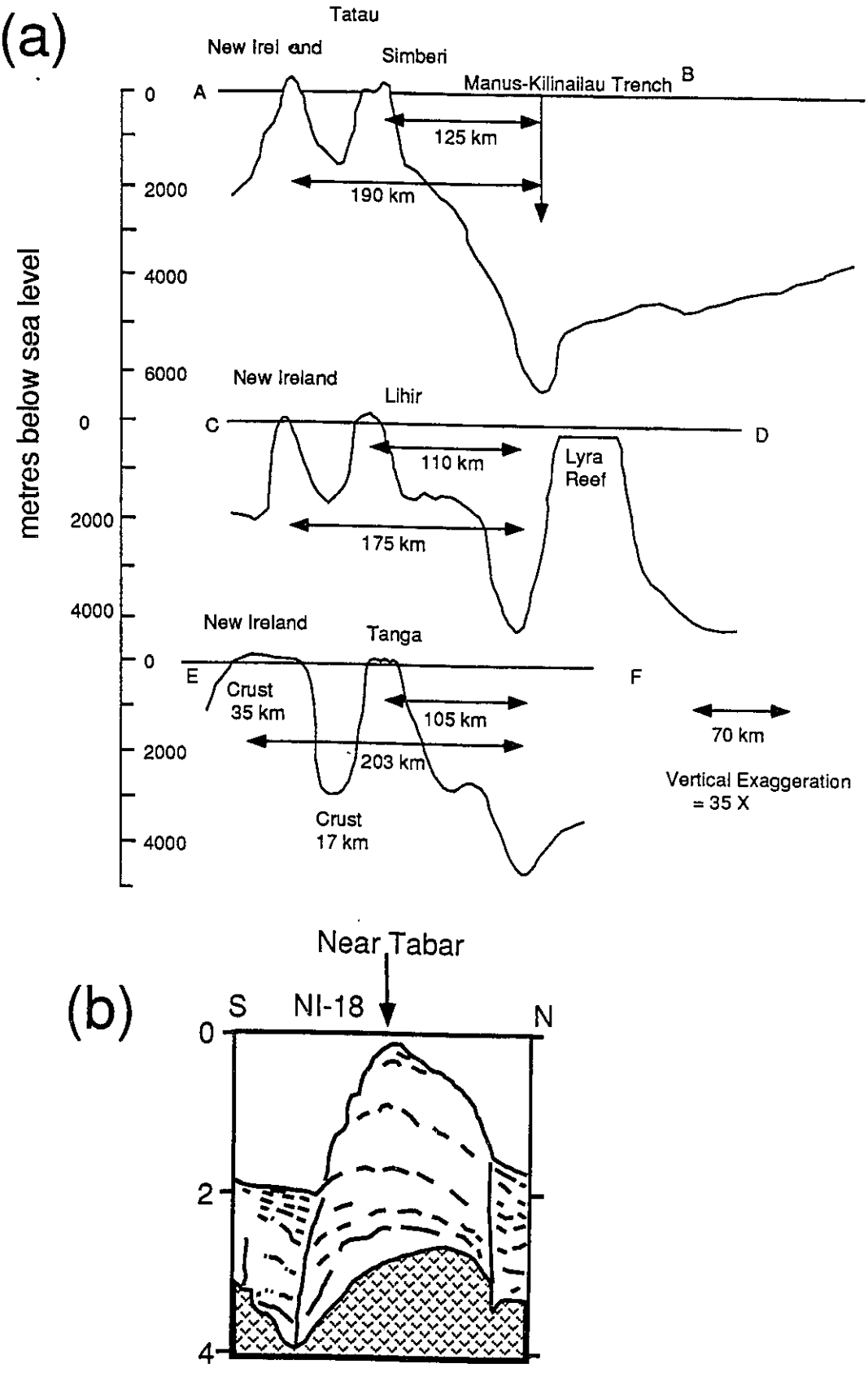
(a)
Tatau
New Ireland
Simberi
Manus-Kilinailau Trench
A
B
125 km
190 km
metres below sea level
0
2000
4000
6000
New Ireland
Lihir
C
D
110 km
Lyra Reef
175 km
New Ireland
Tanga
E
F
Crust 35 km
105 km
70 km
203 km
Vertical Exaggeration = 35 X
Crust 17 km
(b)
Near Tabar
S
NI-18
N
0
2
4

hydrous mantle region. Later oceanographic surveys conducted by a US-Australian-New Zealand research team (Exon *et al.* 1986), confirmed horst-graben development between Tabar and Lihir Islands, and identified 5000 m of inter-island sediments overlying the volcanic basement, observations consistent with a pull-apart basin model proposed by McKenzie (1978).

Extension accompanying pull-apart basin development would cause thinning of the lithosphere and consequent uplift and melting of the underlying asthenospheric mantle by adiabatic decompression (McKenzie, 1978). This process is essentially what Johnson *et al.* (1976) called upon to explain the TLTF volcanism, although the isostatic mechanism they invoked could not produce extension. Since extension-related volcanism in the Bismarck Archipelago is confined to a long and narrow region (New Ireland and the pre-TLTF basin, but not as far as Bougainville), a mechanism, operating locally, must be called upon to create lithospheric extension. A dramatic change in local stress regime accompanying the initiation of Manus backarc spreading (Figure 2) in the late Pliocene (Taylor, 1979) may provide an effective mechanism for lithosphere extension.

The temporal linkage of TLTF volcanism to subduction has obfuscated the development of a simple tectonic model. Taylor (1979) and Hamilton (1979) related volcanism to the extinct, westward-dipping Manus-Kilinailau subduction zone based on a Miocene age for the TLTF arc. A Miocene age for initiation of volcanism would place the TLTF region in the forearc of the Manus-Kilinailau subduction zone. In order to the reconcile age disparity, Johnson (1979) preferred

to link TLTF volcanism to the younger New Britain trench. Reversal in arc polarity at about 10 Ma would place the TLTF region in a backarc setting. The geochemistry of the TLTF volcanoes is, however, inconsistent with either tectonic setting.

An alternate model proposed by Johnson (1979), was that the opening of the Manus Basin caused New Ireland and the TLTF region to be transported to the northwest. The model suggests that during transposition of this region, uplift exerted by the Manus Basin spreading centre caused uplift of the enriched mantle region underlying the TLTF region, resulting in alkaline volcanism. This model proposed that the oldest volcanic rocks should be of late Pliocene age and occur in the Tabar Island Group, with younger volcanism to the southeast. At that time very few age dates were available from TLTF to support this model, and the apparent Miocene age for the Tabar Island Group could not be accounted for in this model.

A Revised Model for the Tectonic Evolution of the Tabar-Lihir-Tanga-Feni Arc

A revised model for the tectonic evolution is proposed below, based on new radiometric evidence and interpreted in the light of transtensional tectonics and adiabatic decompression melting. This model proposes that:

(1) Westward subduction of the Pacific Plate in the Manus-Kilinailau trench hydrated and enriched the asthenospheric mantle below the TLTF region in large-ion lithophile elements (LILE), however subduction-modified mantle regions did not reach the peridotite-H_2O-CO_2 solidus (Wyllie, 1977) during this period of subduction.

(2) Transposition of New Britain to the southeast, following initiation of backarc spreading in the Manus Basin, produced "localized" lithospheric perturbation in the New Ireland and TLTF regions.

(3) TLTF volcanism is the result of partial melting by adiabatic decompression of subduction-modified asthenosphere following lithosphere extension, where extensional lineaments were produced perpendicular to the displacement direction of New Britain.

This model reconciles the arc-type characteristics of TLTF volcanism and its highly alkaline nature as a result of extension-related partial melting of a subduction-modified mantle. It also explains why the TLTF arc volcanics are markedly different to the Bougainville-Solomon Island arc, even though they form a continuous island chain. It predicts that volcanism initiated in the Tabar Island Group at the same time the Manus Basin began spreading ($\approx$3.5 Ma) and that volcanic rocks progressively decrease in age towards Feni Island, as New Britain travelled southeast.

The greatest problem in constructing this tectonic scenario for the TLTF island arc is a paradox produced by micro-paleontological age determination from Simberi Island. Micropaleontological data from limestone overlying volcanic rocks on Simberi Island has been used to suggest a Miocene to Holocene age for TLTF volcanism (D.J. Belford in Johnson *et al.* 1976).

The limited radiometric age determinations from the TLTF arc hinder a detailed assessment of the revised model proposed above, but a synthesis of the

available data does confirm that the oldest dated volcanic rocks are from the Tabar Group on Simberi Island (see Table 1 for Tabar Group dating results). Ankaramitic volcanics form the platform on which the limestone rests, and the ankaramitic unit has provided consistent ages of 3.7 ± 0.2 Ma and 3.5 ± 0.2 Ma using K-Ar techniques (J. Rytuba, unpublished data). Volcanism continued on Simberi Island until 1.9 ± 0.3 Ma (this work) and progressed southward in the Tabar group until approximately 1 Ma (Wallace *et al.* 1983; Johnson *et al.* 1976). A Miocene age for volcanism in the TLTF island arc suggested by micropaleontological data is inconsistent with the new radiometric dating results, which support the revised tectonic model.

The radiometric dating shows a younging of volcanic activity in the island groups from northwest to southeast. In the Lihir group, intrusive rocks in the Luise caldera have been dated from 0.90 Ma to 0.35 Ma (Davies and Ballantyne, 1987). Volcanics in the Tanga group range in age from 1.1 ± 0.08 Ma to 0.19 ± 0.02 Ma (Johnson *et al.* 1976) and in the Feni Group, from 1.53 ± 0.15 Ma on the north island (Babase), to 0.68 ± 0.1 Ma and 0.49 ± 0.1 Ma on southern Ambitle. Ambitle hosts the youngest volcanic activity in the chain with a maar volcano that erupted 2,300 ± 100 years ago blanketing a 9 km^2 area with 5-30 m of trachytic tuff-breccia (Licence *et al.* 1987). The regional younging of volcanism from the TLTF island groups must be linked to lithospheric perturbation during the southeasterly movement of New Britain past New Ireland from 3.5 Ma to present.

Table 1. Radiometric dating of Tabar Island Group volcanics

Sample # (Island)	Rock type	Method	Material dated	Age ± 1σ(Ma)	UTM Coord. AMG Zone 56	Kennecott Survey Grid Coord.	# data	Source
8531 (Simberi)	Alk. Ol. Basalt (oc)	K-Ar	WR	3.5 ± 0.2	3911E 97086N	11180mE 8788mN	1	1
8532 (Simberi)	Alk. Ol. Basalt (sc)	K-Ar	WR	3.7 ± 0.2	3911E 97086N	11180mE 8788mN	1	1
8533 (Simberi)	Mugearite? (float)	K-Ar	WR	2.3 ± 0.4	3899E 97088N	10000mE 8944mN	1	1
8534 (Simberi)	Alk. Ol. Basalt (cc)	K-Ar	WR	3.1 ± 0.3	3901E 97114N	10160mE 10972mE	1	1
8528 (Simberi)	Acid-sulphate altn. (oc)	K-Ar	Al	2.8 ± 0.6	3897E 97102N	9848mE 10055mN	1	1
8537 (Tatau)	Hawaiite? (float)	K-Ar	WR	2.0 ± 0.2	3808E 96898N	----------	1	1
8539 (Tatau)	Hawaiite (outcrop)	K-Ar	WR	1.91 ± 0.1	3816E 96885N	----------	1	1
22 (Simberi)	Hawaiite (outcrop)	Ar-Ar	Am	2.9 ± 0.6	3893E 97065N	9525E 7135N	2	2
SORD PLUT (Simberi)	Mugearite (outcrop)	Ar-Ar	Am	2.94 ± 0.25	3899E 97099N	10000mE 9820mN	6	2
310 (Simberi)	Alk. Ol. Basalt (oc)	Ar-Ar	Cpx	1.92 ± 0.27	3875E 97099N	8100mE 9800mN	1	2
337 (Simberi)	Hawaiite (outcrop)	Ar-Ar	Am	3.13 ± 0.06	3896E 97072N	9735mE 7685mN	3	2
347 (Simberi)	Alk. Ol. Basalt (bldr)	Ar-Ar	Am	3.6 ± 0.8	3901E 97068N	10170mE 7380mN	3	2
TB3/11 (Tabar)	Quartz trachyte (oc)	K-Ar	Pl	0.99 ± 0.08	3840E 96810N	----------	1	3

Abbreviations: WR = whole rock; Al = Alunite; Am = amphibole; Pl = plagioclase; Cpx = clinopyroxene; oc = outcrop; bldr = boulder; altn = alteration; sc = scree; AMG = Australian Map Grid

Source

1. J. Rytuba, USGS, unpublished data provided to Kennecott Exploration (Australia) Ltd.
2. This work, analysis by R. Drake, Institute of Human Origins, U. Cal.(Berkeley)
3. Johnson *et al.* (1976)

The north to northeasterly orientation of each of the island groups, when coupled with marine seismic data (Figure 6b) strongly argues that each of the island groups are horsts (Wallace *et al.* 1983). Radar images (Figure 7) and geophysical data from the Tabar and Lihir groups (Kennecott Explorations, unpublished data) as well as regional geological studies of the arc (Wallace *et al.* 1983; Exon *et al.* 1986; Stewart *et al.* 1986) distinguish two predominant fault directions; a west-northwest to north-northwest trend and a north to north-northeast trend. These structural features are considered consanguineous to those described earlier from New Ireland.

Historical records of seismic activity in the TLTF island arc show a concentration of shallow, low-magnitude earthquakes oriented in the north-northeast direction under the Lihir Island group (Figure 5)(Johnson, 1979; McCue, 1988), extending south towards New Ireland. This indicates that rifting and horst development is continuing. The linear chain of younging southward volcanic islands within the Tabar, Lihir and Feni Island Groups is evidence that extension is propagating southward, and it is possible that submarine volcanic activity is present to the south of the Lihir Island Group.

A model of transtensional-related lithosphere extension leading to adiabatic decompression melting of subduction-modified mantle peridotite best explains the chemical and physical characteristics of TLTF volcanism. The nepheline-normative volcanic rocks are considerably different from the usual andesitic style of volcanism produced in the Bismarck and Bougainville-Solomon island arcs, and have some mineralogical and geochemical characteristics more in common with rift-related

Figure 7. Digital radar image of the Tabar Island Group. The Tabar Island Group comprises, from north to south, Simberi, Tatau, and Tabar Islands.

Simberi Island (9 km wide x 7.5 km long) is the oldest in the group and consists of a central circular volcanic region surrounded by uplifted limestone reefs. Two directions of lineaments crosscut Simberi Island: (1) a set of north to northeast trending structures, and (2) a set of west to northwest trending structures.

Tatau Island (12 km wide x 16.5 km long) consists of a central volcanic region with a uplifted limestone platform to the east and north. Northwesterly oriented lineaments are best displayed in the radar image.

Tabar Island (8 km wide x 20 km long) consists of two young volcanic centres separated by a north trending lineament. The circular feature to the northwest is the Tiripats caldera, which has a central quartz trachyte cumulodome (TB3/11 on Table 1). The western portion of the caldera has down-dropped into the ocean. The southeastern part of Tabar Island consists of the Banessa volcano, which is crosscut by northwest-trending lineaments.

Gold and copper mineralization is associated with volcanic activity in each of the islands.

This digital radar mosaic was produced for Kennecott Explorations (Australia) Ltd., Sydney, Australia by INTERA Technologies Ltd., Calgary, Alberta.

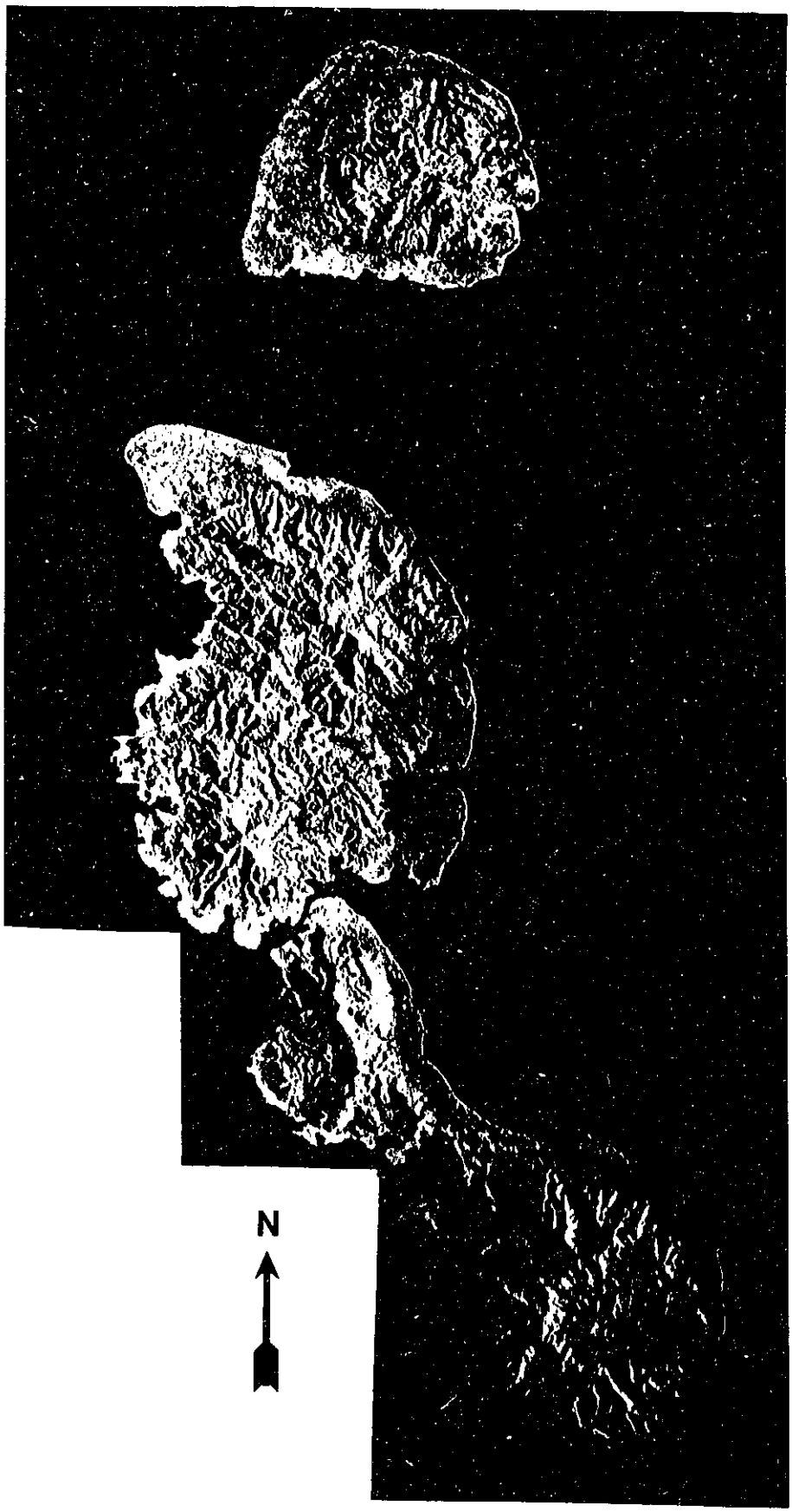
N

volcanics of the Rhine Graben and East Africa. A common denominator in the petrogenesis of these magmas appears to be the presence of a carbonated, hydrated source mantle region enriched in alkali elements. The following sections will discuss the geology, petrology, geochronology and geochemistry of mantle-derived lavas from Simberi Island, and how their contained xenoliths and xenocrysts provide evidence that subduction processes created a carbonated, hydrated enriched mantle region below the TLTF arc.

Chapter 2. Field Nomenclature and Chemical Classification

Simberi Volcanic Nomenclature

A rock classification scheme, based on the modal abundance of porphyritic minerals, was developed during the field component of this work. Table 2 outlines the field names of Simberi volcanics and related information. Clinopyroxene is a predominant mineral in all Simberi volcanics, so the presence of other minerals was used to distinguish rock types. Feldspathoidal minerals (nepheline, haüyne-sodalite, analcite, leucite and nepheline) are common constituents of the nepheline-normative TLTF lavas, and therefore mafic to intermediate volcanic units are given the terms trachybasalt and trachyandesite. These terms do not correlate with the terminology of Johnson *et al.* (1976) and Wallace *et al.* (1983), who classified trachybasalts and trachyandesite using chemical analyses. The majority of rocks described in the field as trachybasalt and trachyandesite plot in the trachybasalt field of the above workers.

Chemical Classification of Simberi volcanic rocks

Chemical and isotopic analysis was performed on the volcanic rocks collected on Simberi Island. Methods of analyses are provided in Appendix A. Simberi and Tatau Island whole rock analyses and previously reported analyses of other rocks from the Tabar Group (Johnson *et al.* 1976; Wallace *et al.* 1983) are given in Appendix A.8.

The rocks of the TLTF arc are difficult to classify using conventional classification schemes because they show characteristics common to both alkali

olivine basalt (continental rift-related and deep subduction environments), calc-alkali series volcanic rocks (subduction related environments) as defined by Irvine and Baragar (1971) and lamprophyres as defined by Rock (1987) and Rock and Finlayson (1990). In addition, the evolution of the volcanic rocks from nepheline-normative to quartz-normative compositions is a trend not displayed by classical monogenetic volcanic suites.

Table 2. Field classification of Simberi volcanic units

Field Classification (Field term)	IUGS Chemical Classification (CIPW norm)	Criterion used in field	Porphyritic minerals in order of abundance	Groundmass minerals
Basalt (Olivine Basalt)	Alkali Olivine Basalt (Basanitoid)	Olivine present	Clinopyroxene ± olivine	Mafic » felsic
Basalt (Clinopyroxenite)	Alkali Basalt (Ankaramite)	Porphyritic clinopyroxene predominant, no olivine		Mafic > felsic
Trachybasalt	Hawaiite	Porphyritic amphibole > plagioclase	Clinopyroxene + amphibole + plagioclase ± apatite	Mafic ≥ felsic
Trachyandesite	Mugearite	Porphyritic plagioclase ≥ amphibole = clinopyroxene	Amphibole + plagioclase + clinopyroxene + apatite	Felsic > mafic
	Benmoreite (uncommon)	Porphyritic plagioclase > amphibole ≥ clinopyroxene	Plagioclase + amphibole + clinopyroxene + apatite ± biotite	Felsic » mafic

Johnson *et al.* (1976) devised a CIPW-normative classification scheme for TLTF rocks based on a plot of Differentiation Index (Thornton and Tuttle, 1960)

versus normative nepheline or normative quartz + silica from normative hypersthene, after recalculating their Fe_2O_3/FeO ratios according to the methods outlined by Irvine and Baragar (1971). Wallace *et al.* (1983) tentatively continued the usage of this scheme without performing the Irvine and Baragar (1971) transformations,

> "on the grounds that the relatively high Fe_2O_3/FeO values and high volatile contents of Tabar-to-Feni rocks may at least in part be intrinsic features of the magmas, and that transforming the data by the above criteria may be an overcompensation."

Glassy, unaltered Simberi rocks have high Fe_2O_3/FeO ratios and low TiO_2 contents and, therefore, calculation of the iron oxidation ratio and rock classification using the method of Irvine and Baragar (1971) is inappropriate. Figure 8a and 9 are oxide-silica plots which have been constructed by recalculating the raw geochemical data in Appendix A.8 to 100% on an H_2O- and CO_2-free basis. Figure 8a is a [illegible] alkalies and silica (TAS) diagram recommended for chemical classification by the IUGS Subcommission on the Systematics of Igneous Rocks (Le Bas *et al.* 1986). The TAS classification diagram must be used with caution since few of the analyses meet the optimal criterion of $<2\%$ H_2O and $<0.5\%$ CO_2. Using the IUGS classification, Simberi volcanic rocks include basalts, trachybasalts, basaltic trachyandesites and trachyandesites. Based on the initial Na_2O/K_2O ratio of 3 for primitive basalts (Figure 8b), the basalts, trachybasalts, basaltic trachyandesites and trachyandesites can be further classified as alkali basalts, hawaiites, mugearites and benmoreites, respectively, according to Le Bas *et al.* (1986). The most mafic alkali basalts contain 5 to 8% normative nepheline, analcimic glass, and can be designated as analcime basanites. "Basanite" is used

Figure 8. Alkali oxides vs. SiO_2 for Simberi Island volcanic rocks.

(a) Total alkali-silica (TAS) diagram with IUGS classification scheme. Simberi rocks are plotted after recalculation to an H_2O- and CO_2-free basis.

(b) Harker diagram showing the variation in alkali element distribution with silica content of Simberi volcanic rocks (raw data).

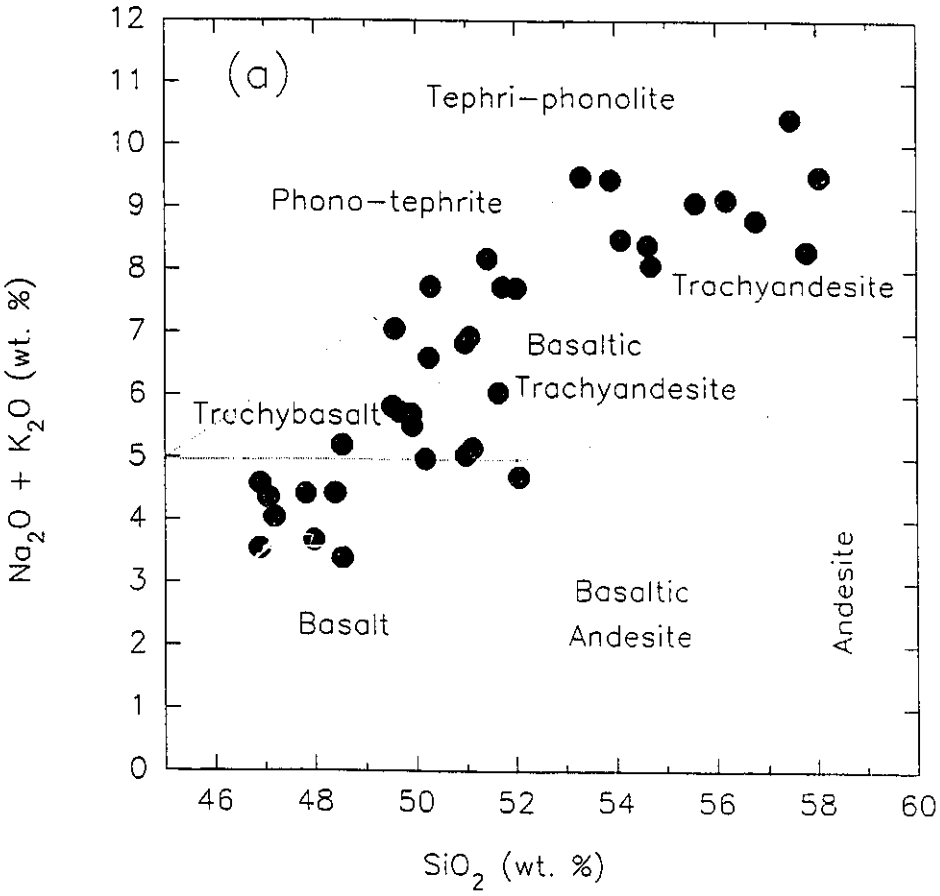
(a)
Tephri–phonolite
Phono–tephrite
Trachyandesite
Basaltic
Trachyandesite
Trachybasalt
Basalt
Basaltic
Andesite
Andesite
$Na_2O + K_2O$ (wt. %)
SiO_2 (wt. %)

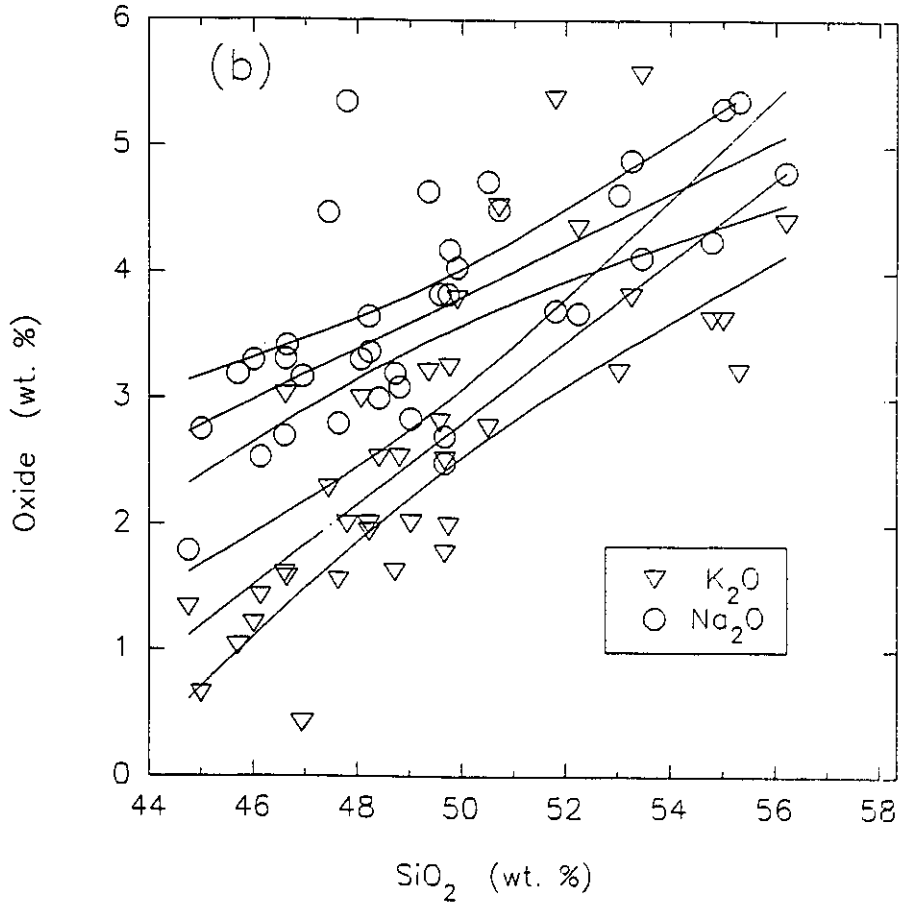
(b)
K_2O
Na_2O
Oxide (wt. %)
SiO_2 (wt. %)

instead of "basanatoid", because basanites and basanatoids are geochemically indistinguishable. Clinopyroxene-phyric basalts have >20% normative clinopyroxene and can be designated as ankaramites (Philpotts, 1989).

Simberi lavas are plotted on a K_2O-silica diagram with designated fields for calc-alkalic, high-K calc-alkalic and shoshonite series volcanic rocks (Figure 9). The most primitive basaltic melts plot within the calc-alkalic to high-K calc-alkalic series, whereas the more evolved intermediate suite plots within the shoshonite field. The shift from high-K calc-alkalic character to shoshonitic character can be attributed to: (1) the rapid and early crystallization of olivine + clinopyroxene + magnetite from primitive basaltic magmas and, (2) the later continuous depletion of Ca and Mg during clinopyroxene fractionation and of Na due to amphibole fractionation. As a result, the evolved liquids are richer in K_2O due to the incompatible nature of K. In this sense, the evolved Simberi volcanic lavas are broadly similar to the 'shoshonite' suite of Joplin (1968), Gill (1970), and Morrison (1980). Other similarities to shoshonites include high Al_2O_3 (12-20 wt. %), high total alkalis (Na_2O+K_2O; Figure 8a), and enrichments in the large ion lithophile elements (LILE) Rb, Sr, Ba, Pb and light rare earth elements (LREE). Unlike shoshonites, Simberi volcanic rocks do not have high K_2O/Na_2O ratios at high silica contents (ie. K_2O/Na_2O ratio is <1 at 55% SiO_2; Figure 8b), rarely contain biotite phenocrysts, are depleted in P, and almost always contain nepheline in normative calculations.

For the purpose of classification, the Simberi lavas are more appropriately described as belonging to the high-K calc-alkalic series volcanic rocks, but the high MgO, Fe_{total}, Cr and Ni abundances of the primitive basalts indicates that they also

Figure 9. Anhydrous K_2O-SiO_2 variation diagram for Simberi volcanic rocks with fields delimiting calc-alkaline, high-K calc-alkaline and shoshonitic compositions.

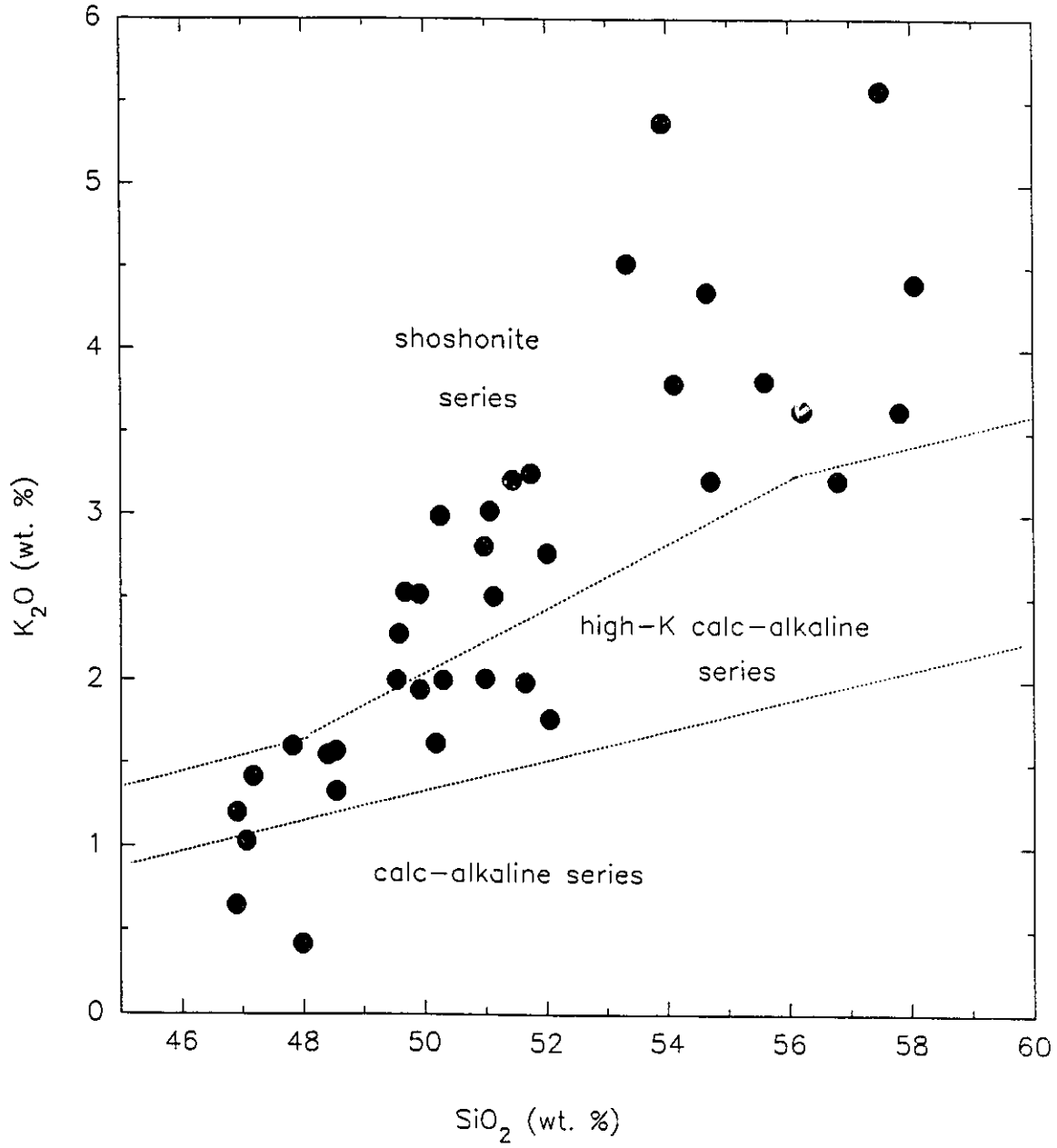
6
5
4
3
2
1
0
46
48
50
52
54
56
58
60
K_2O (wt. %)
SiO_2 (wt. %)
shoshonite
series
high-K calc-alkaline
series
calc-alkaline series

have affinities to the within-plate alkali olivine basalt series. In this respect they resemble the Porgera igneous intrusive suite, associated with the world-class Porgera Au deposit, in the Engu Province of Papua New Guinea. Richards (1990) designated the Porgera igneous rocks as a within-plate, sodic "alkali basalt→hawaiite→mugearite suite". Rock and Finlayson (1990) criticized this, suggesting instead that the suite had shoshonitic affinities, and were more properly classified as appinitic/lamprophyric based on the mineralogical argument that volcanic shoshonites should possess "essential K-feldspar in the groundmass or, especially, as rims to plagioclase", which Porgera rocks do not have. Although sanidine is present in the quartz trachyte group in the TLTF arc (Wallace *et al.* 1983), alkali feldspar is not present in the abundantly nepheline-normative lavas, which led Heming (1979) to point out this mineralogical inconsistency with the shoshonite suite.

The Simberi mafic rocks generally fulfil the somewhat broad criteria for lamprophyre classification (Rock, 1987; Rock and Finlayson, 1990). All rocks contain amphibole except that amphibole in the basalts have been partially to completely destabilized to a high temperature anhydrous assemblage. Rare biotite occurs only in the Simberi mugearites and benmoreites. Other criteria include minerals rich in F, Cl, SO_3, CO_2 and H_2O. The TLTF rocks are characterized by volatile-rich phenocrysts including apatite, haüyne-sodalite and analcime (Wallace *et al.* 1983). In addition, the minerals anhydrite, calcite, sodalite, analcime and Ba-phillipsite have been found within exotic alkali-rich melt inclusions in xenoliths and the cores of apple-green sodian diopside xenocrysts. The occurrence of zoned diopsidic pyroxenes with sodic green cores is itself a common occurrence in alkali

basalts and lamprophyres (Scott, 1980; Bédard *et al.* 1988).

Amphiboles of magnesio-hastingsite composition in Simberi lavas, and ranging from "magnesio-hastingsite through magnesio-hastingsitic hornblende, to edenitic hornblende" in the entire TLTF arc (Wallace *et al.* 1983), would place the Simberi mafic rocks in the calc-alkaline lamprophyre region of Rock (1987, p. 201), although some ultramafic and alkaline lamprophyres also plot in this region. The presence of 'globular structures' in lamprophyres is also argued by Rock (1987) to be a distinguishing characteristic, and these are a relatively common phenomenon in Simberi igneous rocks, to the point where they were used by the author during geological mapping to make the often difficult discrimination between intrusive rocks and massive crystal tuff units. The globular structures on Simberi represent felsic liquids which are immiscible within the mafic groundmass liquid of both mafic and intermediate lavas. The texture is most strongly developed on weathered surfaces where the felsic globules form resistant knobs (Figure 10). The interpretation of these globules as felsic-mafic immiscibility is supported by Philpotts (1972, 1976) and Eby (1980).

Discrimination of lamprophyre type by chemical variation diagrams (Rock, 1987, p. 208) would place the Simberi volcanic rocks within the calc-alkaline lamprophyre region. This is in accord with the marked high-field strength element depletion (Ti, Ta, Nb, Zr, Hf and P) in Simberi rocks, which is a characteristic strongly developed in destructive margin volcanoes. Enrichments in LILE and REE are characteristic of lamprophyres in general, which also matches the TLTF rocks, although the ΣREE abundance of Simberi lavas would be at the lower range of calc-

Figure 10. Outcrop of mugearite near Samat with globular structures. The knobby texture results from differential erosion. Globules contain felsic glasses which are more resistant to erosion than the mafic groundmass glass.

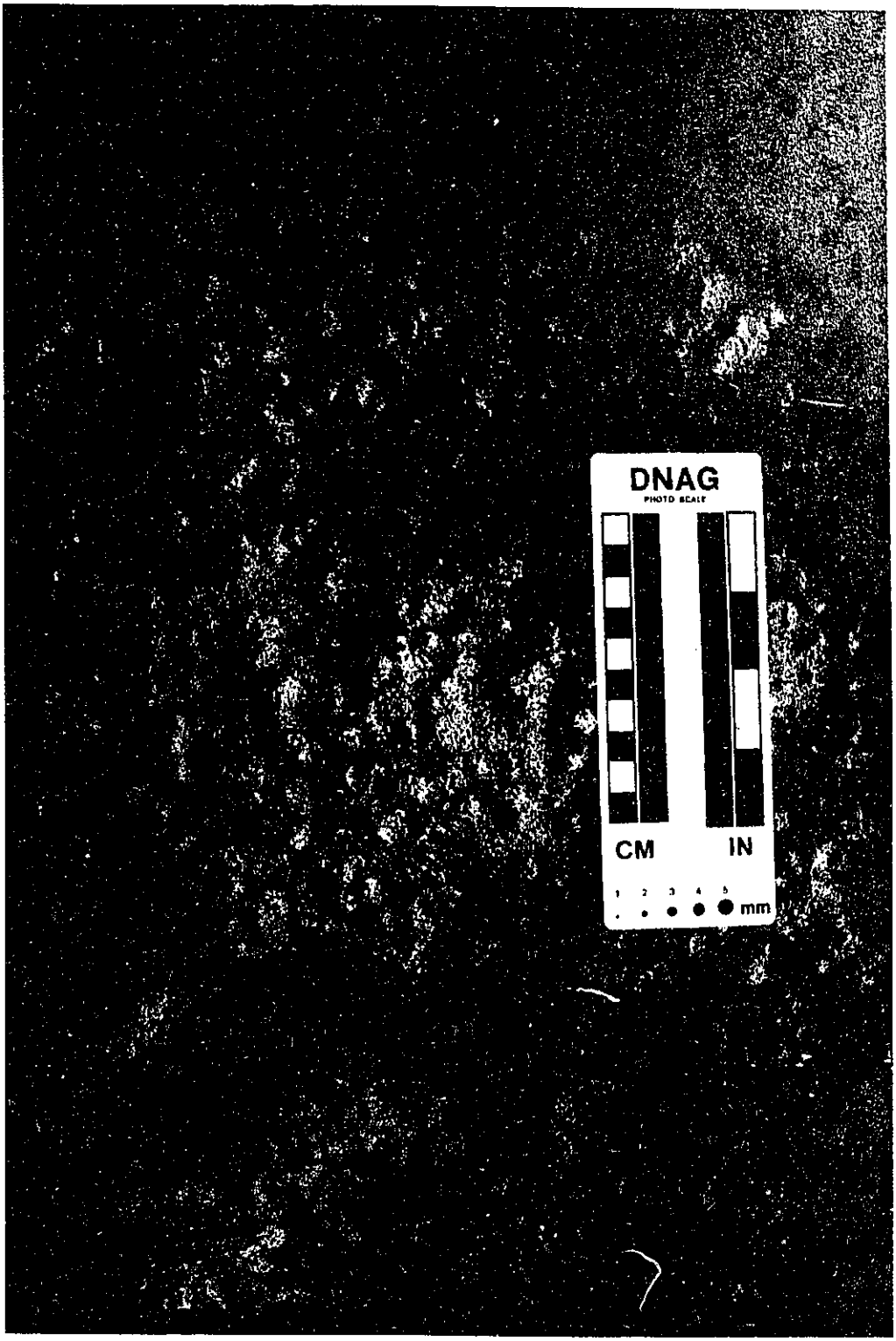
DNAG
CM
IN
mm

alkaline lamprophyres.

Problems of rock classification

The recognition that TLTF mafic rocks have both lamprophyric and calc-alkaline affinities is important in showing their hybrid character with the potential for understanding the petrogenesis of both rock types. The chemical classification scheme for volcanic rocks accepted by the IUGS (Le Bas, 1987) and the mineralogical classification scheme for lamprophyres (Rock, 1987) necessarily produces a dichotomous classification of the same rock unit (e.g. Porgera; Rock and Finlayson, 1990), whereas in reality a continuum exists between the continental within-plate calc-alkaline lamprophyre clan and high-K calc-alkaline rocks. The fundamental process relating them is mantle enrichment by alkali metasomatism, while what differentiates them is post-metasomatism igneous processes (residence time in the mantle, depth of partial melting and crystallization, and degree of partial melting). A corollary of the above discussion is that a primary basalt, similar in composition to the alkali olivine basalts of the Simberi Island volcano, would produce a calc-alkaline lamprophyre if emplaced at mid-crustal levels in a continental environment (Wilson, 1989, p. 397).

Simberi rock classification

Simberi Island and the entire TLTF arc can be regarded as an igneous suite transitional from high-K calc-alkaline to shoshonitic. Since a lamprophyric classification is inappropriate for volcanic rocks (Currie, K., pers. comm. 1991), Simberi rocks will be classified according to the criteria described by Le Bas *et al.* (1986), and shall be described as alkali olivine basalt (basanite, ankaramite and alkali basalt), hawaiite, mugearite and benmoreite despite the objections of Rock

and Finlayson (1990, p. 249) to this terminology.

Importance of igneous rock classification to gold deposit models

The classification of the distinct magma series of the TLTF arc is important because each of the volcanic islands, except Tanga which is largely submerged, hosts Au deposits. That similarities exist between the calc-alkaline TLTF volcanic rocks and the calc-alkaline lamprophyre suite is of significance to the modelling of Au metallogenesis. Rock and Groves (1988a, 1988b) argued for a co-genetic relationship between Au-rich calc-alkaline lamprophyres and Archean mesothermal Au deposit formation (Rock *et al.* 1989). Other researchers (Wyman and Kerrich, 1988; 1989) argued for a geodynamic relationship between lamprophyre emplacement and Au deposit genesis, specifically to transpressional tectonics in subduction zone environments. Economic geologists working in Phanerozoic rocks know that a relationship exists between subduction and Au-Cu deposits (Sillitoe, 1972; Solomon, 1990), although a mechanism to explain gold enrichment in subduction zone magmas has only recently been proposed (McInnes *et al.* 1991). This mechanism, discussed fully in Part C of the thesis, has bearing on the postulated lamprophyre-Archean Au deposit association.

The continuum between Phanerozoic calc-alkaline lamprophyres and alkaline island arc magmas in the genesis of Au deposits in Papua New Guinea (Porgera, Lihir, Simberi) implies a continuum between Phanerozoic and Archean Au mineralization. Since calc-alkaline lamprophyres and alkaline arc magmas share similar source region characteristics (metasomatism), but differ in degrees of partial melting of the source region and mode of emplacement in the earth's crust, then

the formation of Archean Au deposits implies that metasomatism of the mantle wedge above subduction zones occurred as early as 2720 Ma (Corfu and Andrews, 1987). The corollary is that the age of the oldest Au deposit on Earth will constrain the beginning of mantle metasomatism related to subduction processes.

Chapter 3. Geology of southeastern Simberi Island

Introduction

Simberi Island (the northernmost of three islands in the Tabar Island group) is located in equatorial Papua New Guinea (Figure 2), and is covered by dense, primary evergreen rain forest except along the sparsely populated coastal regions. Topography varies from 0 to 250 m with moderate to steep slopes. The climate is hot and humid with rainfall exceeding 2.5 m per year. The drier season occurs in July and August. The vegetation of the Tabar-Lihir-Tanga-Feni (TLTF) island chain is of the mixed lowland tropical rain forest type (Johns, 1972).

Rock exposure in densely vegetated tropical regions is usually poor. Reconnaissance geological surveys of the TLTF arc by Wallace *et al.* (1983) were conducted prior to the discovery of gold deposits on Simberi, Lihir and Feni Islands and carried out by difficult traversing of stream beds in high-relief volcanic terrain without the aid of high quality topographic maps and air photos. Their results provide a framework on which this study builds. This study was restricted to areas in the southeastern quarter of Simberi Island where the greatest amount of mineral exploration activity has occurred, providing the opportunity to investigate new areas of outcrop exposed during road construction. With the cooperation, encouragement and financial support of Kennecott, this study was able to combine geological investigations (mapping of drill access roads and creek beds) with the most advanced digital radar imaging and radiometric dating methods to decipher the geological evolution of the southeastern quarter of Simberi Island.

Geology of Carbonate Units

The topography of Simberi Island is strikingly revealed in the digital radar mosaic (Figure 7). Simberi Island consists of a broad, flat-lying coastal region consisting of raised Quaternary coral-reef surrounding a circular, central plateau of volcanic rocks (Figure 11). Perched on the outermost fringe of the volcanic plateau is a narrow unit of uplifted limestone, possibly of late Miocene to Pliocene age (Wallace *et al.* 1983). This limestone cap attains a height of 180 m and encircles the central volcanic plateau, except in the south and southeastern regions. The limestone is massive, and consists of limestone blocks, corals, and algae and therefore this circular unit represents an uplifted paleo-fringing reef. Observations of the limestone reef unit at Monambur by this author and Wallace *et al.* (1983), indicate that very few of the large (1 to 1.5 m diameter) coral heads are in growth position and that many are fragmented. No volcanic rocks are contained within the unit.

In 1969, four samples of the uplifted limestone cap unit were collected by G.A.M. Taylor and microfaunal assemblages interpreted by D.J. Belford. Three of the assemblages were reported to be of lower Miocene age while the fourth was categorized as Pliocene (Wallace *et al.* 1983). As mentioned in Chapter 1, a paradox exists between these data and radiometric dating of a mafic volcanic unit exposed on a cliff face below the limestone cap (Figure 12; Table 1; Samples 8531 and 8532). This cliff exposure shows a 30-40 m thick deposit of volcanic breccia overlying an approximately 10 m high outcrop of mafic clinopyroxenite dated at 3.5 Ma and 3.7 Ma (K-Ar). The volcanic breccia is a heterolithic assemblage of boulder to pebble sized clasts of predominantly trachyandesitic composition, but

Figure 11. Geology map of southeastern Simberi Island. Line X-Y is a schematic cross-section presented on Figure 12. Lines A-B and C-D are cross-sections of the North and South Samat diatremes, presented in Figures 14 and 17, respectively. Rock sample locations have been determined using a Kennecott detailed survey grid (dashed lines; units in metres).

Geology by the author, except for the carbonate units which were compiled from the maps of Wallace *et al.* (1983) and unpublished Kennecott data. Abbreviations: bx = breccia; AOB = alkali olivine basalt.

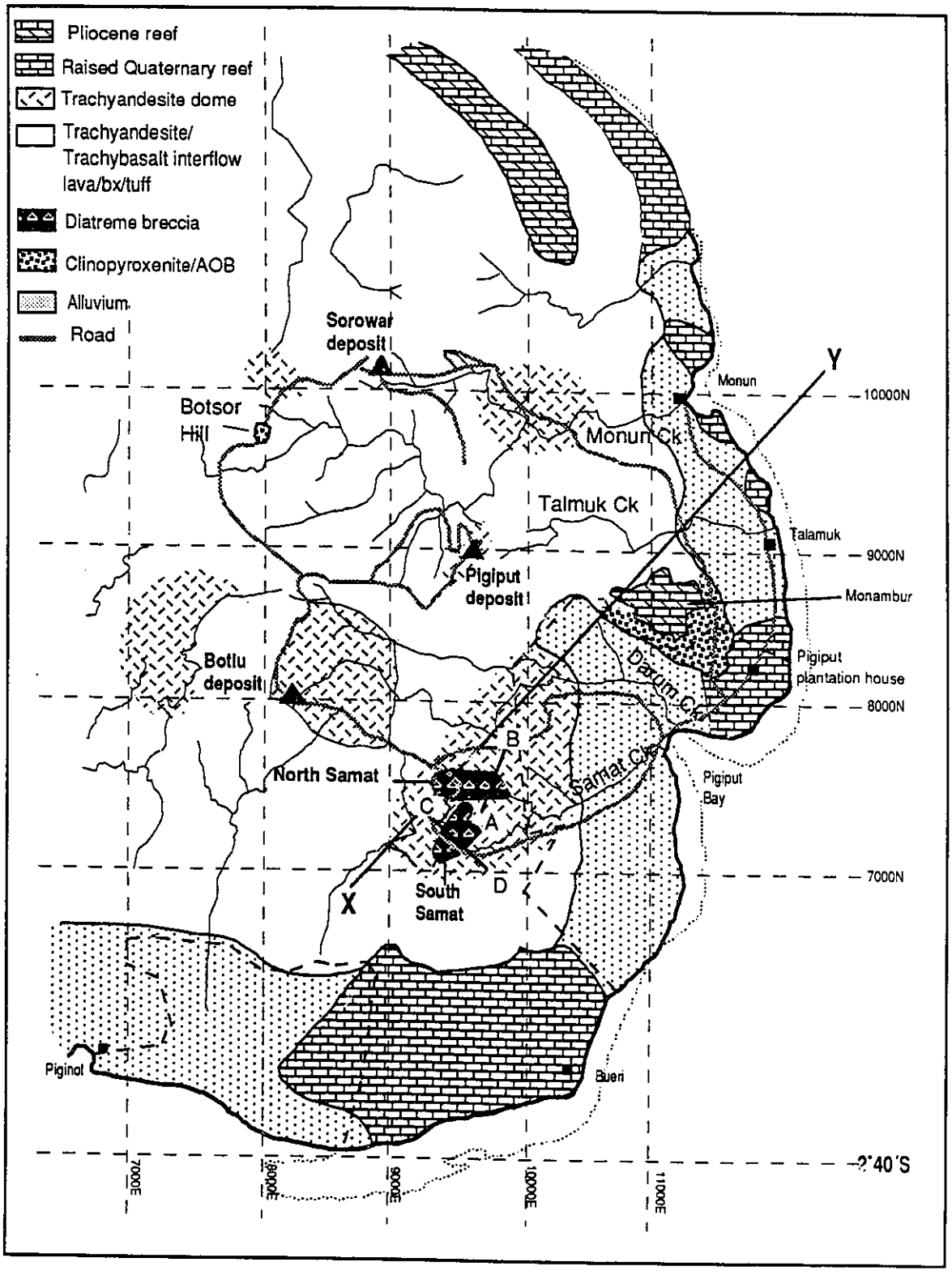
Pliocene reef
Raised Quaternary reef
Trachyandesite dome
Trachyandesite/
Trachybasalt interflow
lava/bx/tuff
Diatreme breccia
Clinopyroxenite/AOB
Alluvium
Road
Sorowar
deposit
Botsor
Hill
Monun
Monun Ck
Talmuk Ck
Talamuk
Pigiput
deposit
Monambur
Botlu
deposit
Pigiput
plantation house
Datum Ck
B
North Samat
Samat Ck
Pigiput
Bay
C
A
D
South
Samat
X
Y
Piginot
Bueri
10000N
9000N
8000N
7000N
2°40'S
7000E
8000E
9000E
10000E
11000E

clinopyroxenite clasts were also noted. A horizontal zone of rounded boulders within this outcrop suggests aqueous reworking of a previous volcaniclastic deposit. The contact between this unit and the overlying limestone is obscured by the development of massive calc-tufa (travertine) deposits which drape over the volcanics. Clearly, this discrepancy in age requires further study.

The southern coastal plains of Simberi Island consist of Quaternary reef complexes, which cover the southerly dipping lower Miocene to Pliocene reef unit (Wallace *et al.* 1983). This indicates that the northern portion of Simberi Island has been uplifted relative to the southern portion since early Pliocene time. Uplift has continued through the Quaternary, and the wider extent of coastal plains in the western and northwestern parts of the island has led Wallace *et al.* (1983) to suggest that Quaternary uplift has tilted the island to the east-southeast. Wave-cut notches 2 m above modern sea-level in the Quaternary limestone between Pigiput plantation and Monun village on the eastern side of the island suggests that the whole island since the Quaternary has been uplifted, although the northwesterly side of the island may be experiencing uplift at a faster rate.

Geology of Volcanic Units

Pluvial erosion rates in tropical regions are estimated to be as high as 0.75 mm yr^{-1} (Ruxton and McDougall, 1967). The radiometric ages determined from Simberi Island volcanics (Table 1) indicate that the geology of Simberi Island (Figure 11) is of a volcano exposed at 2 to 3 km depth. Geological mapping of a densely vegetated, dissected volcano, where individual volcanic units vary diversely in character over several metres, is an impossible task (M. Lambert, pers. comm.), and

therefore this discussion will be restricted to volcanic features of general interest.

Wallace *et al.* (1983) divided the volcanic rock types into two broad categories - a lowermost unit containing mafic to intermediate flows overlain by predominantly intermediate volcaniclastics, which they interpreted as an evolution from an effusive to an explosive style of eruption.

Effusive volcanism

Clinopyroxenite - Ankaramitic basalts

The oldest volcanic unit exposed on the island is a massive unit of clinopyroxene-phyric lavas of ankaramite basalt composition. This unit underlies the uplifted reef limestone at Monambur, the plantation house and main Kennecott exploration camp near Pigiput Bay and is exposed along the drill road constructed just north of its intersection with Talamuk creek. Termed clinopyroxenite in the field, this rock is characterized by its dark green to black colour and its coarse grained (6-15 mm) porphyritic pyroxenes hosted within a glassy groundmass. Samples contain up to 30% black clinopyroxene phenocrysts with columnar to columnar-tabular habit. Magnetite is common in the groundmass, and aeromagnetic surveys indicate that this unit has the strongest positive electromagnetic response on the island, which is located between the base camp and Monambur (KEA, unpublished geophysical data). It is often vesicular with vesicles occasionally making up 30% of the rock volume. Coarse vesicles containing euhedral calcite and analcite, and occasionally pyrrhotite, have been noted.

Figure 12. Schematic cross-section of geological units on Simberi Island.

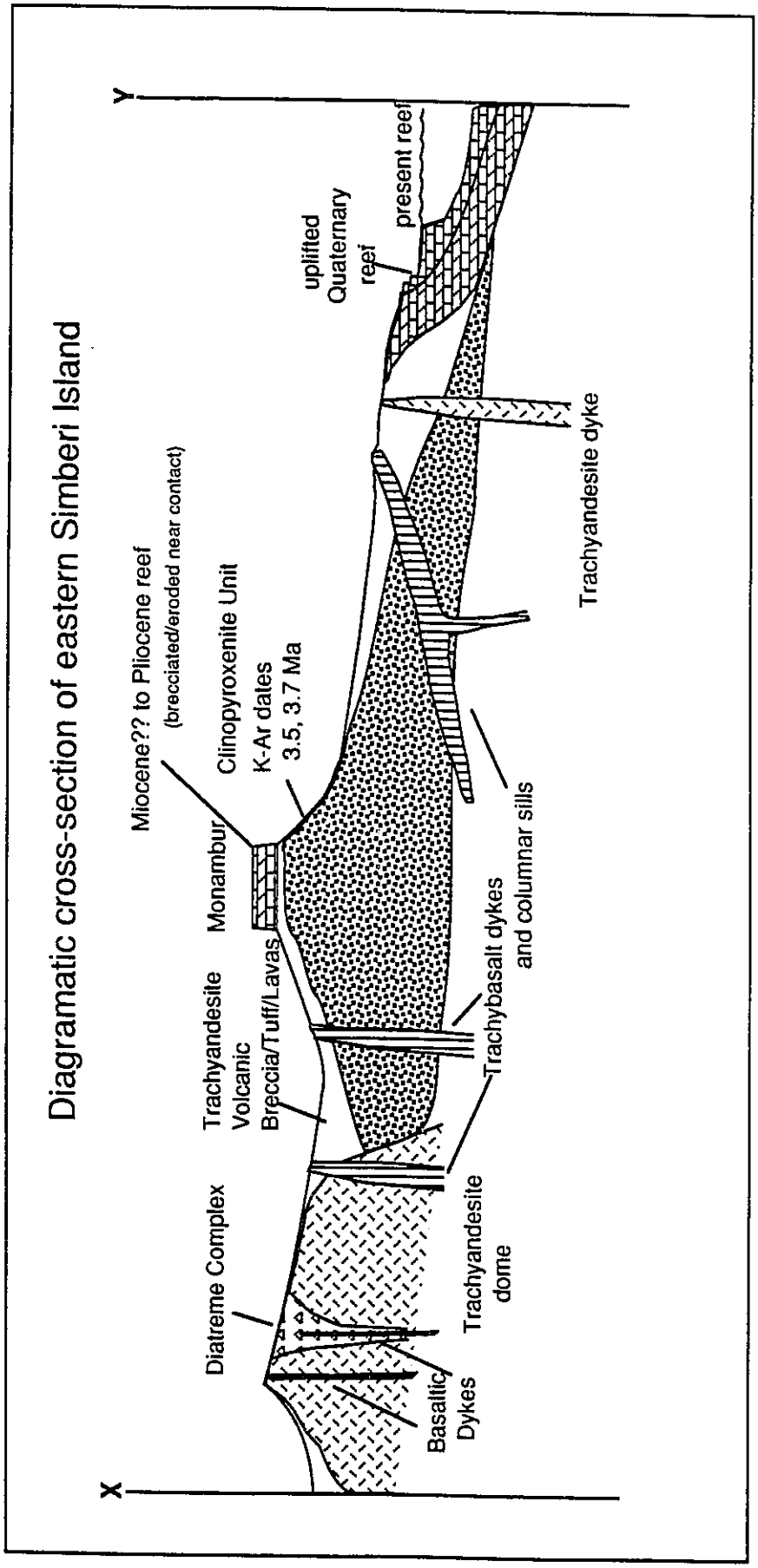
Diagramatic cross-section of eastern Simberi Island
X
Y
Diatreme Complex
Basaltic Dykes
Trachyandesite dome
Trachybasalt dykes and columnar sills
Trachyandesite Volcanic Breccia/Tuff/Lavas
Monambur
Miocene?? to Pliocene reef
(brecciated/eroded near contact)
Clinopyroxenite Unit
K-Ar dates
3.5, 3.7 Ma
uplifted Quaternary reef
present reef
Trachyandesite dyke

Trachybasalts and Trachyandesites

Subaerial weathering and erosion of the clinopyroxenite unit preceded deposition of mafic to intermediate lavas observed along the Sorowar access road and on a cliff face east of Monambur. Observations of contact relationships indicates that the clinopyroxenite and the overlying lavas were intruded by sills and dikes of trachybasalt composition (Figure 12). A 4 m thick, spheroidally weathered, columnar-jointed sill with 0.8 m diameter columns is exposed along the Sorowar access road immediately east of Monambur at grid reference 11330E, 8920N.

The above mentioned mafic to intermediate flows overlying the clinopyroxenite unit correlate with lavas exposed in the nearby Talamuk and Monun Creeks. The lowermost sections of these creeks contain fine-grained trachybasaltic lavas. The mafic flows are generally between 2 and 5 m thick with highly vesiculated and brecciated tops. The vesicles can be quite large (1-2 cm) and are usually flattened, and often contain euhedral calcite, analcite and zeolites.

The relatively thin mafic flows of trachybasalt composition undergo gradual transition to more felsic compositions, and grade into thicker units of blocky lavas of trachyandesite composition in each creek upstream. These trachyandesitic lavas contain coarser and more abundant flow-aligned feldspar and also contain amphibole phenocrysts. Vesiculation is common, with some vesicles lined with pyroxene and infilled with calcite, analcite and zeolites. The trachyandesitic lavas of Talamuk and Monun Creek compare with those exposed in the lowermost sections of Darum and Samat Creeks. The flows are interbedded with coarse to fine pyroclastics, epiclastics and interflow volcanic conglomerates. Both the

thickness of the flows and the proportion of volcanoclastics/lavas increases upstream in each of the creeks (ie. with elevation and distance away from the coast).

Explosive volcanism

Volcanoclastic units vary from poorly sorted volcanic breccias and lahars to well sorted lapilli-tuffs, and coarse to fine ash. None of the pyroclastic units showed any signs of welding, and those units exposed in the Sorowar and Pigiput deposit area are poorly lithified. Volcanic breccias containing less than 25% ash and lapilli particles are relatively common and generally contain angular to subangular blocks of predominantly trachyandesite composition. Breccia clasts attain diameters of 2.5 m. No volcanic bombs have been observed in any of these deposits. Lapilli-tuff units generally contain between 25 to 75% ash matrix with the lapilli being matrix supported. Lapilli are commonly angular to subrounded. Lahars and debris flows containing trachyandesite clasts are frequent and difficult to distinguish from coarse volcanic breccias in weathered/altered exposures.

Subaqueous reworking of pyroclastic material has produced well-bedded volcanic conglomerates, sandstones, siltstones and mudstones exposed at surface (Monun Valley; Figure 13) and in drill core (Sorowar deposit drill hole 13-22 m depth). The absence of ripple marks in the fine grained sediments combined with extreme kaolinitic alteration of these sediments indicates that a quiescent, acidic, crater lake may have previously existed in the region between the Sorowar and Pigiput deposits (e.g., Crater Lake, Ruapehu, New Zealand (Henley, 1986, p. 8). Hydrothermal gypsum recovered from Monun Valley drill core (RC197-77 m) has

$\delta^{34}S$ of 10.6-10.8 ‰, thus ruling out a flux of marine water ($\delta^{34}S$ = 20 ‰) during hydrothermal alteration. The Monun Valley site shows numerous sets of fining upward lapillistone tephra interbedded with thick debris flow units (lahars) containing large blocks of ash (>1 m diameter; Figure 13).

Airfall tephra deposits are uncommon although a particularly well exposed roadcut is present to the west of the Pigiput deposit. In this unit, fallout tephra over 5 m thick overlies a debris flow and massive pyroclastic breccias. The fallout tephra is composed of well-bedded, sorted and rounded lithic fragments with particle size ranging from fine lapillistone (coarse pebble gravel (<2 mm)) to sandstone. The beds are plane parallel, continuous and do not show sedimentary structures apart from a slight degree of upward fining. Bedding planes are gradational and occasionally exhibit erosion of the lowermost beds by overlying beds. These beds and the deposits in Figure 13 are interpreted to represent an irregularly pulsating Plinian eruption (Fisher and Schminke, 1984, p. 142). Deposits west of the Pigiput prospect have an attitude 90°/20°-30°N, whereas similar deposits exposed around the Sorowar prospect roadcuts are horizontal.

Intrusive Volcanism

Dykes and hypabyssal domes are ubiquitous features of the study area, and are predominantly of trachyandesite (mugearite) composition, in accord with the high proportion of trachyandesitic volcanoclastics. Trachyandesite domes are the largest intrusive units identified in the study area. Particularly fresh examples of this rock type are exposed along access roads to the Samat and Sorowar deposits.

Figure 13. Interbedded volcanic debris-flows and subaqueous sediments in Monun Valley.

(a) A series of fining-upward volcaniclastic sediments overlying a 3 m thick unit of lahar with entrained blocks of white volcanic ash. The large block at left is 1 m long. Fine-grained disseminated sulphide imparts a bluish colouration to the outcrop.

(b) A closeup of the central bed of upward fining lapilli tephra.

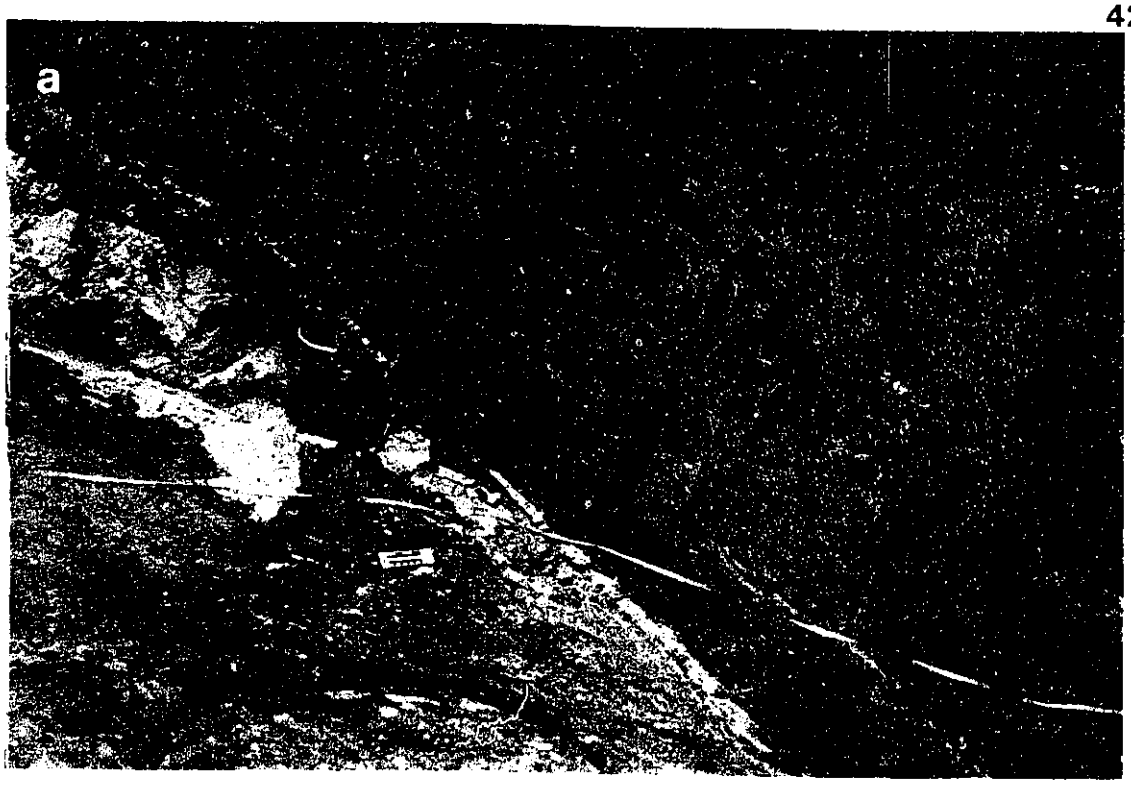
a

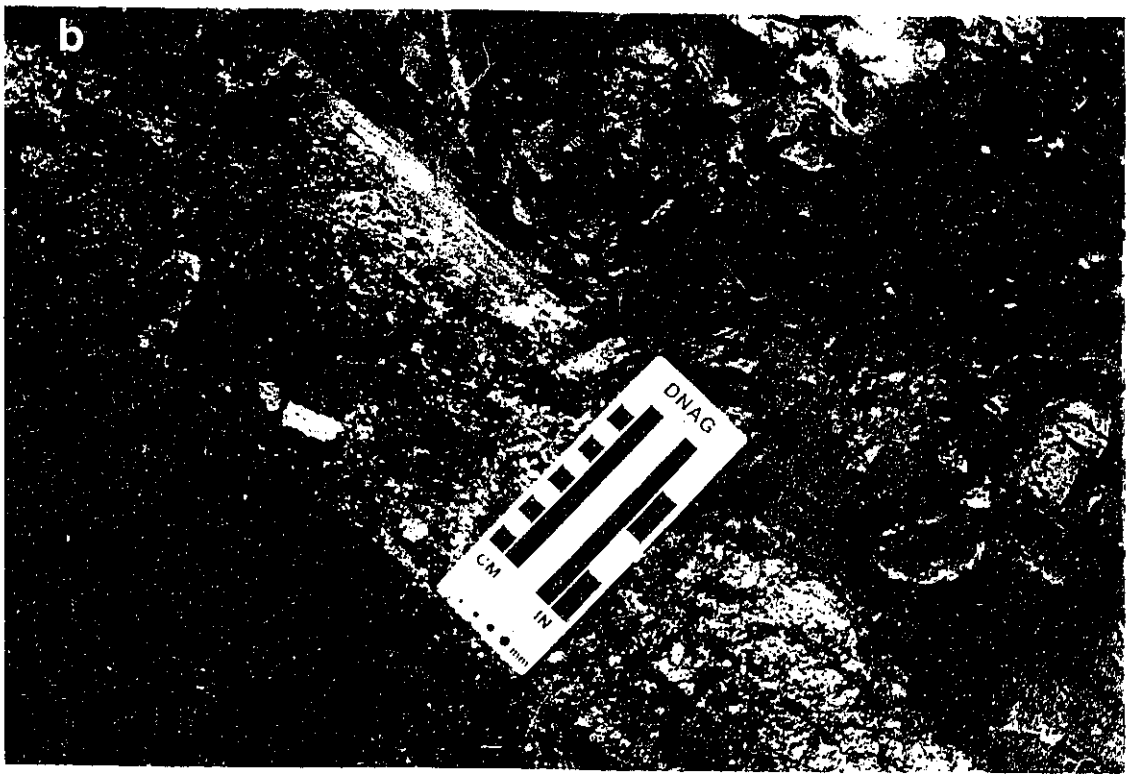
b
DNAG
CM
IN

The Samat road occurrence (10260E, 8000N) coincides with an aeromagnetic anomaly extending northwest past Darum Creek where the unit is most pristine. This is the largest intrusive feature in the study area with a minimum diameter of approximately 1.3 km. The fresh rock in outcrop and creek exposures is massive and well jointed. It weathers spheroidally and the weathered surface often has a knobby appearance with the knobs varying from 0.5 to 2 cm diameter (Figure 10). It is a fine to medium grained intrusion containing phenocrysts (<5 mm) of hornblende, feldspar and clinopyroxene in a glassy groundmass containing fine-grained crystallites of feldspar, pyroxene and magnetite.

The knobby texture is due to the differential erosion of globular structures present in most trachyandesite rocks, but also occurs to a lesser degree, in trachybasalts and alkali olivine basalts. In fresh hand samples this texture is cryptic, but in thin section it is evident by the presence of silica-rich glass globules containing a few microphenocrysts surrounded by phenocryst-rich mafic glass (Figure 20c). Weathering and weak hydrothermal alteration (propylitic) destroys the mafic glass groundmass and accentuates the presence of the silica-rich glass globules due to their higher resistance to devitrification (Friedman and Long, 1984).

Amphibole- and clinopyroxene-rich xenoliths are common within massive trachyandesite domes. A cumulate textured nepheline trachyte xenolith containing coarse grained feldspar, apatite and biotite (with abundant exsolution lamellae of titanomagnetite) in an intercumulus matrix of nepheline, was discovered in the Samat road outcrop, and is the only evidence for the presence of phonolitic melts on Simberi Island.

The Sorowar occurrence (10000E, 9850N) is more limited in areal extent (300 m diameter), but is similar in mineralogy, texture and composition to the Samat occurrence. This unit intrudes trachyandesitic volcaniclastics. It is also intersected in the deeper sections of Sorowar drill holes (SO11-228 m, SO10-203 m). Similar intrusive units occupy the eastern portion of the Pigiput deposit, where intrusive contacts indicate that it has uplifted and tilted the airfall tephra deposits. Weathered and altered outcrops of this unit are also present on surface and intersected in drill holes at the Botlu deposit.

The actual size and continuity of dome-like intrusives depicted in the geology map (Figure 11) is difficult to assess due to incomplete exposure, but similarities in mineralogy, and in particular the presence of globular structures, may indicate that each of the domes is an apophysis of a much larger intrusive body. The emplacement of trachyandesite domes indicates that the Simberi volcanic pile had attained a sufficient crustal thickness to support high level igneous intrusions. Crustal stabilization marks a significant period in the volcanic-metallogenetic evolution of the Simberi volcano. The retention of a juvenile magma in the crust eventually lead to crystallization of a medium to high viscosity intrusion, which did not drain back into the Simberi Island deep magma reservoir, despite evidence for the presence of a tensile stress field in the Tabar Island Group. Kagiyama (1983) noted in a study of Japanese volcanoes, that the highest measured heat discharge was associated with volcanoes which had high level intrusions of medium to high viscosity.

Heat discharge from the cooling trachyandesite domes in the interior of the

Simberi volcano allowed the circulation of metalliferous hydrothermal fluids and the subsequent precipitation of metals from these fluids to produce the Samat, Pigiput, Sorowar and Botlu gold deposits. This point is corroborated by timing relations, where radiometric dating of minerals deposited by auriferous hydrothermal fluids yield similar ages to minerals from trachyandesite intrusive rocks located near the gold deposits (Chapter 5). An alunite age of 2.8 ± 0.6 Ma (Table 1), indicates that the Sorowar mineralization event was contemporaneous with Samat mineralization.

Although the formation of trachyandesite domes may represent the final crystallization product of a voluminous mafic reservoir below the Simberi volcano, the geology does not support a model for gradualistic, monogenetic progression from basalt to trachybasalt to trachyandesite. Numerous minor dykes and sills of mafic composition crosscut clinopyroxenite, trachyandesite volcaniclastics and domes. This may be the result of continuous extensional tectonic activity throughout the crystallization history of the Simberi volcano, which allowed mafic melts sporadic access to the upper crust.

North and South Samat - Discovery of the Raban Diatreme Complex

Two diatreme complexes were discovered by the author within a homogeneous, massive trachyandesite (mugearite) intrusive in the area of the North and South Samat gold deposits. The name given to the diatreme complex originates from a traditional belief among the Simberi people, that a spirit or "Masalai" inhabits a large boulder exposed in the hills of the South Samat area, and the spirit in this boulder is called Raban. Following the discovery that the gold deposits of North and South Samat were hosted by the diatreme complex, a close

inspection of the "Masalai" rock revealed that it was a chunk of diatreme breccia.

North Samat

The North Samat diatreme unit was first identified in four different road exposures at different elevations. On surface, the unit has a dyke-like shape with subvertical contacts, the long axis trending east-west at about 7650 m N latitude (Figure 11). It is up to 75 m wide and strikes for at least 170 m closing off to the west, with the eastern boundary open and undefined.

The intrusive country rock shows signs of increasing alteration and fracture intensity as the margin of the diatreme is approached. Adjacent to the diatreme/intrusion contact, the country rock exhibits jigsaw or crackle brecciation textures. The outer regions of the diatreme contain angular clasts whereas clasts become subrounded to rounded towards the centre, presumably due to milling and attrition of country rock during diatreme formation. The clasts vary from 2 cm to 2 m in diameter and are predominantly of trachyandesite composition. The breccia is increasingly matrix supported towards the centre.

Subvertical to vertical pebble dykes (usually < 3 m) are exposed at surface to the north of the main exposure and are probably linked to the main unit at depth. Cross-sections constructed with the aid of drill intersections indicate that the diatreme is a complex branching structure with a shape similar to an upward-opening trough (Figure 14). Large blocks of the host trachyandesite intrusive may have detached and fallen into the breccia, causing the diatreme to have a branched

Figure 14. Cross-section of the North Samat diatreme breccia. The diatreme has a trough-like shape, with three branches extending upward to the surface. In this section, the central branch is poorly developed compared to the northeast and southwest branches. Only the southwest branch is well exposed at the surface. Hornblende-phyric trachybasalt (hawaiite) dykes intrude parallel to the long axis of the diatreme, and have been dated at 3.13 ± 0.06 Ma (Table 1 and Chapter 5). Gold mineralization is hosted within the highly fractured hanging wall trachyandesite.

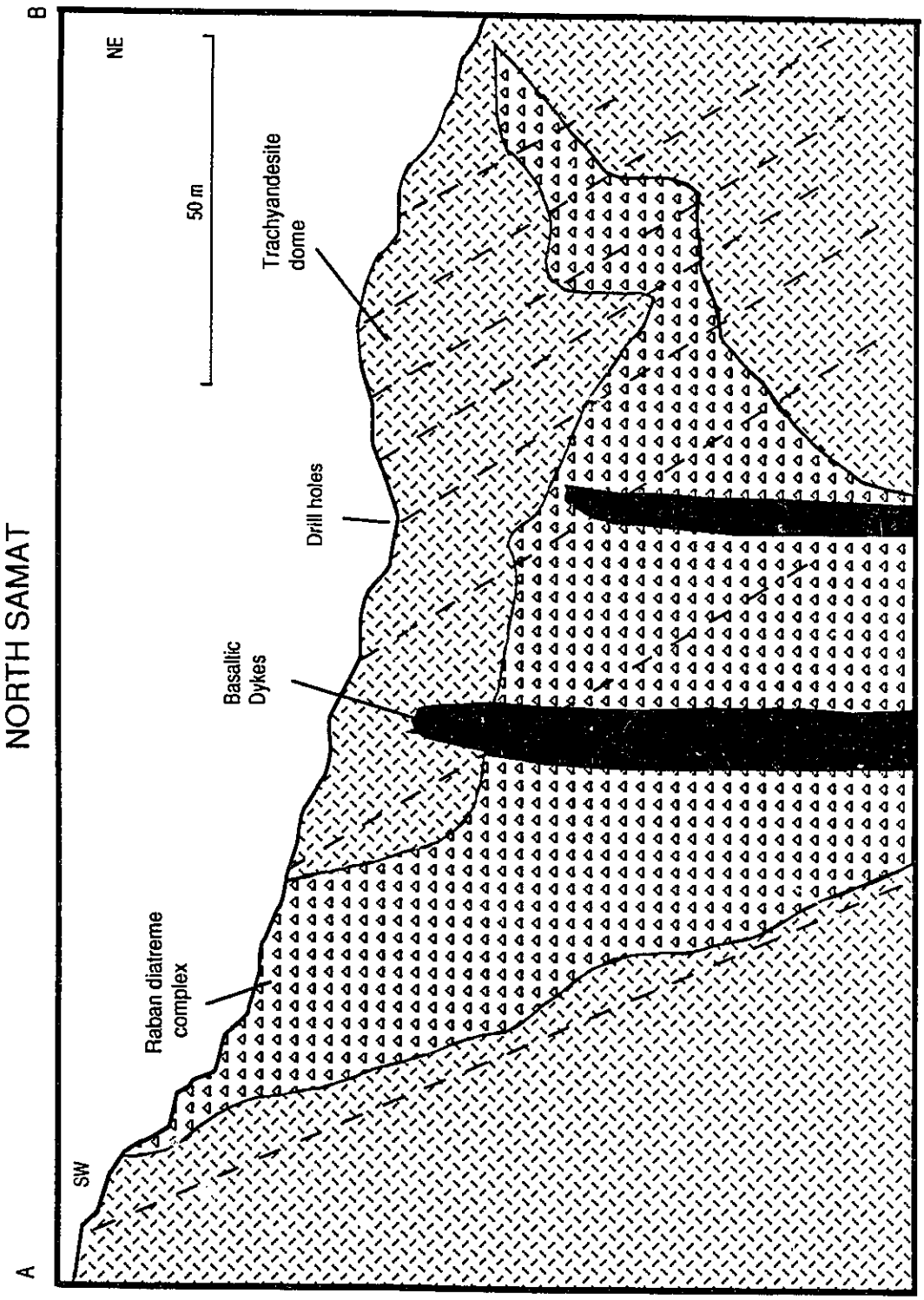
A
B
SW
NE
NORTH SAMAT
50 m
Raban diatreme complex
Basallic Dykes
Drill holes
Trachyandesite dome

appearance. The part of the diatreme exposed at the surface constitutes the south branch whereas the central and northern branches are poorly exposed.

Mafic dykes of trachybasalt (hawaiite) composition (Sample 337; Appendix A.8) intruded the North Samat diatreme and the trachyandesite intrusion approximately 3.13 ± 0.06 Ma (see Table 1). These dykes contain megacrysts (2 cm long) of hornblende and are highly vesicular. Diatreme formation may be related to rapid decompression of a volatile-rich mafic melt, during extensional tectonic activity, along zones of structural weakness in the trachyandesite intrusion. Independent analysis of fracture orientation in the Samat areas by Kennecott consultants (Dames and Moore, unpublished data) shows that the majority of fractures are steeply dipping and oriented east-west and northeast-southwest, parallel to the trend of the North and South Samat diatremes, respectively.

South Samat

Poor surface exposure of rock units led to an early interpretation of the South Samat Au deposit as a steeply dipping volcaniclastic unit sandwiched between two thick sequences of trachyandesite flows. Trachyandesitic volcanoclastic deposits were present in the headwaters of Samat Creek to support this interpretation, but these are intruded by the same trachyandesite dome exposed in the North Samat area. Following the realization that the North Samat mineralization was hosted by a diatreme complex, a re-examination of the South Samat prospect was undertaken.

A contact between weathered trachyandesite and brecciated material was

observed along the main drill access road southeast of the deposit (9500E, 7170N). This trachyandesite unit contained 3 sets of closely spaced joint planes (Figure 15a) which increased in intensity (ie. density) from 7 to 2 m towards the contact. The orientation of the joint planes are:

1) a dominant set, 1-4 cm apart oriented 109/75N. An exposure of a diatreme contact at grid reference 9700E, 7250N had a similar orientation of 108/60N, but only a single joint set spaced 6-10 cm apart was present.

2) a less developed set, 3-5 cm apart, trending 34/76S,

3) a poorly developed set, 5-10 cm apart, trending 65/28W.

From 2 m to the contact margin, the trachyandesite unit passes from a crackle breccia to a jigsaw breccia (Figure 15b). The brecciated outcrop shows similar features to that of North Samat, with increased clast size, rounding and matrix/clast ratio towards the interior of the diatreme (Figure 16a and b). The occurrence of multiplanar joint sets in country rock surrounding diatremes has been reported by Sillitoe (1985), and is interpreted to be the result of deformation following rapid compression/decompression during diatreme emplacement.

Using a series of cross-sections obtained from analysis of drill core and drill logs, the geology of the diatreme was established (Figures 12 and 17). The surface exposure of the diatreme is difficult to interpret due to poor exposure and post-emplacement faulting, but it appears to be about 350 m long and a maximum apparent width of 200 m. The apparent dip of the northwest boundary of the diatreme/intrusive contact varies from 30°NW in the southwest to 70°NW at the northeast end. The northeast end of the diatreme pinches out into a fault zone, and indicates that the diatreme exploited a zone of structural weakness in the host

Figure 15. Field observations of the South Samat trachyandesite/diatreme contact.

(a) Three sets of joint planes located within the trachyandesite, approximately 2 m from the diatreme contact. The multiplanar joint sets are interpreted to be the result of rapid compression/decompression during the explosive eruption of the diatreme. The dominant set of vertically oriented planes in the photo are parallel to the intrusive/diatreme contact.

(b) Jigsaw breccia texture at the intrusive/diatreme contact. The brecciated trachyandesite country rock is relatively undisturbed due to the short distance of transportation and, therefore, the breccia clasts could be refit like a jigsaw puzzle.

a

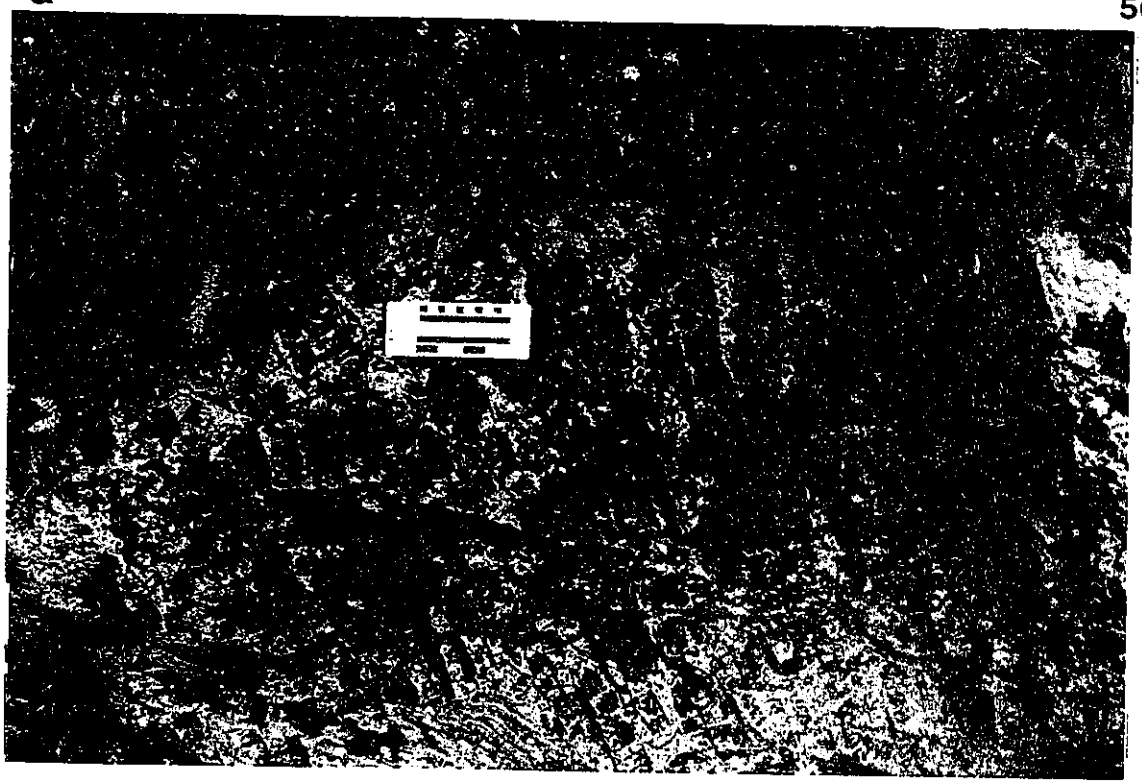

b

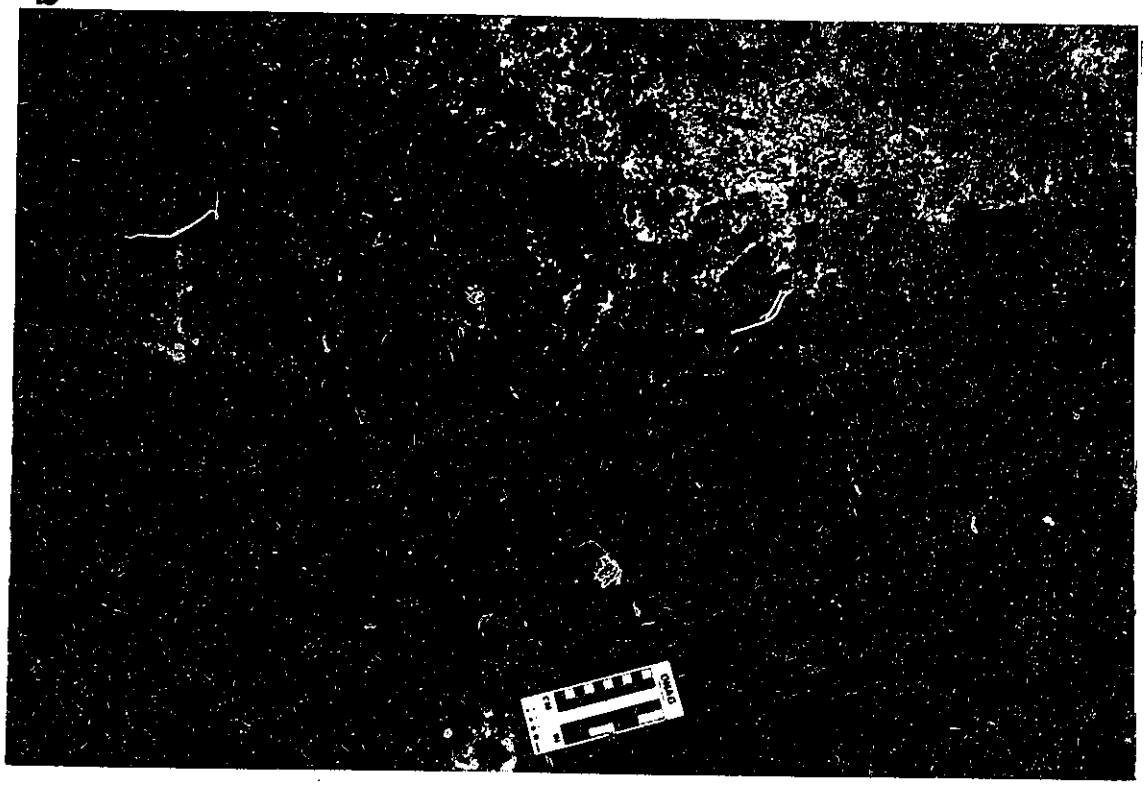

Figure 16. Field observations of the South Samat diatreme.

(a) The outer margin of the diatreme, 3 m from the intrusive/diatreme contact.

(b) The interior of the diatreme, which shows an increase in clast size and clast rounding, and a higher matrix/clast ratio than the outer margin.

a

b

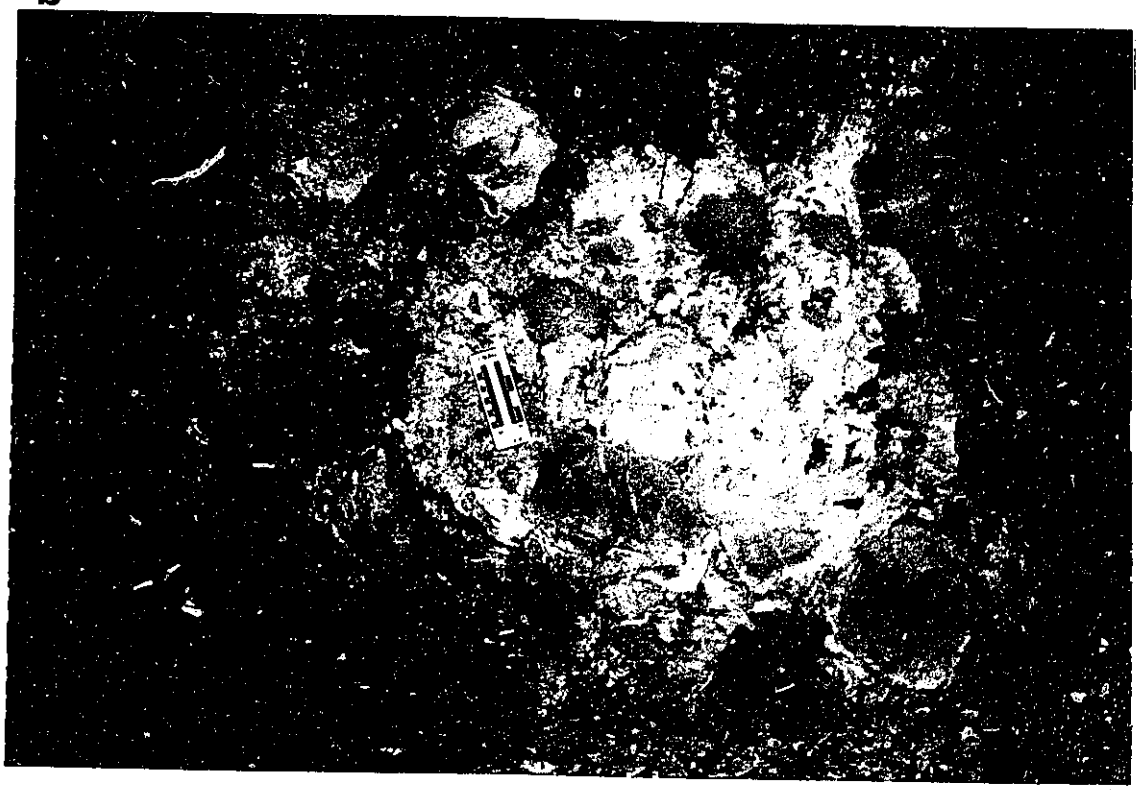

trachyandesite intrusive. Its dip requires a maximum true width of between 20 and 30 m at the surface. The width of the diatreme unit increases with depth.

Similar to North Samat, mafic hornblende-phyric dykes are encountered in the drill core and on surface to the west of the Raban Diatreme Complex. At grid location 9525E, 7135N, to the west of the South Samat Au deposit, a fresh mafic dyke of trachybasalt (hawaiite) composition was sampled for petrographic and geochemical work (Sample 22; Appendix A.8). Within this glass-bearing basaltic dyke was found the first reported occurrence of a calcite-pyroxene-amphibole-magnesiochromite nodule which has profound implications for the nature of the oceanic mantle underlying the TLTF Islands.

Figure 17. Cross-section of the South Samat diatreme. Gold mineralization is located within the highly fractured trachyandesite hanging wall, with the highest grades occurring along the diatreme/trachyandesite contact.

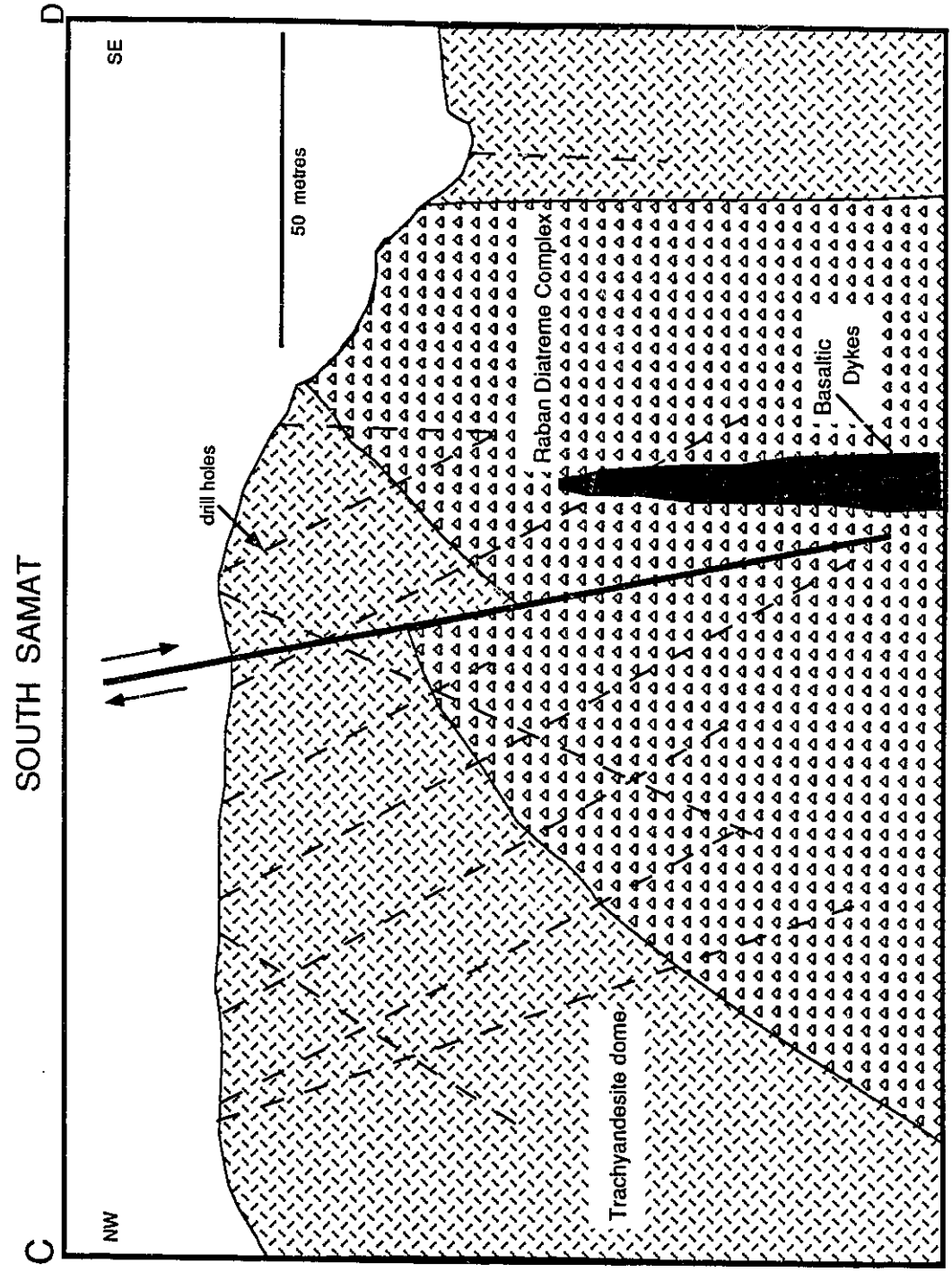
C
D
NW
SE
SOUTH SAMAT
drill holes
50 metres
Raban Diatreme Complex
Basaltic
Dykes
Trachyandesite dome

Chapter 4. Igneous Rocks of Mantle Origin

Botsor Hill Intrusion

A 100 m diameter ultramafic body located near the headwaters of Monun Creek (8100E, 9700N) was exposed during the construction of an access road between the Botlu and Sorowar Au prospects. Referred to as Botsor Hill, it is the most primitive intrusion reported in the TLTF islands. This outcrop of massive alkali olivine basalt is resistant to weathering, forming a steep stony hill surrounded by altered trachyandesite.

The chemical characteristics of rocks collected from this unit (Samples 310, 311 and Botsor-1; Appendix A.8) are consistent with a primary magma extracted from the mantle, with $100MgO/MgO+\Sigma FeO$ = 68-74 and high concentrations of the compatible elements chromium (830 ppm), cobalt (130 ppm) and nickel (400 ppm) (Edgar, 1987). This unit is similar to rocks collected from the clinopyroxenite unit present at the base of Monambur (Samples 305, 312; Appendix A.8), except that the latter is a fractionated unit with lower modal olivine, Cr, Co and Ni concentrations. The Botsor Hill basalts are the most nepheline normative rocks on Simberi Island (5.6 to 8.3% nepheline; CIPW norm), and can be described as basanites. A similar rock (Sample 7440037; Appendix A.8; a boulder in a creek 2 km southeast of Napekur Village) was described by Johnson *et al.* (1976), which they termed a potassic basanite.

The Botsor Hill basanites consist of megacrystic and phenocrystic olivine and clinopyroxene set in a glassy groundmass containing magnetite and microlitic

Figure 18. Olivine megacrysts from the Botsor Hill intrusion.

(a) Olivine (ol) grain (1.2 mm diameter) containing circular fractures and overgrown by a diopside (cp) rim. From rock sample Botsor-1. Cross-polarized light.

(b) Kink-banded olivine megacryst (2 mm diameter) with circular fractures. From rock sample Botsor-1. Cross-polarized light.

a

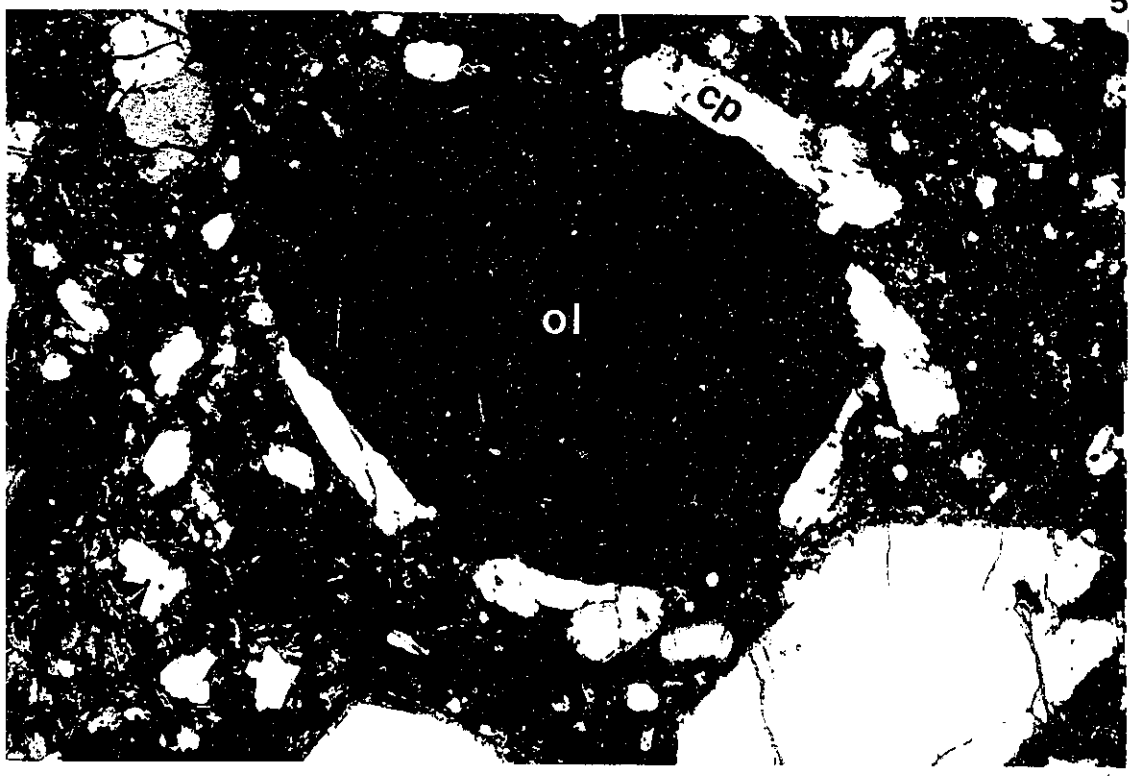

b

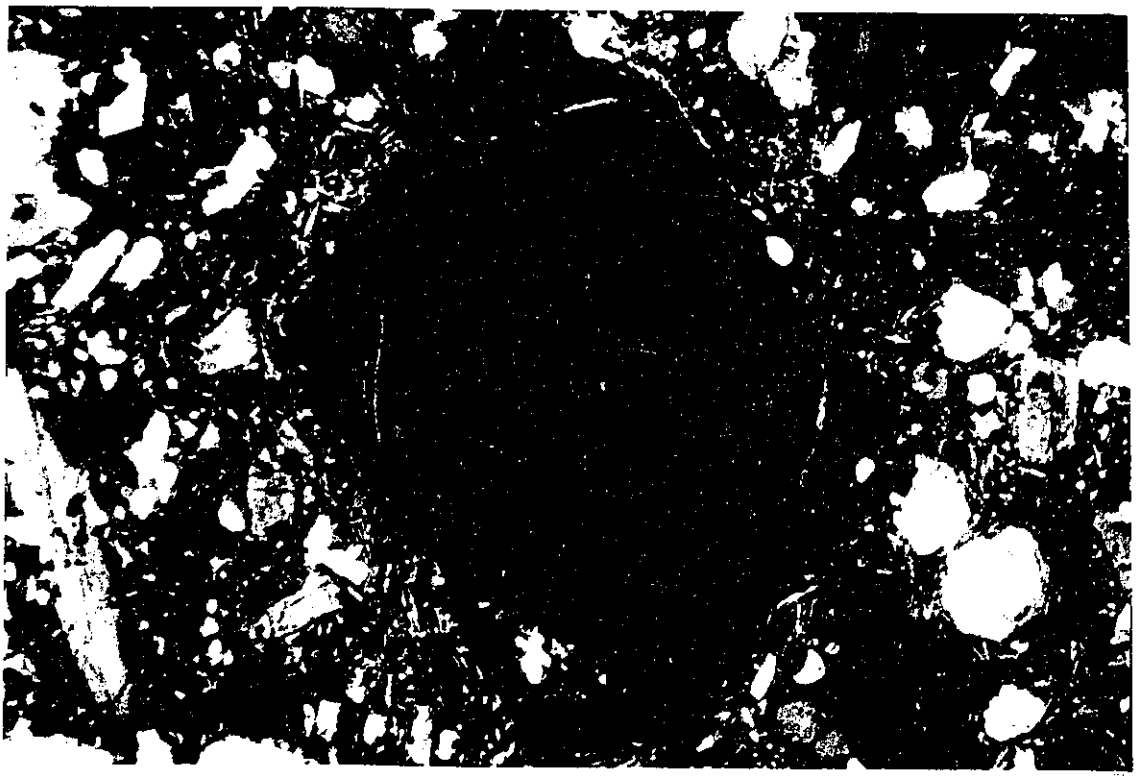

plagioclase. The megacrystic minerals are commonly brecciated and display unusual textures, including stress-induced twinning and circular fracture patterns in forsteritic olivine (Figure 18a and b). Complex and highly distorted zoning in apple-green sodian diopsides from the Botsor Hill intrusion (Figures 19a and 25b) can be contrasted with diopside phenocrysts from ankaramitic basalts (Figure 19b).

The kink-banded olivine megacrysts (up to 4 mm) are forsteritic in composition (Fo_{86-94}), with NiO ranging from 0.20-0.35 wt%. They have low average CaO = 0.11 wt.%, characteristic of primary mantle olivines found in ultrabasic xenoliths in kimberlites (Dawson, 1980), peridotites (Simkin and Smith, 1970) and in Hawaiian spinel lherzolite suites (Sen, 1987). Small groundmass phenocrysts (< 1 mm), and rims on megacrysts have distinctly different compositions, with Fo_{77-83}, NiO < 0.16 wt.% and average CaO = 0.26 wt.%.

Apple-green sodian diopside megacryst cores containing alkaline glass inclusions form a distinct group of clinopyroxenes in the Simberi lavas, with Na_2O values ranging from 1.3 to 2.7 wt.%. Brooks and Prinzlau (1978) described green cores with a high 'acmitic' (aegirine) component similar to Simberi sodian diopsides as common constituents of mafic alkaline provinces of the world (Babkine *et al.* 1968). They argued that green, Na-rich pyroxenes within mantle-derived ultramafic rocks are the phenocrysts of intermediate to salic magmas produced by partial melting of metasomatized mantle, which have mixed with basic magmas within the mantle prior to eruption. Botsor Hill sodian diopsides are <u>phenocrysts</u> of highly alkaline salic magmas present in the mantle wedge beneath Simberi Island.

Figure 19. Clinopyroxene megacrysts from Simberi Island basanites and ankaramites.

(a) Apple-green sodian diopside from the Botsor Hill intrusion containing an inner core of calcite-bearing melt inclusions, a middle region of CO_2-rich inclusions and an outer rim of inclusion-free diopside. The megacryst is 3.5 mm long. The area within the rectangle is enlarged in Figure 26. From rock sample 310. Plane-polarized light.

(b) Well zoned diopside megacryst within an ankaramite outcrop located at the base of Monambur. Field of view is 3 mm long. From rock sample 305. Cross-polarized light.

a

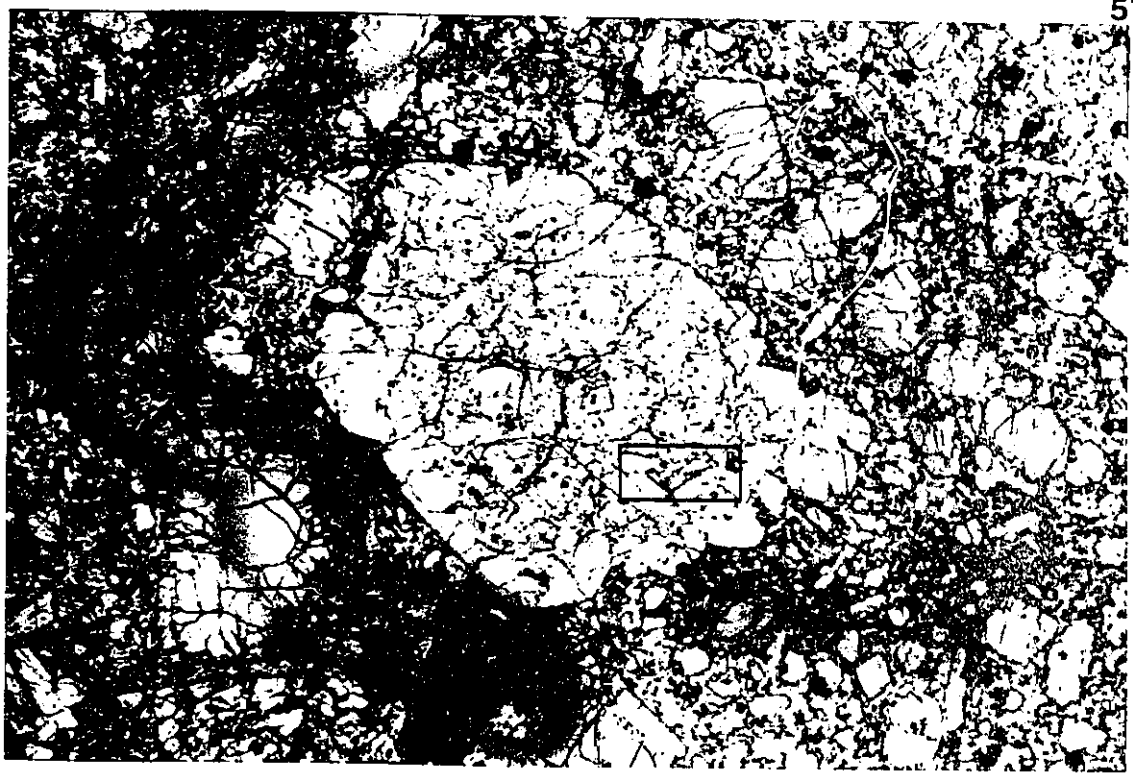

b

Figure 20. Petrographic textures of the Botsor Hill basanites.

(a) Kink-banded olivine megacryst (2 mm diameter) with circular fractures. From rock sample Botsor-1. Cross-polarized light.

(b) Olivine megacryst containing melt inclusions (mi) with carbonate, sodian diopside, apatite, sodalite and titanian phlogopite surrounded by an alkaline glass matrix. From rock sample 310. Plane-polarized light.

(c) Coarse-grained (1.5 mm), well zoned, euhedral diopside phenocrysts with zoning accentuated by the presence of CO_2 vapour-rich melt inclusions. The presence of vapour-rich melt inclusions may reflect periods of CO_2 saturation in the basaltic liquid. The phenocryst rims rarely have CO_2 inclusions. The central area of the photo contains immiscible globules of high SiO_2 glass (ranging from jadeitic to analcimic composition; 3.6 to 17 wt. % Na_2O) surrounded by mafic glass. The linear features within the high SiO_2 glass are apatite microlites. From rock sample 311. Plane-polarized light.

(d) Enlargement of CO_2 vapour-rich melt inclusions (ave. size $\approx$ 20 μm) in diopside. Inclusions consists of 3 phases: glass, CO_2-vapour (v) and an opaque mineral (o). Based on the presence of magnetite-only inclusions occurring in vapour-rich melt inclusion zones, the opaque phase within the melt inclusions is probably magnetite. From rock sample 311. Plane-polarized light.

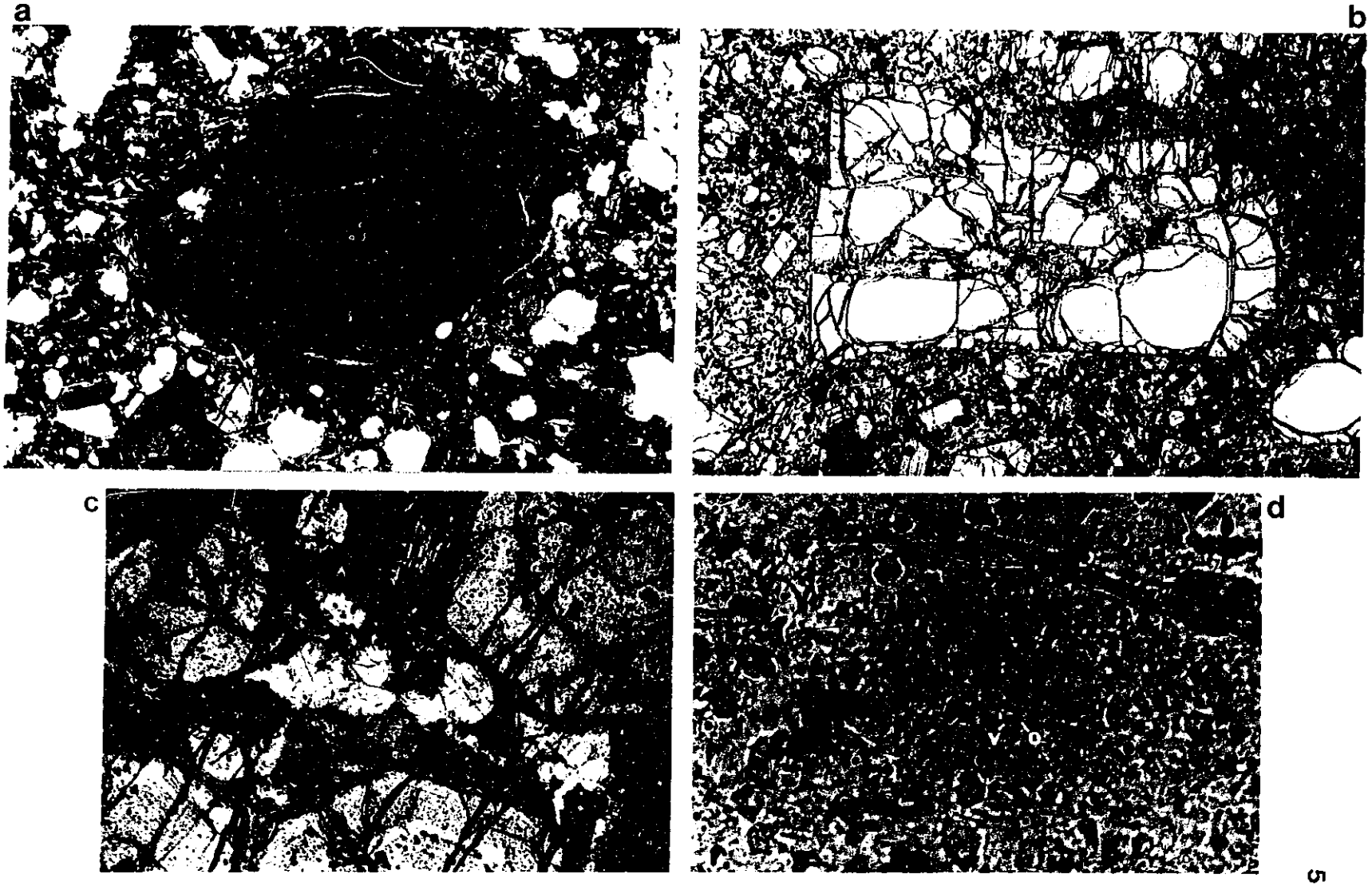
a
b
c
d

Evidence for the formation of the apple-green pyroxenes was found within melt inclusions in olivine and sodian diopside megacrysts. The latter show a zonation (Figure 19a) from vapour-absent, daughter mineral-rich melt inclusions in the cores of the megacrysts, to CO_2 vapour-rich melt inclusions in the middle regions (Figures 20c and 20d), to inclusion-free rims (Figures 19a and 20c).

The mineral-rich melt inclusions (usually $< 100\ \mu m$ diameter; Figures 19a and 21), regardless of the composition of the host mineral, contain a primary assemblage of high Sr calcite (1800-4900 ppm Sr; Table 3, col. 4), often with hexagonal cross-sections (Figures 22, 23, 25, 26, 27, 28), anhydrite (Figure 27), sodalite (Figure 22), titanian phlogopite (Figure 22, 23, 24, 25, 26, 27, 28; Table 3, col. 8 and 11), fluorapatite (Fig. 22, 23, 27; Table 3, col. 5) and titanomagnetite (Table 3, col. 6). These minerals have crystallized in a matrix of alkaline glass unmixed to Na- (Table 3, col. 1 and 2) and K-rich (Table 3, col. 3) glasses.

The negligible content of mafic components in the melt inclusion glasses and their low Mg# (Table 3), combined with their extreme sodic and potassic nature, indicate that they can not be derived from melting of mantle peridotite. Rather, they are metasomatic agents reacting with megacrystic olivine to produce a metasomatic mineral assemblage of titanian phlogopite, sodian diopside and titanomagnetite. Crystallization of the daughter minerals anhydrite, calcite, fluorapatite and sodalite indicate that the metasomatic agent was a sulphate-, carbonate-, H_2O- and alkali-rich aluminosilicate magma (SCHARM) with dissolved Cl, F, P, Ti and Sr with high fO_2.

Table 3. Chemical composition of Botsor Hill melt inclusion minerals and glasses

	1	2	3	4	5	6	7	8	9	10	11
SiO_2	56.44	51.45	60.34	-.-	0.43	0.18	41.09	37.85	48.89	39.36	38.26
TiO_2	-.-	0.0	0.88	-.-	0.04	2.60	-.-	7.41	1.76	-.-	4.16
Al_2O_3	24.34	29.36	19.23	-.-	.04	1.35	-.-	13.12	5.60	-.-	13.69
FeO	0.08	0.2	0.61	0.34	0.37	85.04	8.77	5.37	4.13	13.81	7.04
MnO	-.-	0.0	0.02	0.07	0.07	0.67	-.-	-.-	-.-	-.-	-.-
MgO	0.02	0.0	0.04	0.22	0.18	1.39	50.67	20.40	14.47	45.80	20.72
CaO	1.35	4.11	3.30	50.15	54.82	0.36	0.16	0.08	22.48	0.23	0.06
K_2O	0.10	0.14	13.59	-.-	0.00	-.-	-.-	9.47	0.01	-.-	9.60
Na_2O	9.29	15.68	0.74	-.-	0.04	-.-	-.-	1.20	1.37	-.-	0.95
P_2O5	0.03	0.07	0.03	-.-	40.94	-.-	-.-	0.04	0.17	-.-	-.-
F	-.-	0.05	-.-	-.-	3.93	-.-	-.-	1.38	-.-	-.-	1.45
Cl	0.02	0.02	0.07	-.-	0.15	-.-	-.-	0.04	-.-	-.-	0.04
BaO	0.07	-.-	-.-	-.-	-.-	-.-	-.-	-.-	-.-	-.-	-.-
Cr_2O_3	-.-	-.-	-.-	-.-	-.-	0.19	-.-	-.-	0.20	-.-	-.-
NiO	-.-	-.-	0.04	-.-	0.06	0.23	-.-	0.05	-.-	-.-	-.-
ZnO	0.12	-.-	-.-	-.-	0.42	-.-	-.-	-.-	-.-	-.-	-.-
SrO	0.04	0.07	0.61	0.58	0.45	-.-	-.-	0.09	0.10	-.-	0.09
V_2O_3	0.01	-.-	-.-	-.-	0.10	0.72	-.-	-.-	-.-	-.-	-.-
SO_3	0.07	-.-	-.-	-.-	0.17	-.-	-.-	-.-	-.-	-.-	-.-
Mg#	20.0	0.0	6.2	-.-	-.-	-.-	85.2	79.0	77.8	77.2	74.6
TOTAL	91.97	101.16	99.48	99.60	102.13	93.06	100.70	96.46	99.28	99.20	96.07

Note: Mg# = 100 MgO/(MgO + FeO) from microprobe analysis

1. 310-2e: Na-rich glass
2. 310-7g: Na-rich glass
3. 310-2f: K-rich glass
4. 310.2.5: calcite (assuming CO_3^{2-} anion makes up the residual)
5. 310.2a: fluorapatite
6. 310.2c: titanomagnetite
7. 10.2h: olivine
8. 10.2j: titanian phlogopite replacing 7
9. 10.2g: sodian diopside replacing 7
10. 10.12m: olivine
11. 10.12b: titanian phlogopite replacing 10

Normative calculations for the glasses and cation calculations for the minerals are provided in Appendix A.7.

Figure 21. Olivine (ol) megacryst from the Botsor Hill intrusion (rock sample 310) containing calcite-phlogopite-sodian diopside-apatite-sodalite melt inclusions.

(a) Plane-polarized light. Olivine is 4 mm long.

(b) Cross-polarized light. Two glass-rich melt inclusions (boxed areas) contain the metasomatic mineral assemblages. The melt inclusions are connected by an early set of fractures running from the bottom left to the top right area of the megacryst. The lowermost box is enlarged in Figure 22, and the uppermost box is enlarged in Figure 23.

a

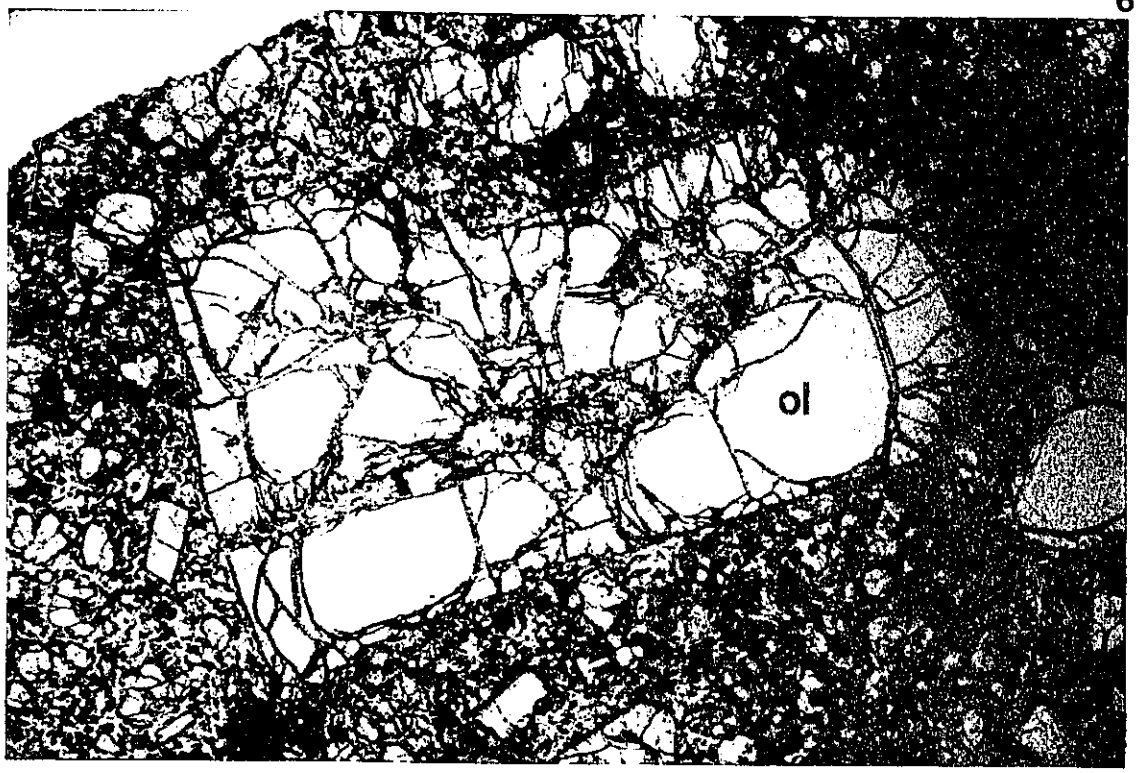

b

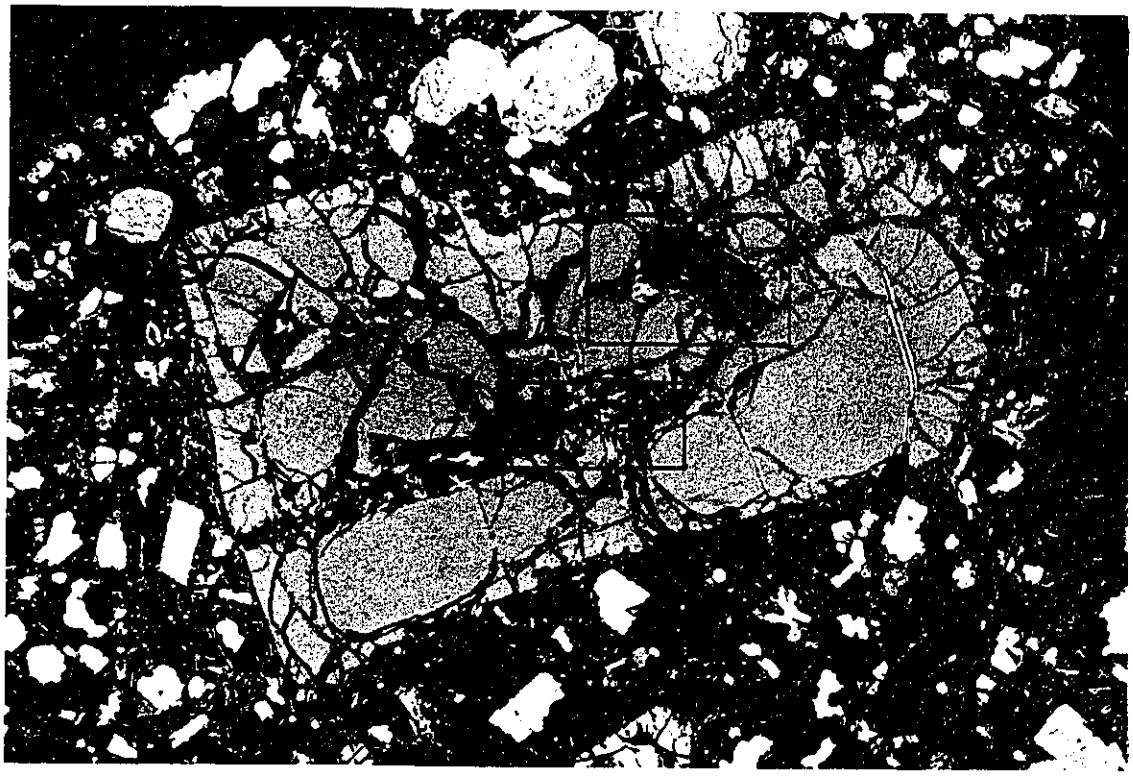

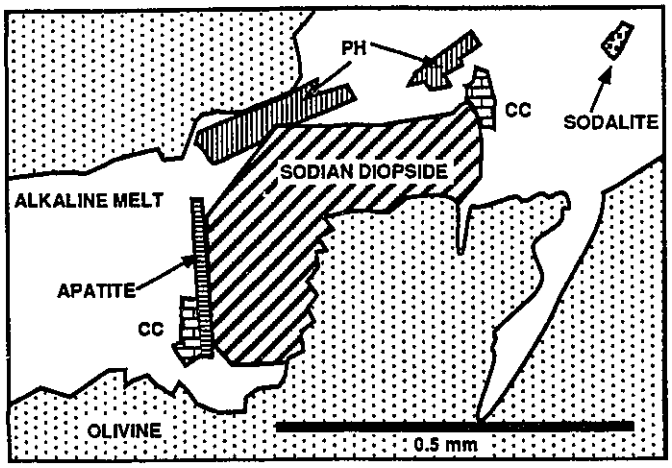

Figure 22. Melt inclusion within megacrystic olivine (ol).

(a) Metasomatic sodian diopside (cp), titanian phlogopite, calcite, fluorapatite and titanomagnetite (opaques at far right) crystals within alkaline aluminosilicate glass (gl). Plane polarized light.

(b) The alkaline melt has begun to crystallize leucite to the right of the sodian diopside. Within this region sodalite was also identified by SEM-EDS. Cross-polarized light. For scale see schematic diagram.

(from rock sample 310)

a

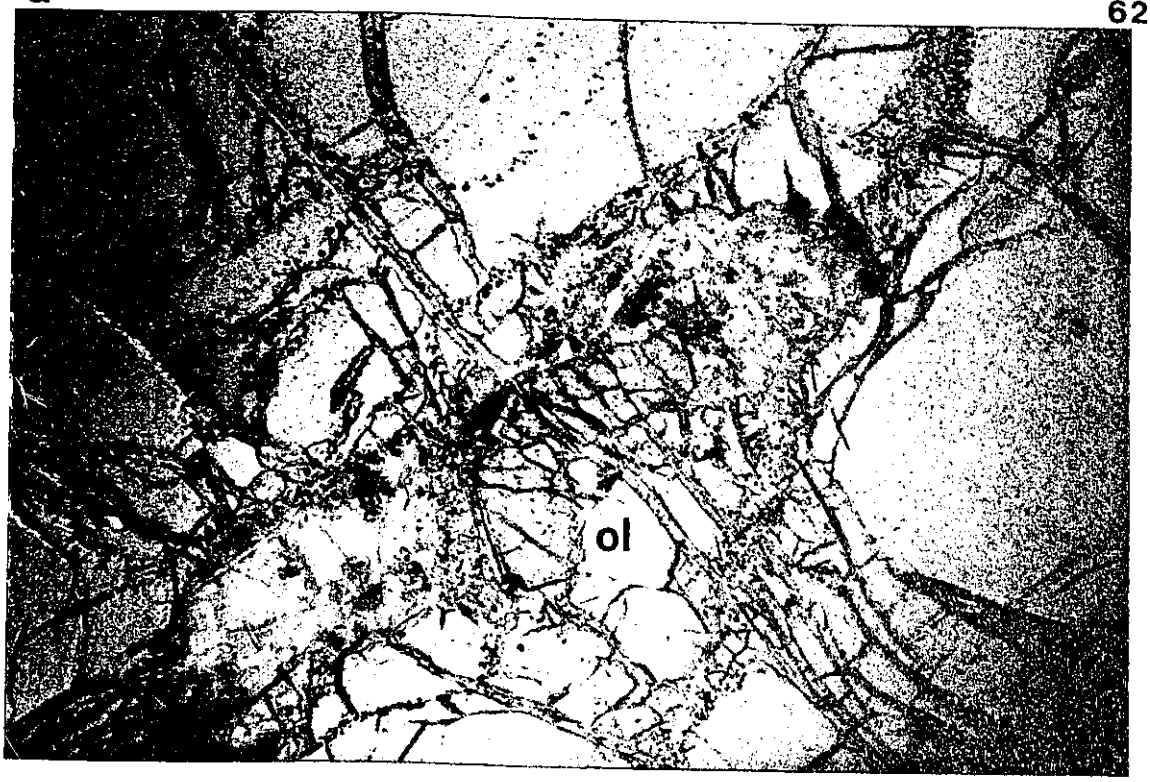

b

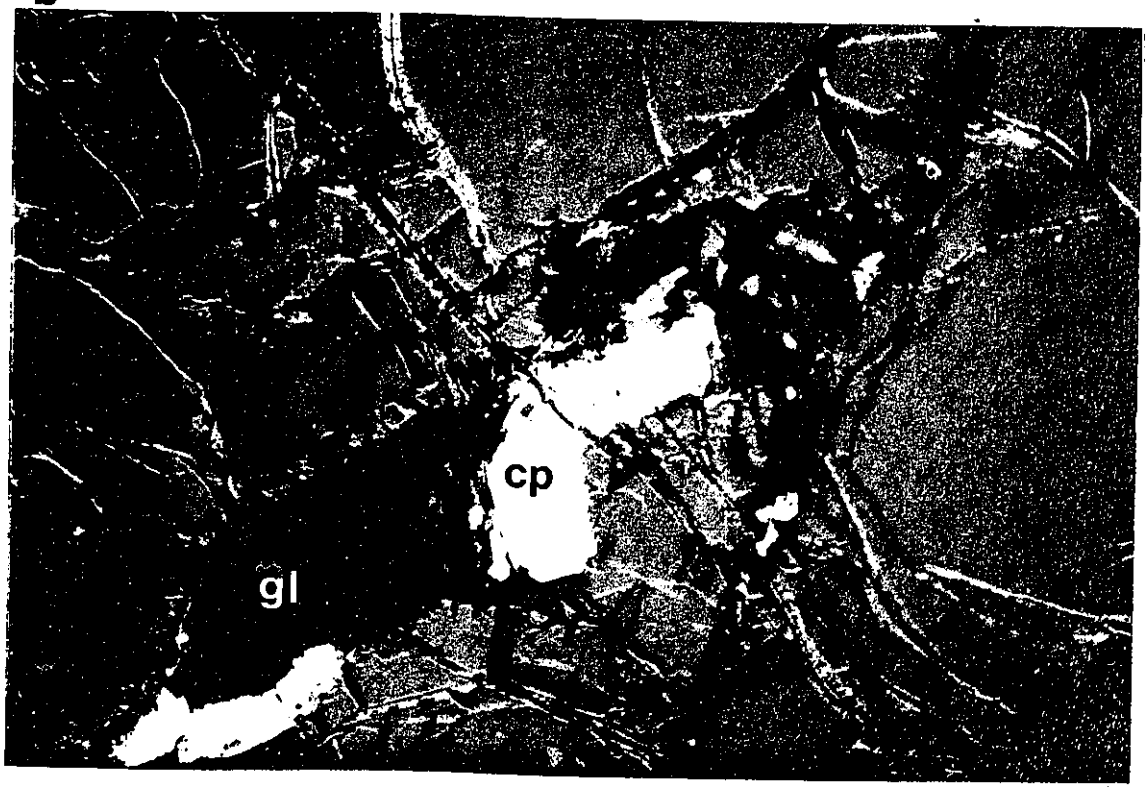

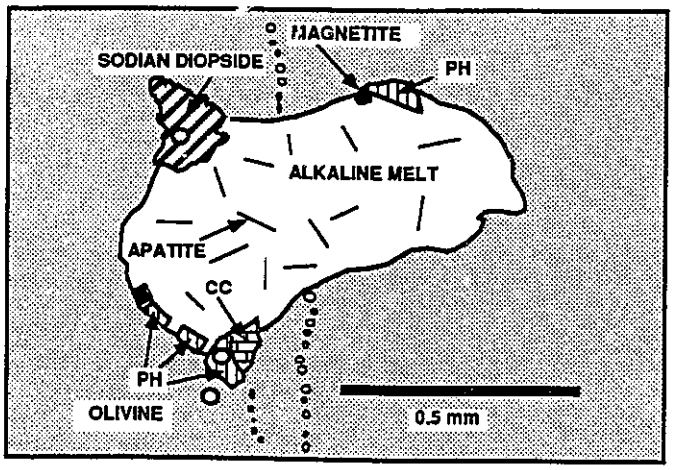

Figure 23. Melt inclusion within megacrystic olivine (for analysis see Table 4, col.7).

(a) Metasomatic sodian diopside (Table 4, col. 9), titanian phlogopite (p; Table 4, col. 8), calcite (cc), fluorapatite and titanomagnetite crystals between the host olivine and the alkaline aluminosilicate glass (gl). Circles on the schematic diagram represent locations of microprobe analyses (Table 4). Plane polarized light.

(b) Melt inclusion (mi) trails are enlarged in Figure 24. Cross-polarized light. For scale see schematic diagram.

(from rock sample 310)

a

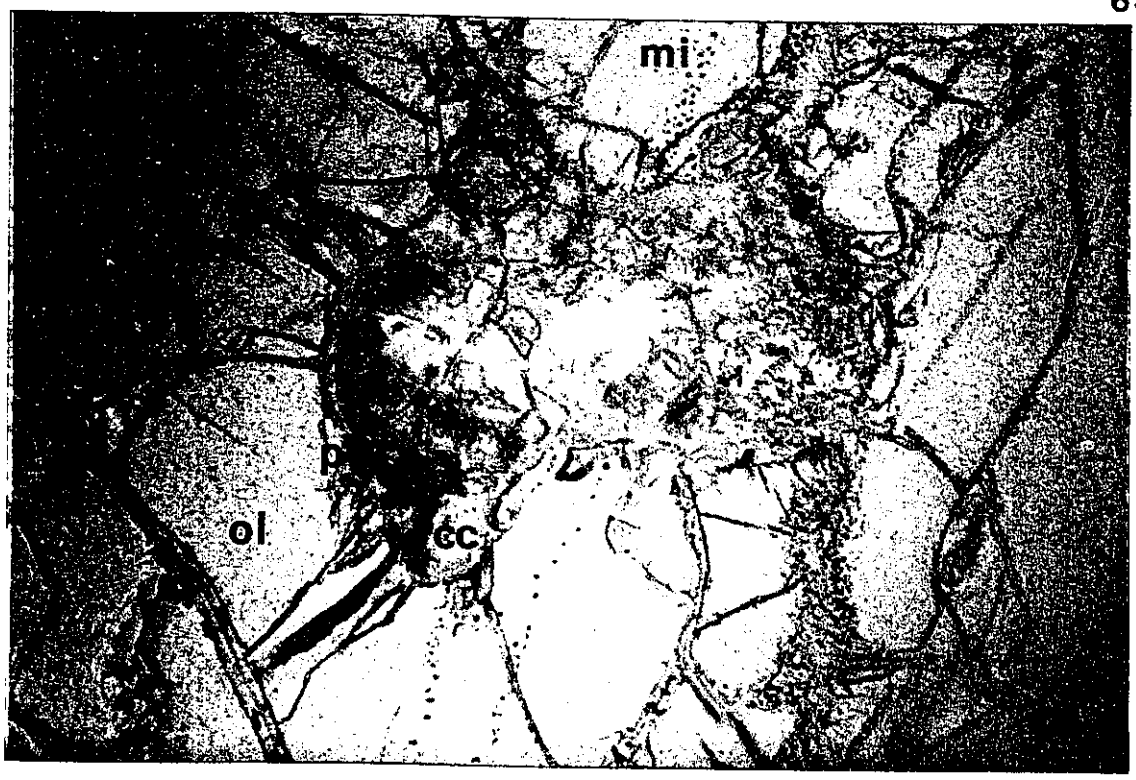

b

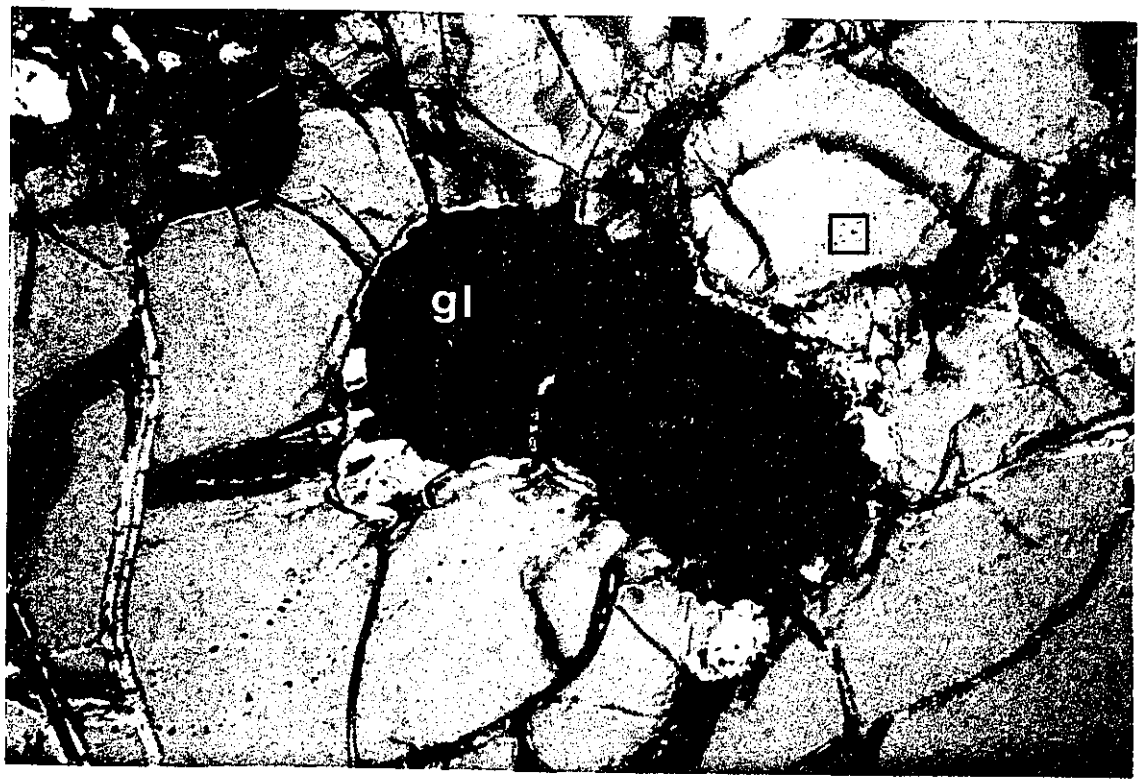

Figure 24. Annealed fracture plane in olivine (ol) of phlogopite (p)-bearing melt inclusions. Inclusions consist of alkaline aluminosilicate glass and CO_2-rich vapour phase (v). Large inclusion at left is 20 μm long. From rock sample 310.

Figure 25. Inner core of a sodian diopside megacryst from rock sample 310 of the Botsor Hill intrusion.

(a) Scanning electron microscope back-scatter image (SEM-BSE). Note the hexagonal calcite crystals. Phlogopite laths surround magnetite crystal faces. The alkaline glass has unmixed to leucitic glass (medium gray at upper right) and analcimic glass (dark). Scale bar is 100 μm.

(b) Cross-polarized light image shows highly distorted zoning in the melt inclusion-bearing core of the clinopyroxene. Field of view is 1 mm.

(c) Magnetite, Ti-phlogopite and euhedral, hexagonal calcite crystals within an alkaline aluminosilicate glass matrix. Plane-polarized light.

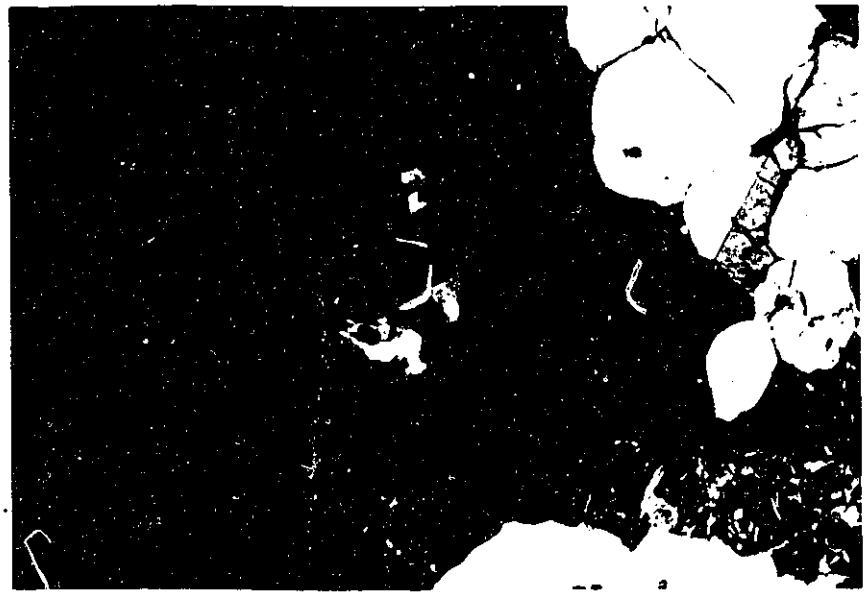

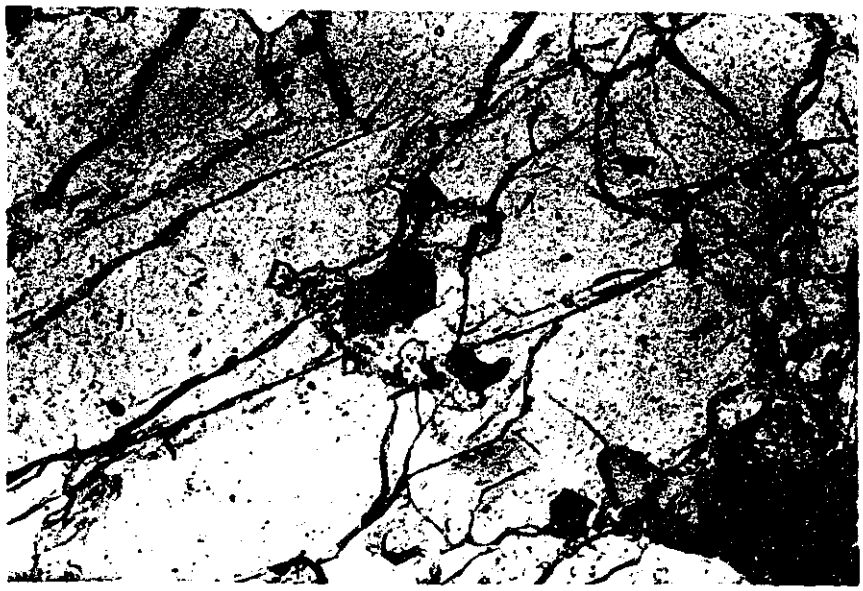

Figure 26. Enlargement of melt-inclusion core of sodian diopside (sd) from Figure 19a. From rock sample 310.

(a) Euhedral intergrowths of Ti-phlogopite (p), magnetite and calcite (c) within an inclusion-rich alkaline aluminosilicate glass matrix. Phlogopite grain is 130 μm long. Plane-polarized light.

(b) Cross-polarized microphotograph. Calcite is hexagonal. Leucite (l) has crystallized from the alkaline glass (ag).

a

b

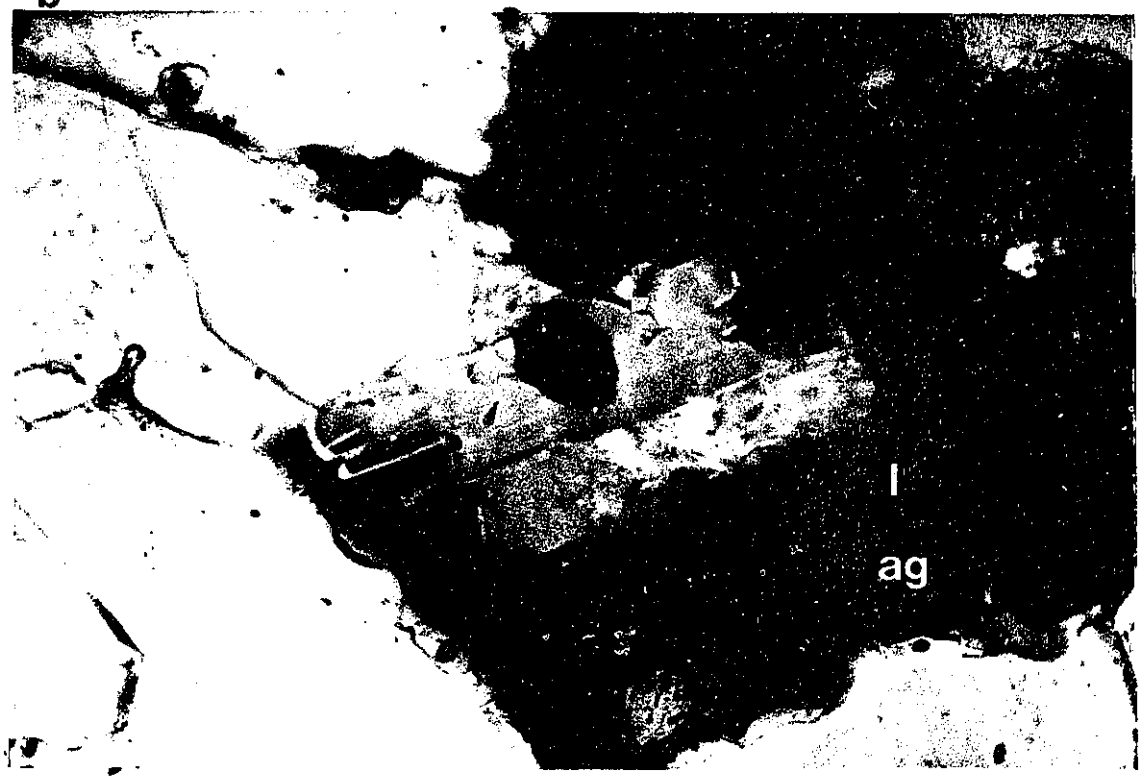

Figure 27. Back-scattered electron (BSE) image showing the compositional complexity of melt inclusions in sodian diopside (sd) from rock sample 310 of the Botsor Hill Intrusion. Light coloured regions in the metasomatic sodian diopside host correspond to the highest Na and Fe^{3+} concentrations (aegirine component).

(a) BSE image of Figure 26. Euhedral Ti-phlogopite (p), calcite (c) and magnetite (m) and apatite (a) are daughter minerals within unmixed Na-Ca glasses (Na; dark regions) and K-rich glasses (l; medium gray regions).

(b) BSE image of lamellae of anhydrite (an), magnetite (m) and calcite (c; Table 3, col. 4) microphenocrysts within a region of alkaline glass unmixed to analcimic (dark regions; Table 3, col. 1) and leucitic (light regions; Table 3, col. 3) composition. Strontium is partitioned into the leucitic glass, calcite, apatite and anhydrite within the melt inclusions.

The composition of the alkaline melt prior to unmixing was estimated using a Cambridge Instruments Quantimet 970 image analyzer. The relative proportions of analcimic and leucitic glass within six circular areas of 30 μm diameter were measured using a difference in grey levels to discriminate between the phases. Five areas gave consistent ratios of analcimic/leucitic glass of 1.02 $\pm$ 0.12, while the sixth gave a ratio of 0.45. The first five measurements have been used to estimate the composition of the combined alkaline melts as $K_{0.38}Na_{0.62}AlSi_2O_6*nH_2O$, with a range of $K_{(0.31\text{-}0.42)}Na_{(0.69\text{-}0.58)}AlSi_2O_6*nH_2O$.

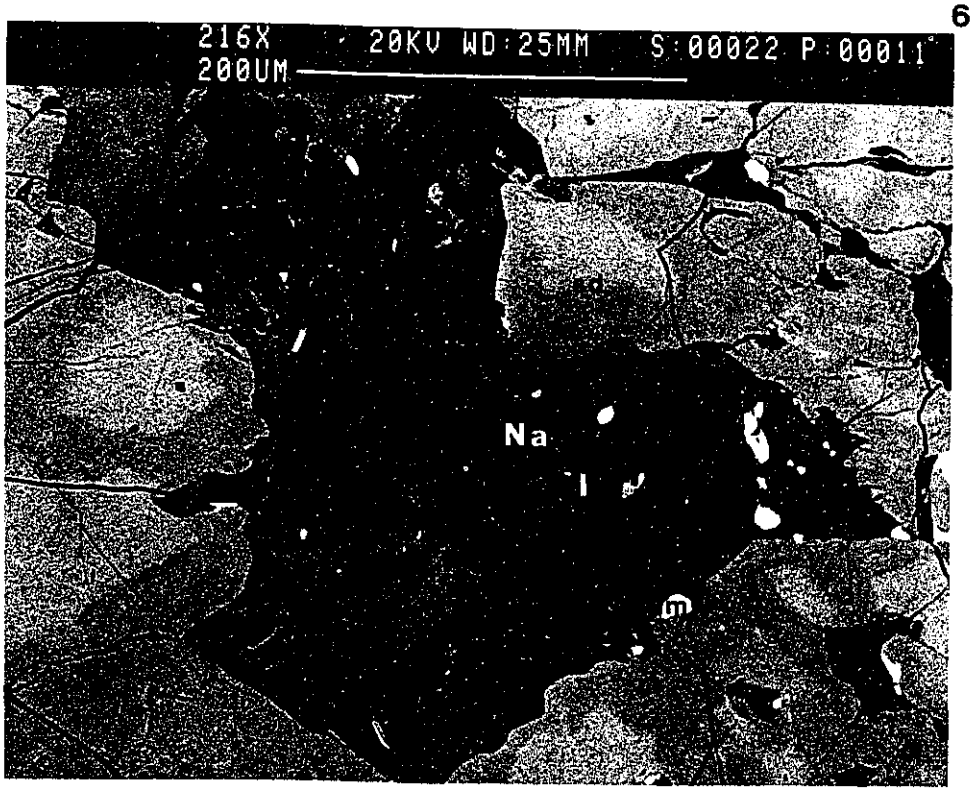
216X 20KV WD:25MM S:00022 P:00011
200UM
Na
I
m

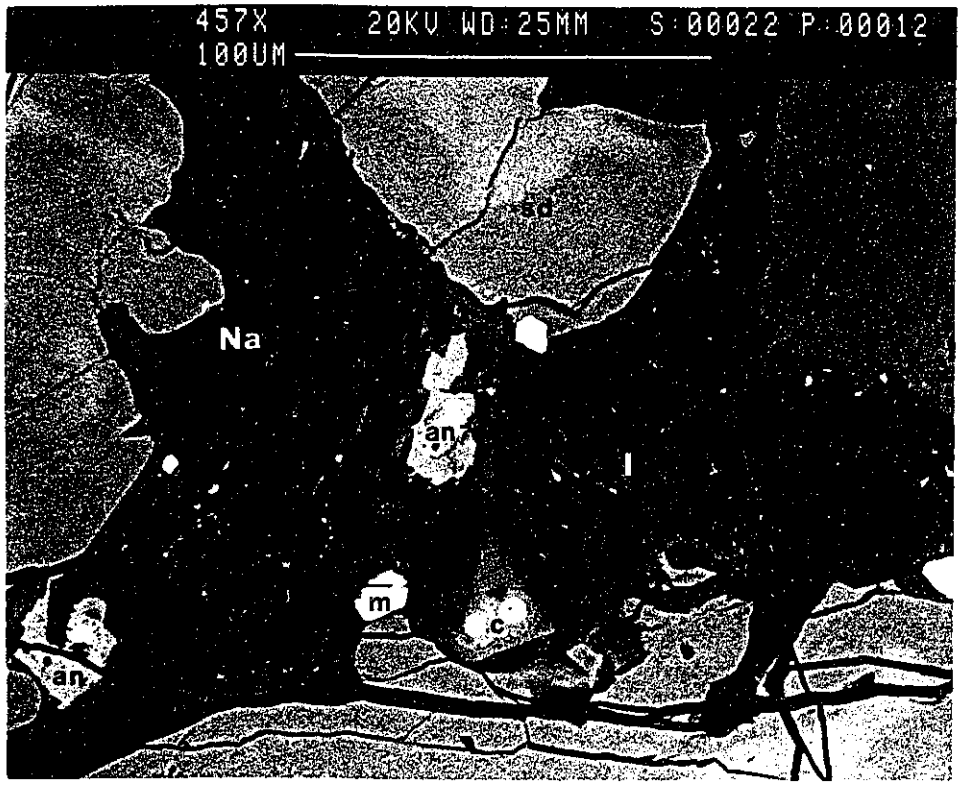
457X 20KV WD:25MM S:00022 P:00012
100UM
Na
ad
an
I
m
c
an

Figure 28. Melt-inclusions within sodian diopside (sd) megacryst from rock sample 310.

(a) Melt inclusion containing Ti-phlogopite (ph), alkaline aluminosilicate glass (gl) and calcite (c). Note the increase in fluid inclusion density towards the interior of the melt inclusion. The rectangular opaque mineral within the phlogopite grain at left is ilmenite, interpreted as a subsolidus exsolution product of Ti-phlogopite. All other opaques are titanomagnetite. Field of view is 0.35 mm.

(b) Cross-polarized light.

a

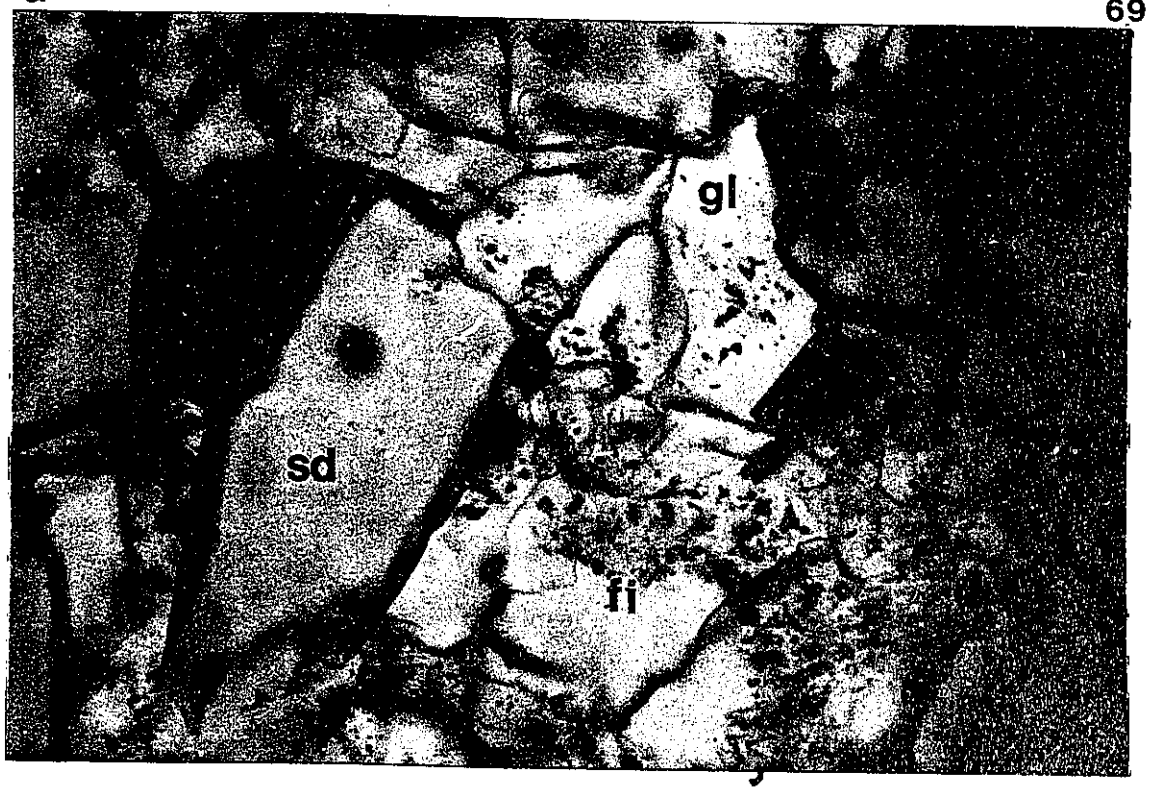

b

melt. The high TiO_2 content of xenocryst phlogopites formed in the presence of an alkaline melt highly deficient in TiO_2, suggests that k_D^{Ti}phlogopite-alkaline melt»1 and that phlogopite metasomatism occurred under high fO_2 conditions. This is supported by the presence of anhydrite in the melt inclusions, where anhydrite + magnetite assemblages are stable in magmas only at FMQ+4 (4 log units above the fayalite-magnetite-quartz buffer; Carroll and Rutherford, 1987).

Also conspicuous is the presence of large (2 mm) xenocrystic amphibole pseudomorphs (Figure 29), which now consist of a fibrous, radiating assemblage of olivine (Table 4, col. 2), Al-Ti diopside (Table 4, col. 3), labradorite (Table 4, col. 4), titanomagnetite and rhönite (Table 4, col. 5). A similar occurrence of rhönite in Figure 29 was described by Tomita (1934) as an alteration product of kaersutite in analcime-bearing teschenites from the Oki Islands, Japan.

Rhönite (ferric-rich member of the aenigmatite series) is a relatively rare mineral typically found in oxidized, undersaturated, alkaline mafic rocks (Cameron, 1970; Johnston and Stout, 1984; Johnston *et al.* 1985). Johnston and Stout (1984) reported rhönite with Fe^{3+}/Fe^{2+} ratios of 8.9, in an oxidized alkali gabbro and contained mantle xenoliths from Kauai, Hawaii. Clinopyroxene overgrowths of pseudomorphed amphibole are common (Figure 30).

Globular structures of microlite-poor Na-rich glass surrounded by mafic, microlite-rich groundmass glass are also present (Figure 20c). These high silica glasses (52-62 wt.% SiO_2) contain microlites of clinopyroxene and apatite. The similarity in composition between the melt inclusion glasses and the globular

Table 4. Microprobe analyses of mineral phases in amphibole pseudomorphs

	1	2	3	4	5
SiO_2	41.53	40.54	48.03	52.44	23.14
TiO_2	1.20	0.03	1.04	0.09	6.95
Al_2O_3	14.12	0.09	6.95	29.36	19.29
FeO	9.90	12.80	6.40	0.61	23.14
MnO	0.10	0.41	0.32	0.00	0.28
MgO	14.87	46.47	14.63	0.01	13.14
CaO	12.02	0.28	21.05	11.77	11.69
Na_2O	2.35	0.03	0.74	4.26	1.19
K_2O	1.51	0.03	0.02	0.33	0.02
F	0.0	nd	nd	nd	nd
Cl	0.0	nd	nd	nd	nd
NiO	nd	0.04	0.00	nd	nd
Cr_2O_3	nd	0.00	0.00	nd	nd
Total	97.60	100.72	99.18	98.87	98.59

1. 22c: magnesio-hastingsite amphibole, average of 5 analyses
2. 310.8: olivine
3. 310.8: Ti-rich clinopyroxene
4. 310.8: plagioclase
5. 310.8: rhönite

Figure 29. Xenocrystic amphibole pseudomorph in Simberi hawaiite (sample 22). The pristine central core is magnesio-hastingsite. The rim is composed of a fibrous, radiating assemblage of olivine, Al-Ti augite, titanomagnetite, labradorite and rhönite. Pseudomorphed amphibole is 2 mm long. Plane-polarized light.

Figure 30. Clinopyroxene overgrowth of completely pseudmorphed amphibole in rock sample 337. Clinopyroxene is 1.5 mm long. Plane-polarized light.

glasses indicates a common lineage in the source region of the basanite, preserved by immiscibility between the alkaline melt globules and the host mafic melt.

Interpretation of the origin of the Botsor Hill Intrusion

The mineralogical and chemical characteristics of Botsor Hill rocks are indicative of a mantle origin. Deformed olivine megacrysts, combined with the presence of carbonate-bearing alkaline melt inclusions in both olivine and clinopyroxene megacrysts, provide textural arguments for a xenocrystic origin. Magnesiochromite grains contained within clinopyroxene megacrysts also support a mantle origin for this unit (Bailey, 1989). The highly brecciated nature of the xenocrystic minerals, and particularly olivine, within the unit may be similar to disaggregation textures described by Boyd and Gurney (1982) from garnet-bearing xenoliths in South African kimberlites. Wyllie *et al.* (1983) postulated that these textures were the result of rapid compression-decompression of silicate minerals occurring within a carbonate-rich groundmass, due to net volume increase during dissociation of the carbonate, at the moment of kimberlite eruption. Although experimental evidence for the formation of these textures is lacking (Canil, 1990), the circular fractures in olivine hosting carbonate-rich melt inclusions from Botsor Hill favours the hypothesis of Wyllie *et al.* (1983).

The chemistry of the melt inclusion minerals and the textures of the xenocrysts may be evidence that the Botsor Hill basanite outcrop is the mafic, hypabyssal portion of a diatreme complex. A lack of outcrop surrounding the hill prevented a characterization of the shape of this unit and its relationship with the surrounding rocks, but the preservation of calcite- and titanian phlogopite-bearing

melt inclusions (an assemblage stable at P>30 kbar; Wendlandt and Eggler, 1980; Green and Wallace, 1988) within the xenocrysts support the hypothesis that this basanite unit is a mantle-derived melt brought to the surface in a high-speed liquid eruption (Bailey, 1987).

A carbonate nodule from a mafic dyke associated with the Raban Diatreme Complex

Outcrops of hornblende-phyric mafic dykes occur in and around the Raban Diatreme Complex. To the west of the South Samat Au deposit (grid location 9525E, 7135N), a fresh mafic dyke of hawaiite composition was sampled for petrographic and geochemical work. Within this dyke was discovered the first reported occurrence of a carbonate nodule of mantle origin.

Microprobe analyses of representative mineral phases within the xenolith are provided in Table 5. The nodule (2x3x4 cm; Figure 31) is subdivided into two portions: (1) a massive, microcrystalline calcite portion which contains megacrysts of magnesiochromite and fine blebs (< 10 μm) of Cu-Fe-Ni, Fe-Cu-Ni and Co-rich Cu-Fe-Ni sulphides, and (2) a silicate portion of coarse-grained (8 mm) amphibole surrounding Al-rich diopside grains, and hosted within a vesicular alkaline glass matrix.

Description of the massive calcite portion of the nodule

Massive, low Sr calcite (<300 ppm; Table 5, column 1) encloses euhedral Mg-Al-chromite (Figure 31a, 31c, 32a; Table 5, col. 6), magnesio-hastingsitic amphibole and aluminous diopside. Fluid inclusions within the calcite contain CO_2 vapour (determined by microthermometry), and when decrepitated by the electron

1. 22c: massive calcite adjacent to magnesiochromite
2. 22c.8.2: carbonate undergoing dissociation
3. 22c.8.a: apatite within 3 (*contaminated by glass)
4. 22c.7ci: clinopyroxene core inside 5
5. 22c.7cii: amphibole overgrowth of 4
6. 22c.10f: magnesiochromite
7. 22: coarse diopside armour between carbonate and basaltic glass
8. 22. fine diopside armour between carbonate and matrix
9. 22c.7c: titanomagnetite
10. 22c.7d: alkaline glass
11. 22c.7h: feldspar within 10
12. 22c.9a: vesicular phillipsite
13. 22c.7f: vesicular analcime

Table 5. Microprobe analyses of xenolith minerals

	1	2	3	4	5	6	7	8	9	10	11	12	13
SiO_2	nd	nd	1.64*	46.10	41.31	0.05	52.34	54.29	0.21	53.81	51.21	47.30	52.37
TiO_2	nd	nd	0.16	0.69	1.29	0.18	0.39	0.00	3.71	0.46	0.15	0	0.01
Al_2O_3	nd	nd	3.12*	8.77	14.26	14.62	3.22	0.68	5.16	22.32	29.86	21.33	25.07
FeO	0.22	0.22	0.39	8.37	9.71	24.69	6.75	4.42	78.77	3.39	0.90	0.02	0.06
MnO	0.48	0.00	0.00	0.14	0.10	0.89	0.18	0.37	0.44	0.05	0.03	nd	0.01
MgO	0.09	0.00	0.23	11.70	15.14	7.83	15.09	18.03	4.78	1.26	0.09	0.02	0.01
CaO	40.05	40.05	41.93	23.43	11.89	0.02	23.00	21.04	0.03	2.01	12.09	7.66	0.06
Na_2O	0.06	nd	0.68	0.29	1.43	0.03	0.29	0.37	nd	8.77	3.80	0.44	13.53
K_2O	0.00	nd	0.05	0.00	1.54	0.03	0.00	0.00	nd	1.09	0.41	1.65	0.03
P_2O_5	nd	nd	39.17	nd	nd	0.00	nd	nd	nd	0.12	0.00	0.04	nd
F	nd	nd	3.45	nd	0.00	0.00	nd	nd	nd	0.00	0.00	0.25	nd
Cl	nd	nd	0.42	nd	0.00	0.00	nd	nd	nd	0.02	0.00	0.01	nd
BaO	nd	nd	0.15	nd	nd	0.00	nd	nd	nd	0.01	0.00	6.41	nd
SrO	0.00	0.19	0.29	nd	nd	nd	nd	nd	nd	0.07	0.60	0.57	nd
NiO	nd	nd	0.02	0.00	0.00	0.05	nd	nd	0.16	0.00	0.00	nd	nd
Cr_2O_3	nd	nd	nd	0.00	0.00	50.53	0.03	0.00	0.05	0.00	0.00	0.00	nd
SO_3	nd	nd	0.59	nd	nd	0.00	nd	nd	nd	0.07	0.00	0.04	nd
Total	100.78	100.40	92.32	99.49	97.46	99.82	101.28	99.20	94.26	93.49	100.12	86.16	91.16

beam of the microprobe, registered K and Cl peaks. Experimental studies by Wyllie and Huang (1976) and Olaffson and Eggler (1978) have demonstrated the stability of carbonate in the mantle at P>17 kbar, whereas at lower pressure carbonate dissociates to CO_2 vapour and CaO. Dissociation of calcite leads to supersaturation of CaO, which, in a mafic melt at high pressure, would cause crystallization of calcic pyroxene.

The massive calcite portion of the xenolith is rounded where it is in contact with the surrounding glassy lava (Figure 31a and 32a), indicating it has undergone partial resorption by the host basaltic magma. Complete decarbonation was prevented by the development of an insulating armour of clinopyroxene crystallites between the magma and the massive carbonate (Figure 31a, 31c, and 32). Evidence for this is the coarse grained Al-rich diopside (Table 5, col.7) in Figure 32b and Figure 33, interpreted to represent dissociation under mantle conditions, and the fine-grained rim of diopside crystallites, (Table 5, column 8; Figures 32 and 33), which may have occurred during emplacement at the surface.

Four euhedral aluminous magnesiochromite grains are enclosed within the massive calcite portion of the xenolith, and one is in contact with magnesio-hastingsitic amphibole replacing aluminous diopside. Magnesiochromite compositions (Table 5, col. 6) from core to rim are essentially identical, except for iron enrichment in the outermost rim. They have Cr/Cr+Al ratios of 0.65 to 0.72 and 100Mg/Mg+Fe" of 42 to 58, values similar to magnesiochromite inclusions in pyroxene from the Botsor Hill intrusion. Their high Al and Cr content distinguish them from melt opaques in the glassy groundmass of the xenolith and in the

Figure 31. Carbonate nodule from a hawaiite dyke (rock sample 22) near the Raban Diatreme Complex.

(a) Photomicrograph of the nodule (long dimension is 2.2 cm) surrounded by the hawaiite groundmass. The round shape of the nodule and the development of a diopside + magnetite rim adjacent to the calcite indicates the calcite has undergone dissociation. The nodule consists of two portions: (1) an upper portion consisting of massive, microcrystalline calcite and euhedral megacrystic magnesiochromite (black crystals), and (2) a silicate portion of coarse-grained (8 mm) amphibole surrounding Al-rich diopside grains, and hosted within a vesicular alkaline glass matrix. Much of the calcite was lost from the section during polishing. Plane-polarized light.

(b) A BSE image of a remarkably well preserved calcite dissociation texture within the silicate portion of the nodule. Destabilization of the central Sr-rich calcite grain (Table 5, col. 2) containing a fluorapatite inclusion (Table 5, col. 3), produced CO_2 vapour, which caused the film of Na-rich aluminosilicate glass to "balloon". Dictyaxitic texture is present between the amphibole (am) megacrysts.

(c) A BSE image of the massive calcite portion of the nodule, with a euhedral grain of magnesiochromite grain (white; Table 5, col. 6). An insulating armour of fibrous diopside grains has grown between the calcite and the hawaiite magma (upper right).

(d) A BSE image of showing complex late stage resorption of analcime (a) by alkaline glass (ag; Table 5, col. 10) with concomitant formation of augite (p). Vesicles (v) are common and occasionally contain botryoidal Cu-sulphides (cu-s). Magnetite (Table 5, col. 9) and laths of labradorite (Table 5, col. 11) have crystallized from alkaline glass. Calcite is present at lower right.

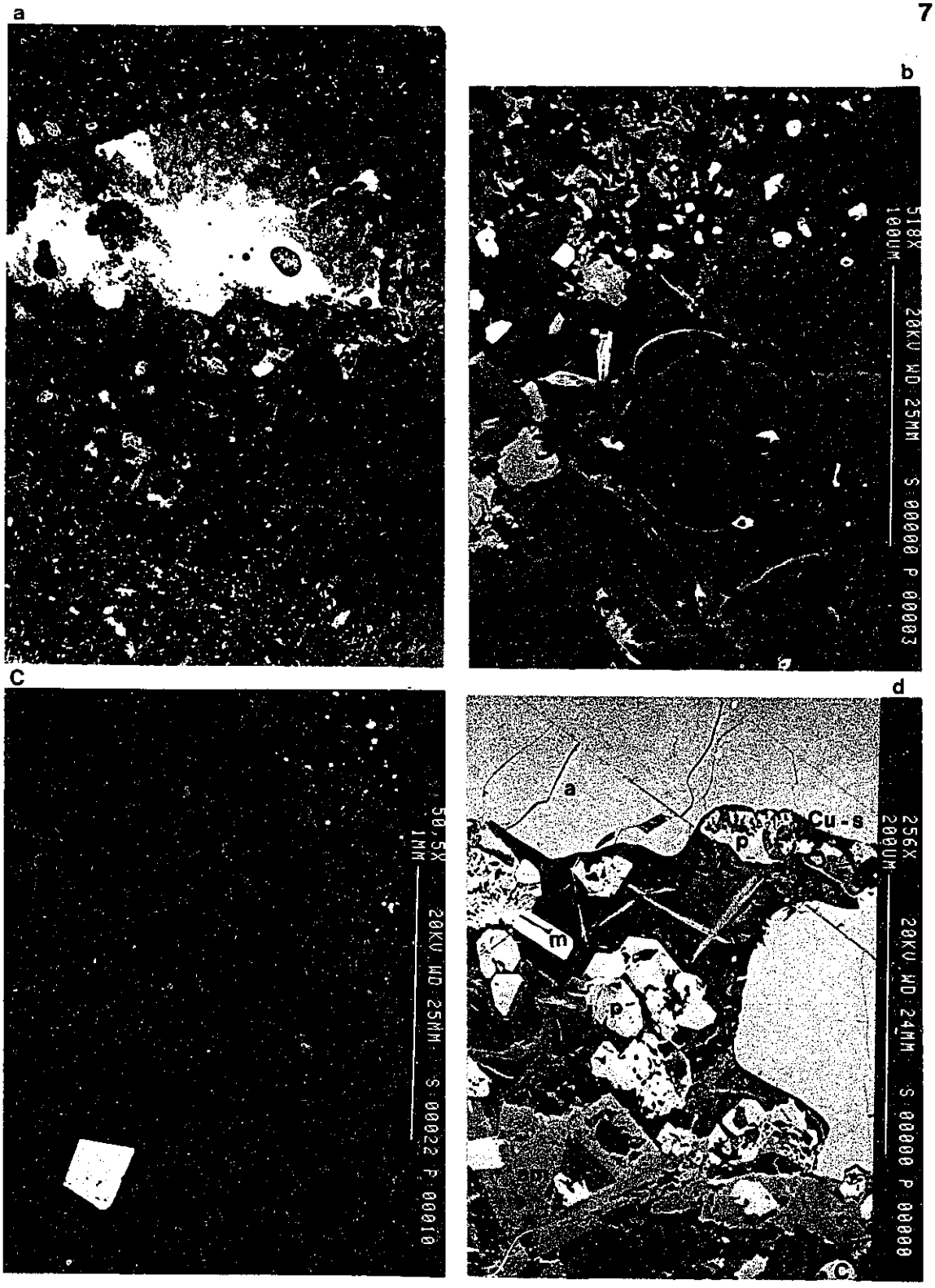
a
b
518X 20KV WD 25MM S 00000 P 00003
100UM
C
50.5X 20KV WD 25MM S 00022 P 00010
1MM
d
256X 20KV WD 24MM S 00000 P 00000
200UM
a
Cu-s
p
m
p
C

Figure 32. Massive calcite portion of the carbonate nodule from rock sample 22.

(a) Enlargement of the rounded portion of the carbonate nodule. Contained within the massive microcrystalline calcite is euhedral magnesiochromite (mgc). The massive calcite is rimmed by a radiating assemblage of pure diopside (cp) crystallites, and titanomagnetite (dark region between cp and basalt groundmass). The magnetite is interpreted to have formed during a localized increase in fO_2 during decarbonation. Plane-polarized light. Field of view is 5 mm.

(b) Another fragment of the nodule found elsewhere in rock sample 22. Two generations of clinopyroxene are associated with this fragment; an early medium-grained aluminous diopside (al cp; Table 5, col. 7) at top, and a late-stage, fine-grained pure diopside (similar to (a); Table 5, col. 8) rimming the xenolith at the lower left and right. Plane-polarized light. Field of view is 3 mm.

a

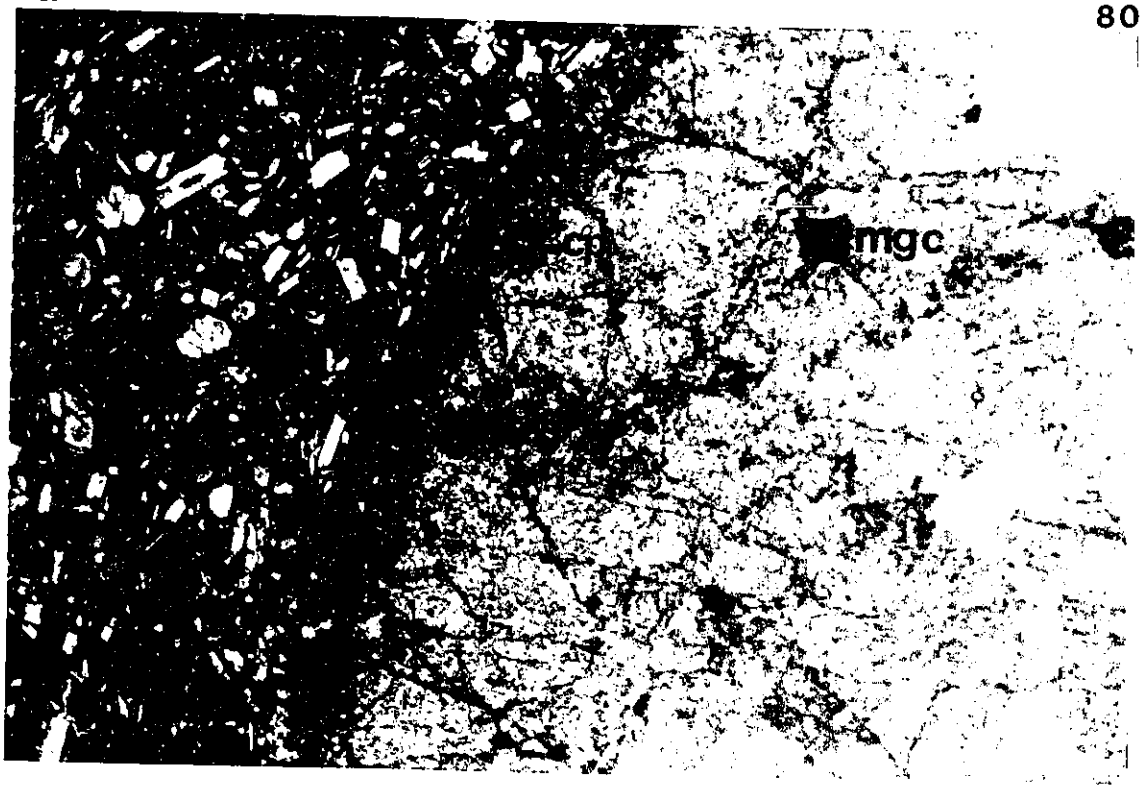

b

Figure 33. Xenolith fragment (from Figure 33) under cross-polarized light. Field of view is 3 mm.

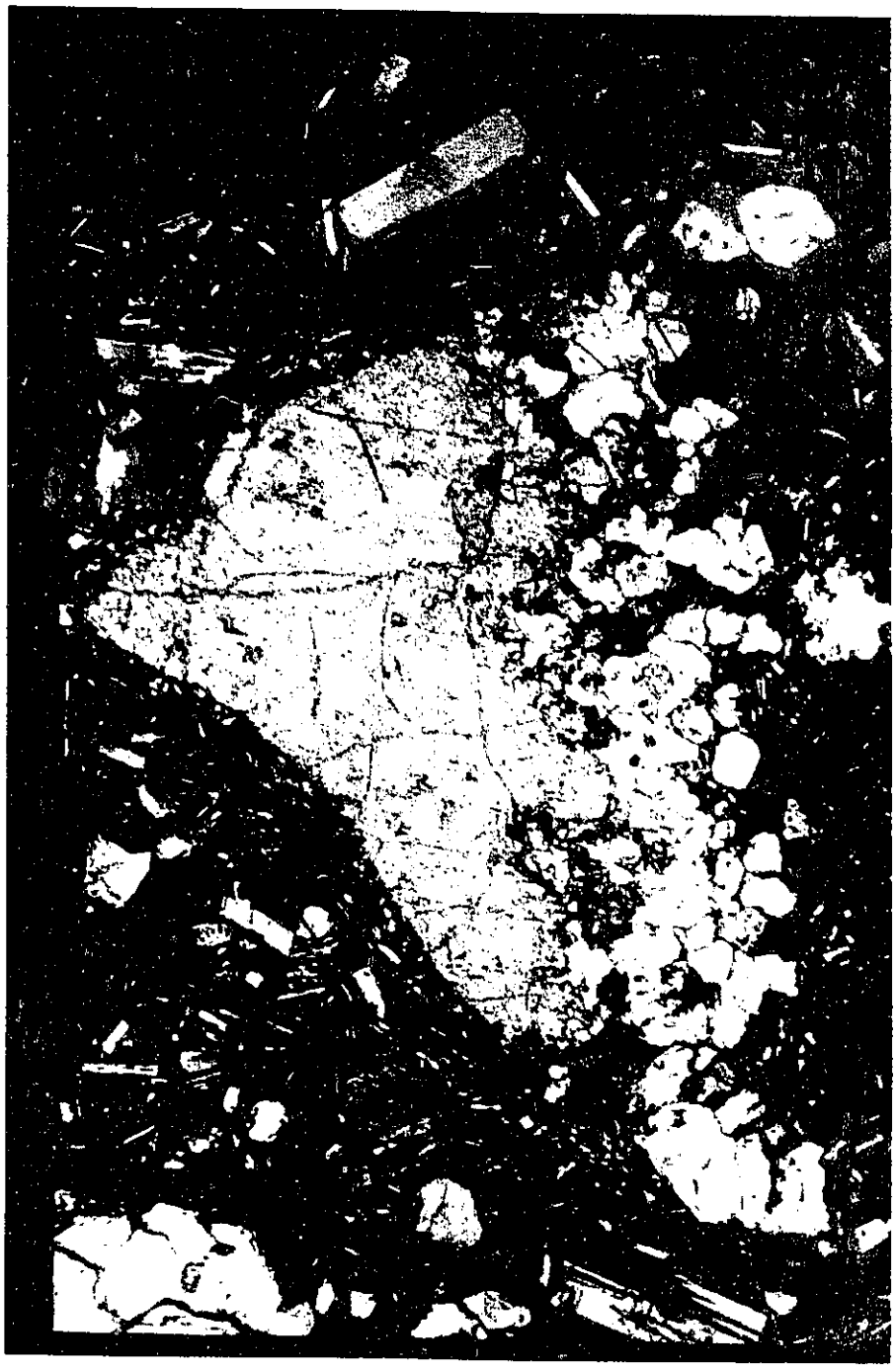

Simberi lavas, which are predominantly Ti-magnetite.

The magnesiochromites are compositionally similar to those in ultramafic rocks of mantle origin (Irvine, 1967; Smith and Dawson, 1975; Haggerty, 1979). Bailey (1989) has also reported magnesiochromites in carbonate lapillae from the Rufunsa carbonatite volcanoes. The high Cr and low Al content of the Simberi spinels are similar to early-crystallizing spinels from kimberlites and lamproites (Mitchell, 1991; Mitchell and Bergman, 1991), characteristics argued by Bailey to indicate a deep mantle origin.

An amphibole megacryst intergrown with one Mg-Al-chromite grain contains abundant Co-Cu-Fe-Ni sulphide minerals. Similar sulphide minerals are contained within the massive calcite.

Description of the silicate portion of the nodule

Three types of clinopyroxene occur within the silicate portion of the xenolith: (1) a coarse grained euhedral chromian to aluminous diopside, which is replaced and overgrown by magnesio-hastingsitic amphibole (Figure 34, Table 5, col. 4), (2) microlitic diopside occurring within the vesicular alkaline glass matrix, and (3) fibrous grains of Al-Ti augite occurring within magnesio-hastingsitic amphibole pseudomorphs, inferred to have formed by the high temperature, low pressure destabilization of amphibole (Huckenholz *et al.* 1988).

The aluminous diopside in the nodule has the highest octahedrally co-ordinated Al content (Al^{vi} =0.10 to 0.11) of all the Simberi lavas. High Al_2O_3 (6.6

Figure 34. Overgrowth and replacement textures from the silicate portion of the nodule from rock sample 22.

(a) Multiple generations of magnesio-hastingsite (am) overgrowing a central core of aluminous diopside (al dp). Microlites of labradorite and diopside are present within a vesicular (v) glassy groundmass. Glass at bottom has been converted to palagonite, whereas the glass at the top right is anhydrous. Plane-polarized light. Field of view is 3 mm.

(b) Magnesio-hastingsite (am; Table 5, col. 5) overgrowth of aluminous diopside (al dp; Table 5, col. 4). The interior of the aluminous diopside contains amphibole inclusions. Plane-polarized light. Field of view is 1.5 mm.

a

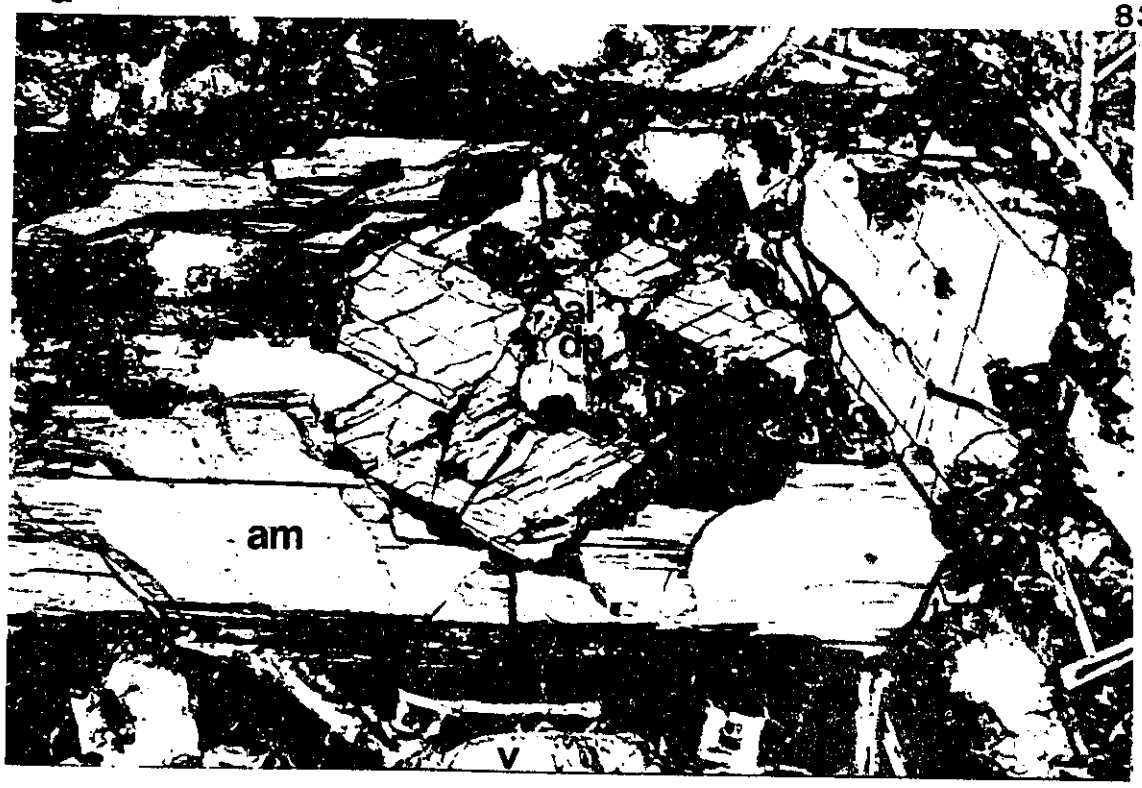

b

to 8.8 wt.%), Al^{vi}/Al^{iv} and $Al+Cr_{(atomic)}/Na+K_{(atomic)}$ content of pyroxenes in the xenolith and the Botsor Hill intrusion indicates formation under high pressure conditions (Kushiro, 1960; Le Bas, 1962), similar to those from spinel peridotite xenoliths (Aoki and Shiba, 1973).

The euhedral aluminous diopside (Table 5, col. 4) is overgrown and partially replaced by euhedral magnesio-hastingsite (Table 5, col. 5) (Figure 34). Multiple generations of amphibole growth are observed (Figure 34a). Phlogopite is present, but is rare compared to amphibole in the nodule. Amphibole is in contact with a mesostasis of alkaline glass similar to those described within the xenocrysts. Where xenolith amphibole is in contact with the mafic lava, it has undergone transformation to an anhydrous assemblage of Al-Ti augite, olivine, labradorite, titanomagnetite and rhönite. Experimental determinations on the stability of these assemblages (Huckenholz *et al.* 1988), allow an estimation of eruption temperatures of the mafic intrusions of the Raban Diatreme Complex and Botsor Hill of between 1050-1140° C.

Vesicular alkaline glass (Table 5, col. 10) forms the matrix between the coarse amphibole grains. Vesicularity is so well developed that dictyaxitic texture (Philpotts, 1989, p. 127), where vesicles are bounded by crystal faces, is often displayed. The matrix glass is predominantly Na-rich glass approaching analcimic to jadeitic to albitic composition, apart from the presence of minor Mg, Fe and Ca (Table 5, col. 10). The glass analysis indicates that it is hydrous, which may be a primary feature. Although palagonite occurs in some areas of the xenolith, the palagonite contains high Cl contents due to the Cl-rich nature of the Simberi

Figure 35. Amygdaloidal analcime (an) and calcite (cc) surrounded by amphibole (am) and vesicular (v) alkaline aluminosilicate glass. Microlites of labradorite have crystallized from the glass. From rock sample 22. Plane-polarized light. Field of view is 1.5 mm.

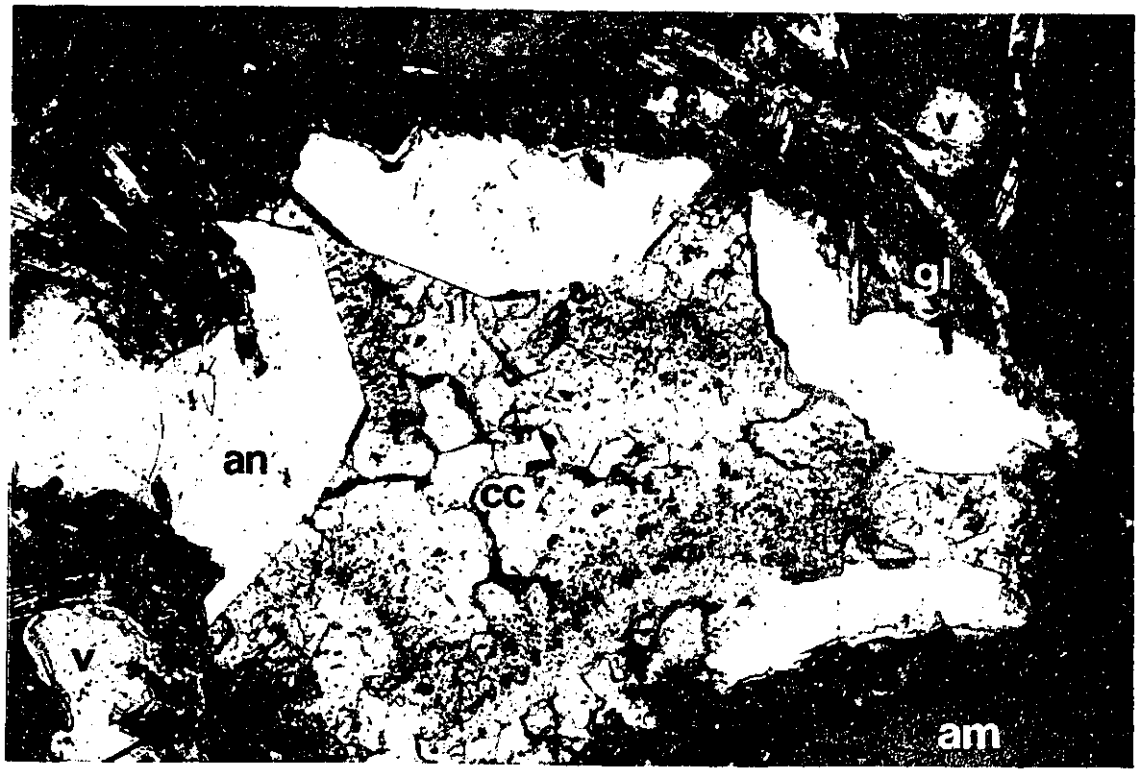
v
gl
an
cc
v
am

groundwaters, while the analysis in column 10 of Table 5 shows low Cl content. The glass differs from the Botsor Hill melt inclusion glasses (Table 3), in the relative absence of K-rich glass, as well as the high ferromagnesian content. Minerals present within the glass include titanomagnetite (Table 5, col. 9) and microlitic diopside and labradorite (Table 5, col. 11).

Evidence for carbonate dissociation as a mechanism for gas exsolution and vesicularity is provided in Figure 31b, where a grain of high Sr calcite (Table 5, col. 2) with a fluorapatite inclusion (Table 5, col. 3), is surrounded by a thin layer of Na-rich aluminosilicate glass. The preservation of this carbonate dissociation texture is remarkable, considering the fragility of the glass rim. It is an important observation because the presence of high Sr calcite with apatite in the xenolith, indicates a potential relationship between the calcite in this xenolith and the calcite contained within melt inclusions in the Botsor Hill outcrop.

There are two separate occurrences of analcime. An early euhedral, massive analcime (Figure 31d) which undergoes resorption by alkaline glass, and an amygdaloidal occurrence of euhedral analcime (Table 5, col. 13), intergrown with calcite (Figure 35) and Ba-rich phillipsite (Table 5, col. 12; identified by G.N. Robinson, Canadian Museum of Nature), within vesicles in the alkaline glass.

Similar to the calcite portion of the nodule, sulphate-bearing fluorapatite is intergrown with Cu-Fe-sulphide minerals occurring as inclusions within megacrystic amphibole. A distinct occurrence of globular Cu-only sulphides occurs within vugs created by decarbonation reactions (c.f. Lowenstern *et al.* 1991), and within

feldspar crystallites in the glassy groundmass (c.f. Heming, 1979).

Interpretation of the origin of the nodule

A paragenesis of the nodule mineralogy is complicated by a polybaric mineral assemblage where minerals stable under high pressure conditions of the mantle, became unstable during isothermal eruption to the surface. The nodule is interpreted to be of mantle origin based on the presence of Mg-Al-chromite, aluminous diopside and calcite. The replacement of Al-diopside by an assemblage of megacrystic magnesio-hastingsite intergrown with fluorapatite and Cu-Fe sulphides, and the precipitation of phlogopite and possibly analcime indicates that Na, K, P, S, F, and H_2O were introduced during mantle metasomatism. The occurrence of calcite and alkaline glass, similar to that found in olivine and clinopyroxene xenocrysts from Botsor Hill, infers that the metasomatizing agent was a sulphate-, carbonate-, H_2O-, and alkali-rich aluminosilicate melt (SCHARM).

Nodules with the mineralogy described above have not been reported previously, although various authors (McGetchin and Benanscon, 1973; Berg, 1986; Bailey, 1989; Rovetta and Mathez, 1982; Bulanova, 1986) have provided natural evidence of mantle carbonate (calcite to dolomite compositions) hosted within mineral inclusions in mantle nodules.

Wallace and Green (1988) and Green and Wallace (1988) have demonstrated the stability of carbonated silicate melts at pressures greater than 21 kbar. Green and Wallace (1988) hypothesized that these melts will react with mantle harzburgite or lherzolite to produce a metasomatic assemblage of pargasitic

amphibole-carbonate clinopyroxenite at 21 kbar < P < 30 kbar and 930 < T < 1080°C. Natural evidence of metasomatism by carbonated, silicate melts, cited by Wallace and Green (1988), is found in spinel-apatite-bearing wehrlite xenoliths within basanites from Victoria, Australia (Frey and Green, 1974; Kleeman, Green and Lovering, 1969), where they argued that enrichment in apatite and Na-rich pyroxenes could only be produced during mantle metasomatism by an ephemeral, carbonated alkaline melt.

The metasomatic textures identified within the Botsor Hill xenocrysts and the Raban Diatreme Complex xenolith provides strong evidence that carbonated melts do exist in the mantle. The difference between the results of this work and the experimental work of Wallace and Green (1988) and Green and Wallace (1988) is that the carbonate melt described in this work is only a minor phase associated with a hydrous, undersaturated aluminosilicate melt (SCHARM), whereas they experimented on carbonatite melts. SCHARM reacts with mantle minerals to produce metasomatic apatite-phlogopite-calcite clinopyroxenite at high P (> 30 kbar), and apatite-amphibole-calcite clinopyroxenite at 21 kbar < P < 30 kbar (Figure 36). Canil (1990) argued that the absence of nodules with this mineralogy was explained by experimental evidence which indicated that even at the high eruption velocity of kimberlites, a carbonate nodule would completely dissociate before reaching the surface. The carbonate nodule reported above appears to have been unaware of these results. That these delicate assemblages were preserved is likely a combination of two factors: (1) development of an insulating armour of diopside between the massive calcite and the mafic melt, and (2) eruption at high velocity (1-5 m/s; Spera, 1984; 1987).

Figure 36. Pressure-temperature diagram indicating the possible depth of origin of the Simberi xenolith and xenocryst metasomatic mineral assemblages. Experimental solidi have not been determined for these bulk assemblages. Experimental stability fields are known for phlogopite-carbonate-lherzolite (Wendlandt and Eggler, 1980) and amphibole-carbonate-pyrolite (Wallace and Green, 1988).

Pressure estimates: The apatite-phlogopite-SCHARM-clinopyroxenite assemblage is stable at P > 30 kbar, whereas the apatite-magnesio-hastingsite-calcite nodule may have formed between 21 and 30 kbar. At temperatures above 980°C, the carbonate destabilization boundary is at 21 kbar. Carbonate-rich melts ascending above this boundary will become CO_2-saturated, causing encapsulation of CO_2-rich melt inclusions during clinopyroxene crystallization.

Temperature estimates: Although SCHARM is always above its liquidus in oceanic peridotite, its reaction with peridotite minerals causes metasomatic crystallization of phlogopite at high P, and of amphibole at low P. Eruption temperatures for the Botsor Hill basanites and the basaltic dykes of the Raban Diatreme Complex can be estimated from experimental work on amphibole destabilization (Huckenholz *et al.* 1988). Assuming direct ascent to the surface, minimum eruption temperatures are 1050°C. If the basanites and basalts were derived during adiabatic decompression melting of SCHARM-modified peridotite, mantle metasomatism by SCHARM was occurring at 1050° < T < 1080°C.

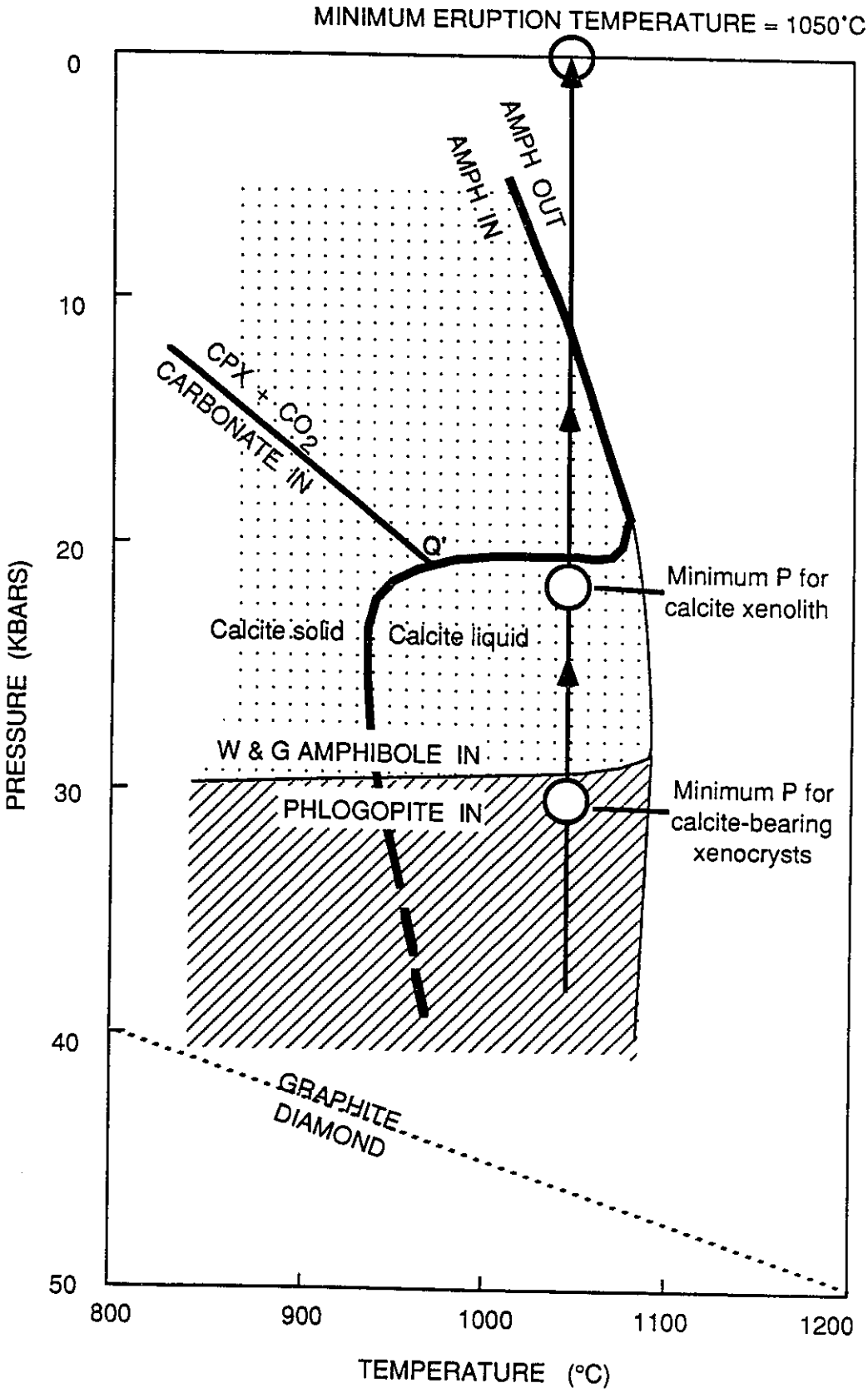
MINIMUM ERUPTION TEMPERATURE = 1050°C
AMPH OUT
AMPH IN
CPX + CO2
CARBONATE IN
Q'
Minimum P for
calcite xenolith
Calcite solid
Calcite liquid
W & G AMPHIBOLE IN
PHLOGOPITE IN
Minimum P for
calcite-bearing
xenocrysts
GRAPHITE
DIAMOND
PRESSURE (KBARS)
0
10
20
30
40
50
800
900
1000
1100
1200
TEMPERATURE (°C)

A carbonated mafic melt, derived during extensionally related adiabatic decompression melting of carbonated mantle regions, would rapidly exsolve large amounts of high pressure, low density CO_2 gas into the melt. Carbonate dissociation would create a propellant for high speed eruption of mafic melts to the surface, called *mafic melt diatresis* by Bailey (1987), and would provide an effective mechanism for the formation of the Raban diatreme complex.

Following eruption at the surface at about 1100°C from a depth greater than 70 km (Green and Wallace, 1988), a low temperature suite of minerals formed until quenching occurred. Amphibole destabilization, decarbonation resulting in vesicularity in the alkaline glass, and the crystallization of titanomagnetite, labradorite and diopside occurred during cooling of the basalt magma. The alkaline glass resorbed coarse-grained analcime with concomitant crystallization of augite. Dissociation of calcite at low pressure led to the high temperature remobilization of volatile elements and subsequent reprecipitation of analcime, calcite, Ba-phillipsite and Cu-sulphides in vesicles.

A working hypothesis on the origin of sulphate-, carbonate-, H_2O-, alkali-rich aluminosilicate magmas (SCHARM)

The negligible Mg and Fe content and low Mg# of the melt inclusion glasses indicates that the sulphate-, carbonate-, H_2O-, alkali-rich aluminosilicate magmas (SCHARM) were not derived from partial melting of mantle mineral assemblages. The replacement of mantle minerals by phlogopite and amphibole indicates that SCHARM is in disequilibrium with the depleted mantle wedge underlying the TLTF arc. The ensimatic setting of the island arc, combined with the sub-crustal origin of the

xenolith and xenocryst assemblages, limits the possible source regions of SCHARM to a subducting slab. Although westward subduction along the Manus-Kilinailau trench ended approximately 10 Ma, a portion of an oceanic slab nevertheless remains.

A subducting oceanic slab consisting of basalt will undergo dehydration, recrystallization and partial melting in response to prograde metamorphism from the relatively cool lithospheric to hot asthenospheric regions of the upper mantle. The chemical composition of SCHARM may represent a magma derived during partial melting of mineral phases in the subducted basaltic slab. The low Fe and Mg content of SCHARM indicates that a ferromagnesian mineral is not undergoing fusion in the slab. The alkali-rich aluminosilicate composition of SCHARM is more compatible with melting of a feldspathic mineral, which could be plagioclase if it was both alkali-enriched and Ca-depleted. Melting of feldspar cannot account for the high carbonate, sulphate, water and halogen content of SCHARM. A possible feldspathic phase that could account for the chemical properties of SCHARM however, is scapolite. Seawater alteration enriches mid-ocean ridge basalts in Na, K, $(CO_3)^{2-}$, Cl, H_2O, $(SO_4)^{2-}$, Mg, U and Sr (Hart *et al.* 1974; Staudigel *et al.* 1981; Ito *et al.* 1983; Albarède and Michard, 1986), and alkali-enriched feldspars undergoing prograde metamorphism during subduction of altered basaltic crust could crystallize scapolite. A simple end member equation describing the incongruent melting of scapolite to produce SCHARM can be written:

$$\underset{\text{marialite}}{\{3\ Na(K)AlSi_3O_8\}\cdot NaCl\ (s)} + \underset{\text{meionite}}{3\ CaAl_2Si_2O_8\}\cdot CaCO_3\ (s)\}} + \underset{\text{olivine}}{2\ (Mg,Fe)SiO_4} =>$$

{feldspar altered by seawater and converted to anorthite and scapolite during prograde metamorphism}

$Ca(Mg,Fe)_2Al_2Si_3O_{12}$ (s) + $\{NaAlSi_2O_6\text{-}2(Mg,Fe)SiO_3\}$ (s) + 2 Al_2SiO_5 (s) + 4 SiO_2 (s) +
grossular omphacite kyanite quartz
[----------QUARTZ ECLOGITE----------]

[$CaCO_3$ (l) + NaCl (l) + O_2 + $NaAlSi_2O_6$ (l) + $K(Na)AlSi_2O_6$ (l)]
[----------CARBONATE ALKALINE MELT----------]

Similar equations can be written using sulphate meionite to produce a sulphate-rich alkaline melt. The formation and stability of scapolite in conditions similar to oceanic crust at high pressure is unknown (R.C. Newton, 1991, pers. comm.), but the above reaction between scapolite and oceanic basalt is consistent with the Green and Ringwood (1972) and Nicholls and Ringwood (1973) hypothesis that melts produced during the basalt-quartz eclogite transition will be hydrous siliceous melts. The abundant CO_2 contained within the oceanic crust as $CaCO_3$, survived prograde metamorphism (Huang *et al.* 1980), perhaps as scapolite, and produced carbonated, silica-undersaturated alkaline melts during partial melting.

The occurrence of melt inclusions consisting of Na- and K-rich glass phases provides valuable information about the mantle source region of the TLTF arc, and represent a "missing link" between the subduction of oceanic crust and the extrusion of calc-alkaline rocks, and is crucial to an advancement of the understanding of subduction zone processes.

Chapter 5. Geochronology

Introduction

Among the recommendations of Wallace *et al.* (1983) for further work was a systematic geochronological study of the TLTF islands. A program of age dating was undertaken to constrain the timing relationships between the initiation and cessation of volcanic activity and to place the gold mineralization event(s) within a volcanological context. A compilation of K-Ar age determinations for the Tabar Islands conducted by Johnson *et al.* (1976; 1 determination) and J. Rytuba (1987, Kennecott unpublished data; 5 determinations) are presented in Table 1 along with five $^{40}Ar/^{39}Ar$ dates obtained from this study.

K-Ar and Ar-Ar dating techniques determine the time when a given mineral or rock was closed to Ar diffusion, and therefore age determinations are cooling ages, which approximate intrusion ages if cooling is rapid. Hornblende has a closure temperature of around 700°C (Berger and York, 1981). Since plagioclase has a much lower closure temperature for Ar ($\approx$175°C; Berger and York, 1981), it is possible to evaluate the cooling history of a rock by comparing the age of minerals with differing Ar closure temperatures.

Methodology

$^{40}Ar/^{39}Ar$ dating of mineral separates was conducted at the Institute of Human Origins (Berkeley) by R. Drake using a laser fusion, total Ar release method.

The work was conducted during two periods, February, 1990 and June, 1991. The samples were irradiated in two separate batches (ie., two different *J*-values) in a 5 megawatt reactor at Los Alamos using Fish Canyon sanidine (27.84 Ma) as an age monitor. All accumulated mass spectrometry data for the $^{40}Ar/^{39}Ar$ analysis are provided in Appendix B.

Discussion of Results

The Sorowar Road intrusion (Sord Plut) yielded 6 reliable hornblende ages (2.79 Ma to 3.29 Ma) with a mean age of 2.94 ± 0.25 Ma. Flagioclase separates from this rock produced scattered (Appendix B) dates ranging from 0.6 to 4.2 Ma. Hydrothermal mineralization containing Au at the Sorowar deposit has been dated at 2.8 ± 0.6 Ma (K-Ar), suggesting a temporal consistency between intrusion of mugearitic domes and Au mineralization.

In the Samat area, geological evidence indicates that mugearitic domes of similar composition to the Sorowar Road intrusion were cut by diatremes and related mafic dykes of hawaiite composition, culminating in hydrothermal Au mineralization of the diatreme and the surrounding mugearite intrusion. To provide age constraints on these events in the Samat area, a hawaiite dyke (Sample 337) intruding the Raban Diatreme Complex at North Samat (Figure 14) and a megacrystic, amphibole-bearing carbonate xenolith (Sample 22XEN) from a hawaiite dyke near the South Samat deposit were dated.

The North Samat sample (337) returned 3 consistent hornblende ages with a mean age of 3.13 ± 0.06 Ma. This is interpreted as the date of the diatreme-

forming event. The host trachyandesitic Samat intrusion is therefore temporally (as well as compositionally) similar to the Sorowar Road intrusion (2.94 ± 0.25 Ma), within analytical error.

The South Samat sample of magnesio-hastingsitic amphibole hand-picked from a amphibole-carbonate-magnesiochromite xenolith in a dyke of hawaiite composition exposed near the Raban Diatreme Complex at South Samat yielded two ages of 2.49 ± 0.80 and 3.38 ± 0.63, with a mean age of 2.9 ± 0.6 Ma. Considering the errors involved, this is essentially similar to the 3.13 Ma age of the North Samat dykes.

Interpretation of the Results

The geological history of Simberi Island volcanism and hydrothermal Au mineralization can be interpreted as follows. The combined K-Ar and Ar-Ar dating suggest that primary mantle liquids of alkali olivine basalt composition were extruded on Simberi from about 3.6 Ma to 3.1 Ma (Samples 8531, 8532, 8534, 347). Fractional crystallization of this mafic reservoir led to later eruptions of trachybasalt and trachyandesite melts from 3.1 to 2.3 Ma.

Trachyandesite domes intruded the Sorowar and Samat regions from 3.3 Ma to 2.9 Ma. Structural deformation of the mugearite intrusions in the Samat area, perhaps initiated by regional scale pull-apart rifting and graben development provided zones of weakness exploited by rapidly rising, volatile-rich mafic melts of basalt to trachybasalt composition, leading to diatreme formation between 3.1 and 2.9 Ma. Geological relationships indicate that gold mineralization post-dated diatreme formation and this is supported by the direct dating of Sorowar

hydrothermal mineralization at 2.8 Ma. The geological similarity between the development of structures and concomitant intrusion of mugearitic domes and dykes at Sorowar, Pigiput, Samat and Botlu may therefore represent consanguineous intrusive/hydrothermal activity which produced gold mineralization on Simberi.

If a relationship does exist between mugearite intrusion and gold mineralization on Simberi Island, it has consequences for mineral exploration in the other islands of the Tabar Group, and for the TLTF arc as a whole. Two samples of trachybasalt from Tatau Island returned K-Ar ages of 1.9 and 2.0 Ma. Mugearitic volcanism should therefore be younger, and perhaps not exposed on the surface to the extent that Simberi mineralization is. An exploration criterion for Tatau and Tabar Island therefore, is to develop deep target exploration strategies with techniques capable of penetrating uneroded, volcanic cover.

Excess Radiogenic Argon in the Botsor Hill Intrusion

An attempt was made to date the basanite outcrop because it appears to intrude weathered trachyandesitic volcanic rocks, and based on geological relationships should be a young unit. Ferromagnesium minerals were dated by Ar-Ar and returned five improbably old dates ranging from 52 to 604 Ma. A 6th date, (Botsor-1; Sample 1, Appendix B) returned an age of 1.92 ± 0.27 Ma, but requires confirmation. If correct, this basanitic outcrop would be the youngest yet dated on Simberi Island. It would also indicate that volcanism was not a simple evolutionary progression from basaltic to intermediate compositions based on fractional crystallization in the underlying reservoir, but that continuous extension in the Tabar

Island Group allowed several aliquots of primitive mafic melts to ascend to crustal regions.

A high pressure origin (P>30 kbar) for the Botsor Hill basanite has been discussed. The most likely explanation for the old dates is that the whole rock mineral separates contain xenocrysts which trapped radiogenic ^{40}Ar from the source region. This radiogenic ^{40}Ar may be contained within SCHARM which is a contaminant of the xenocrystic olivine and sodian diopside. The pyroxene megacryst cores were insulated from the basaltic melt which extruded at ≈1100°C (Kennedy *et al.* 1990b) and retained the radiogenic ^{40}Ar contaminant trapped during pyroxene formation in the mantle source region, unlike the other minerals dated in the study which do not retain Ar until lower temperatures were attained. The old ages indicate that the bulk of the ^{40}Ar released during mineral fusion was excess Ar. Excess Ar has also been found to occur in diamonds (Ozima *et al.* 1983) and kimberlite pipes (Faure, 1986), in accord with the observations in this study.

In order to assess the role of excess ^{40}Ar in the Botsor Hill sample, all the data from Appendix B were plotted on an Ar isotope correlation diagram (Figure 37). The concept and usage of Ar isotope correlation diagrams are discussed in Faure (1986; p. 110). The data set presented in Figure 37 reveals that a straight line relationship (r=0.99) is obtained for all samples, apart from the Botsor-1 samples that produced the 52-604 Ma ages. Determination of the slope ± error of the regression line allows calculation of the age ± error of the total mineral data set, similar to Rb-Sr dating techniques. The calculated age of 3.06 ± 0.10 Ma represents the bulk age of Simberi volcanism, determined in this study. The initial

Figure 37. Isotope Correlation Diagram for Ar released by fusion of Simberi igneous minerals

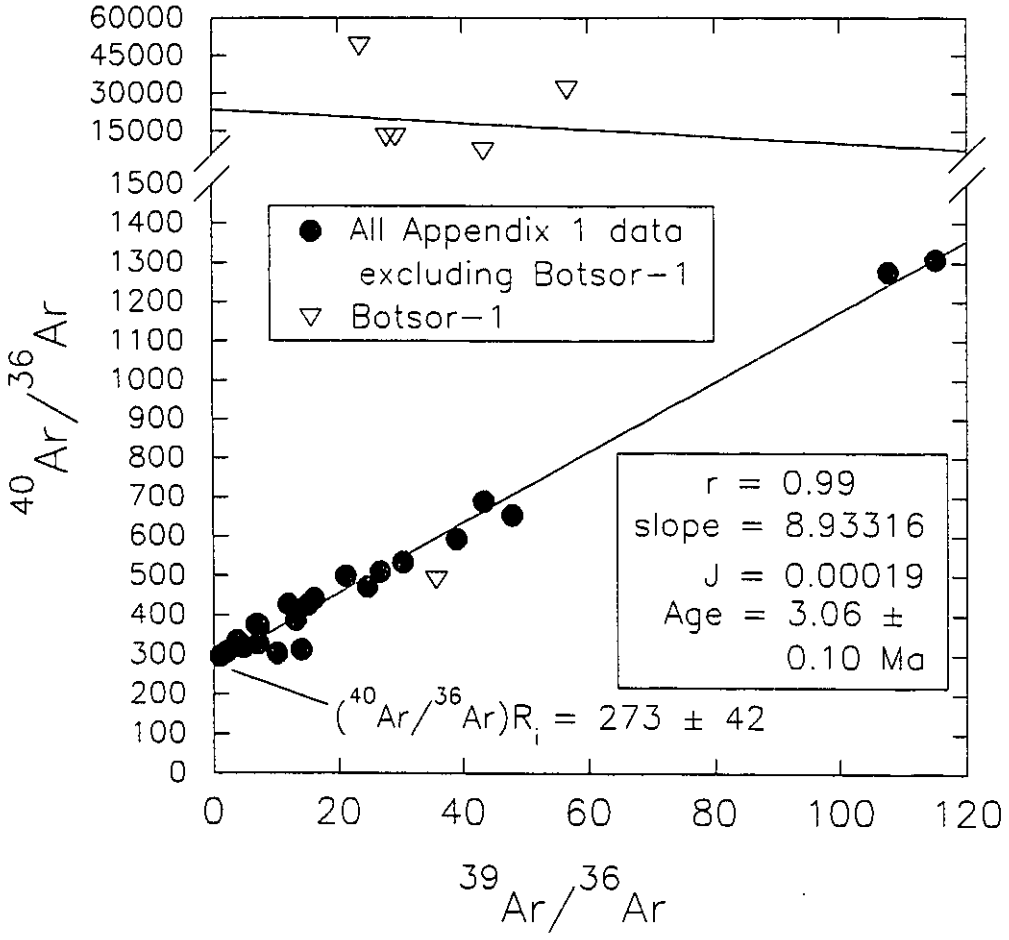

ratio of $^{40}Ar/^{36}Ar$ of 273 ± 42 is similar to the $^{40}Ar/^{36}Ar$ atmospheric ratio of 295.5 determined by Nier (1950), and is evidence that the majority of mineral samples have not been contaminated by excess radiogenic ^{40}Ar.

The five anomalously old Botsor-1 samples have initial $^{40}Ar/^{36}Ar$ ratios between 7,000 and 48,000. These ratios confirm that excess radiogenic ^{40}Ar is responsible for the old ages and preclude reliable age determination of this rock. High $^{40}Ar/^{36}Ar$ ratios have been found elsewhere in mantle derived basaltic rocks. Allegre *et al.* (1983) reported values as high as 25,000 from oceanic basalts. Mid-ocean ridge basalt glasses reported by Fisher (1981) and Marty *et al.* (1983) have ratios of about 10,000. The conventional interpretation of these high ratios is that the mantle of the Earth is strongly enriched in ^{40}Ar produced by decay of ^{40}K contained in mantle minerals. The solubility of Ar in melts increases with increasing pressure (Carroll and Stolper, 1991). Glassy basalts quenched under high hydrostatic pressure on the ocean floor will retain Ar gas with a high $^{40}Ar/^{36}Ar$ in glass, which is a reflection of the $^{40}Ar/^{36}Ar$ ratio in the source region (Faure, 1986).

Mantle metasomatism by SCHARM and production of high $^{40}Ar/^{36}Ar$ ratios

The Botsor Hill basanite did not form on the ocean floor, and therefore the high $^{40}Ar/^{36}Ar$ ratios were inherited from the source region by retention of Ar in pyroxene melt/fluid inclusions. Evidence presented in Chapter 4 indicates that the melt inclusions contain a quenched sulphate-, carbonate-, H_2O-, alkali-rich aluminosilicate magma (SCHARM) in disequilibrium with mantle peridotite.

Based on the preliminary experimental results of Carroll and Stolper (1991), which show a correlation between Ar solubility and pressure, SCHARM could potentially dissolve a large amount of Ar. This is consistent with the high total Ar yields from the Botsor-1 pyroxene fusions compared to the other minerals (Appendix B). The extreme incompatibility of Ar combined with high Ar solubility in melts at high pressure would indicate that the source region for these metasomatic melts is "old", with high $^{40}Ar/^{36}Ar$ ratios. These features would be characteristic of melts released during fusion of feldspathic minerals contained within seawater-altered oceanic crust subducted in the former Manus-Kilinailau trench, prior to collision of the Ontong Java Plateau.

Other studies indicate that metasomatic processes can transport and create mantle reservoirs with excess ^{40}Ar. Villa (1990) reported that excess Ar in metasomatic amphiboles in peridotite from Zabargad Island (Red Sea) precluded their age determination. Release spectra for Zabargad amphiboles show that the majority of excess Ar is released at temperatures less than 800°C. Based on this evidence he concluded that the high concentrations of excess Ar found in the metasomatized peridotite were the result of subsolidus reactions with hydrothermal fluids rich in excess Ar.

It is recommended that further $^{40}Ar/^{39}Ar$ work using microanalytical step-

heating techniques be conducted to elucidate the metasomatic history of the Simberi mineral assemblages.

Chapter 6. Geochemistry of Simberi volcanic rocks

The Tabar-Lihir-Tanga-Feni (TLTF) rocks show chemical enrichment and depletion trends characteristic of calc-alkaline rocks (Johnson *et al.* 1976; Heming, 1979; Wallace *et al.* 1983; Johnson *et al.* 1986) with enrichments in the large-ion lithophile elements (LILE; K, Rb, Sr, Ba, Th, U), light rare-earth elements (LREE; La, Ce, Pr, Nd, Sm, Pm), and depletion in high-field strength elements (HFSE; Ta, Ti, Nb, P, Zr, and Hf). The rarity of primitive magmas in island arcs often limits geochemical studies to an assessment of the evolution of a magma series with regard to fractional crystallization.

The identification of mantle-derived mafic units at Botsor Hill and in the Raban Diatreme Complex allow a determination of chemical variations due to contamination and metasomatism by a sulphate-, carbonate-, H_2O- and alkali-rich aluminosilicate magma (SCHARM). The assessment of chemical (element enrichment and saturation) and physical (fo_2, T) conditions imparted on the mantle source region by SCHARM, facilitates a better understanding of the subsequent path of fractional crystallization, and its control on the chemical variation of evolved lavas.

Which composition represents a primary magma derived from the mantle?

Three Botsor Hill basanite samples (Appendix A.8; Botsor-1, SI89-310, SI89-311) from this study and the potassic basanite sample from Johnson *et al.* (1976; #74400037) have high MgO content (10.5-13.7 wt.%), and may represent primary

mantle-derived magmas. The high MgO basalts Botsor-1 and SI89-310 (13.5 and 13.7 wt.% MgO) show lower CaO and Al_2O_3 content than those with MgO ≈ 11 wt.% (Figure 38). The dilution of CaO and Al_2O_3 in the high MgO basalts may result from either olivine accumulation, or contamination by xenocrystic olivine.

The two remaining samples, SI89-311 (MgO = 10.5 wt.%; Table 6) and 74400037 (MgO = 11 wt.%; Table 6) are possible candidates for primary melts extracted from partial melting of the mantle wedge. A primary origin for these two samples is supported by their high Mg* = 69 and high concentrations of the compatible elements Cr (320 ppm), Ni (140 ppm) and Sc (27.3 ppm). If these samples represent unfractionated partial melts derived from the metasomatized mantle wedge below Simberi Island, it is possible to compare their elemental compositions to those of mid-ocean ridge basalts (N-MORB) derived from partial melting of depleted mantle regions (Table 6). This is a qualitative comparison only and does not take into account chemical variations produced by depth and degree of partial melting of the source region.

The major element data in Table 6 shows that the Simberi primary basalts are enriched in CaO, Na_2O, K_2O and H_2O, and depleted in SiO_2 and TiO_2 relative to MORB. The chemical enrichments in the Simberi primary magmas can be attributed to contamination of the mantle source region by SCHARM, because of its carbonate-, H_2O- and alkali-rich nature. The high primary Fe_2O_3/FeO is a reflection of the high fo_2 conditions imparted to the mantle source region by SCHARM, which has caused the preferential incorporation of TiO_2 into titanian phlogopite. The low SiO_2 could be due to partial melting under high CO_2/H_2O conditions (Eggler, 1974).

Table 6. Chemical comparison of mid-ocean ridge basalt with primary lavas from Simberi Island

Oxide (wt.%)	N-type MORB[1]	Botsor Hill SI89-311	74400037[2]
SiO_2	48.77	46.94	46.6
TiO_2	1.15	0.78	0.75
Al_2O_3	15.90	12.79	12.9
Fe_2O_3	1.33	4.97	3.95
FeO	8.62	4.36	5.1
MgO	9.67	10.53	11.0
CaO	11.16	13.42	12.3
Na_2O	2.43	3.17	2.7
K_2O	0.08	0.42	1.6
P_2O_5	0.09	0.29	0.38
MnO	0.17	0.17	0.18
H_2O	0.30	2.40	2.14
Mg#	66.6	81.2	79.4
Mg*	63.7	68.0	69.4

$Mg\# = 100Mg/(Mg + Fe^{2+}(FeO\ only))_{molar\ proportions}$
$Mg^* = 100Mg/(Mg + Fe^{2+}(total\ Fe\ as\ FeO))_{molar\ proportions}$
References:
1. Schilling *et al.* 1983
2. Johnson *et al.* 1976

Chemical variations caused by mineral fractionation from primary lavas

Major element variations represented by Simberi Island lavas are presented in a series of Harker diagrams (Figure 39). A comparison of trends in Figure 39 with the high-K calc-alkaline series lavas from Rindjani volcano in the Sunda arc (Foden, 1983), shows that Simberi lavas have higher K_2O and lower CaO, TiO_2 and Fe_{total}

Figure 38. Major element variation diagrams for Simberi volcanic rocks. Primary magma composition (P) can be modified to MgO-rich compositions by accumulation or contamination by olivine, and to MgO-poor compositions by fractionation of olivine, clinopyroxene and amphibole. Inflections in the major element patterns coincide with the appearance of phenocrysts of clinopyroxene and amphibole.

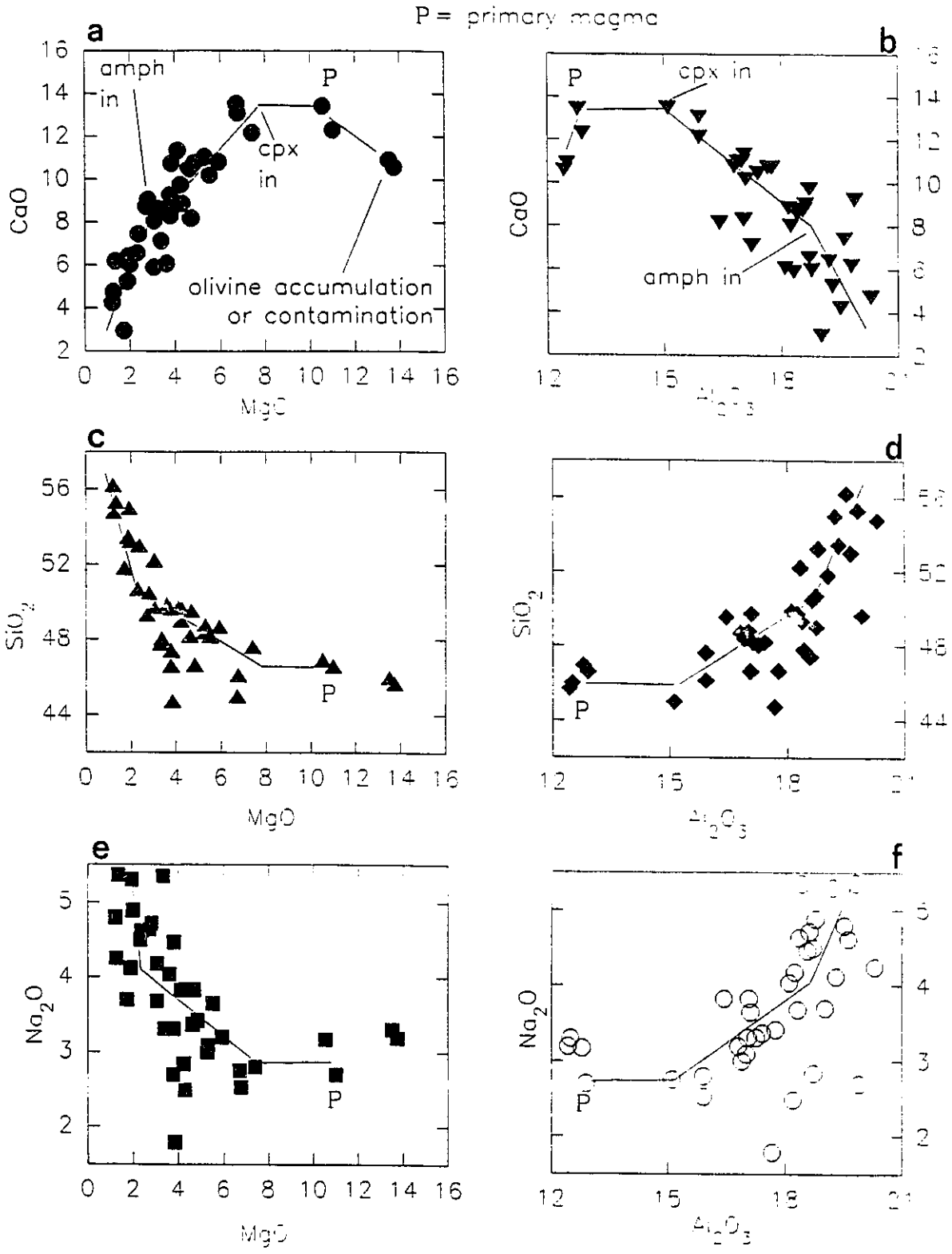
P = primary magma
a
amph in
P
cpx in
olivine accumulation or contamination
CaO
MgO
b
P
cpx in
amph in
CaO
c
P
SiO_2
MgO
d
P
SiO_2
Al_2O_3
e
P
Na_2O
MgO
f
P
Na_2O
Al_2O_3

Figure 39. Harker diagrams for major and minor element oxides vs. SiO_2 for Simberi volcanic rocks, compared with the high-K calc-alkaline series lavas from Rindjani volcano, Sunda arc, Indonesia (Foden, 1983).

(a) TiO_2, MnO and P_2O_5 vs. SiO_2. Note the significantly lower concentration of TiO_2 in Simberi lavas compared with Rindjani.

(b) Al_2O_3 and total iron vs. SiO_2. The depletion in iron and TiO_2 in Simberi lavas compared with Rindjani may be due to the early crystallization of magnetite at high fO_2 (Kennedy *et al.* 1990b).

(c) MgO and CaO vs. SiO_2.

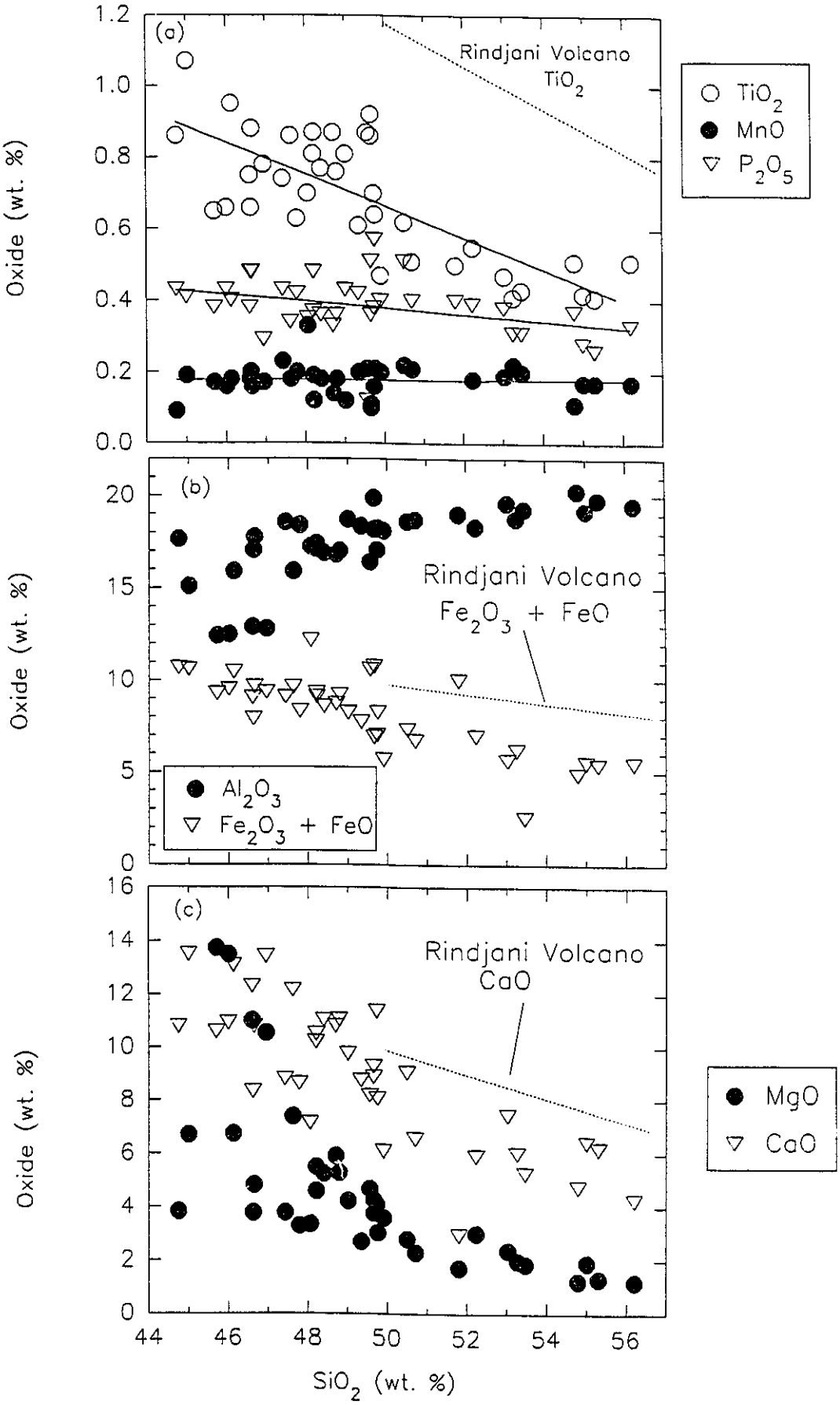
(a)
Rindjani Volcano
TiO2
TiO2
MnO
P2O5
(b)
Rindjani Volcano
Fe2O3 + FeO
Al2O3
Fe2O3 + FeO
(c)
Rindjani Volcano
CaO
MgO
CaO
Oxide (wt. %)
Oxide (wt. %)
Oxide (wt. %)
SiO2 (wt. %)

for similar ranges in SiO_2.

Variations in major element chemistry in Simberi lavas are due primarily to fractional crystallization of a high temperature magma under high fO_2 conditions, in a high level crustal reservoir underlying the Simberi volcano. Figure 38 is a series of Harker diagrams depicting major element trends with respect to MgO and Al_2O_3. These trends are not strictly linear, but show multiple inflection points, which correlate with the appearance of minerals as phenocryst phases.

Petrographic observations indicate that olivine, clinopyroxene and magnetite are liquidus phases within the most mafic samples. Olivine fractionated rapidly to produce ankaramitic basalts. The early saturation of clinopyroxene resulted in rapid enrichment in Al_2O_3, gradual enrichment in SiO_2 and depletion in CaO and MgO (Figure 38a->d) in basaltic and trachybasaltic lavas (45-50 wt.% SiO_2). Titanomagnetite fractionation led to a gradual depletion in total Fe and TiO_2 throughout the crystallization sequence from basalt to trachyandesite (Figure 39a and b).

An inflection at 50 wt.% SiO_2 (Figure 38c and d) is coincident with the presence of unresorbed amphibole and plagioclase phenocrysts in thin section, and indicate that these minerals have become liquidus phases. Amphibole crystallization indicates saturation in H_2O and Na_2O in undersaturated lavas (Cawthorn and O'Hara, 1976). Fractionation of amphibole and Ca-plagioclase (silica-undersaturated minerals cf. clinopyroxene) lead to rapid enrichment in SiO_2 Na_2O and K_2O, gradual enrichment in Al_2O_3, and a decrease in the rate of CaO and

MgO depletion (Figure 38). The Na_2O/K_2O ratio varies from the primary mantle source value of 3/1 at 45 wt.% SiO_2 to ≈4/4 at 55 wt.% SiO_2 indicating that K acts as an incompatible element throughout the fractionation sequence.

Petrographic observations and chemical variations are consistent with results of Kennedy *et al.* (1990b), who experimented with liquidus assemblages using a primary basalt from Lihir Island. Liquidus temperatures were determined using fo_2 controlled, 1 atmosphere, anhydrous melt experiments. At fo_2=FMQ, they determined a liquidus temperature of 1175°C where olivine crystallizes, followed by clinopyroxene at ≈1155°, plagioclase at ≈1137° and titanomagnetite at ≈1110°C. They also found that at log fo_2>FMQ+1, titanomagnetite crystallized at ≈1137°C, and argued that the

> "high phenocryst content of many of the Tabar-Feni lavas may reflect crystallization in response to a sudden increase in oxygen fugacity".
> (Kennedy *et al.* 1990b, p. 730)

Independent evidence on sulphide/sulphate mineral stability (Part C), combined with evidence of clinopyroxene and magnetite formation adjacent to the calcite nodule (Figure 32), may indicate that carbonate dissociation at P<21 kbar is a trigger mechanism for an increase in oxygen fugacity in mantle derived magmas. Possible first and second order reactions representing this process are:

(1) $$CaCO_3\ (s) = CaO\ (l) + CO_2\ (v,l);$$

and (2) $$CO_2\ (l) = CO\ (l) + 1/2\ O_2\ (l)$$

The liquidus mineral assemblage of the primitive Botsor Hill intrusion on

Simberi Island, interpreted in the context of the experiments of Kennedy *et al.* (1990b), would indicate that the magma was emplaced at the surface at a temperature of ≈1150°C. This temperature compares favourably with the inferred temperatures of amphibole destabilization in Botsor Hill samples of between 1050-1140° C (Huckenholz *et al.* 1988). Magnetite inclusions in clinopyroxene xenocrysts and phenocrysts are evidence that crystallization under high fO_2 conditions occurred. Kennedy *et al.* (1990b) hypothesized that the high fO_2 of the Lihir lavas was a result of water influx into a shallow magma chamber, but the high fO_2 melt inclusion assemblages in the Botsor Hill samples are evidence for SCHARM-induced oxidation of the mantle source region.

Trace elements

The volcanic rocks of Simberi Island possess trace element characteristics of subduction zone lavas. These include very high abundances of the large ion lithophile elements (LILE) Sr (1400-2900 ppm), Ba (100-600 ppm) and Rb (10-110 ppm) relative to the high field strength elements (HFSE) Ta (<0.5-2.2 ppm), TiO_2(0.4-0.9 wt.%), Zr (40-100 ppm) and Nb (<3-24 ppm). In addition, the LILE/REE (eg. Sr/Nd) ratio of Simberi basalts (60-110) are high compared with ocean island basalts (23), continental basalts (15-22) and mid-ocean ridge basalts (15-20) (Wilson, 1989).

Spiderdiagrams

Spiderdiagrams (Figure 40) are a convenient method of demonstrating trace-element variation. The Simberi island volcanic rock geochemical data was normalized to an average MORB composition (Pearce, 1983), which represents the

Figure 40. Spiderdiagrams for primitive, intermediate and evolved intermediate basalts from Simberi Island and for the Tabar Island quartz trachyte (TB 1/1 of Wallace *et al.* 1983). The geochemical data was normalized to an average MORB composition (Pearce, 1983).

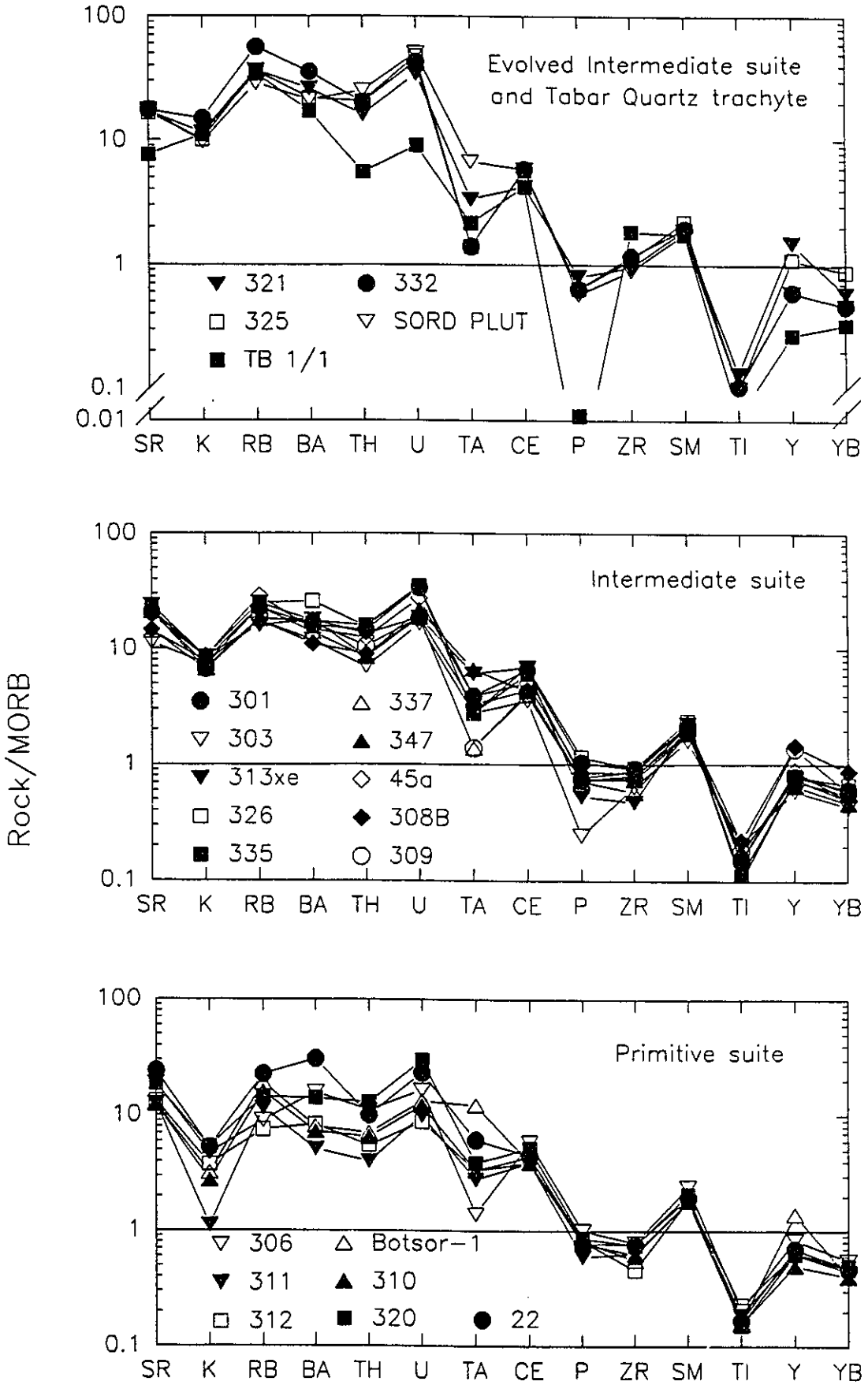
Evolved Intermediate suite
and Tabar Quartz trachyte
321
332
325
SORD PLUT
TB 1/1
Intermediate suite
301
337
303
347
313xe
45a
326
308B
335
309
Primitive suite
306
Botsor-1
311
310
312
320
22
Rock/MORB
100
10
1
0.1
0.01
SR K RB BA TH U TA CE P ZR SM TI Y YB

original trace element concentration of melts derived from depleted asthenospheric mantle wedge, before contamination by SCHARM. According to convention (Pearce, 1983; Wilson, 1991), the elements on left hand side of Figure 40 are the most mobile in aqueous fluids (Sr to U), while the elements to the right are least mobile (Ta to Yb). Twenty-one samples from the Simberi database and one sample of the Tabar Island quartz trachyte (TB 1/1 of Wallace *et al.* 1983) were subdivided into three groups of primitive, intermediate and evolved intermediate chemical composition based on the abundance of potassium (an incompatible element) in the sample. Primitive rocks are those with 1.1 to 5.3 times the MORB value, intermediate rocks range from 5.4 to 8.6 times the MORB value and evolved intermediate rocks are those with greater than 8.7 times the potassium concentration of MORB.

Trace element enrichment by SCHARM metasomatism

The primitive suite includes the primary magmas from the Botsor Hill intrusion (Botsor-1, 310, 311), the carbonate xenolith-bearing mafic dyke from the Raban Diatreme Complex (22) and other basalts with Mg* between 43 and 74 and SiO_2 less than 48 wt. % SiO_2. This primitive suite is enriched in the large-ion lithophile elements (LILE) Sr, K, Rb, Ba, Th, U and the light rare earth elements (LREE) Ce and Sm. These enrichments are the result of metasomatism of the mantle wedge by SCHARM, and indicate that SCHARM has a high capacity for the solubilization of LILE and LREE. Fractional crystallization of the primitive suite to the intermediate and evolved intermediate groups caused further enrichments in the incompatible LILE and LREE (Figure 40).

HFSE depletion: A link between SCHARM metasomatism and the TLTF Daly gap?

The Tabar quartz trachyte is a member of the evolved intermediate group (Figure 40). These small volume quartz trachyte domes are one of the most intriguing volcanic products of the TLTF arc, since they represent the high silica end member of a pronounced Daly compositional gap between rocks with 44-55 wt % SiO_2 and those with 65 wt.% SiO_2. The domes are present in all the TLTF island groups, and represent the youngest and final volcanic event (Wallace *et al.* 1983). Their origin is a petrogenetic paradox since nephelinitic lavas cannot fractionally crystallize to quartz-saturated compositions before they completely crystallize (a thermal divide separates quartz-saturation from nepheline-saturation). The origin of these basalt-trachyte "Daly gaps" has been a long standing problem in igneous petrology (Daly, 1925, 1927). A review of the data by Chayes (1977) and Yoder (1973) led to the conclusion that the gap was real and that it was not the result of continuous fractional crystallization. Although the Daly gap problem remains enigmatic for ocean island volcanoes, I propose a unique solution to the Daly gap exhibited in the TLTF which calls upon evidence from melt inclusion glasses, immiscibility textures, HFSE depletion and REE patterns (Chapter 7).

The similarity in the major element compositions of the melt inclusion glasses contained within mantle xenocrysts and the Tabar Island quartz trachytes, allows the formation of an hypothesis relating the two salic magmas (Part B). The hypothesis states that the quartz trachyte domes represent the vestigial component of SCHARM, after it has become silica saturated during the formation of silica-undersaturated metasomatic minerals (phlogopite and amphibole) in the mantle wedge. This concept can be demonstrated by the following end-member reactions

between the silica undersaturated alkali aluminosilicate melt components of SCHARM and mantle peridotite:

Metasomatic phlogopite production

$$\{3KAlSi_2O_6 + 2H_2O\}\ (l) + 3Mg_2SiO_4\ (s) = 2[KMg_3AlSi_3O_{10}(OH)_2]\ (s) + KAlSi_3O_8\ (l)$$

leucitic melt — olivine — phlogopite — orthoclase

Metasomatic amphibole production

$$\{2\ NaAlSi_2O_6 + CaAl_2SiO_6 + H_2O\}(l) + 3MgSiO_3\ (s) + CaMgSi_2O_6\ (s) =$$

analcimic melt component — orthopyroxene — clinopyroxene

$$NaCa_2Mg_4Al_3Si_6O_{22}(OH)_2\ (s) + NaAlSi_3O_8\ (l) + SiO_2\ (l)$$

amphibole — albite — quartz

The low solidus temperature of SCHARM ensures the transition from an original nepheline-normative composition to a quartz-normative composition during its transit through the mantle wedge. The occurrence of silica-rich globules throughout the Simberi Island suite (Figures 10) and, in particular, globules of salic glasses within the mafic glass of the Botsor Hill intrusion (Figure 20c), is evidence for immiscibility between mafic-salic liquids. The salic globules in the Botsor Hill rocks were trapped due to quenching upon eruption, but a slowly cooling magma chamber would allow the immiscible salic glass globules to coalesce as the mafic melt crystallizes. Density contrasts between the salic melts and the mafic magma would cause the low solidus salic melts to rise to the top of the magma chamber, forming a late-stage quartz trachyte dome. This marks the complete crystallization and death of the original magma reservoir.

The spiderdiagram confirms that similarities exist between the trace element composition of the Simberi rocks and the Tabar quartz trachyte. The trachyte pattern displays similar enrichments in Sr, K, Rb, Ba, Ce, and Sm, and depletions in HFSE. The strong depletion in titanium and phosphorus in the quartz trachyte relative to the Simberi suite is due either to fractional crystallization of titanomagnetite and apatite, respectively, or is an indication of the initial depletion of Ti and P in the slab source region of these salic melts. Uranium and thorium concentrations are quite low, but the U/Th ratios are comparable to the Simberi rocks.

Depletions in the high field strength elements (Ta, P, Zr, Ti, Nb and Hf; the latter two elements were below the limit of detection) in the Tabar Island Group samples are characteristic traits of island arc lavas (Figure 40). The mechanism(s) of HFSE depletion are a highly debated topic in igneous petrogenesis. Various interpretations (Arculus and Johnson, 1981; Kelemen *et al.* 1990) include:

(1) stabilization of a mineral phase with k_D for HFSE > 1 in the arc magma source (Hellman and Green, 1979; Saunders *et al.* 1980b; Green and Pearson, 1986, 1987; Ryerson and Watson, 1987),

(2) metasomatism of the mantle wedge source by a fluid or magma depleted in HFSE (Ryerson and Watson, 1987),

(3) high degrees of partial melting,

(4) early fractionation of magnetite,

(5) scavenging of HFSE by mantle minerals with high k_D during ascent of basaltic magma (Kelemen *et al.* 1990).

Items (3) and (5) are not considered valid explanations of the HFSE depletions in Simberi basalts since geochemical and petrographic evidence indicates that they are not high-degree partial melts and that they have ascended rapidly from mantle regions in high-speed liquid eruptions.

The dominant mechanism for HFSE depletion, however, could be a combination of the above interpretations, with ultimate control exercised by the chemical and physical characteristics of SCHARM. Derivation of SCHARM during the basalt-eclogite transition would lead to the stabilization of the assemblage omphacitic pyroxene-garnet-rutile ± kyanite ± quartz. An interesting consequence of the metasomatic melt-eclogite formation hypothesis is that stabilization of rutile (TiO_2), zircon ($ZrSiO_4$) and apatite ($Ca_5(PO_4)_3(F,OH,Cl)_3$ within the slab could explain the depletion in HFSE and P in subduction related magmatic arcs. Ryerson and Watson (1987) experimentally constrained that, if Ti-Nb-Ta depletion in the mantle wedge source region of island-arc magmas was imparted by hybridization (metasomatism) of the mantle wedge by rutile saturated melts, the hybridizing agent would have to be a felsic, hydrous melt created at low temperature (900°C). Similar arguments can be made for phosphorus, as experimental evidence (Green and Watson, 1982) indicates that low temperature (800-950°C) silicic melts of trachytic composition (65-70 wt.% SiO_2) will be saturated in apatite at 0.12-0.24 wt.% P_2O_5. Apatite, therefore, will remain in the eclogitic slab residue and the metasomatic melt will be 'depleted' in P_2O_5 and will impart its depleted P content to the overlying mantle wedge. This is in accord with the marked depletion of P on Figure 40 for the Tabar Island quartz trachyte and for the analyzed compositions of the melt inclusion glasses where P_2O_5 contents were found to be between 0.02 and

0.22 wt.% P_2O_5 (Table 3). The low temperature conditions of SCHARM formation and the siliceous character of SCHARM support the experimental evidence for retainment of HFSE in the slab (Ryerson and Watson, 1987; Green and Watson, 1982).

The highly oxidized nature of SCHARM (fO_2 > FMQ + 4 log units; sulphate + magnetite stable; Carrol and Rutherford, 1987, p.785) causes the metasomatic crystallization of Ti-phlogopite (Foley, 1989), Ti-magnetite and titanite in the mantle wedge, and also causes the early crystallization of Ti-magnetite from mantle derived magmas. Thus the basalt-eclogite transition hypothesis may not solely cause retainment of HFSE in the slab. Infiltration and metasomatism of the mantle wedge by highly oxidized SCHARM continues to cause HFSE depletion, thus a number of linked processes may control HFSE depletion, and therefore an explanation of HFSE depletion in the TLTF arc can best be encompassed by a combination of the above items (1), (2) and (4). Nevertheless SCHARM production and its interaction with the overlying mantle wedge is the fundamental process controlling LILE, REE and HFSE abundances.

In summary, the spiderdiagrams (Figure 40) illustrate the following points about Simberi island volcanic rocks:

1) Simberi volcanic rocks possess chemical characteristics of the calc-alkaline rock association.

2) Calcium, Na, K, Rb, Sr, Ba, Th, U and LREE are enriched in primary mantle-derived samples due to metasomatism by SCHARM.

3) The incompatible elements become highly enriched during subsequent fractional crystallization of primary magmas derived from partial melting of

metasomatised mantle.

3) Troughs at Ti, Ta and Zr reflect retainment of these elements in a mineral phase in both the subducted slab and in the mantle wedge, due to their low solubility in salic melts and their partitioning into metasomatic minerals during oxidative metasomatism by SCHARM.

4) Quartz trachytes have major and trace element characteristics similar to Simberi Island volcanic rocks and to alkaline glasses contained within mantle-derived primary magmas. Although it is impossible to derive quartz trachyte magmas by fractional crystallization of a nephelinitic rock, quartz normative melts may be a by-product of alkali depletion which occurred during the metasomatic formation of silica-undersaturated minerals (phlogopite and amphibole) from mantle peridotite minerals. The low temperature solidus of SCHARM, combined with its low density and immiscibility in mafic melts, would allow it to coalesce into a late stage quartz-normative dome during gradual cooling and crystallization of a mafic, nepheline-normative magma in a crustal magma chamber.

Chapter 7. Rare Earth Elements

Introduction

Enrichment and depletion trends in rare earth element (REE) abundances reflect the sensitivity of these elements to magmatic processes (Allègre *et al.* 1977; Hanson, 1980). A chondrite-normalized (Anders and Grevesse, 1989) plot of a representative suite of Simberi Island volcanic rocks is presented in Figure 41. The suite has been divided into a primitive volcanic series and a more evolved series based on Mg* number and incompatible element (K) abundance. Also plotted on Figure 41 is the Tabar Island quartz trachyte sample reported by Wallace *et al.* (1983). Although Wallace *et al.* (1983) and Johnson *et al.* (1986) suggested quartz trachyte formation by a crustal melting processes, an hypothesis has been proposed in this work that they are the vestigial component of silica-undersaturated, carbonated alkaline melts of slab origin, depleted in alkalies during the metasomatic production of phlogopite and amphibole (silica-undersaturated minerals) within the asthenospheric mantle wedge.

In general, both primitive and evolved series show enrichments in light rare-earth elements (LREE) over heavy rare-earth elements (HREE), which is characteristic of high-K calc-alkaline rocks. The slope of the REE patterns for both Simberi suites are similar to the Tabar Island quartz trachyte. The Simberi REE patterns indicate that the primitive and evolved suites are related through simple fractional crystallization processes, where REE enrichment from primitive to evolved samples is due to the incompatible nature of the REE. The concave upward shape

Figure 41. Chondrite normalized rare earth element patterns for Simberi lavas and Tabar Island quartz trachyte (TB 1/1 of Wallace *et al.* 1983). Primitive lavas in the top diagram have lower abundances of REE, and distinct negative Ce anomalies and positive Eu anomalies compared to the evolved lavas (below). The Tabar Island quartz trachyte has low ΣREE abundances, and a pronounced negative Ce anomaly. Data normalized to the chondritic values (Anders and Grevesse, 1989).

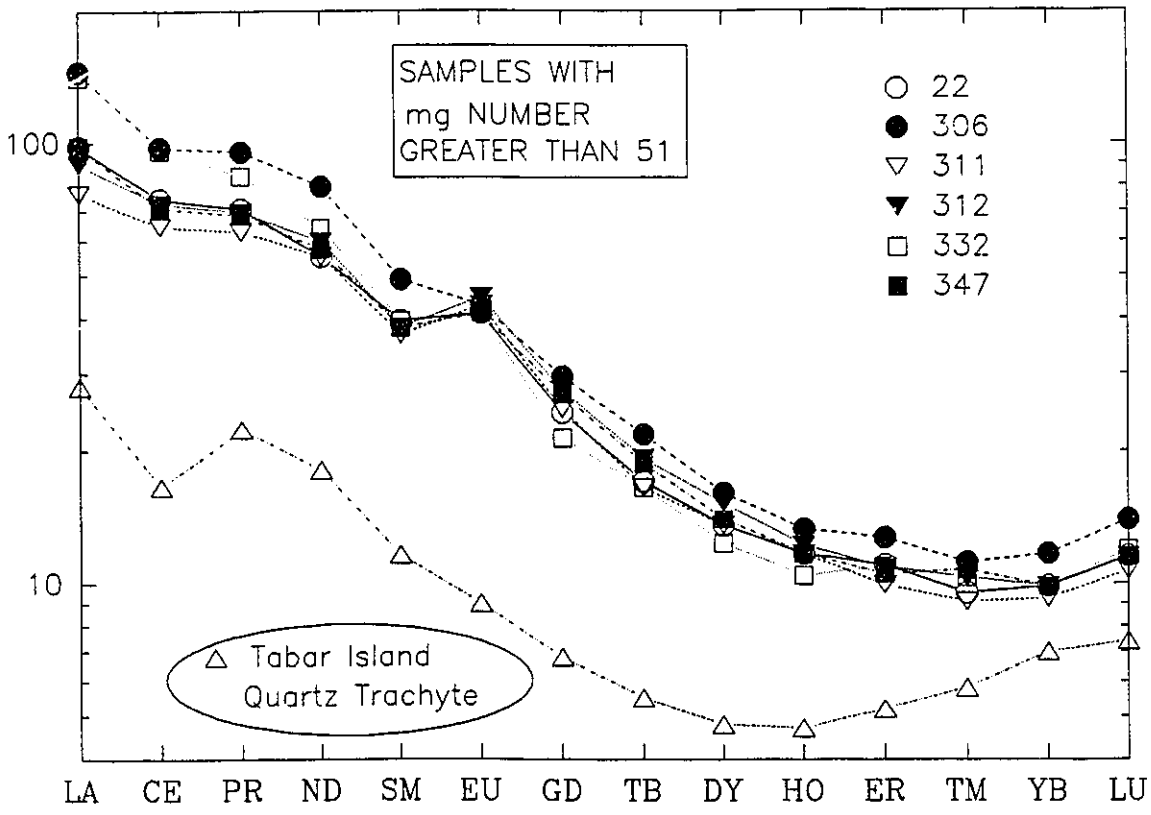
SAMPLES WITH
mg NUMBER
GREATER THAN 51
22
306
311
312
332
347
100
10
Tabar Island
Quartz Trachyte
LA
CE
PR
ND
SM
EU
GD
TB
DY
HO
ER
TM
YB
LU

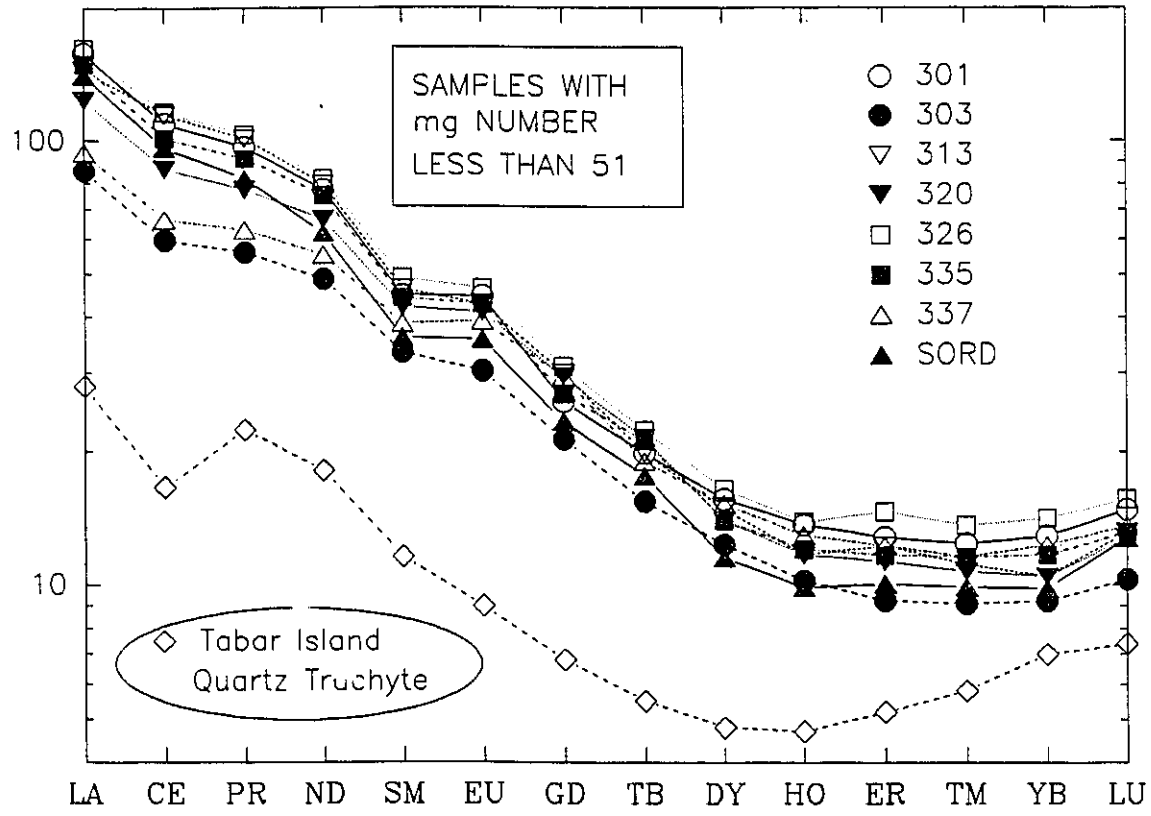
SAMPLES WITH
mg NUMBER
LESS THAN 51
301
303
313
320
326
335
337
SORD
100
10
Tabar Island
Quartz Trachyte
LA
CE
PR
ND
SM
EU
GD
TB
DY
HO
ER
TM
YB
LU

for the HREE is present in both the primitive and evolved Simberi rocks, and in the Tabar quartz trachyte (Figure 41).

Two significant single element anomalies (positive Eu and negative Ce) occur in the Simberi and Tabar Island volcanic rocks and reflect the high oxygen fugacity of the igneous melts. Europium and Ce are the only REE which can have stable divalent states, and under oxidizing conditions the reactions $Eu^{2+} \rightarrow Eu^{3+}$ and $Ce^{3+} \rightarrow Ce^{4+}$ occur (Neal and Taylor, 1989). The Eu and Ce anomalies in the TLTF lavas are important geochemical tracers, useful in determining the nature of the REE source.

Positive Europium Anomaly

A positive Eu anomaly is present in both the primitive and evolved suites (Figure 41). It is most strongly developed in the mantle-derived olivine basalt and diatreme basalts (with Eu/Eu^* ranging from 1.2 to 1.5; Eu^* is the value interpolated from a straight line between Sm and Gd), with the strongest positive Eu anomaly developed in the most primitive rocks. Positive Eu anomalies are traditionally observed where plagioclase accumulation has occurred. In most igneous melts of low to moderate oxidation state, Eu is present as Eu^{2+}, and is preferentially incorporated into plagioclase by substitution for Ca^{2+}. The mineralogy of the primitive suite however, does not suggest plagioclase accumulation has occurred. In the most mafic rocks plagioclase is not even a liquidus mineral and xenoliths present within the mafic lavas do not contain significant plagioclase. The inferred depth of origin for the primitive lavas (≈ 60 km) is greater than that at which plagioclase lherzolite is stable (< 30 km; Wyllie, 1981). This indicates that

plagioclase was not a mineral phase in the mantle wedge source region of the Simberi lavas.

Petrographic arguments, therefore, require that the positive Eu anomaly in the Simberi island lavas be due to a process other than plagioclase accumulation in the Simberi magma reservoir or melting of plagioclase-bearing mantle wedge. Nevertheless, plagioclase is the only abundant mineral preferentially enriched in Eu relative to the other REE, and it can be therefore inferred that the source region of the REE should have contained plagioclase, and that melting of plagioclase or a plagioclase-rich component was responsible for the Eu anomaly in the Simberi rocks. The only other potential plagioclase source is feldspar contained within subducted oceanic basalt. Melting of a feldspathic phase (i.e. scapolite) at the basalt-eclogite transition can produce SCHARM with a positive Eu anomaly.

The preservation of the Eu anomaly in the Simberi rocks compared with Lihir (Kennedy *et al.* 1990a) and other rocks from the TLTF Island (Wallace *et al.* 1983) is a result of the following:

(1) the more primitive nature of the Simberi rocks (cf. Lihir) and their derivation from metasomatized mantle regions,

(2) the high proportion of metasomatic agent (SCHARM) in the primary magmas, with the ultimate control of REE concentrations exerted by SCHARM contamination, and

(3) the stability of trivalent Eu under high fO_2 conditions.

The absence of negative Eu anomalies in all the TLTF rocks, and particularly in the

most highly evolved quartz trachyte rocks indicates the prevalence of Eu as Eu^{3+}, and is consistent with the high primary Fe_2O_3/FeO ratios and overall high oxidation state of the TLTF magmas.

Negative Cerium Anomaly

The negative Ce anomaly is not as strongly developed as the positive Eu anomaly, but it is prevalent throughout the Simberi suite. The largest negative Ce anomaly is displayed by the Tabar Island quartz trachyte, which, along with the general slope of the REE patterns, indicates a common lineage between the nepheline-normative mafic to intermediate lavas and the quartz-bearing trachytes. The Ce/Ce^* ratio of the Simberi lavas ranges from 0.83 to 0.91, while the Tabar Island quartz trachyte has a Ce/Ce^* ratio of 0.66.

Negative Ce anomalies have been reported in basaltic lavas from other ensimatic island arcs in the south Pacific, including the Solomon Islands (Jakes and Gill, 1970; Ramsay *et al.* 1984), New Britain (Heming and Rankin, 1979), the Mariana Islands (Dixon and Batiza, 1979; White and Patchett, 1984), and in mantle peridotite xenoliths from an alnöite intrusion on Malaita Island (Solomon Islands; Neal and Taylor, 1989). Cerium anomalies have also been reported in garnet in Group C eclogite nodules (Taylor and Neal, 1989) and in apatite from carbonatites at Oka, Quebec (Eby, 1975) and Kaiserstuhl, Germany (Puchelt and Emmerman, 1976).

Experiments on Ce solubility in melts (conditions: 1 atmosphere, anhydrous, controlled fO_2) reported by Schrieber *et al.* (1980), severely constrain the potential

for the development of quadrivalent Ce in the presence of Fe^{2+} because of the reaction

$$Ce^{4+} + Fe^{2+} = Ce^{3+} + Fe^{3+}.$$

There is no known igneous process for the production of negative Ce anomalies by oxidation of Ce to its tetravalent state in basaltic melts since there will always be excess Fe^{2+} present (ie. only one distribution coefficient for Ce compared to Eu). This line of reasoning led Heming and Rankin (1979) and Hole *et al.* (1984) to argue that negative Ce anomalies must be present in the source region prior to partial melting.

Seawater contains a strongly pronounced negative Ce anomaly due to oxidation of soluble Ce^{3+} to insoluble Ce^{4+} species (Elderfield and Greaves, 1982). The Ce^{4+} is scavenged by Fe-Mn particles which produce manganese nodules and associated sediments with positive Ce anomalies (Elderfield *et al.* 1981). Pelagic sediments contain negative cerium anomalies because the accumulated nanofossil ooze consists of planktonic tests which grew in a Ce-depleted water column. A mixture of 95% nanofossil ooze and 5% ferruginous clay was used by Hole *et al.* (1984) to model the possible PAWMS (Pacific Authigenic Weighted Mean Sediment) contribution to the source region of the Mariana arc. Although a PAWMS contribution of 0.3 to 0.5% could potentially produce a negative Ce anomaly in Mariana basalts, the distinct positive Gd anomaly of PAWMS was not present. Furthermore, the Rb/Ba ratio of PAWMS is too low to produce the Rb/Ba ratio or the Mariana basalts. Hole *et al.* (1984) suggested that an additional hydrothermal fluid component could meet this requirement, but H_2O-rich fluids will only be locally present due to amphibole-and phlogopite-producing buffer reactions

in the subducted slab and mantle wedge (Schneider and Eggler, 1986). In light of this study, it is unlikely that a sedimentary contribution is responsible for the negative Ce anomaly in Simberi lavas and the Tabar quartz trachyte cumulodome.

Mid-ocean ridge basalt (MORB) lavas studied by Ludden and Thompson (1979) are enriched in REE during seawater alteration processes. Their study demonstrated that the LREE in altered basalt were significantly enriched (2-6x) over fresh basalt, except for Ce, which showed erratic but overall minor enrichment. Seawater-altered basalt (SWAB), therefore, can have a pronounced negative Ce anomaly. Ludden and Thompson (1979) also observed a correlation between REE enrichment and age of the basaltic rocks, indicating that strong negative Ce-anomalies are likely to be present where old oceanic crust (which have experienced relatively high water/rock ratios) is subducting.

The presence of negative cerium anomalies in the nepheline-normative Simberi lavas and the quartz-normative Tabar Island trachyte indicates that the source region for the two rock types contained a negative cerium anomaly. Subduction of early Cretaceous oceanic crust of the Pacific plate below the TLTF arc, prior to the collision of the Ontong Java Plateau, would have provided an old, seawater-altered, Ce-depleted basalt (SWAB) source region.

REE Interpretation

The observations given above indicate that the mantle wedge has no control over the production of negative Ce and positive Eu anomalies. These anomalies can be produced by seawater alteration of basalt and subsequent melting of feldspathic

phases within the basalt, respectively.

The concave upward shape for the HREE pattern is characteristic of melts, formed in the presence of garnet, where garnet has a mineral/melt partition coefficient (k_D) for the HREE Gd to Lu greater than 1 (Henderson, 1982, p. 93). Kennedy *et al.* (1990b) argue that garnet is not a residual phase in the mantle source region of the TLTF arc because $(Lu/Yb)_{cn}$ is greater than 1 in all of the primitive Lihir lavas. This statement is certainly true if one considers the k_D values for basaltic systems however, for siliceous melts k_D values for HREE in garnet are reversed such that $(Lu/Yb)_{cn}$ is less than 1 (Henderson, 1982, p. 93). Therefore the concave upward HREE pattern for the Simberi Island lavas and the Tabar Island quartz trachyte is consistent with a siliceous melt, enriched in LREE, forming in the presence of garnet, somewhere other than in the mafic mantle wedge.

Primitive Simberi lavas containing evidence of high pressure (> 21 kbar) metasomatism of mantle minerals by sulphate-, carbonate-, hydrous, alkali-rich magmas (SCHARM), argue for addition of REE to the mantle wedge by the metasomatic melt. Enrichment of LREE over HREE in this siliceous melt can be attributed to the retention of garnet in the siliceous melt source region. The low Mg# and the alkali-rich nature of the metasomatic melt are consistent with melting of plagioclase or of a prograde metamorphic mineral which was originally plagioclase (ie. scapolite; Goldsmith, 1976; Burnham, 1979, p. 93). During partial melting, feldspar tends to melt more rapidly than co-existing mafic rock and would produce a melt with a positive Eu anomaly and a relatively high LREE/HREE ratio (2-

10x) (Hanson, 1978; Rogers and Hawkesworth, 1982; Henderson, 1982). Retention of garnet during the incongruent melting of a feldspathic phase would deplete SCHARM in HREE due to the high garnet k_D values for HREE (Table 7).

Feldspar has a higher k_D for Sr, Ba, and Eu than non-feldspathic minerals present in the subducting basaltic slab (Mason *et al.* 1982; Irving and Frey, 1984). Enrichments in Eu, Sr, Ba, K and Rb and depletion of Ce in the TLTF rocks suggests that a seawater-altered feldspathic phase is melting during prograde metamorphism of the oceanic slab. Melting arguments, presented in previous chapters, indicate that scapolite may be the feldspathic phase undergoing melting. An equation can be written to describe the hypothetical process of the incongruent melting of scapolite to produce an eclogite residue (garnet + omphacite + kyanite) and a carbonate-bearing, alkali-rich siliceous melt:

$$\underset{\text{marialite}}{\{3\ Na(K)AlSi_3O_8\}\cdot NaCl\ (s)} + \underset{\text{meionite}}{\{3\ CaAl_2Si_2O_8\}\cdot CaCO_3\ (s)} + \underset{\text{olivine}}{2\ (Mg,Fe)SiO_4} =>$$

{feldspar altered by seawater and converted to anorthite and scapolite during prograde metamorphism and reacting with basaltic minerals in slab}

$$\underset{\text{grossular}}{Ca(Mg,Fe)_2Al_2Si_3O_{12}\ (s)} + \underset{\text{omphacite}}{\{NaAlSi_2O_6 \cdot 2(Mg,Fe)SiO_3\}} + \underset{\text{kyanite}}{2\ Al_2SiO_5\ (s)} + \underset{\text{quartz}}{4\ SiO_2\ (s)}$$

[----------QUARTZ ECLOGITE----------]

+

$$[CaCO_3 + NaCl + O_2 + NaAlSi_2O_6 + K(Na)AlSi_2O_6]$$

[----------CARBONATED ALKALINE MELT----------]

Similar reactions can be written using sulphate meionite in place of meionite to produce a sulphate-bearing alkali-rich melt in place of a carbonate melt, or to

produce a carbonated sodalite melt (sodalite and hauyne are phenocryst phases in TLTF lavas). The phases in the closed brackets represent the metasomatic melt which has metasomatized the mantle source region of the TLTF arc, to produce phlogopite-carbonate clinopyroxenite at $P > 30$ kbar and amphibole-carbonate clinopyroxenite at 21 kbar $< P < 30$ kbar (Wallace and Green, 1989). This hypothesis on the derivation of SCHARM by partial melting during the basalt-eclogite transition in the subducted slab, can be tested by modelling of rare earth element distribution.

REE Modelling: Partial Melting of Feldspathic Components and Eclogite Genesis During Prograde Metamorphism of Oceanic Crust in Subduction Zones

Equations defining the distribution of trace elements during partial melting (Shaw, 1970) and fractional crystallization (Neuman *et al.* 1954) are based on the distribution laws determined by Rayleigh (1896). These equations were used to test the hypothetical incongruent melting model proposed above, where a feldspathic mineral within subducted SWAB melts incongruently to form a garnetiferous (eclogite facies) slab residue. As discussed by Wilson (1989, p. 63), a number of assumptions must be made before trace element modelling equations can be used. The assumptions implicit to the calculations (Table 7) are:

(1) That the original REE concentration of the SWAB basalt sample 8-16A collected from the margin of a 5 Ma MORB pillow from the Atlantic Ocean (Ludden and Thompson, 1979) are similar to the bulk REE concentration in the Pacific oceanic crust present in the former subduction zone below the TLTF arc.

(2) That the total REE concentration in the basaltic slab is contained within

feldspar, which has been enriched in all REE except Ce during seawater alteration.

(3) That no redistribution of REE has occurred during conversion of plagioclase to scapolite during prograde metamorphism.

(4) That incongruent melting of scapolite occurs, and can be modelled assuming that $k_D$scapolite = $k_D$plagioclase.

(5) That k_D values for plagioclase and garnet at high P, T and fO_2 are similar to the values given in Henderson (1982).

(6) That the overlying asthenospheric mantle wedge is depleted and does not contribute to the total REE concentration of Simberi basalts.

Taking into account the considerable restrictions placed on the modelling equations by the above assumptions, a simplistic model consisting of batch partial melting of feldspar (ie. as an analogue of scapolite) was performed (Table 7).

These calculations indicate that a melt produced by 93% partial melting of a feldspathic phase in SWAB and subsequent crystallization of 7% garnet from this melt will produce an alkali-rich, siliceous melt with an overall REE concentration and a LREE/HREE ratio similar to the primitive Simberi lavas. Figure 42 shows that the concentrations of the majority of REE except for Ce and Eu can be reproduced by the models. The modelled Ce/Ce* of 0.66 is less than the Simberi primitive lavas but similar to the Tabar Island quartz trachyte. The modelled Eu concentration does not match the Simberi primitive lavas because the Eu concentration of plagioclase in SWAB is actually greater than bulk SWAB values.

Following the above arguments that the quartz trachyte magmas represent

the vestigial component of SCHARM, derived during the incongruent melting of scapolite at the basalt-eclogite transition in the subducted slab, then the quartz trachytes should contain the highest concentrations of REE. Figure 42 demonstrates that this is not the case. Ryerson and Hess (1978) determined that liquid-liquid distribution coefficients were controlled by degree of melt polymerization, and that immiscible granitic and ferrobasaltic liquids had $k_D^{\text{ferrobasalt-granite}}$ for REE = 10. The calculated k_D for primitive Simberi basalts and the Tabar Island quartz trachyte is a constant with $k_D^{\text{basalt-SCHARM}}$ for REE ≈ 3, possibly reflecting the lower degree of polymerization of SCHARM relative to granitic melts. Therefore, the similarity in REE patterns between the Simberi basalts and the Tabar Island quartz trachyte can be explained by polymerization controlled REE partitioning into the mafic melt-SCHARM immiscibility in the mantle wedge source region.

Table 7. Modelling of SWAB partial melting with garnet retained in residue by crystal fractionation.

Parameters		**Batch Partial Melting of Plagioclase-rich Source Region** $C_{La} = C_0(F + k_D - F^* k_D)^{-1}$; F = 0.93 (wt. fraction of melt formed)		**Fractional Crystallization of Garnet in Source Region (Eclogite formation)** $C_{Lb} = C_{La}(F^*(1-k_D) + k_D)^{-1}$; F = 0.93 (wt. fraction of liquid remaining)		
REE	SWAB (C_0) 8-16A.mar (ppm)	Plagioclase k_D (Henderson, 1982)	Modelled (C_{La}) Concn.(ppm)	Garnet k_D (Henderson 1982)	Modelled (C_{Lb}) (ppm)	Simber Basalt - 311 (ppm)
La	16.35	0.14	17.4	0.28	17.1	18
Ce	24.78	0.14	26.4	0.35	25.8	39
Nd	19.70	0.08	21.1	0.53	20.3	25
Sm	5.30	0.08	5.7	5.5	4.2	5.4
Eu	1.63	0.32	1.7	1.5	1.6	2.4
Gd	(4.22)	0.10	4.5	13.6	2.4	4.9
Tb	1.06	0.03	1.1	19.6	0.5	0.6
Ho	1.49	0.08	1.6	28	0.6	0.65
Yb	4.14	0.07	4.4	43	1.2	1.5
Lu	0.72	0.08	0.8	38	0.22	0.26

Figure 42. Chondrite normalized rare earth element plot showing rare earth element modelling for the partial melting of seawater altered basalt (SWAB) at the basalt-eclogite transition in subduction zones. The concentrations of the majority of REE (except Ce and Eu) can be reproduced by models requiring 93% melting of SWAB and retention of 7% garnet in the slab. The modelled Ce/Ce^{*} of 0.66 is less than that of the Simberi primitive lavas, but similar to the ratio of the Tabar Island quartz trachyte.

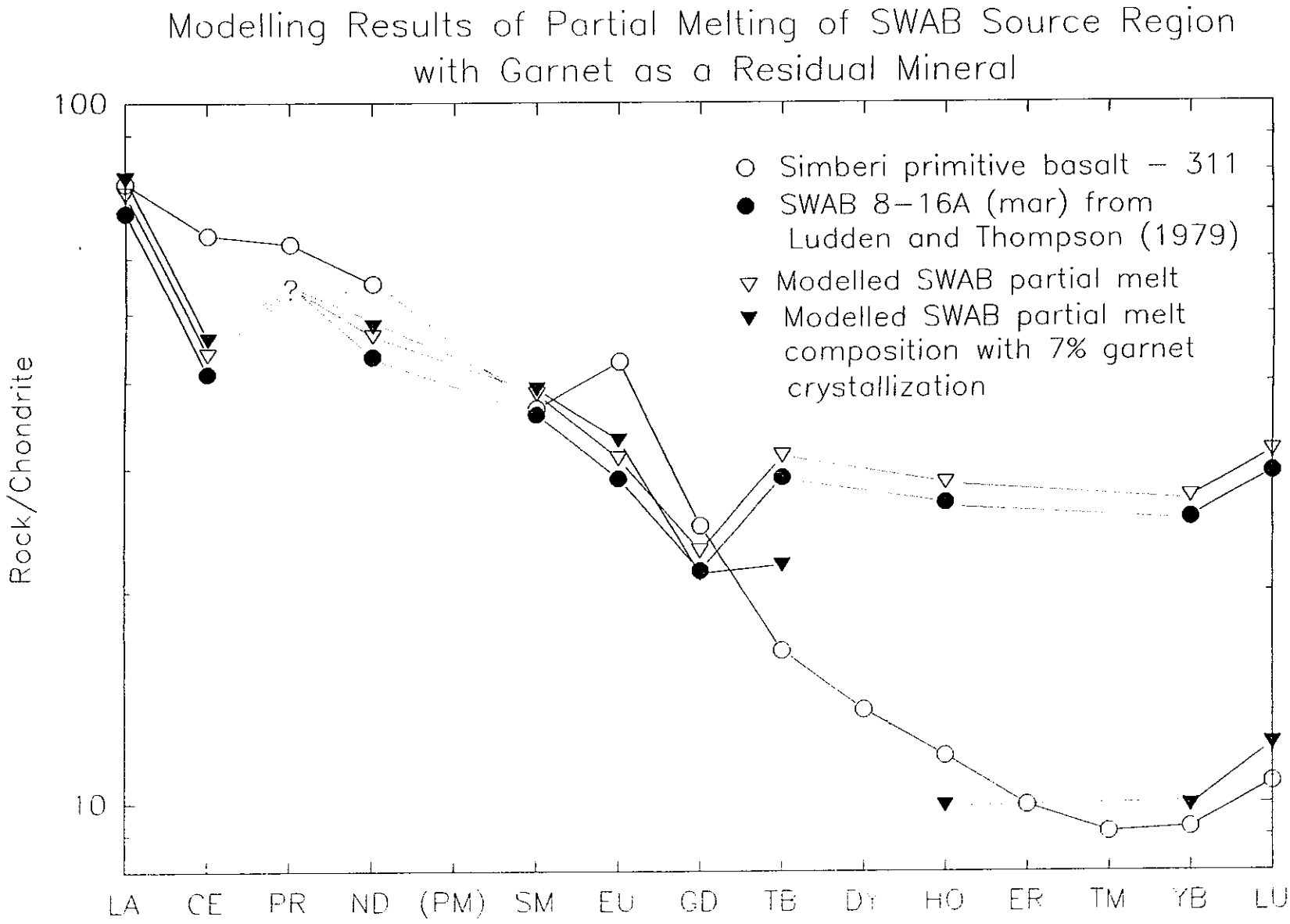
Modelling Results of Partial Melting of SWAB Source Region
with Garnet as a Residual Mineral
100
10
Rock/Chondrite
Simberi primitive basalt – 311
SWAB 8–16A (mar) from
Ludden and Thompson (1979)
Modelled SWAB partial melt
Modelled SWAB partial melt
composition with 7% garnet
crystallization
?
LA
CE
PR
ND
(PM)
SM
EU
GD
TB
DY
HO
ER
TM
YB
LU

Chapter 8. Isotopic Systematics of Mantle-Derived Basalts and Nodules

In the previous chapters, an hypothesis has been developed regarding the origin of SCHARM by partial melting of subducted, seawater-altered basalt at the basalt-eclogite transition. In particular, the rare earth element data indicate that a feldspathic mineral is undergoing incongruent melting. Eutectic melting constraints suggest that scapolite, produced during prograde metamorphic reactions accompanying deep subduction, is a potential mineral phase undergoing fusion to produce sulphate-, carbonate-, H_2O-, alkali-rich aluminosilicate magmas (SCHARM). Interaction of SCHARM during ascent through mantle peridotite has produced metasomatic phlogopite, amphibole and sodian diopside, and consumed olivine and possibly orthopyroxene. In this chapter, whole rock and mineral $^{18}O/^{16}O$, $^{13}C/^{12}C$ and $^{87}Sr/^{86}Sr$ isotopic data from mantle-derived basalts and nodules and fractionated lavas, are presented. This information is potentially useful for constraining the origin of SCHARM, and the amount of SCHARM contamination of the mantle wedge necessary to produce the Simberi arc lavas.

The use of isotopes as petrogenetic indicators for igneous rocks is discussed by James (1981), Faure (1986), Wilson (1989), Taylor (1986) and Taylor and Sheppard (1986). The limited range in $^{87}Sr/^{86}Sr$ of n-MORB (0.7024-0.7030) is representative of depleted mantle $^{87}Sr/^{86}Sr$ ratios, whereas seawater ($^{87}Sr/^{86}Sr = 0.707$-0.709) and continental crust ($^{87}Sr/^{86}Sr > 0.706$) generally have high $^{87}Sr/^{86}Sr$. The absence of continental crust in ensimatic island arcs allows the development of binary strontium mixing models for two isotopically distinct Sr

reservoirs (slab and mantle).

The use of binary strontium mixing models in arc petrogenesis is limited however, by the lack of knowledge of the Sr content of each reservoir. The low Sr abundance of the depleted mantle reservoir (50-200 ppm) however, necessitates a significant contribution of subducted slab Sr to the mantle wedge in order to produce the high Sr abundances characteristic of arc magmas (500-1800 ppm). The concentration of Sr in the subducted slab component is unknown, but is likely an order of magnitude greater than that of depleted mantle. In this sense, the $^{87}Sr/^{86}Sr$ isotope systematics of arc magmas are controlled entirely by the slab component because the mantle $^{87}Sr/^{86}Sr$ signature is swamped by a small addition of Sr-enriched subducted material. The high $^{87}Sr/^{86}Sr$ of marine sediments (usually greater than 0.706; Dasch, 1969) and carbonates (0.707 - 0.709 (Mesozoic to Present; Burke *et al.* 1982), as well as their high Sr abundance (500-10,000 ppm Sr) limits their contribution to subduction zone magmas to generally less than 1% (Ito and Stern, 1985).

By combining $^{18}O/^{16}O$ and $^{87}Sr/^{86}Sr$ ratios in petrogenetic studies the problem of one isotopic reservoir overwhelming another is avoided, since mantle and crustal rocks have similar oxygen abundances (Taylor, 1986; Taylor *et al.* 1987). At temperatures of 1100 to 1200°C, fractionation between ^{18}O and ^{16}O is $\approx 0‰$, therefore determination of the $\delta^{18}O$ in volcanic rocks and minerals is also a record of the $\delta^{18}O$ value of the melt. The use of oxygen isotope data in igneous petrogenesis however, also has limitations. Retrograde isotopic exchange during low-temperature hydration of volcanic rocks causes enrichment in ^{18}O (Kyser,

1986).

Strontium Isotopes Ratios for Tabar-Lihir-Tanga-Feni volcanic rocks

The range in $^{87}Sr/^{86}Sr$ ratios for the TLTF volcanic rocks measured by other workers is 0.70382-0.70452 (average of 0.70408 ± 17 for 44 samples; Wallace *et al.* 1983; Johnson *et al.* 1988; Kennedy *et al.* 1990a), with the high end of the range dominated by samples of quartz trachyte cumulodomes.

On a Nd-Sr diagram (Figure 43), the TLTF samples plot to the high $^{87}Sr/^{86}Sr$ side of the mantle array (Kennedy *et al.* 1990a). Island arc volcanic rocks plotting to the right of the mantle array are interpreted tc have incorporated $^{87}Sr/^{86}Sr$ from seawater-altered basalt during subduction. Altered submarine basalts are enriched in ^{87}Sr by reaction with seawater (Dasch *et al.* 1973; Hart *et al.* 1974) to give $^{87}Sr/^{86}Sr$ values of ≈ 0.704. The alteration of oceanic basalt by seawater is the only process known which can affect the $^{87}Sr/^{86}Sr$ without affecting the Nd isotopic ratios (DePaolo and Wasserburg, 1977; Hawkesworth and Powell, 1980). Although TLTF Nd and Pb isotope systematics are relatively homogeneous, Sr isotopic heterogeneity exists and has been attributed by Kennedy *et al.* (1990a) to assimilation of reef carbonate or altered overlying oceanic crust by mantle-derived magmas.

Strontium Isotope Ratios of Simberi rocks and nodules

A series of alkali olivine basalts (Btsr-1, 310, 311), trachybasalts (22) and trachyandesites (45A, Sord Plut) were selected for $^{18}O/^{16}O$ and $^{87}Sr/^{86}Sr$ isotopic analysis. The whole rock data (Table 8) show high $\delta^{18}O$ compared with mantle-

Figure 43. Nd-Sr diagram for Tabar-Lihir-Tanga-Feni lavas (from Kennedy *et al.* 1990a). TLTF samples plot to the high $^{87}Sr/^{86}Sr$ side of the mantle array and are interpreted in this work to be due to the contamination of mantle wedge peridotite by ^{87}Sr-enriched SCHARM, derived during partial melting of seawater altered basalt. BE = Bulk Earth.

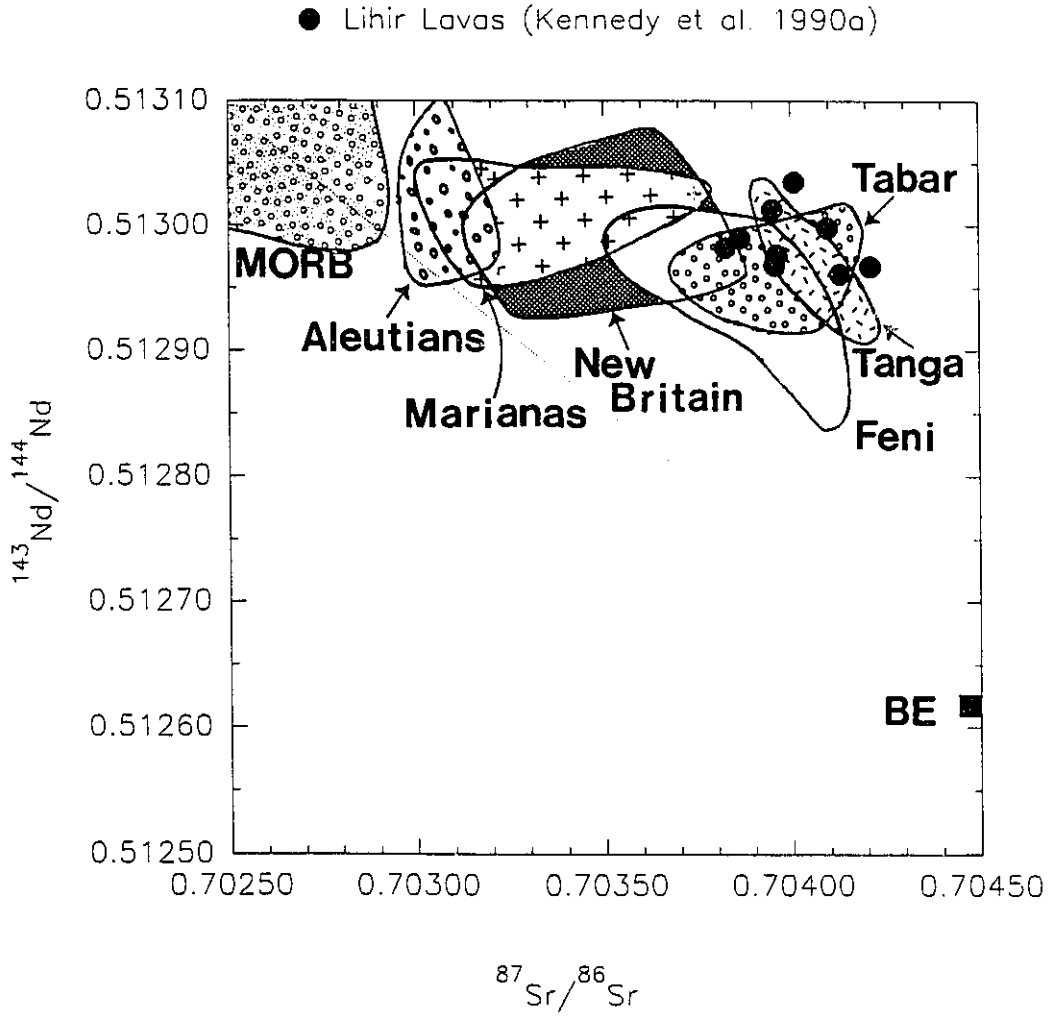
● Lihir Lavas (Kennedy et al. 1990a)
0.51310
0.51300
0.51290
0.51280
0.51270
0.51260
0.51250
$^{143}Nd/^{144}Nd$
0.70250
0.70300
0.70350
0.70400
0.70450
$^{87}Sr/^{86}Sr$
MORB
Aleutians
Marianas
New Britain
Tabar
Tanga
Feni
BE

derived arc basalts and arc lavas: $\delta^{18}O = +5.6$ to $+6.8‰$; Ito and Stern, 1985), while $^{87}Sr/^{86}Sr$ ratios of the olivine basalts and trachybasalts are the lowest in the TLTF arc. The trachyandesite values fall within the general range of TLTF lavas.

Table 8. Whole rock isotopic results of Simberi rocks

Sample	$\delta^{18}O$(‰)	$^{87}Sr/^{86}Sr$	Sr (ppm)	CaO (wt.%)	H_2O (wt.%)	Mg*
310	10.05	0.70362	1480	10.6	1.9	73.5
311	11.35	0.70354	1516	13.4	2.4	68
Btsr-1	10.89	0.70370	1500	10.9	2	72.8
22	12.38	0.70372	2889	11.4	2.2	52.5
45A	12.33	0.70400	2325	12.3	2.3	40
Sord Plut	10.95	0.70391	2100	6.4	1.5	40

Three $^{87}Sr/^{86}Sr$ analyses of massive microcrystalline calcite displayed $^{87}Sr/^{86}Sr$ heterogeneity (0.70359, 0.70398 and 0.70417; Table 10), some of the lowest and highest values obtained for the entire arc. Although it is possible that this heterogeneity was produced by subaerial weathering processes, weathering does not lower $^{87}Sr/^{86}Sr$ ratios in rocks (Faure, 1986, p. 183), and therefore the data must be considered as maximum values of the primary $^{87}Sr/^{86}Sr$ isotopic composition of the calcite in the carbonate nodule. If the massive calcite portion of the nodule represents a carbonate liquid derived from SCHARM by immiscibility in the mantle wedge, then SCHARM must have an initial $^{87}Sr/^{86}Sr$ ratio less than 0.70417.

Oxygen Isotope Ratios of Simberi rocks and nodules

Whole rock $\delta^{18}O$ and weathering

Whole-rock $\delta^{18}O$ values for Simberi lavas are high, ranging from 10.05‰ to

12.38 ‰ (Table 8). The high-Sr, xenolith-bearing lava (22) has the highest $\delta^{18}O$. The rocks that were chosen for ^{18}O analysis contain optically fresh groundmass glass and, although signs of alteration are present in the trachyandesite samples, the basalts are generally free of palagonite.

Whether the whole-rock $\delta^{18}O$ values of the basalts are primary is equivocal. Tropical weathering is a pervasive problem, limiting pristine samples. Extensive cutting and slabbing of weathered rinds from boulder-sized samples was conducted to reach a core of glassy basalt. Although the degree of freshness was determined by the presence of optically fresh groundmass glass, this can be an unreliable method of ascertaining post-crystallization alteration (H.P. Taylor, Jr., pers. comm., 1990). Microprobe analysis of groundmass glasses in the basalts showed both anhydrous and hydrous compositions, but this variation may be a primary feature since hydrous Na-rich (Table 3, col. 1) and anhydrous K-rich (Table 3, col. 3) glass coexist within melt inclusions. Analysis of palagonitized glass near oxide-coated fractures showed a high Cl content (3.5%), possibly contributed by sea spray to local ground water or by seawater interaction. All other glasses analyzed have less than 0.6% Cl.

Methods of correcting for post-crystallization alteration involving correlation with H_2O and Fe_2O_3/FeO ratios (Muehlenbachs and Clayton, 1972; Staudigel *et al.* 1981) are inapplicable to TLTF lavas since the high values of these components are primary features (Johnson *et al.* 1976; Wallace *et al.* 1983; Johnson *et al.* 1988). The possibility that the high $\delta^{18}O$ values of basaltic lavas are due to secondary alteration processes requires a separate evaluation of the oxygen isotope

systematics using mineral separates. Unlike the glassy groundmass of the basalts, phenocryst phases will retain primary $^{18}O/^{16}O$ ratios during low to moderate degrees of weathering. Determination of $\delta^{18}O$ of high temperature phenocryst phases will be an indication of the primary $\delta^{18}O$ of the lava, since mineral-melt fractionation at mantle temperatures are likely to be negligible (Garlick *et al.* 1971; Kyser *et al.* 1981; 1982).

Basaltic mineral separates and $\delta^{18}O$ disequilibrium produced by SCHARM

Evidence for ^{18}O-enrichment of the mantle by SCHARM metasomatism is provided by ^{18}O analyses of hand-picked, bulk mineral separates (Table 9) from mantle-derived, high Mg basalts. In these samples, petrographic evidence indicates that mantle xenocrysts of olivine are metasomatized by SCHARM to produce clinopyroxene, and that both clinopyroxene and magnetite are early liquidus minerals ($T > 1100°C$, Chapter 6). Olivine separates are homogeneous in $\delta^{18}O$ at ≈ 5 ‰ and reflect primary mantle compositions (Kyser, 1986). Basalt sample 310 records clinopyroxene-olivine disequilibrium values of 1.07-1.88 ‰, whereas basalt samples 311 and 312 show magnetite-olivine disequilibrium between 0.97-1.29 ‰.

The extent of disequilibrium recorded by these mineral separates (Figure 44a) is remarkably high when compared to peridotite nodules exhibiting pyroxene-olivine disequilibrium (Kyser *et al.* 1981). Coliquidus clinopyroxene and magnetite are in equilibrium and form a cluster of values (Figure 44b), indicating that the basaltic magmas are enriched in ^{18}O by ≈ 1.2 ‰ relative to mantle olivine. Two clinopyroxene bulk separates (310-4 and 310-7) with extraordinary enrichments in

$\delta^{18}O$ of 1.8‰ and 5 ‰ indicate, however, that the 1.2 ‰ value may represent the lower limit of ^{18}O-enrichment.

Table 9. Oxygen isotope data for mineral separates

Sample	Mineral	$\delta^{18}O_{SMOW}$ (‰)	Comments	Location
310-1	olivine	4.94	coarse grained	Botsor Hill
310-1a	olivine	5.00	replicate of 1	Botsor Hill
311-2	olivine	5.07	coarse grained	Botsor Hill
310-4	clinopyroxene (xenocrysts)	6.88	sodian diopside (1200 ppm Sr)	Botsor Hill
310-5	clinopyroxene	6.20	sodian diopside	Botsor Hill
310-6	clinopyroxene	6.07	augite (250 ppm Sr)	Botsor Hill
310-7	clinopyroxene	10.29	sodian diopside - suspect?	Botsor Hill
312-8	magnetite	6.04		Monambur
311-9	magnetite	6.33		Botsor Hill
312-10	magnetite	6.36		Monambur

The 1.2‰ enrichment in the Simberi primary basalts relative to mantle olivine can be used to estimate the $\delta^{18}O$ of slab-derived SCHARM. Unlike two-component Sr isotope mixing curves which are hyperbolic due to the difference in Sr concentrations of each end member (Faure, 1986, p. 142), mixing of oxygen reservoirs under mantle conditions is a simple linear function since the O content of each reservoir is essentially the same (James, 1981; Taylor and Sheppard, 1986). The oxygen isotopic composition of a slab melt contaminating a homogeneous mantle reservoir ($\approx$5‰) can be determined using the mineral separate data,

Figure 44. $\delta^{18}O$-$\delta^{18}O$ plot showing the oxygen isotope disequilibrium recorded by Botsor Hill mineral separates.

(a) Clinopyroxene-olivine and clinopyroxene-magnetite mineral pairs. Two of the three clinopyroxene-magnetite pairs are in isotopic equilibrium (i.e. they plot near the 0‰ fractionation line). Clinopyroxene-olivine pairs from Simberi record strong $\delta^{18}O$ disequilibrium, compared to peridotite nodules (Kyser *et al.* 1981) which display a lesser degree of isotope disequilibrium.

(b) Olivine-clinopyroxene and olivine-magnetite mineral pairs indicate that the Botsor Hill basanite melt was enriched in $\delta^{18}O$ by 1.2‰ compared with its xenocrystic mantle olivine.

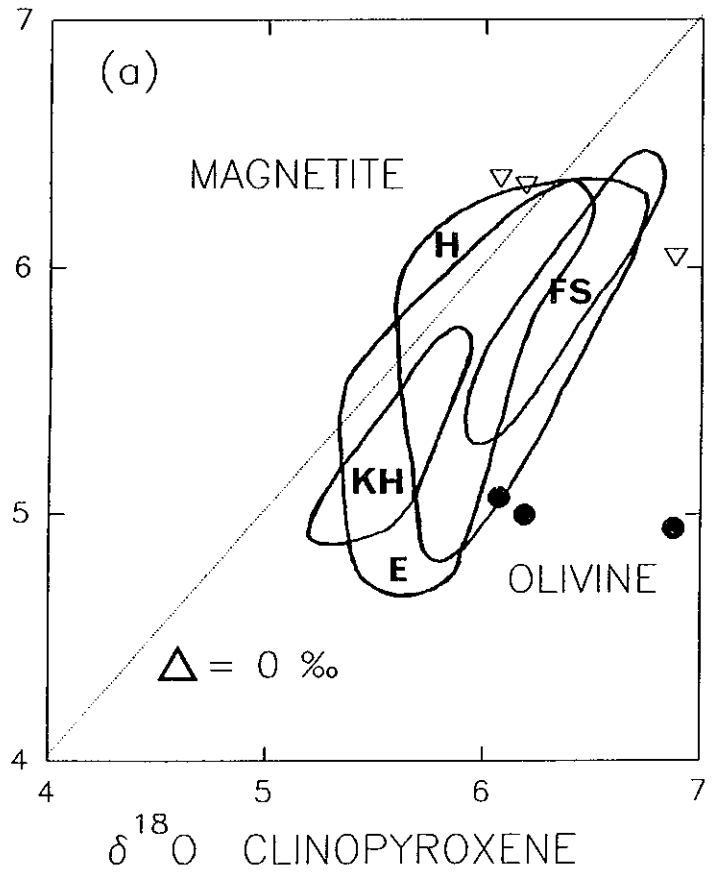

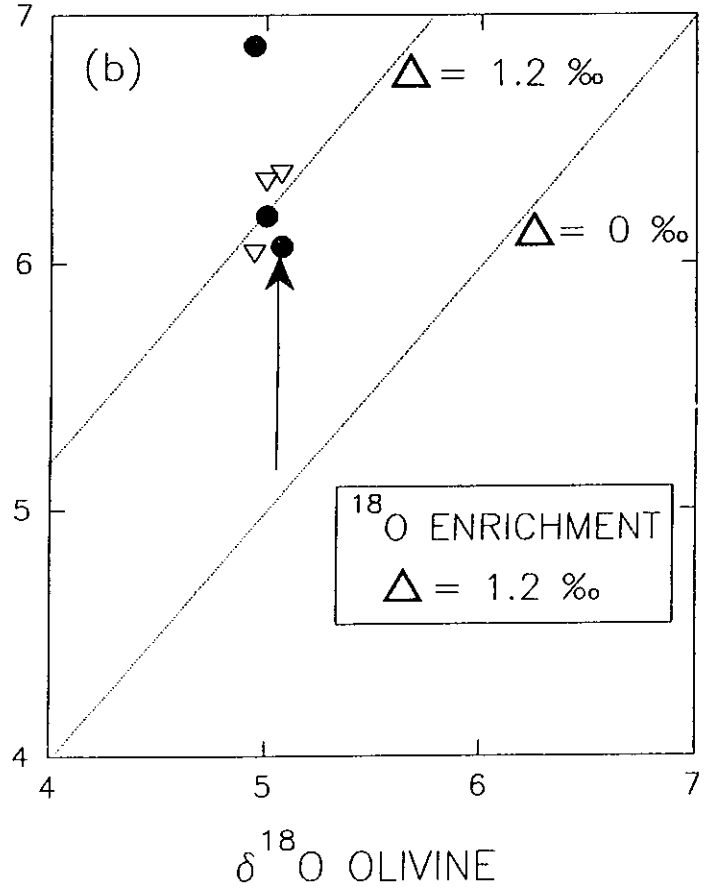

δ18O (MINERAL)

FS = Garnet peridotite, Frank Smith kimberlite pipe, South Africa
KH = Spinel peridotite, Kilbourne Hole, N. Mexico
H = Spinel peridotite, Salt Lake Crater, Hawaii
E = Eifel xenoliths
(Data from Kyser et al. 1981)

● CLINOPYROXENE
▽ MAGNETITE

assuming the O concentration of each component is equal:

$$x \cdot \delta^{18}O \text{ (mantle)} + y \cdot \delta^{18}O \text{ (slab melt)}/ (x + y) = \delta^{18}O \text{ (mantle-derived basalt)}$$
$$1 \cdot (5) + 1 \cdot (\delta^{18}O \text{ (slab melt)})/2 = 6.2;$$
$$\text{therefore, } \delta^{18}O \text{ (slab melt)} = 7.4 \text{ ‰}$$

If the higher clinopyroxene values of 6.88 and 10.29 ‰ are used to represent the $\delta^{18}O$ of mantle-derived basalts, the $\delta^{18}O$ value of the slab melt component could be as high as 8.8 and 15.6 ‰ respectively. The value of 7.4‰ for the slab melt is consistent with the hypothesis that SCHARM is derived by partial melting of seawater-altered oceanic crust, since numerous researchers have documented that the upper 1-2 km of oceanic crust is ^{18}O-rich with values ranging from 6.5 to 12‰ (Gregory and Taylor, 1981; Cocker *et al.* 1982; Muehlenbachs, 1986).

Modelling slab melt contribution to the mantle wedge

The ensimatic tectonic setting of the TLTF arc, and evidence for the rapid intrusion and cooling of the Botsor Hill alkali olivine basalt (AOB) are strong arguments for negligible contamination of these samples by shallow-level crustal rocks. Primary AOB lavas from ensimatic arcs are the best candidates for determining the relative contributions of the slab and the mantle to arc magma petrogenesis. James (1981) and Sheppard and Taylor (1986; p. 255) discuss methods of using Sr and O isotope data for modelling slab melt contamination of the mantle source region. By combining the oxygen isotope data from Botsor Hill mineral separates with the whole rock Sr isotope data, a series of binary mixing models can be constructed (James, 1981) to estimate the degree of slab melt contamination of the mantle required to produce the observed isotopic signatures.

An assumption inherent to these simplistic model calculations are that the isotopic composition of each end-member is known or can be reasonably estimated. The mineral separate data allow a reasonable estimate of the oxygen isotope composition of the mantle ($\approx$ 5 per mil) and the slab melt ($\approx$ 7.4 per mil). The Sr isotope composition of depleted oceanic mantle is similar to n-MORB at $^{87}Sr/^{86}Sr$ = 0.7025. The Sr isotope composition of SWAB is heterogeneous, with $^{87}Sr/^{86}Sr$ increasing with the degree of seawater alteration, but a value of $^{87}Sr/^{86}Sr = 0.704$ (Dasch *et al.*, 1973; Hart *et al.* 1974) is considered representative for these purposes. The absolute abundances of Sr in the slab melt and the mantle are not well defined, but only their ratios are critical to the mixing curve calculations. The abundance of Sr in the mantle is probably less than 200 ppm. The abundance of Sr in the slab melt at its point of origin is unknown.

Using the above end member compositions, binary component mixing curves were calculated using a series of Sr_{mantle}:$Sr_{slab\ melt}$ ratios. The calculated curves, the oxygen isotope compositions of mineral separates (Table 9; 310-5, 310-6 and 311-9) and the whole rock $^{87}Sr/^{86}Sr$ (Table 8) for the Botsor Hill primary magma are presented on Figure 45. The clinopyroxene separates indicate that a 45-50% contribution of slab melt is required to produce the isotopic signatures of the primary Botsor Hill lavas at a Sr_{mantle}:$Sr_{slab\ melt}$ ratio $\approx$ 1:3.5. Other researchers have also suggested a contribution of up to 50% subducted crustal material to the mantle wedge in the production of ensimatic arc volcanic rocks (eg. Lesser Antilles, Davidson, 1987; South Banda, McCulloch *et al.* 1983 and Margaritz *et al.* 1978). This compares with a contribution of less than 1% pelagic sediments, if they are able to survive transportation during subduction and undergo melting (Figure 46a

Figure 45. Modelled binary component mixing curves for slab melt and mantle end member compositions. The mixing curves were calculated using a series of Sr_{mantle}:$Sr_{slab\ melt}$ ratios. The $\delta^{18}O$ of mineral separates and $^{87}Sr/^{86}Sr$ (WR) for the Botsor Hill samples are also plotted. The clinopyroxene separates indicate that a 45-50% contribution of slab melt is required to produce the isotopic signatures of the primary Botsor Hill lavas.

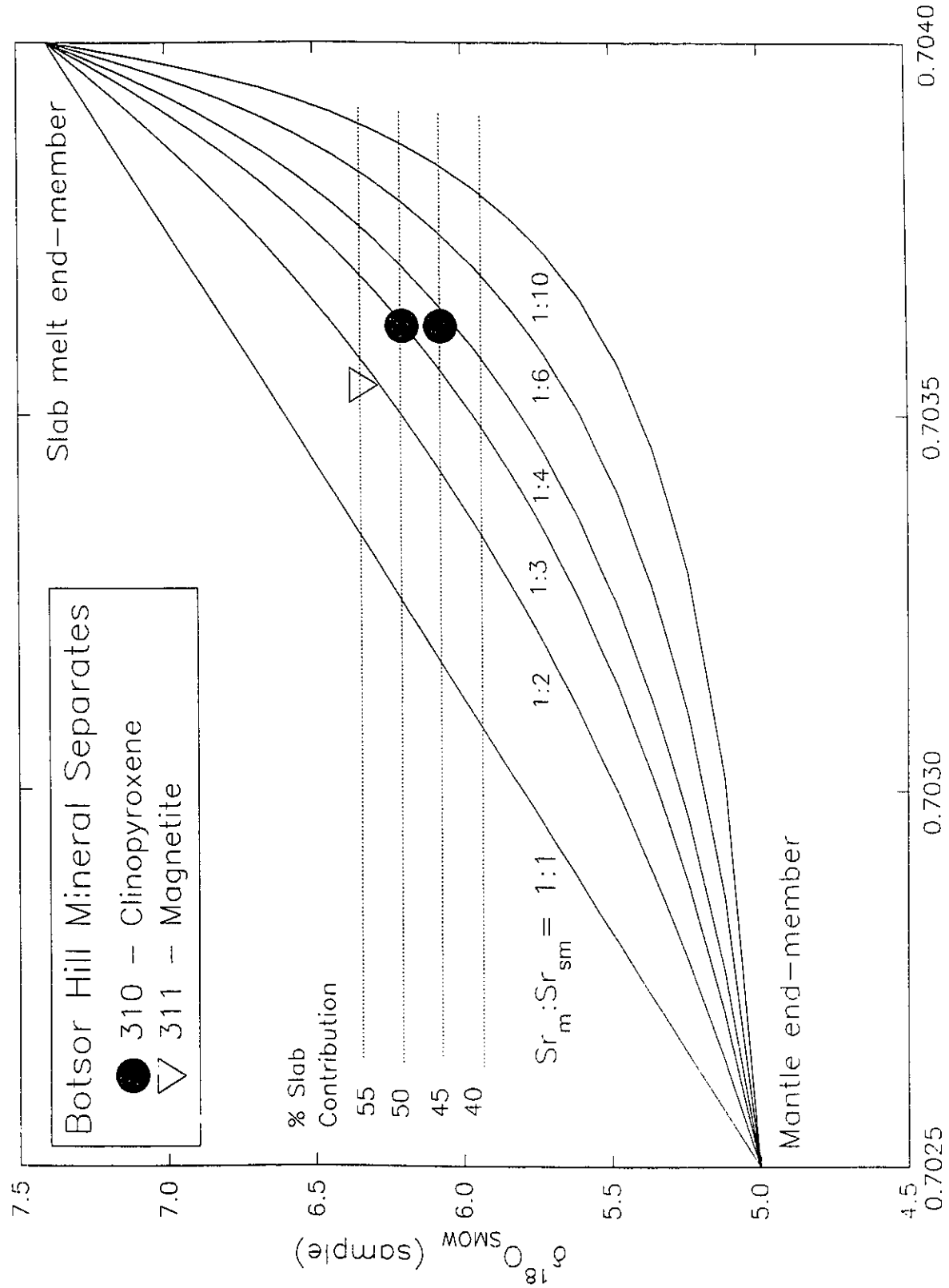
Botsor Hill Mineral Separates
310 – Clinopyroxene
311 – Magnetite
Slab melt end–member
Mantle end–member
% Slab Contribution
55
50
45
40
$Sr_m:Sr_{sm}$ = 1:1
1:2
1:3
1:4
1:6
1:10
$\delta^{18}O_{SMOW}$ (sample)
$^{87}Sr/^{86}Sr$
7.5
7.0
6.5
6.0
5.5
5.0
4.5
0.7025
0.7030
0.7035
0.7040

and Ito and Stern, 1985).

The modelling results in Figure 45 must be viewed as preliminary since they are highly model-dependent. This is typified by the low Sr_{mantle}:$Sr_{slab\ melt}$ ratio ≈ 1:3.5, which cannot account for the high Sr abundance of the Botsor Hill intrusion (≈ 1500 ppm Sr), unless the mantle contains an unlikely 430 ppm Sr. Model dependency is demonstrated by the fact that a more appropriate Sr_{mantle}:$Sr_{slab\ melt}$ ratio ≈ 1:10 is obtained if the mantle has a bulk oxygen isotope composition of 5.5 to 6 per mil. In addition, the oxygen isotope composition of the slab melt is a minimum value, since SCHARM is a complex multi-component magma composed of at least two distinct oxygen isotope reservoirs consisting of $(CO_3)^{2-}$ and $(SiO_4)^{4-}$ ions. If the oxygen isotope ratios of the massive calcite in the carbonate nodule are primary, then the contribution from this reservoir must also be considered in modelling calculations.

Oxygen, carbon and strontium isotopic composition of the carbonate nodule

Three types of carbonate occur in Simberi alkaline olivine basalts, of which three occur within the carbonate nodule. The types are:

Type I - Occurring in alkali-rich melt inclusions in olivine and sodian diopside xenocrysts from the Botsor Hill intrusion (Figures 22, 23, 25, 26, 27 and 28) and also within the xenolith in rock sample 22 (Figure 31b), this high Sr calcite (1800-4900 ppm Sr) can occur as euhedral crystals, often with hexagonal shape (Figure 25a). Sodalite, anhydrite, fluorapatite, titanian phlogopite and titanomagnetite are present, and are sometimes intergrown with the calcite.

Type II - Occurring in the xenolith in basalt sample 22, type II is a massive, low Sr calcite (283 ppm Sr), enclosing magnesiochromite, magnesio-hastingsite and Al-rich diopside. The massive calcite portion of the xenolith is rounded where it is in contact with the surrounding glassy lava, indicating it has undergone partial resorption by the host liquid. Complete decarbonation was prevented by an armour of pure diopside crystallites radiating from the massive carbonate border (Chapter 4; Figure 32).

The low Sr abundance of this type in comparison with Type I is enigmatic, but could be either primary or secondary in origin. At high pressure (>21 kbar), trace element distribution between an immiscible Type I calcite melt and a mafic melt would be controlled by the degree of melt polymerization (Ryerson and Hess, 1978 and Chapter 7). The high concentration of Sr in the xenolith-bearing sample 22 (2890 ppm) and the low Sr content of Type II calcite (283 ppm) could be produced by liquid-liquid distribution coefficients if $k_D^{\text{basalt-carbonate}}$ for Sr $\approx$ 10. Alternatively, the low Sr content of Type II calcite could be due to the leaching of Sr from the calcite by groundwater (Hay and O'Neil, 1983).

Type III - Occurring in the xenolith and basalt vesicles along with analcime and Ba-zeolites (phillipsite), this low Sr calcite (<200 ppm) may be interpreted as carbonate re-precipitated from volatilized Type I and II calcite upon destabilization at P<21 kb (Hay and O'Neil, 1983).

Due to their small size (<30 μm), Type I calcite could not be analyzed

isotopically using available techniques. The data for Types II and III are presented in Table 10. Oxygen isotope ratios for xenolith calcite are homogeneous ($\delta^{18}O$ = 21.7 to 22.3 ‰; n=7), while carbon isotopes reveal a bimodal population of massive calcite with $\delta^{13}C$ = -0.6 to -1.5 ‰ (n=4) and vesicular carbonate with $\delta^{13}C$ = -5.8 to -8.4 ‰ (n=3). The heavier $\delta^{13}C$ ratios are considered primary while the lower values may reflect Rayleigh degassing of CO_2 vapour enriched in ^{13}C by ≈4 ‰ (Pineau and Javoy, 1983), occurring during carbonate dissociation at P<21 kbar.

Table 10. Isotopic composition of xenolith carbonates from Simberi Island

Sample #	Type	$\delta^{18}O$‰ (SMOW)	$\delta^{13}C$‰ (PDB)	$^{87}Sr/^{86}Sr$	Comments
22-1	II	22.3	-5.8	nd	Massive calcite
22-1	II	22.0	-0.9	nd	Massive calcite adjacent to magnesiochromite
22-3	II	21.7	-1.3	nd	Massive calcite
22-4	II	21.8	-0.6	0.70398	Massive calcite; 283 ppm Sr
22-5	II	22.1	-1.5	0.70417	Massive calcite
22-6	III	22.8	-7.0	0.70359	Analcime present
22-7	III	22.1	-8.4	nd	Vesicle between two pyroxene grains
45B-1	III	23.5	-1.3	0.70432	Analcime, FeO present
337-1	III	26.0	0.0	nd	Secondary
305-1	III	24.4	-12.6	nd	Secondary

The distinct $\delta^{18}O$ disequilibrium between the calcite nodule (22 ‰) and its host trachybasalt (Sample 22; 12.38 ‰) could be either a primary or secondary phenomenon. The secondary effects have been previously discussed. If the values are primary, then the $\delta^{18}O$ and $\delta^{13}C$ values of the xenolith calcite are similar to

Figure 46. Plot of $\delta^{18}O$ vs. $^{87}Sr/^{86}Sr$ and Sr abundances in Simberi volcanic rocks.

(a) $\delta^{18}O$ vs. $^{87}Sr/^{86}Sr$ for Simberi volcanic rocks, mineral separates and xenolith calcite. Also plotted is a binary mixing curve for Ontong Java Plateau carbonate sediments and mantle peridotite, which shows that neither the mineral separates nor the xenolith calcite isotopic values can be obtained by sediment contamination of mantle peridotite.

(b) Co-variation in $\delta^{18}O$ and Sr in Simberi volcanic rocks. Note that the calcite xenolith-bearing lava (22) contains the highest Sr content of any lava yet analyzed in the Tabar-Lihir-Tanga-Feni arc. Dotted line indicates 95% confidence level on regression line ($r = 0.81$).

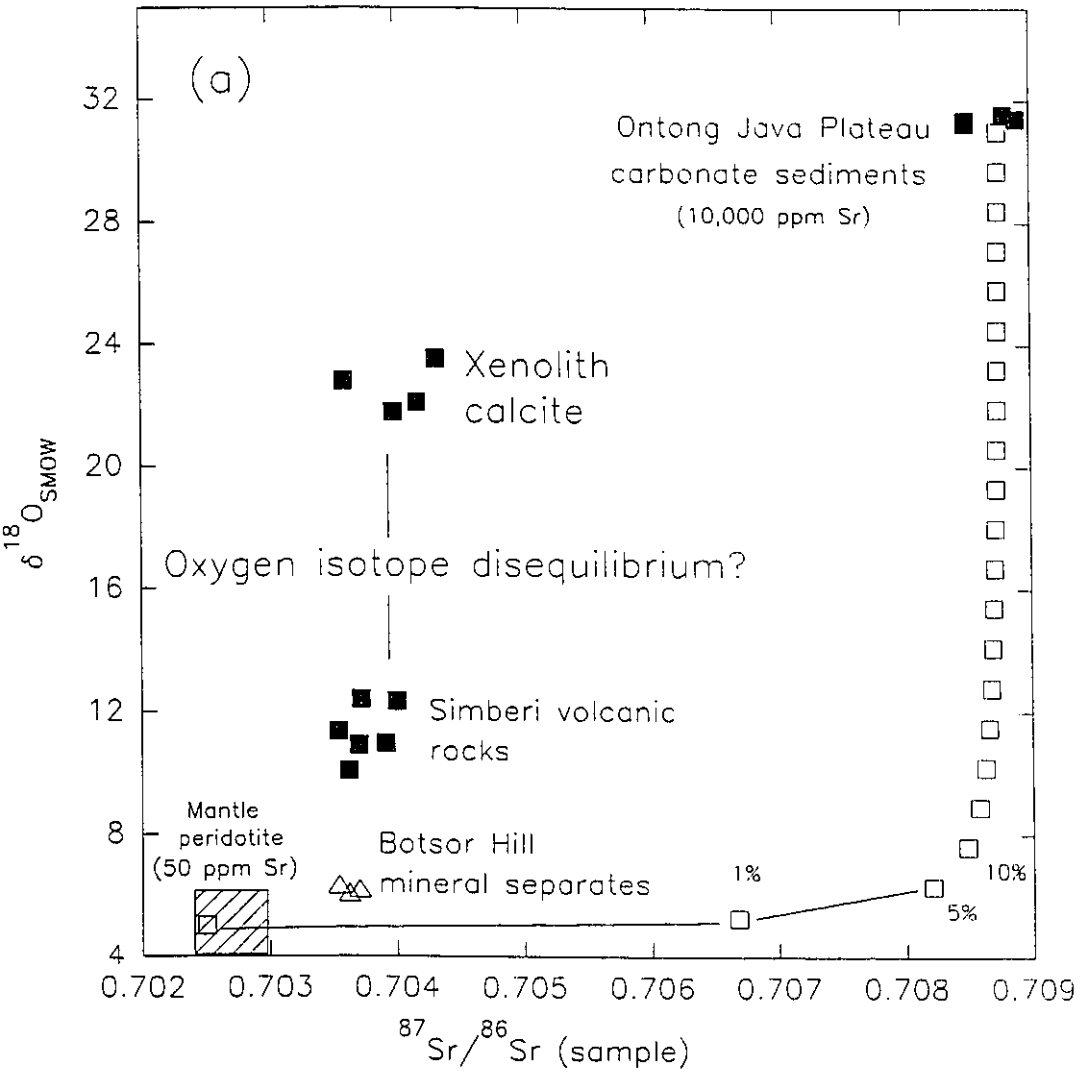
(a)
Ontong Java Plateau
carbonate sediments
(10,000 ppm Sr)
Xenolith
calcite
Oxygen isotope disequilibrium?
Simberi volcanic
rocks
Mantle
peridotite
(50 ppm Sr)
Botsor Hill
mineral separates
1%
5%
10%
$\delta^{18}O_{SMOW}$
$^{87}Sr/^{86}Sr$ (sample)

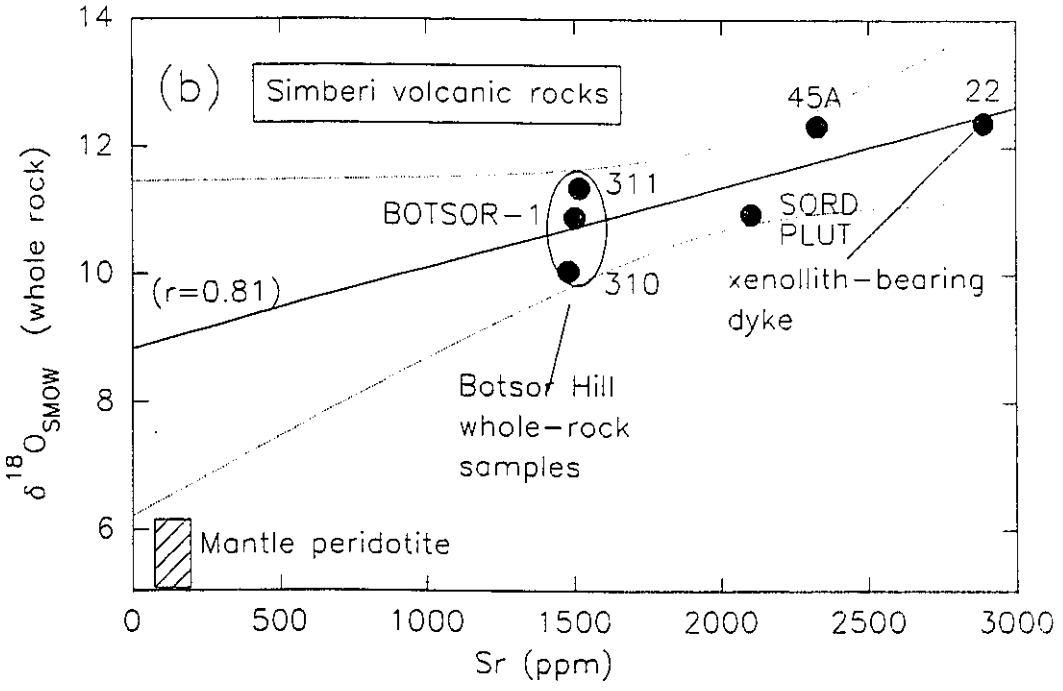
(b)
Simberi volcanic rocks
45A
22
311
BOTSOR-1
SORD
PLUT
310
(r=0.81)
xenollith-bearing
dyke
Botsor Hill
whole-rock
samples
Mantle peridotite
$\delta^{18}O_{SMOW}$ (whole rock)
Sr (ppm)

calcite precipitated in fractures in oceanic basalt crust (Muehlenbachs and Clayton, 1972; Muehlenbachs, 1987). Calcite from sulphate-bearing bergalite lavas from the Rhine Graben also have similar values (Hubberton *et al.* 1988).

The isotopic compositions of the nodule calcite are compared to calcite in carbonatites (Deines, 1970; Deines and Gold, 1973; Deines, 1989), nephelinitic alkaline rocks at the Kaiserstuhl alkaline complex (Hubberten *et al.* 1988), kimberlites (Kobelskii *et al.* 1979; Ito, 1988) and African carbonatites (Vinogradov *et al.* 1978; Nelson *et al.* 1988) in Figure 47. The high $\delta^{18}O$ values in the carbonatites and kimberlites have been explained as resulting from secondary processes, such as hydrous alteration by groundwater or by low temperature magmatic fluids (Kobelskii *et al.* 1979), assimilation of sedimentary carbonate and isotopic fractionation during degassing. Miocene reef carbonates are exposed on Simberi Island, but they are distant from the volcanic core and assimilation of these carbonates can be ruled out by the low $^{87}Sr/^{86}Sr$ ratios, as well as by the magnesiochromite grains within the calcite.

The $^{87}Sr/^{86}Sr$ ratios of the xenolith calcite are too low to represent a contribution solely from seawater-altered basalt (SWAB) calcite. Calcite precipitated from marine water ($^{87}Sr/^{86}Sr = 0.709$), even if precipitation occurred during the Mesozoic ($^{87}Sr/^{86}Sr = 0.707$), is high in radiogenic Sr, and would require a low $^{87}Sr/^{86}Sr$ source contribution. The mantle ($^{87}Sr/^{86}Sr = 0.702$-0.703) contains too little Sr (50-200 ppm) to effectively buffer the dominant contribution of seawater carbonate and produce nodule $^{87}Sr/^{86}Sr$ values of 0.70398 to 0.70417, unless the total seawater carbonate contribution is less than 0.5%. This is shown

Figure 47. Plot of $\delta^{13}C$ vs. $\delta^{18}O$ for Type II and III xenolith calcite and secondary calcite from Simberi Island. Also presented are data for calcite from carbonatites, kimberlites and marine carbonates.

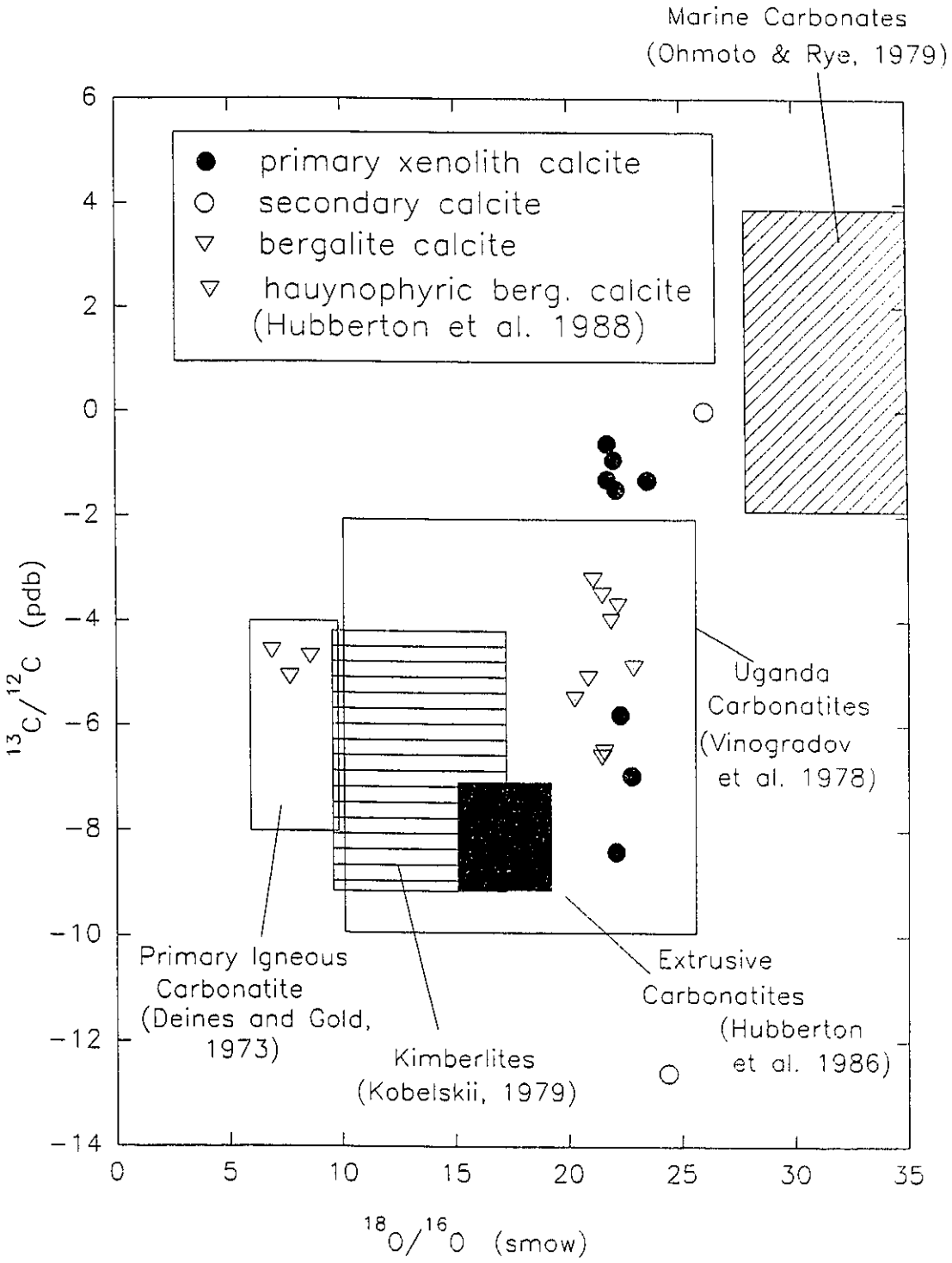
Marine Carbonates
(Ohmoto & Rye, 1979)
primary xenolith calcite
secondary calcite
bergalite calcite
hauynophyric berg. calcite
(Hubberton et al. 1988)
Uganda
Carbonatites
(Vinogradov
et al. 1978)
Primary Igneous
Carbonatite
(Deines and Gold,
1973)
Kimberlites
(Kobelskii, 1979)
Extrusive
Carbonatites
(Hubberton
et al. 1986)
$^{13}C/^{12}C$ (pdb)
$^{18}O/^{16}O$ (smow)
6
4
2
0
−2
−4
−6
−8
−10
−12
−14
0
5
10
15
20
25
30
35

by two component mixing curves between mantle and marine carbonate from the Ontong Java Plateau in Figure 46a. From the above arguments it is evident that the $^{87}Sr/^{86}Sr$ of both the primary basalts and the massive calcite from the nodule must be due to Sr homogenization within the subducted oceanic slab itself.

Most n-MORB have low Sr abundances (127 ppm; Basaltic Volcanism Study Project 1981, p. 144). Strontium in MORB will be concentrated within modally abundant plagioclase, ($k_D^{plag.-melt} = 1.8$; Wilson, 1989, p. 138), that mineral having a $^{87}Sr/^{86}Sr$ ratio of 0.7024-0.7030. Scapolite formed by the reaction of plagioclase ($^{87}Sr/^{86}Sr = 0.7025$) with $CaCO_3$ or $CaSO_4$ ($^{87}Sr/^{86}Sr = 0.709$) at a 3:1 ratio (Goldsmith and Newton, 1977), can conceivably produce a scapolite reservoir with $^{87}Sr/^{86}Sr = 0.7041$, assuming that both plagioclase and calcite have equal concentrations of Sr. This deduction will remain speculative until a study is conducted on the stability of scapolite in subduction zones.

Solubility mechanisms and oxygen isotope disequilibrium

Similarity in $^{87}Sr/^{86}Sr$ ratios between the primary basalts and the carbonate nodule is at odds with apparent disequilibrium in $^{18}O/^{16}O$ (Figure 46a). This phenomenon can be reconciled by a consideration of solubility mechanisms (Lasaga, 1981). Melting of scapolite (P > 30 kbar) would produce at least two potential oxygen isotope reservoirs: $(CO_3)^{2-}$ (Mysen and Virgo, 1980; Stolper *et al.* 1987) and $(SiO_4)^{4-}$ (Zachariasen, 1932), whereas Sr exists as Sr^{2+}. At high pressure, there are no barriers to $^{87}Sr/^{86}Sr$ exchange between the carbonate and silicate melt reservoirs, even though it is possible that Sr content may be affected by polymerization-controlled distribution coefficients (Ryerson and Hess, 1978).

Within SCHARM, oxygen exchange between stable carbonate and silicate ions would require dissociation of strong covalent Si-O and C-O bonds (Eggler and Rosenhauer, 1978). Oxygen isotope exchange at P > 21 kbar is a diffusion-controlled process, since $(CO_3)^{2-}$ is stable. Isotopic exchange by diffusion is a sluggish process (Cole and Ohmoto, 1986), and it may be possible to maintain oxygen isotope disequilibrium between immiscible carbonate melts and either mantle silicates or alkali aluminosilicate melts, if the carbonate has a short residence time in the mantle. Although there is no experimental data to evaluate this claim, other studies indicate that even at mantle temperatures (> 1000° C), it would take tens of millions of years for the metasomatized region to attain isotopic equilibrium (Taylor *et al.* 1987). Tectonic arguments indicate that there was a 6 million year time lag between the cessation of subduction below the TLTF chain and extension-related volcanism. SCHARM and the TLTF peridotite mantle wedge have not had time to reach oxygen isotope equilibrium, as indicated by the mineral separate and carbonate nodule isotopic data. Given sufficient time however, the carbonate melt will reach equilibrium with mantle peridotite, and attain values approaching the 'primary igneous carbonatite' region on Figure 47.

An interesting implication of the immiscibility-disequilibrium hypothesis is that when the ^{18}O-rich carbonate-component in SCHARM ascended above the carbonate stability boundary (P < 21 kbar), dissociation of calcite led to rapid evolution of CO_2 vapour and concomitant saturation in Ca. Therefore, clinopyroxene formed due to Ca saturation, should record marked enrichments in $\delta^{18}O$. If this calcite melt is enriched in Sr (i.e. Type I and II), a correlation between Sr and $\delta^{18}O$ should be evident in minerals and lavas. Such a co-variation is

exhibited by Simberi lavas (Figure 46b). If this correlation is a primary igneous feature, the process of decarbonation of ^{18}O-rich calcite ($\delta^{18}O = 22$ ‰) may account for the high $\delta^{18}O$ values in the lavas, and secondary alteration need not be invoked. Whether the clinopyroxene mineral separates (Table 9; 310-4 and 310.7) with high $\delta^{18}O$ of 6.88 and 10.29 ‰ are the result of this process is uncertain, but will be tested in future work using microbeam isotopic analysis of the diopside rim surrounding the calcite nodule. Experimental investigations of oxygen isotope disequilibrium in carbonate-rich melts should also be conducted.

Isotopic constraints: The origin of SCHARM, the degree of SCHARM contamination in the mantle wedge and oxygen isotope disequilibrium in the mantle

The possibility that the whole rock and calcite nodule ^{18}O data may have been reset by secondary weathering, and/or that isotopic disequilibrium may exist between carbonate and silicate melts, makes quantitative modelling of the degree of possible slab involvement in the production of the Simberi arc lavas tenuous. Mineral separates from mantle-derived magmas are in isotope disequilibrium, with high-temperature (1100°C) clinopyroxene and magnetite, enriched in ^{18}O by 1.2‰ over olivine megacrysts. This is a significant ^{18}O enrichment and supports contamination of the mantle wedge by SCHARM, which has a minimum $\delta^{18}O$ of 7.4 ‰. This value is consistent with the proposed derivation of SCHARM by partial melting of subducted, sea-water altered basalt at the basalt-eclogite transition at $P > 30$ kbar. Binary mixing models indicate that the Simberi arc lavas were derived from a mantle source composed of up to 50% SCHARM.

Strontium isotopic analyses of the calcite nodule rule out a reef assimilation

origin for the calcite. The overlap in nodular massive calcite ($^{87}Sr/^{86}Sr \approx 0.70359$-0.70417) and its host basalt ($^{87}Sr/^{86}Sr \approx 0.70372$), and the other Simberi volcanic rocks ($^{87}Sr/^{86}Sr \approx 0.70354$-0.70400), argues for a genetic relationship, originating in the mantle source region of the basalts. Oxygen ($\delta^{18}O \approx 22$ ‰) and carbon (2 populations: $\delta^{13}C = -0.6$ to -1.5 ‰ and $\delta^{13}C = -5.8$ to -8.4 ‰) isotope ratios determined on calcite separated from the nodule, show striking similarities to that of calcite veins sampled within seawater altered oceanic basalts (Staudigel *et al.* 1981). Devolatilization of CO_2 may account for the population of calcite depleted in ^{13}C. Contrasting solubility mechanisms are hypothesized to account for the contrast in the Sr isotope equilibrium and the O isotope disequilibrium between the calcite nodule and its host basalt.

Strontium, O and C isotopic evidence supports the hypothesis of SCHARM derivation from subducted SWAB at the basalt-eclogite transition at $P > 30$ kbar. An evaluation of whether the isotopic composition of the carbonate nodule is primary must be conducted in further work. This can be done by determining the oxygen isotope composition of the calcite within the melt inclusions (as well as of the diopside armour surrounding the carbonate) using microbeam techniques (ion microprobe (Freer and Dennis (1982) or laser-based techniques (Sharp, 1990).

Part B

THE NATURE OF SLAB MELTS AND THEIR EFFECT ON THE MANTLE WEDGE: TABAR-LIHIR-TANGA-FENI ARC, PAPUA NEW GUINEA

Brent I.A. McInnes[1,3] and Eion M. Cameron[1,2]

[1]Ottawa-Carleton Geoscience Centre, Department of Geology, University of Ottawa, Ottawa, Canada K1N 6N5

[2]Geological Survey of Canada, Ottawa, Canada K1A 0E8

ABSTRACT

Subduction of oceanic crust is an effective mechanism for enriching the overlying mantle wedge in volatile and lithophile elements. However, the agents responsible for the enrichment (magmas or fluids) are enigmatic. Here we describe melts of apparent slab derivation and the reaction of these melts with the overlying mantle wedge. Contained within mantle-derived xenoliths and xenocrysts from Simberi Island, Papua New Guinea are quenched glass melt inclusions which represent sulphate-, carbonate-, H_2O-, alkali-rich aluminosilicate magma (SCHARM) that are of phonolitic composition. These magmas are highly enriched in large ion lithophile elements (LILE) and rare earth elements (REE), such that the SCHARM component dominates the chemical and isotopic composition of arc magmas. REE and isotopic data indicate that SCHARM is derived by partial melting of feldspathic minerals in seawater-altered basalt (SWAB) during the basalt-eclogite transition. SCHARM reacts with mantle peridotite to create a vertically zoned mantle wedge consisting of phlogopite-clinopyroxenite at P> 30 kbar and amphibole-clinopyroxenite at 21 to 30 kbar. These reactions deplete SCHARM in K, Ca, Na, Al and H_2O, and produce a silica-saturated feldspathic liquid which, due to its immiscibility in mafic liquids, produces late-stage quartz trachyte cumulodomes within the silica-undersaturated calderas of the Tabar-to-Feni arc.

[3]Present address: Division of Geological and Planetary Science, California Institute of Technology, Pasadena, California 91125

INTRODUCTION

Based on experiment, Green and Ringwood (1972) and Nicholls and Ringwood (1973) proposed that hydrous, siliceous magmas are generated during melting of subducted oceanic crust, and that these magmas react with the overlying mantle wedge to produce a hybrid mantle capable of producing calc-alkaline rocks. Confirmation of these experiments by observation of volcanic rocks in nature has been difficult because hybridization and subsequent melting of hybrid mantle regions lead to the obliteration of the slab-derived melt. Field studies of arc volcanic rocks have allowed the characterization of the isotopic and elemental contribution of slab melts to the mantle wedge, yet due to their ephemeral nature, no direct evidence of the nature of the melts exists.

During investigations of the relationship between alkaline volcanism and gold metallogenesis on Simberi Island (McInnes *et al.* 1991), the first author discovered mantle-derived xenocrysts and xenoliths associated with basanites and alkali olivine basalts (AOB) in diatremes. Partial melting of the subduction-modified mantle wedge along extensional, pull-apart structures permitted the rapid ascent of mantle fragments, including rare carbonate-bearing samples.

GENERAL GEOLOGY

Simberi Island is the northernmost volcanic island in the Tabar-to-Feni island arc, a chain of alkaline, silica-undersaturated volcanoes which form an ensimatic island arc on the leading edge of the Bismarck microplate. Until late Miocene time (Coleman and Kroenke, 1981; Kroenke, 1984), there was oblique subduction of the Pacific plate beneath the Bismarck microplate along the Manus-Kilinailau trench.

Subduction ceased following accretion of an oceanic subcontinent, the Ontong Java Plateau (Figure 1), and the junction of the plates became a transform boundary. Alkaline volcanism is related to interplate extension between sinistral transforms, the Manus-Kilinailau boundary (Hamilton, 1979) and the Manus basin spreading centre (Johnson, 1979). Volcanism commenced in the Tabar Island group, in the northern part of the arc at 3.7 Ma (McInnes, 1991), and migrated southeastward with time. The arc is notable for containing the richest (47 million oz Au) and youngest (< 1 Ma; Davies and Ballantyne, 1987) gold deposit in the world, Ladolam, which is hosted within the Luise caldera on the island of Lihir.

DESCRIPTION OF BASALTS

Basanites and alkali olivine basalts (AOB) were sampled on Simberi Island (Figure 1, inset) in the Tabar Group. These are the oldest and most primitive magmas in the arc, with $100Mg/(Mg+\Sigma Fe_{atomic})$ of 68-74, and high Ni (140-450 ppm) and Cr (320-830 ppm), values consistent with direct partial melting of a mantle source (Edgar, 1987). Hypocrystalline basalts have euhedral phenocrysts of olivine (10%, up to 2.5 mm in diameter), clinopyroxene (20%, 2mm), titanomagnetite (3%, often as inclusions in diopside), and large (2 mm) amphibole pseudomorphs. The latter now consist of a fibrous, radiating assemblage of clinopyroxene, olivine, labradorite, rhönite and titanomagnetite. The glassy mafic groundmass contains immiscible globules of K-rich and Na-rich glass with microlitic plagioclase and apatite. The basanites contain carbonate-amphibole pyroxenite nodules of mantle origin and xenocrysts of olivine and sodian diopside in the size range 3 to 5 mm.

DESCRIPTION OF XENOLITHS

A 2x3x4 cm nodule composed of calcite, magnesio-hastingsitic amphibole, aluminous diopside, magnesiochromite and minor phlogopite was discovered within a Simberi AOB. The nodule is rounded and equally divided into two portions: (1) a massive calcite portion which contains euhedral phenocrysts of magnesiochromite and very fine grained Fe-Cu-Ni sulphides (McInnes *et al.* 1991); (2) a silicate portion of the nodules which is mainly coarse-grained (8 mm) amphibole overgrowing Al-rich diopside.

Magnesiochromite is characteristic of rocks of mantle origin (e.g., Bailey, 1989). Magnesio-hastingsite is intergrown with apatite and is in contact with alkaline aluminosilicate glass. Where xenolith amphibole is in contact with the mafic lava, an anhydrous assemblage of clinopyroxene, olivine, labradorite, titanomagnetite and rhönite allows estimation of eruption temperatures between 1050-1140° (Huckenholz *et al.* 1988).

DESCRIPTION OF XENOCRYSTS

Kink-banded xenocrysts of olivine (Fo_{86-94}), up to 3 mm in diameter, contain 1600-2700 ppm Ni and a low average CaO content of 0.11%, compositions consistent with olivine of mantle origin that occur in kimberlites (Dawson, 1980), peridotites (Simkin and Smith, 1970) and Hawaiian spinel lherzolite (Sen, 1987). Phenocrysts of olivine and rims around xenocrystic olivine have a different composition (Fo_{77-83}, <1300 ppm Ni and average CaO of 0.26%). The phenocrysts and rims have crystallized in equilibrium with the basaltic magma and do not contain melt inclusions.

Xenocrystic clinopyroxene, up to 3 mm, is apple-green sodian diopside with Na_2O of 1.4-2.7%. This contrasts with colourless diopside phenocrysts which contain only 0.2% Na_2O. Melt inclusions have been trapped through the crystallization history of the diopside, but inclusions containing alkaline melt and daughter minerals are confined to the sodian diopside cores. Inclusions in the diopside rims and phenocrysts contain glass with a CO_2-rich vapour phase and magnetite.

MELT INCLUSIONS IN XENOCRYSTS

Melt inclusions (SCHARM) within the xenocryst cores of olivine and diopside comprise alkaline glass and calcite with the daughter minerals titanomagnetite, titanian phlogopite, titanite, apatite, anhydrite and sodalite. Additionally, sodian diopside daughter minerals are present within the melt inclusions hosted by olivine.

Infiltration and interaction of SCHARM with xenocrystic olivine and clinopyroxene is illustrated in Figure 2. The original SCHARM is now represented by two unmixed phases consisting of Na-rich and K-rich glass (Figure 2a, b, d). The glasses are of alkali aluminosilicate composition and their chemistry is unlike any rock type reported in the literature, but most closely resembles an alkali-rich phonolite. Na-glasses contain 0-2% K_2O, 5-22% Na_2O, 0-4% CaO, 42-68% SiO_2, 19-29% Al_2O_3, 0 to 0.67% SrO and have normative nepheline, wollastonite and sodium metasilicate. The ideal composition of the Na-glass phase ranges from jadeitic ($NaAlSi_2O_6$) to analcimic ($NaAlSi_2O_6 \cdot H_2O$) to albitic ($NaAlSi_3O_8$) with minor potassic and calcic components. The K-rich glass contains 11-14% K_2O, 0.7-5.3% Na_2O, 0.3-3.3% CaO, 59-65% SiO_2, 18.8-21.4% Al_2O_3, and 0.2-2% SrO.

The majority of K-glasses have normative quartz and wollastonite. The ideal composition of the K-rich phase ranges between leucitic ($KAlSi_2O_6$) and K-feldspar ($KAlSi_3O_8$) with minor sodic and calcic components (sodic leucite to Ca-rich alkali feldspar). The K-rich phase contains anisotropic sections, which may indicate the early stages of leucite crystallization. The lamellar texture displayed by the analcimic and leucitic glasses may be a subsolidus exsolution phenomenon related to rapid quenching of the host basanite (Fudali, 1963).

Compositions of glasses (Table 1; col. 1,2,3) illustrate their alkaline, hydrated nature, and the negligible content of mafic components (Cr, Ni, Mg, Fe). On a ternary Ca-Na-K plot (Figure 3) they have a composition distinctly different from coexisting mafic glasses and normative AOB melts. Unlike lherzolite xenolith glasses (Frey and Green, 1974; Francis, 1976; Amundsen, 1987), the extreme alkaline nature of the Simberi glasses and their low concentration of mafic components indicate that they cannot be derived from the melting of metasomatized mantle. Rather, we interpret the glasses to represent an alkaline melt which was the metasomatising agent. Upon eruption and rapid cooling of the lava, this alkaline melt, which had not completely reacted with the mantle xenocrysts, unmixed into Na- and K-rich phases. Analyses of daughter minerals, phlogopite (Table 1, col. 7,10), apatite (Table 1, col. 4), anhydrite and sodalite (Fig. 2a,b,c,d) in the melt inclusions indicate that the alkaline melt had a significant content of Sr, dissolved volatiles (F, Cl, S), in addition to CO2 and H_2O.

The composition of the alkaline melt prior to unmixing was estimated using a Cambridge Instruments Quantimet 970 image analyzer. The relative proportions of

Na-rich (analcimic composition) and K-rich (leucitic composition) glass within six circular areas (30 μm diameter) were measured using a difference in grey levels in Figure 2a to discriminate between the phases. Five areas gave consistent ratios of analcimic/leucitic glass of 1.02 ± 0.12, while the sixth gave a ratio of 0.45. The first five measurements have been used to estimate the composition of the combined alkaline melts as $K_{0.38}Na_{0.62}AlSi_2O_6*nH_2O$, with a range of $K_{(0.31\text{-}0.42)}Na_{(0.69\text{-}0.58)}AlSi_2O_6*nH_2O$. The Na/K ratio of SCHARM (Fig. 3) overlaps that of Simberi AOB as well as quartz trachyte samples from the arc, suggesting that the lavas inherited their alkali metal contents from SCHARM.

REACTION OF SCHARM WITH MANTLE MINERALS

Direct evidence for olivine and clinopyroxene replacement by SCHARM is preserved in the xenocrysts and xenolith, respectively. The consumption of orthopyroxene, due to the infiltration of the lherzolitic mantle by SCHARM has been inferred by both experimental results (Wallace and Green, 1988; Green and Wallace, 1988; Wyllie, 1987; Eggler, 1987) and natural samples (Frey and Green, 1974). The consumption is inferred because orthopyroxene was not observed in the samples.

Reaction between mantle and SCHARM produces a hydrous, alkali-rich mantle wedge peridotite while saturating the residual SCHARM in SiO_2, towards alkali feldspar composition. Thus reaction with olivine produces phlogopite plus an alkali-feldspar liquid (Figure 2c,e):

$$3Mg_2SiO_4\ (s) + \{3KAlSi_2O_8 + 2H_2O\}\ (l) = 2[KMg_3AlSi_3O_{10}(OH)_2]\ (s) + KAlSi_3O_8\ (l)$$

The olivine contains Fe^{2+} (Table 1, col. 6,9). Titanomagnetite inclusions in the

phlogopite indicate that the reaction caused oxidation of some Fe^{2+} to Fe^{3+}. The high Ti content of the phlogopite is also indicative of high fO_2 conditions of formation (Ryabchikov and Green, 1978; Arima and Edgar, 1981; Foley, 1989) (Table 1, col.7,10). Titanite grains have also been observed in the metasomatic assemblages.

Formation of amphibole is at the expense of clinopyroxene and orthopyroxene (inferred), enriching the residual melt in silica:

$$\{2\ NaAlSi_2O_6 + CaAl_2SiO_6 + H_2O\}(l) + 3MgSiO_3\ (s) + CaMgSi_2O_6\ (s) =$$

analcimic melt component orthopyroxene clinopyroxene

$$NaCa_2Mg_4Al_3Si_6O_{22}(OH)_2\ (s) + NaAlSi_3O_8\ (l) + SiO_2\ (l)$$

amphibole albite quartz

Analcimic glass, with an ideal composition of $NaAl(Al_{0.15}Si_{1.85})O_6{*}nH_2O$, has substantial substitution of Ca and K to produce the variation on Figure 3. Some analcimic glasses are oversaturated in sodium and contain normative sodium metasilicate ($NaAlSi_2O_6{*}nH_2O + Na_2O$). Simple end-member reactions between the analcimic melt component and olivine can be written to produce metasomatic sodian diopside (Fig. 2b,c,d) and a melt enriched in normative sodium metasilicate.

CARBONATE AND SULPHATE MINERALS

Euhedral crystals of calcite and anhydrite, containing 1800-4900 ppm Sr, are present within the leucitic and analcimic glasses in the xenocrysts (Figure 2 a, b, d). Microcrystalline Sr-rich calcite is also present in the xenolith, but the massive

calcite portion is enigmatically Sr-poor (200 ppm). Strontium isotopic ratios of massive calcite range from $^{87}Sr/^{86}Sr$ = 0.70359 to 0.70417 (n=3) which overlap the lower range of Simberi AOB whole rock values of $^{87}Sr/^{86}Sr$ = 0.70354 to 0.70400. The higher values are similar to those reported for quartz trachyte cumulodomes (Wallace *et al.* 1983). These $^{87}Sr/^{86}Sr$ ratios are too low to represent a contribution solely from seawater-altered basalt (SWAB) calcite. Marine water ($^{87}Sr/^{86}Sr$=0.709), even if precipitation occurred during the Mesozoic (0.707), is high in radiogenic Sr, therefore requiring a source with low $^{87}Sr/^{86}Sr$ to contribute to the Sr content of SCHARM.

Metasomatic mineral assemblages, interpreted in the light of experimentally determined phase relationships (Wendlandt and Eggler, 1980; Wallace and Green, 1988; Green and Wallace, 1988), indicate that the xenocryst population formed at P>30 kbars, and the xenolith formed at 21 kbar<P<30 kbar at 1050° to 1080°C. At these temperatures, carbonate is unstable at depths less than about 60 km (Wyllie and Huang, 1976; Olaffson and Eggler, 1978). The very low probability of survival of the carbonate nodule during ascent past the decarbonation boundary (Canil, 1990) was likely enhanced by a combination of two factors: (1) development of an insulating armour of diopside between the massive calcite and the mafic melt, and (2) eruption at high velocity (1-5 m/s; Spera, 1984; 1987). The calcite that is preserved is undoubtedly only a small fraction of the carbonate that was initially entrained within the basaltic melt. Dissociation of $CaCO_3$ in mantle melts above a depth of 60 km liberates CO_2 and increases the concentration of CaO into the silicate melt. For significant quantities of $CaCO_3$, this will cause early saturation of clinopyroxene in the melt, producing pyroxene-phyric basaltic

lavas, characteristic features of island-arc volcanics. Carbonate-rich melts ascending above the carbonate destabilization boundary will become CO_2-saturated, and this is supported by a change from calcite-bearing melt inclusions to CO_2-rich melt inclusions in zoned sodian diopside xenocrysts.

ORIGIN OF SCHARM

Simberi Island lavas are enriched in Sr, Ba, K, Na and Rb. They have REE patterns with positive Eu anomalies (Eu/Eu* = 1.2 to 1.5), negative Ce anomalies (Ce/Ce* = 0.83 to 0.91; quartz trachyte = 0.66), and a LREE/HREE ratio = 10. We have calculated (McInnes, 1991) that these chemical characteristics can be imparted to Simberi lavas by SCHARM derived by the melting of a seawater-altered feldspathic phase in a basaltic slab, with concomitant formation and retention of garnet within the slab. This requires that garnet, crystallizing in equilibrium with SCHARM, have negative Ce and positive Eu anomalies. Such a feature has been observed by Taylor and Neal (1989) in a study of Group C eclogites. Taylor and Neal (1989) also report occurrences of Na- and K-rich glasses in eclogites. If SCHARM represents a eutectic melt, scapolite is a potential mineral undergoing incongruent melting, and a simple end member equation can be written:

$$\underset{\text{marialite}}{\{3\ Na(K)AlSi_3O_8\}\cdot NaCl\ (s)} + \underset{\text{meionite}}{3\ CaAl_2Si_2O_8\}\cdot CaCO_3\ (s)\}} + \underset{\text{olivine}}{2\ (Mg,Fe)SiO_4} \Rightarrow$$

{feldspar altered by seawater and converted to anorthite and scapolite during prograde metamorphism}

$$\underset{\text{grossular}}{Ca(Mg,Fe)_2Al_2Si_3O_{12}\ (s)} + \underset{\text{omphacite}}{\{NaAlSi_2O_6\text{-}2(Mg,Fe)SiO_3\}\ (s)} + \underset{\text{kyanite}}{2\ Al_2SiO_5\ (s)} + \underset{\text{quartz}}{4\ SiO_2\ (s)} +$$

[----------QUARTZ ECLOGITE----------]

$$[CaCO_3\ (l) + NaCl\ (l) + O_2 + NaAlSi_2O_6\ (l) + K(Na)AlSi_2O_6\ (l)]$$

[----------CARBONATE ALKALINE MELT----------]

Similar equations can be written using sulphate meionite to produce a sulphate-rich alkaline melt. The formation and stability of scapolite in conditions similar to oceanic crust at high pressure is unknown (R.C. Newton, pers. comm., 1991), but the above reaction between scapolite and oceanic basalt is consistent with the Green and Ringwood (1972) and Nicholls and Ringwood (1973) hypothesis that melts produced during the basalt-quartz eclogite transition will be hydrous siliceous melts. The abundant CO_2 contained within the oceanic crust as $CaCO_3$ survived prograde metamorphism (Huang *et al.* 1980), perhaps as scapolite, and produced silica-undersaturated alkaline melts during partial melting. The prediction (Nicholls and Ringwood, 1973) that these melts would produce a hybrid mantle region consisting of olivine pyroxenite must be revised, since we report xenocrysts and xenoliths consisting of phlogopite-clinopyroxenite and amphibole-clinopyroxenite. The presence of a metasomatised mantle wedge, vertically zoned with respect to K and Na, would explain the increase in K/Na ratios of volcanic products with distance from the oceanic trench.

The hydrous, carbonated alkaline aluminosilicate melts reported in this paper may provide clues to the resolution of some of the fundamental problems in igneous petrogenesis and chemical geodynamics such as:

(1) agents of mantle metasomatism and their role in enrichment of large ion lithophile (Sr, K, Rb, Ba) and depletion of high field strength elements (Ti, Ta, Nb) in subduction zone magmas;

(2) the nepheline-normative, alkaline nature of Tabar to Feni volcanism is unusual for an island arc, being more characteristic of continental rifts such as the Rhine graben and East Africa. The presence of SCHARM in Phanerozoic subduction zones

lends credence to the formation of carbonated, amphibole- and phlogopite-rich mantle by former subduction zones beneath continental crust (Taylor and Neal, 1989);

(3) the removal of low density fractional melts from subducted slabs creates high seismic wave attenuation zones in the mantle wedge (Anderson *et al.* 1980), with the concomitant formation of high-density eclogite as a passive force driving subduction (Ringwood and Green, 1966);

(4) the recycling of crustal material (Armstrong, 1981) and particularly the subduction of carbonate (Javoy *et al.* 1982) and sulphate into the mantle;

(5) elevated oxygen fugacity measured in subduction modified upper mantle regions (Ballhaus *et al.* 1990) with linkages to Au-Cu metallogenesis and transfer of metals from asthenosphere to atmosphere (McInnes *et al.* 1991); and

(6) the production of enriched (high μ) mantle "reservoirs" (Chase, 1981; Hoffman and White, 1982), by melting of U-enriched and Pb-depleted seawater-altered oceanic basalt (Albarède and Michard, 1986).

Part B: Figure captions

Figure 1. Location map of the Tabar-Lihir-Tanga-Feni island arc, Papua New Guinea. Inset is the geology of the Pliocene aged Simberi volcano (2°37'S, 152°00'E) flanked by uplifted Pliocene and Pleistocene fringing reefs. Basanite outcrop located within the boxed area.

Figure 2. Melt inclusions within olivine and sodian diopside xenocrysts of the basanite.

(a) Scanning electron microscope back-scattered electron (SEM-BSE) image showing the compositional complexity of melt inclusions in sodian diopside (sd) xenocrysts. Light coloured regions in the metasomatic sodian diopside host correspond to the highest Na and Fe^{3+} concentrations (aegirine component). Anhydrite (an), magnetite (m) and calcite (c; Table 3, col. 4) microphenocrysts within a region of alkaline glass unmixed to lamellae of analcimic (dark regions; Table 3, col. 1) and leucitic (light regions; Table 3, col. 3) composition.

(b) BSE image of melt inclusions in sodian diopside xenocryst. Euhedral Ti-phlogopite (p), calcite (c) and magnetite (bright white) are contained within unmixed Na-Ca glasses (Na; dark regions) and K-rich glasses (l; medium gray regions).

(c) Tracing of a melt inclusion within megacrystic olivine (ol). Metasomatic sodian diopside, titanian phlogopite (PH), calcite (CC), fluorapatite and sodalite crystals are contained within a matrix of unmixed alkaline aluminosilicate glass.

(d) SEM-BSE image of hexagonal calcite crystallized from an alkaline aluminosilicate melt within sodian diopside xenocryst. Phlogopite laths surround magnetite crystal faces (bright white). The alkaline glass has unmixed to leucitic glass (medium gray at lower left) and analcimic glass (dark). Scale bar is 100 μm.

(e) Melt inclusion within megacrystic olivine (for analysis see Table 1, col.7). Metasomatic reactions between the alkaline melt and the olivine have produced sodian diopside (Table 1, col. 9), titanian phlogopite (PH; Table 1, col. 8) and titanomagnetite. Calcite (CC) and fluorapatite are daughter minerals crystallized from the alkaline aluminosilicate melt. Circles on the schematic diagram represent locations of microprobe analyses (Table 1).

Figure 3. Ternary Ca-Na-K diagram with analyses of alkaline glasses contained within xenoliths, xenocrysts and immiscible intercumulus glasses within alkaline olivine basalts. The compositional range of the original alkaline melt prior to immiscibility is represented by the rectangle, determined by image anlaysis of Figure 2a. The high silica end members (quartz trachyte) of the TLTF Daly gap have similar ranges in Na and K composition. Cation ranges for Simberi alkaline basalts and basanites (outlined area) and the Nunivak lherzolite glasses (Francis, 1976) are also provided. Tie lines join adjacent glass phases.

Figure 1.

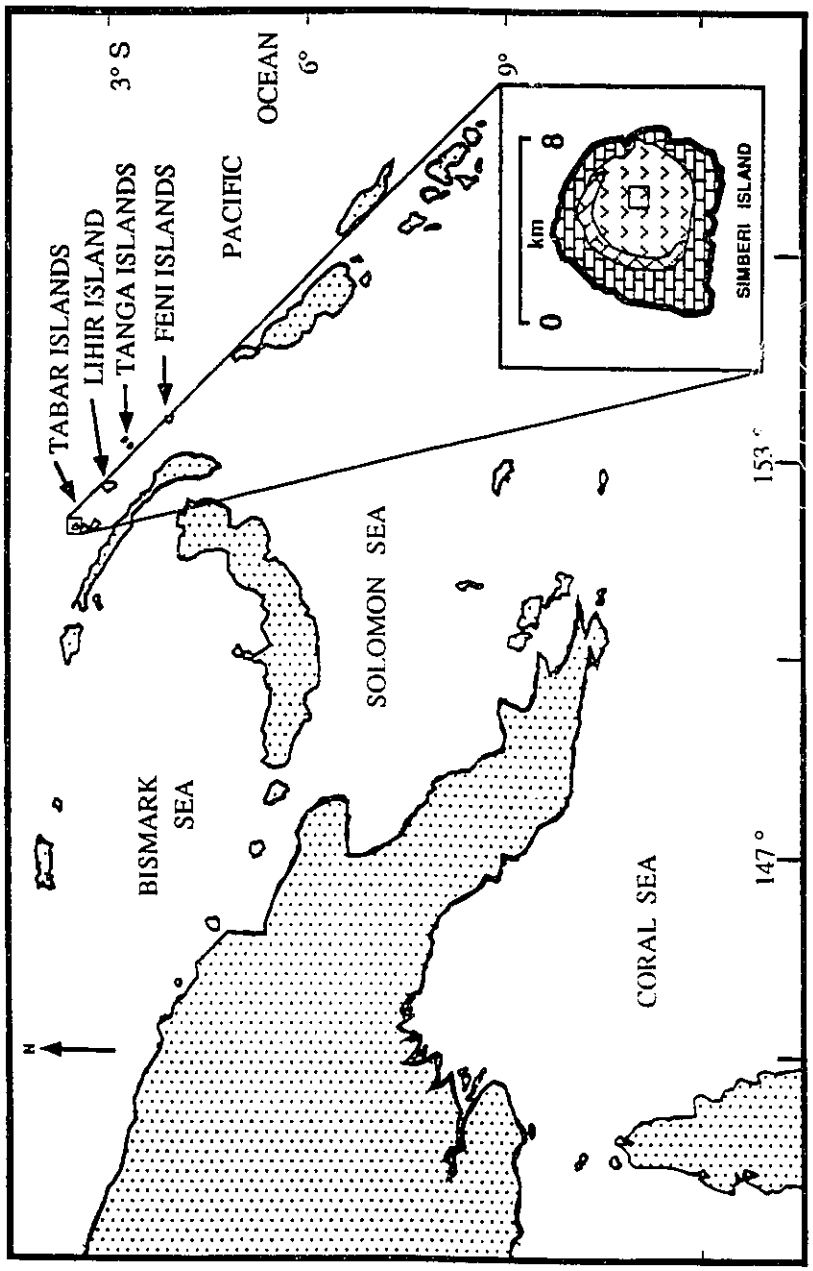
TABAR ISLANDS
LIHIR ISLAND
TANGA ISLANDS
FENI ISLANDS
3° S
6°
9°
PACIFIC
OCEAN
SOLOMON SEA
BISMARK
SEA
CORAL SEA
147°
153°
N
0
km
8
SIMBERI ISLAND

Figure 2.

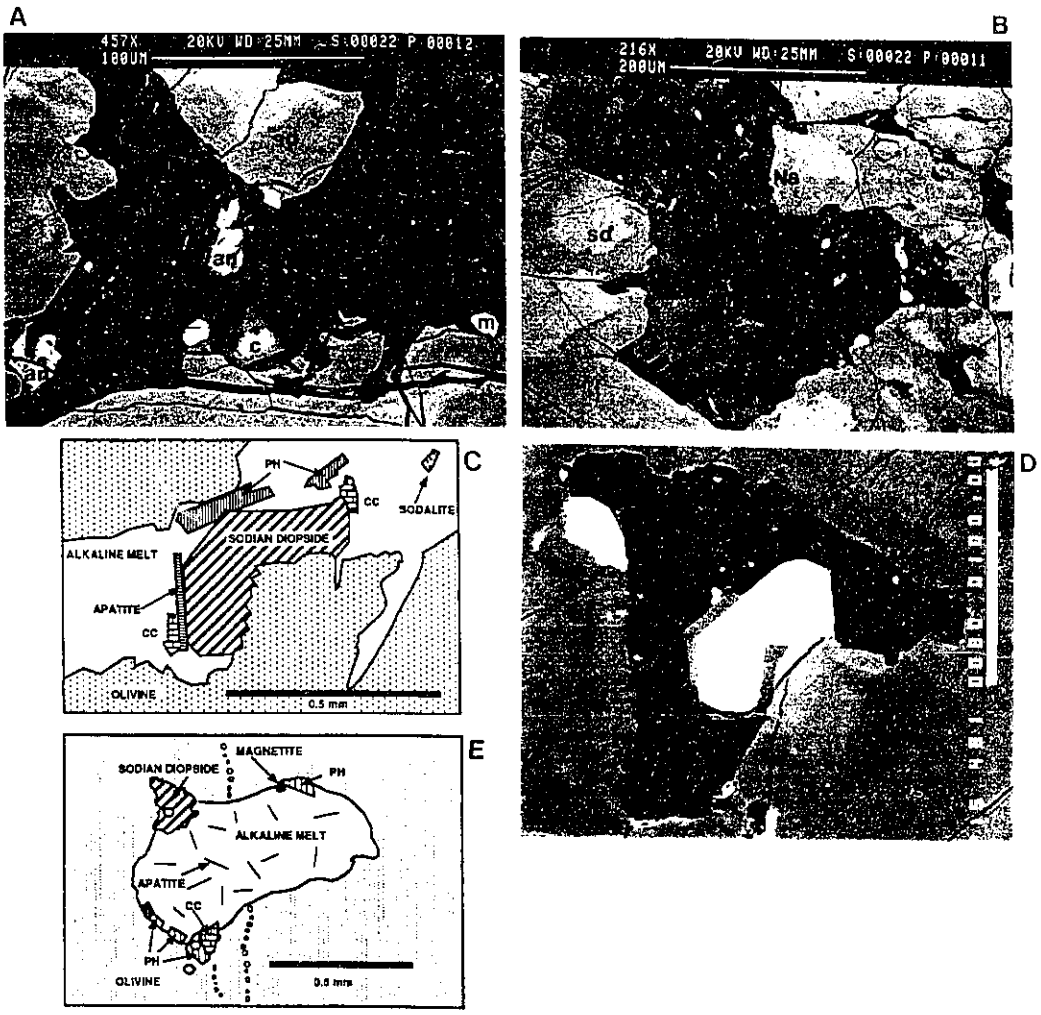
A
457X 20KV WD:25MM S:00022 P:00012
100UM
ap
c
m
B
216X 20KV WD:25MM S:00022 P:00011
200UM
Ne
sd
C
PH
CC
SODALITE
SODIAN DIOPSIDE
ALKALINE MELT
APATITE
CC
OLIVINE
0.5 mm
D
E
MAGNETITE
SODIAN DIOPSIDE
PH
ALKALINE MELT
APATITE
CC
PH
OLIVINE
0.5 mm

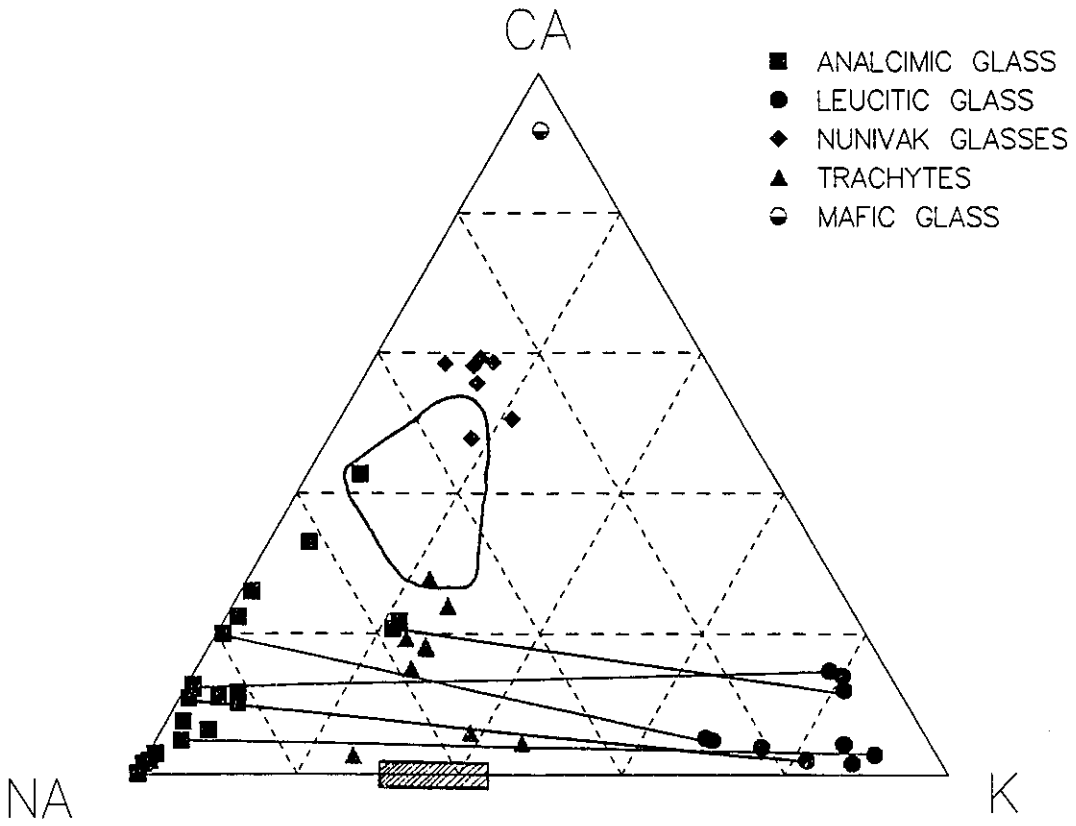
CA
NA
K
ANALCIMIC GLASS
LEUCITIC GLASS
NUNIVAK GLASSES
TRACHYTES
MAFIC GLASS

Figure 3.

Table 1. Chemical composition of melt inclusion minerals and glasses

	1	2	3	4	5	6	7	8	9	10	11
SiO_2	56.44	51.45	60.34	-.-	0.43	0.18	41.09	37.85	48.89	39.36	38.26
TiO_2	-.-	0.0	0.88	-.-	0.04	2.60	-.-	7.41	1.76	-.-	4.16
Al_2O_3	24.34	29.36	19.23	-.-	.04	1.35	-.-	13.12	5.60	-.-	13.69
FeO	0.08	0.2	0.61	0.34	0.37	85.04	8.77	5.37	4.13	13.81	7.04
MnO	-.-	0.0	0.02	0.07	0.07	0.67	-.-	-.-	-.-	-.-	-.-
MgO	0.02	0.0	0.04	0.22	0.18	1.39	50.67	20.40	14.47	45.80	20.72
CaO	1.35	4.11	3.30	50.15	54.82	0.36	0.16	0.08	22.48	0.23	0.06
K_2C	0.10	0.14	13.59	-.-	0.00	-.-	-.-	9.47	0.01	-.-	9.60
Na_2O	9.29	15.68	0.74	-.-	0.04	-.-	-.-	1.20	1.37	-.-	0.95
P_2O5	0.03	0.07	0.03	-.-	40.94	-.-	-.-	0.04	0.17	-.-	-.-
F	-.-	0.05	-.-	-.-	3.93	-.-	-.-	1.38	-.-	-.-	1.45
Cl	0.02	0.02	0.07	-.-	0.15	-.-	-.-	0.04	-.-	-.-	0.04
BaO	0.07	-.-	-.-	-.-	-.-	-.-	-.-	-.-	-.-	-.-	-.-
Cr_2O_3	-.-	-.-	-.-	-.-	-.-	0.19	-.-	-.-	0.20	-.-	-.-
NiO	-.-	-.-	0.04	-.-	0.06	0.23	-.-	0.05	-.-	-.-	-.-
ZnO	0.12	-.-	-.-	-.-	0.42	-.-	-.-	-.-	-.-	-.-	-.-
SrO	0.04	0.07	0.61	0.58	0.45	-.-	-.-	0.09	0.10	-.-	0.09
V_2O_3	0.01	-.-	-.-	-.-	0.10	0.72	-.-	-.-	-.-	-.-	-.-
SO_3	0.07	-.-	-.-	-.-	0.17	-.-	-.-	-.-	-.-	-.-	-.-
Mg#	-.-	-.-	-.-	-.-	-.-	-.-	85.2	79.0	77.8	77.2	74.6
TOTAL	91.97	101.16	99.48	99.60	102.13	93.06	100.70	96.46	99.28	99.20	96.07

Note: Mg# = 100 MgO/(MgO + FeO) from microprobe analysis

1. 310-2e: analcimic glass
2. 310-7g: jadeitic glass
3. 310-2f: leucitic glass
4. 310.2.5: calcite
5. 310.2a: fluorapatite
6. 310.2c: titanomagnetite
7. 10.2h: olivine
8. 10.2j: titanian phlogopite replacing 7
9. 10.2g: sodian diopside replacing 7
10. 10.12m: olivine
11. 10.12b: titanian phlogopite replacing 10

Part C

THE ROLE OF SUBDUCTION IN GOLD-COPPER METALLOGENESIS: EVIDENCE FROM THE TABAR-LIHIR-TANGA-FENI ISLAND ARC, PAPUA NEW GUINEA

McInnes, Brent I.A., Evans, Noreen J.
Department of Geology, University of Ottawa, Ottawa, Canada K1N 6N5

Gregoire, D. Conrad
Geological Survey of Canada, Ottawa, Canada K1A 0E8

ABSTRACT

The world's largest volcanic-hosted gold deposit (42.7 M oz. contained Au) is located within the 2 km diameter Luise caldera on Lihir Island. Volcanic-hosted gold deposits have also been discovered elsewhere on the Tabar and Feni Island groups. The ensimatic Pliocene-Holocene arc volcanics are derived from partial melting of subduction-modified mantle at > 60 km depth along extensional, pull-apart structures. The absence of continental crust indicates that the observed LILE and Au-Cu enrichments in fresh lavas are of mantle origin. Isotopic and mineral chemistry of metasomatic carbonate-phlogopite and carbonate-amphibole pyroxenite nodules and xenocrysts indicate that the mantle wedge has been intruded and metasomatized by hydrous, carbonated, alkaline melts of slab origin. Oxidation of the mantle during metasomatism by carbonated alkaline slab melts increases fO_2 > Ni-NiO, causing destabilization of Cu-Fe-Ni sulphides. This increases both sulphur and chalcophile element (Au and Cu) solubility in partial melts derived from metasomatized mantle regions. Melts saturated in sulphate sulphur under mantle conditions become supersaturated in crustal magma chambers, resulting in hauyne crystallization and degassing of SO_2, CO_2, and Cl volatiles. The volatile-rich fluid is enriched in Au and Cu. The volatiles disproportionate (SO_2), react (CO_2) and dissociate (Cl complexes) in crustal waters, concentrating Au and Cu. This process may lead to the formation of porphyry-Cu-Au deposits at high temperature and precious metal enriched magmatic-hydrothermal high-sulphidation systems at low temperature.

INTRODUCTION

The tectonic relationship between subduction-related magmatism at convergent margins and porphyry copper-gold (Cu-Au) metallogenesis has long been recognized (Sillitoe, 1972; Mitchell and Garson, 1972; Sawkins, 1972), yet the fundamental mechanisms responsible for this relationship are unknown. Solomon (1990) suggested arc reversal as a mechanism to explain the formation of porphyry Cu-Au deposits in island arcs. Although the late Miocene arc reversal was an important tectonic event, affecting the geology and geography of the Bismarck Archipelago in the northeastern Papua New Guinea region (Coleman and Kroenke, 1981; Kroenke, 1984), porphyry-related mineralization on some of the islands is temporally and spatially separated from the influence of arc reversal. For example, Cu-Au prospects on Manus Island and the Pleysumi and Pelapuna prospects on New Britain were emplaced prior to arc reversal (Francis, 1988), while the Wild Dog deposit in New Britain, and the Ladolam and Simberi deposits in the Tabar-Lihir-Tanga-Feni (TLTF) island arc, are physically separated from the influence of subducted slabs in collision (Cooper and Taylor, 1987).

Nor does arc reversal explain the continuum that exists between porphyry mineralization in island-arc and continental environments and, therefore, we are left without a common mechanism to explain the relationships between porphyry Cu-Au metallogenesis and subduction. Herein we provide petrographical and geochemical evidence from mantle-derived alkaline olivine basalts, nodules and xenocrysts from Simberi Island indicating that slab-derived melts infiltrate and oxidize the mantle wedge. Oxidation of mantle sulphides liberates the chalcophile elements Au and

Cu, and increases the solubility of Au and Cu in subduction zone magmas. Primary enrichment of Au and Cu in the mantle source region of subduction zone magmas is a critical factor in the generation of porphyry Cu-Au deposits at shallow levels (Burnham, 1979).

REGIONAL TECTONICS

Oblique subduction of the Pacific Plate along the Manus-Kilinailau trench ceased during the late Miocene, following collision of the Ontong Java Plateau (Figure 1). After the collision, two major tectonic events occurred in the region: (1) transition from an oblique convergent boundary to a transform boundary parallel to the Manus-Kilinailau trench, and (2) arc reversal and initiation of subduction along the New Britain-San Cristobal trench. Backarc spreading in the Manus Basin at 3.5 Ma (Taylor, 1979) transferred New Britain to the southeast, creating a transtensional tectonic regime to the east of New Britain. Interplate extension between the northwesterly trending transform boundaries of the Manus Basin spreading center (Weitin, Sapom and Baining Faults) and the Manus-Kilinailau trench caused partial melting of subduction-modified mantle and produced alkaline volcanism in the TLTF islands (Figure 2).

The highly alkaline nature of the TLTF arc is unique among the dominantly calc-alkaline arcs of the Bismarck Archipelago in that it is comprised of nepheline-normative rocks, including alkaline olivine basalt, olivine nephelinite, basanite, tephrite, phonolitic tephrite, trachybasalt and trachyandesite (Johnson, 1979). These rocks are conspicuous in containing phenocrysts of hauyne, nosean and

1979; Glaessner, 1915; Johnson *et al.* 1976; Wallace *et al.* 1983; Johnson *et al.* 1988), minerals which crystallize in magmas saturated in sulphate and chlorine. Another exception is the apparent proclivity of TLTF volcanoes for producing Au mineralization and, in particular, the Ladolam Au deposit (≈47 million oz.), hosted within the 4 x 6 km diameter Luise Caldera on Lihir Island (Davies and Ballantyne, 1987).

Volcanic rocks from extensional tectonic regimes often carry xenoliths derived from mantle source regions (Nixon, 1987) and, apart from experimental studies, are the only way to study deep mantle processes. Xenoliths and xenocrysts were discovered near diatreme complexes on Simberi Island of the Tabar Island Group. They provide a unique view of the mantle wedge above a former subduction zone, and are a key to the understanding of arc volcanism, metallogenesis and the relationship between the two.

PETROGRAPHIC OBSERVATIONS

Mantle-derived alkaline olivine basalts from Simberi Island host xenocrysts and xenoliths which contain evidence of primary, anhydrous mantle mineral assemblages (olivine and clinopyroxene) undergoing replacement to alkali-rich, hydrous minerals (phlogopite and amphibole). Contained within melt inclusions in xenocrystic olivine and clinopyroxene are alkali-rich glasses of nepheline-normative composition which, because they are devoid of Fe and Mg and have a low Mg# (0 to 20), are not in equilibrium with mantle melts (McInnes and Cameron, submitted). The melt inclusions contain daughter minerals of anhydrite, calcite, fluorapatite and

sodalite (Figure 3). The alkaline glasses represent magmas which have reacted with the xenocryst host to produce metasomatic crystals of sodian diopside (acmitic), titanian phlogopite, magnetite and titanite.

These alkaline magmas, hereafter referred to as SCHARM (sulphate-, carbonate-, H_2O-, alkali-rich aluminosilicate magmas), are ephemeral in nature and normally obliterated by subduction zone processes. They originated during partial melting of feldspathic phases in the subducted Pacific Plate during the basalt-eclogite transition (McInnes and Cameron, submitted). Low density SCHARM infiltrated and "fertilized" the overlying lherzolitic mantle wedge during metasomatic reactions with anhydrous ferromagnesian minerals. During metasomatism, the mantle wedge is oxidized by SCHARM. Oxidation reactions in the xenocrysts are typified by the conversion of Fe^{2+} in olivine to Fe^{3+}, which is incorporated into the metasomatic acmitic clinopyroxene and magnetite.

A xenolith containing an assemblage of calcite, magnesio-hastingsite, aluminian diopside and magnesiochromite was discovered in a glass-bearing, basaltic dyke adjacent to the diatreme-hosted South Samat Au deposit on Simberi Island. The low survival potential of a carbonate nodule in an 1100°C basaltic melt during "normal" eruptions (c.f. Canil, 1990), requires that the xenolith was brought to the surface at high velocity (Spera, 1984; 1987), from a depth greater than 70 km (Green and Wallace, 1988), and quenched upon eruption.

The xenolith (2x3x4 cm) is subdivided into two portions: (1) massive

microcrystalline calcite which contains phenocrysts of magnesiochromite (c.f. Bailey, 1989), fine blebs (< 10 μm) of Cu-Fe-Ni, Fe-Cu-Ni and Co-rich Cu-Fe-Ni sulphides and KCl-bearing fluid inclusions, and (2) a silicate portion of coarse-grained (8 mm) magnesio-hastingsitic amphibole, overgrowing Al-rich diopside and surrounded by a vesicular alkaline glass matrix. The silicate portion contains peculiar sulphur-bearing assemblages. Occurring as inclusions in the amphibole are sulphate-bearing fluorapatite (0.59 wt.% SO_3) and Cu-sulphide minerals. Globular Cu-sulphide occurs within vugs created by decarbonation reactions (c.f. Lowenstern *et al.* 1991), and within feldspar crystallites in the glassy groundmass. Heming (1979) also reported the latter texture in feldspar from Feni Island.

The textures described above provide evidence of subduction-related metasomatic processes occurring within the mantle wedge, prior to arc volcanism. Subsequent partial melting of this fertile, carbonated wedge during rift-related adiabatic decompression produced the distinct TLTF alkaline volcanoes. Carbonate-dissociation during decompression melting may have provided a propellant for high speed eruption of mafic melts to the surface (Bailey, 1987). These high speed eruptions carried mantle xenoliths and xenocrysts to the surface, where mineral phases within them underwent low pressure destabilization. Amphibole xenocrysts are pseudomorphed by an anhydrous assemblage of olivine, titanomagnetite, rhönite, labradorite and augite at ≈ 1050-1140°C (Figure 4b) (Huckenholz et al. 1988). Rhönite (ferric-rich member of the anaegmatite mineral series) is a relatively rare mineral, typically found in oxidized, undersaturated, alkaline mafic rocks

(Cameron, 1970; Johnston and Stout, 1984; Johnston et al. 1985). Sulphide inclusions within amphibole in the insulated interior of the carbonate-amphibole xenolith are preserved as euhedra (Figure 4d), while mantle sulphides within amphibole xenocrysts destabilized at low P and high fO_2 show evidence of resorption (Figures 4a, b, c). The SEM-EDS spectra (Figure 5) shows that both Cu and S have been lost to the melt during the replacement.

SCHARM-INDUCED METASOMATISM AND MANTLE OXIDATION

Metasomatism of peridotite by SCHARM creates a vertically zoned mantle wedge enriched in volatile, alkali and trace elements (Figure 2). The principal difference between the metasomatic assemblages in the xenocryst and xenolith samples is the absence of amphibole in the xenocryst population. The carbonate-phlogopite-bearing xenocryst assemblage was formed during metasomatism by SCHARM under conditions beyond the stability of amphibole, whereas the carbonate-amphibole xenolith was formed within the amphibole stability field.

Based on experimental studies (Wendlant and Eggler, 1980; Wallace and Green, 1988; Green and Wallace, 1988) metasomatism at T=950-1100°C would have produced a vertically zoned mantle wedge consisting of carbonate-phlogopite pyroxenite at depths greater than 100 km, and a carbonate-amphibole pyroxenite between 70 and 100 km. The massive calcite in the carbonate-amphibole pyroxenite xenolith is interpreted to represent a carbonate melt which has become immiscible from SCHARM during ascent through the mantle wedge.

The xenocryst mineral assemblage anhydrite, calcite, fluorapatite and sodalite requires that SCHARM are saturated in $(SO_4)^{2-}$, $(CO_3)^{2-}$, OH^-, F and Cl at high fO_2. The occurrence of this assemblage in mantle-derived basalts indicates that the source region of these magmas was oxidized and volatile-rich. The high primary Fe_2O_3/FeO ratio of 1, the high acmitic component of diopside, the occurrence of magnetite early on the liquidus (Kennedy *et al.* 1990b) and the presence of rhönite (Johnston *et al.* 1985), hauyne and nosean indicate that the magmas have an inherently high fO_2 (>FMQ+1 buffer conditions). The fact that SCHARM are powerful oxidizing agents is consistent with fO_2 measurements on subduction zone xenoliths, ranging from FMQ to FMQ> +3 (Ballhaus, Berry and Green, 1990).

Petrographic textures indicate that mantle sulphides are undergoing oxidation to sulphate. These observations lead to the hypothesis that an increase in fO_2 accompanying metasomatism of the mantle wedge is responsible for destabilization of mantle sulphides. This results in concomitant enrichment of chalcophile elements in magmas derived from subsequent partial melting of the metasomatised mantle wedge. This hypothesis implies that the primary TLTF magmas should have Au and Cu abundances in excess of mantle values. Highly sensitive analyses of Au, Cu, Ni and PGE were conducted to test this hypothesis.

ANALYTICAL RESULTS

Platinum (Pt), palladium (Pd), ruthenium (Ru), rhodium (Rh), iridium (Ir), nickel (Ni), Au and Cu analysis (Appendix 1) was conducted on Simberi Island alkaline olivine basalts and trachybasalts. The analytical data (Table 1) shows low overall

abundances of the siderophile elements, Ru, Ir, Rh, Pt and Ni, with only the most primary (high Mg) rocks containing detectable amounts of Ru, Ir and Rh. The depletion of Ru, Ir and Rh may be due to the low solubility of siderophile PGE in high fO_2 basaltic melts (Amossé *et al.* 1990) and/or to their partitioning into early fractionated spinel crystals, as evidenced by the high concentrations of PGE in magnetite separates (Table 2). Palladium abundance is similar to spinel lherzolite with minor depletions occurring in evolved rock types (mg<57). The chalcophile elements Au and Cu are enriched by a factor of 2-40 times relative to spinel lherzolite mantle (Figure 6). Since Au and Cu can be transported in vapour phases (Meeker et al. 1991; Lowenstern *et al.* 1991), their concentration in devolatilized magmas should be considered as minimum values.

The ensimatic setting of the TLTF arc indicates that Au and Cu in fresh lavas is either of mantle or of slab origin. Analysis of spinel and garnet lherzolite xenoliths (Mitchell and Keays, 1981) and other mantle rocks (Barnes *et al.* 1988 and references within) indicate that the mantle is depleted in Au and Cu (Table 1) relative to model mantle compositions. Mitchell and Keays (1981) determined that the bulk (60-80%) of the platinum-group elements (PGE) and Au in the mantle is contained in sulphide-rich intergranular components in spinel lherzolite xenoliths. This sulphide phase was proposed to be retained in mantle regions after extraction of a sulphur-saturated MORB-type melt. Chalcophile elements were partitioned into high density, immiscible sulphide liquids and retained in the mantle (Hamlyn *et al.* 1985). In order, therefore, to enrich a mantle-derived melt in Cu and Au and transport these metals to crustal regions where porphyry Cu-Au deposits form,

these mantle sulphide phases must be destabilized by oxidation.

SULPHIDE DESTABILIZATION DURING OXIDATIVE-METASOMATISM OF MANTLE REGIONS

The metasomatic assemblages described above indicate that both reduced and oxidized forms of sulphur exist in metasomatized mantle regions below the TLTF arc, and can, along with P-T data for the metasomatic assemblages, be plotted on a log fO_2-T diagram (Figure 7). Asthenospheric mantle wedge and SCHARM represent two end-member components with dichotomous redox potentials. SCHARM emanate from the slab at relatively low temperatures (800°C?), and are saturated in anhydrite. SCHARM melt inclusion assemblages (Figure 3) contain anhydrite + magnetite, and may indicate that SCHARM has an initial fO_2 as high as FMQ+4 (Fayalite-Magnetite-Quartz buffer)(Carroll and Rutherford, 1987). Prior to metasomatism by SCHARM, the asthenospheric mantle wedge should have low oxidation potential, with fO_2 = FMQ (T=1100°C). Oxidation of mantle peridotite by SCHARM during metasomatism increases fO_2 to FMQ+2 to FMQ+3, the conditions required to stabilize the carbonate nodule assemblage containing Cu-Fe-Ni sulphides and SO_3^{2-}-bearing apatite. Melting of the metasomatized mantle wedge during pull-apart related adiabatic decompression further increases oxidation to FMQ> +3, conditions where sulphide replacement by magnetite occurs, and SO_4^{2-}-bearing minerals are stable (Carroll and Rutherford, 1987).

The stability of sulphide phases in the carbonate nodule suggests that carbonate dissociation during decompression at P<21 kbar (Wallace and Green, 1988), is an oxidation process which increases the potential for sulphide destabilization.

Chlorides within fluid inclusions in the calcite nodule may provide a metal ligand which would partition into the volatile phases created.

Possible simplified reactions are:

(1) $$CaCO_3\ (l) = CaO\ (l) + CO\ (l) + 1/2\ O_2\ (l)$$

followed by (2),

$$CuFeS_2\ (l) + 3\ CaCO_3\ (l) + HCl\ (v) + 11/3\ O_2\ (l) =$$

$$2\ CaSO_4\ (l) + 1/3\ Fe_3O_4\ (s) + 3\ CO_2\ (v) + CuCl\ (v) + CaOH\ (l)$$

This reaction is in accord with investigations which have demonstrated correlations between: (1) sulphur solubility and CaO content in melts under oxidizing conditions (Katsura and Nagashima, 1974), (2) Au solubility and oxygen activity in magmatic solutions (Henley, 1971; Ryabchikov *et al.* 1985), and (3) high CO_2/H_2O, Cl, Cu and S concentrations in vapour-rich melt inclusions within Cu-poor magmas (Lowenstern *et al.* 1991).

The products of this reaction may also help to explain the following: (1) the propellant mechanism for high velocity eruptions necessary for the preservation of carbonate nodules and diatreme formation; (2) replacement of Cu-sulphides by magnetite (Figure 3d), and the release of Cu (and chalcophile Au) to the melt where it can react with chloride complexes (Henley, 1971; Burnham, 1979); (3) the presence of sulphate-bearing phenocrysts in TLTF lavas; (4) a magmatic volatile-rich fluid phase into which chalcophile-chloride complexes will partition (Krauskopf, 1964; Henley and McNabb, 1978); (5) CO_2 and SO_2 (due to eventual dissociation of $CaSO_4$) volatile phases, which react with crustal water to produce metal-enriched

sulphide/sulphate and carbonate haloes (associated with mineralization on Simberi Island), and possibly, the high anhydrite content of the Ladolam deposit on Lihir Island (Davies and Ballantyne, 1987).

In subduction zone settings, the significance of oxidative-metasomatism by SCHARM ascending from 100 km depth, can be compared to the minor oxidation role played by H_2O during slab dehydration at shallower levels. Boninite volcanoes occur in the forearc region, and are derived by high degree partial melting of H_2O-saturated mantle peridotite at depths of 30 to 60 km (Green, 1973; Tatsumi, 1981). The low oxidation potential of H_2O is evidenced by the low Fe_2O_3/FeO ratio of boninite lavas (Hickey and Frey, 1982). The fact that boninites are depleted in Cu and S (Hamlyn *et al.* 1985) is an indication that oxidation of mantle sulphides has not occurred under water saturated conditions.

MECHANISM FOR GOLD-COPPER ENRICHMENT IN ISLAND ARCS

Experimental studies on sulphate sulphur solubility in magmas are limited (Carroll and Rutherford, 1985; 1987). Sulphur solubility in magmas increases with increasing T, P, and fO_2. At fO_2 conditions slightly above FMQ (ie., island arc basalts have $fO_2 = FMQ + 1$), sulphide is stable, whereas at log $fO_2 = FMQ + 3$ sulphate is the predominant sulphur phase. The same study determined that the solubility of S as sulphate (3000 ppm) is three times greater than sulphide at $T = 1000°C$ and 3 kbar. Extrapolation of these experiments to $P = 20$-30 kbar is tenuous, however if SO_4^{2-} and CO_3^{2-} solubility mechanisms (Mysen and Virgo, 1980; Fine and Stolper, 1985; Stolper *et al.* 1987) are analogous, as suggested by

Carroll and Rutherford (1987), the total dissolved S and C as sulphate and carbonate in highly oxidized melts in the mantle could be in the wt. % range. This is evidenced by the abundance of carbonate and anhydrite in melt inclusions (SCHARM) found in this study.

In accord with these solubility mechanisms and the antipathetic relationship between polymerization and CO_3^{2-} solubility, SCHARM has a lower sulphur capacity than mafic melts derived from metasomatised mantle wedge regions. The implication is that slab melts themselves have a limited potential for the transport of metals from the subducted slab (c.f. Sillitoe, 1972) and that the bulk of the Au and Cu originates from mantle regions which have experienced oxidative-metasomatism by SCHARM. Delayed partial melting of metasomatized regions produces oxidized calc-alkaline magmas which transport Au and Cu to crustal levels.

MAGMA DEVOLATILIZATION AND METAL REMOBILIZATION

Gold and copper-enriched sulphate saturated magmas produced during partial melting of metasomatized mantle wedge will become sulphate oversaturated during ascent and storage in crustal magma chambers. High temperature crystallization of clinopyroxene and plagioclase will deplete the melt in Ca^{2+}, destabilize coordinated $CaSO_4$ (Carroll and Rutherford, 1985; Katsura and Nagashima, 1974) and degas SO_2. The high sulphur content (up to 0.9 wt. %) of the TLTF magma series (Heming, 1979; Wallace *et al.* 1983) is due to the stability of hauyne, but in magmas where SO_4^{2-}-bearing minerals do not crystallize, evidence of high original sulphur content is lost to the atmosphere as SO_2 (Pacaya volcano, Guatemala;

Stoiber and Jepsen, 1973) and as SO_2 gas and SO_4^{2-} particles (El Chichon, Mexico; Devine *et al.* 1984).

Enrichments of Au, Cu, As and Cl have been measured in SO_2-rich vent gases from White Island, New Zealand (Le Cloarec *et al.* 1989), Mt. Etna (Buat-Menard and Arnold, 1978), Kamchatka (Menyailov and Nikitina, 1980), Mt. Erebus, Antarctica (Meeker et al. 1991) and Momotombo and Cerro Negro, Nicaragua (Gemmel, 1987). Magmatic degassing of Au (Zoller *et al.* 1983), Cu (Nriagu, 1989; Lowenstern *et al.* 1991), As (Walsh *et al.* 1979) and S (Devine *et al.* 1984) enriches the atmosphere in trace-metals, and represents a major contribution to the Earth's metal budget. The variability of metal enrichment in the atmosphere can be attributed to differences in the chemical and eruptive nature of volcanoes, but the fact that calc-alkaline volcanoes are major contributors to the metal budget is evidence that oxidative-metasomatism processes operating in subduction zones is the catalyst linking metal transfer from the asthenosphere to the atmosphere.

This transit can be short circuited if the magmatic volatiles encounter a crustal water table. High temperature, metalliferous, volatile-rich fluids that mix with an overlying water column will deposit metals in response to a destabilization of metal-chloride complexes with decreasing temperature (Sillitoe, 1989; Henley and McNabb, 1978; Eastoe, 1978; Seward, 1984). Disproportionation of SO_2 in aqueous fluids at low temperature ($< 400°C$) where $Au(HS)_2^-$ predominates over $AuCl_2^-$(Seward, 1989), producing auriferous magmatic-hydrothermal acid-sulphate systems overlying deeper porphyry Cu-Au systems (Sillitoe, 1973, 1983;

Hedenquist, 1986; Rye *et al.* 1991).

CONCLUSIONS

Petrographic observations of the occurrence of sulphide/sulphate minerals in xenoliths and xenocrysts leads to the hypothesis that oxidation of the mantle wedge in convergent margins occurs during infiltration and metasomatism by sulphurous, carbonaceous, hydrous, alkali-rich magmas of slab origin. The resultant oxidation state of the metasomatised mantle wedge below the TLTF island arc is greater than FMQ +2 to FMQ +3, and leads to sulphur undersaturation during partial melting and the destabilization of mantle Cu-Fe-Ni sulphides. Carbonate dissociation at $P < 21$ kbar may be an important mechanism for further increasing melt fO_2 such that sulphate abundance greatly predominates over sulphide. Sulphate-rich, mantle-derived lavas from Simberi Island are also enriched in chalcophile Au and Cu, consistent with mantle sulphide destabilization. Transport of sulphate saturated melts from mantle to crustal regions produces a volatile- and metal-rich aqueous fluid. A continuum of metal deposition from chloride and bisulphide complexes from high to low temperature environments may explain the various ore deposit-types found in volcano-plutonic arc complexes.

The hypothesis presented in this paper implies that magmas derived from metasomatized mantle regions should show a positive correlation between fO_2, CO_2, total S, Cl, Cu and Au. This work has the following implications for future research: (1) Mineral exploration - Although the formation of economic Cu-Au deposits is a result of a combination of lithospheric processes, this work

demonstrates that oxidized mantle source regions underlying the TLTF arc may be a significant factor in the genesis of the world's largest volcanic-hosted Au deposit on Lihir Island. If the El Chichon and the Mount Lamington, Papua New Guinea (Arculus *et al.* 1983) volcanoes, as well as those of the Roman Comagmatic Province in Italy (Cavarretta and Lombardi, 1990), achieved sulphate saturation by sulphide destabilization during oxidative-metasomatism of their mantle source regions, then they should show chalcophile element enrichment trends similar to Figure 6. Recent data on the Au content of the Roman Comagmatic Province (6-7 ppb; Bencini *et al.* 1990) indicates that Au is enriched over mantle values, however segregation of metal-rich vapour would indicate that these are minimum values (eg. Lowenstern *et al.* 1991); and (2) Volcanic flux and global studies - Atmospheric scientists have demonstrated that sulphate particles act as catalysts in ozone destruction. The 1982 El Chichon eruption of SO_4^{2-} particles into the stratosphere led to a global ozone depletion of 6 to 7% (Pitari *et al.* 1991). The role of oxidative-metasomatism of the mantle wedge in the production of sulphate-saturated magmas established in this work, must be parameterized and quantified so that the degree of ozone destruction due to future volcanic eruptions can be modelled.

APPENDIX 1. ANALYTICAL METHODS

Platinum (Pt), palladium (Pd), ruthenium (Ru) and iridium (Ir) were measured by isotope dilution induced coupled plasma mass spectrometry (ICP-MS), whereas rhodium (Rh) and gold (Au) were determined by external calibration ICP-MS. Total PGE contents were determined using an hydrofluoric acid and aqua regia digestion procedure (Gregoire, 1988), but with spike solutions added to solid material at the start of the procedure. Prior to analysis by ICP-MS, Te co-precipitation was used to pre-concentrate and separate analyte from matrix components (Elson and Chatt, 1983). Detection limits using a 5 g sample for Pt, Pd were 0.1 ppb, Ru and Ir were 0.05 ppb, Rh (0.02 ppb) and Au 0.2 ppb. The average of four determinations of USGS standard W-1 by this method, in ppb, are: Pt, 11.5 (13); Pd, 13.1 (14); Ru, 0.17 (0.2); Ir, 0.30 (0.3); Rh, 0.042 (no data); Au, 4.0 (4.3). Data in parentheses are accepted values. Precision was determined to be 13% (Pt), 7% (Pd), 6% (Ru), 7% (Ir), 21% (Rh) and 16% (Au). Copper was determined by ICP-ES following acid (10% HCl) dissolution and fusion of remaining residue. The estimated validity of the Cu analyses are ± 10 ppm + 5% of total concentration. Nickel was determined on fused disks by X-ray fluorescence analysis, with an estimated error of ±50% for analyses between 10 and 30 ppm, and ±10% for values exceeding 30 ppm.

FIGURE CAPTIONS

FIGURE 1: Location map for Tabar-Lihir-Tanga-Feni (TLTF) island arc showing known porphyry-related copper and gold deposits in the region: 1 = Simberi Island (Sorowar, Pigiput, Samat and Botlu Prospects) of the Tabar Island Group; 2 = Ladolam Au-Cu deposit on Lihir Island of the Lihir Island Group; 3 = Ambitle Island (Kabang prospect) of the Feni Island Group; 4 = Panguna Cu-Au deposit; 5 = Wild Dog; 6 = Kulu; 7 = Pleysumi; 8 = Pelapuna; 9 = Arie.

FIGURE 2: Cartoon depicting events occurring after accretion of the oceanic subcontinent Ontong Java Plateau into the Manus-Kilinailau trench approximately 10 Ma. Oblique convergence transitional to strike-slip tectonism created extensional, pull-apart structures which have penetrated subduction-modified (metasomatized) mantle wedge. Slab melts (SCHARM; black) infiltrate mantle wedge peridotite and produce metasomatized mantle regions consisting of carbonate-phlogopite pyroxenite at $P > 30$ kbar and carbonate-amphibole pyroxenite at 21 kbar $< P <$ 30 kbar (Wendlandt and Eggler, 1980; Wallace and Green, 1988). Partial melting of these regions due to extensionally related adiabatic decompression produces alkaline, silica-undersaturated TLTF lavas with high fO_2.

FIGURE 3: Scanning electron microscope back-scatter electron (SEM-BSE) image of alkaline glass melt inclusion in metasomatic sodian diopside (sd). Light coloured areas in the sodian diopside host correspond to the highest Na and Fe^{3+} concentrations (aegirine component). Phenocrysts of anhydrite (an), calcite (cc) and magnetite (mg) are present within lamellae of alkaline aluminosilicate glass. Light areas have leucitic (K) composition and dark areas have analcimic (Na) composition.

FIGURE 4: SEM-BSE images of sulphide occurrences within Simberi xenocrysts and xenoliths.

(a) Cu-Fe sulphide blebs within a titanomagnetite xenocryst. Sulphides are confined to the interior region. SEM energy dispersive x-ray (EDX) spectrum of sulphides and magnetite are shown on Figure 5.

(b) Coarse-grained titanomagnetite megacryst with Cu-Fe sulphide blebs in a matrix of destabilized amphibole pseudomorph. The fine grained light areas in the matrix are titanomagnetite of the pseudomorph assemblage (olivine + augite + titanomagnetite + rhönite + plagioclase).

(c) Enlargement of the Cu-Fe sulphide blebs from (b). Rounding of the original hexagonal sulphides indicates resorption under high fO_2 conditions.

(d) Sulphide inclusions within amphibole from the carbonate-amphibole xenolith. The light gray area at left is magnesiochromite. These unresorbed Cu-Fe-Co-Ni sulphides retain their original euhedral habit and are not rounded compared to those in (c).

FIGURE 5: SEM-EDX spectrum of sulphides (white shading) and titanomagnetite (thick black line) from Figure 4a.

FIGURE 6: Lherzolite-normalized PGE-Au-Cu patterns for Simberi Island lavas subdivided into primary and evolved groups based on mg number ($mg = MgO/MgO + \Sigma FeO_{molar}$). Elements to the right have a greater tendency to partition into sulphide phases (chalcophile) and are liberated during oxidation of mantle sulphides. Elements to the left (siderophile) have low solubility in high fO_2 basaltic melts (Amossé *et al.* 1990) and may be partitioned into early fractionated spinel, as evidenced by the high concentrations of PGE in magnetite separates (Table 2).

FIGURE 7: Temperature-log fO_2 diagram showing experimental buffer curves and experimentally established mineral stability curve (Carroll and Rutherford, 1985, 1987).

(1) Slab melts (SCHARM), which may have a melting temperature as low as 800°C, are sufficiently oxidizing to stabilize anhydrite + magnetite at FMQ + 4.

(2) Low viscosity slab melts infiltrate mantle wedge peridotite (T = 1100°C) at FMQ.

(3) Oxidation reactions during metasomatism of the mantle wedge increases oxygen fugacity from FMQ -> FMQ + 2 - FMQ + 3 (conditions where carbonate + Cu-Fe-Ni sulphide + SO_3^{2-}-bearing apatite stable).

(4) Delayed partial melting of metasomatized mantle wedge during adiabatic decompression causes sulphide destabilization (possibly due to an increase in fO_2 during carbonate dissociation at P < 21 kbar; see text for details) to > FMQ + 3 and allows for saturation of SO_4^{2-} to occur, resulting in hauyne crystallization.

Figure 1.

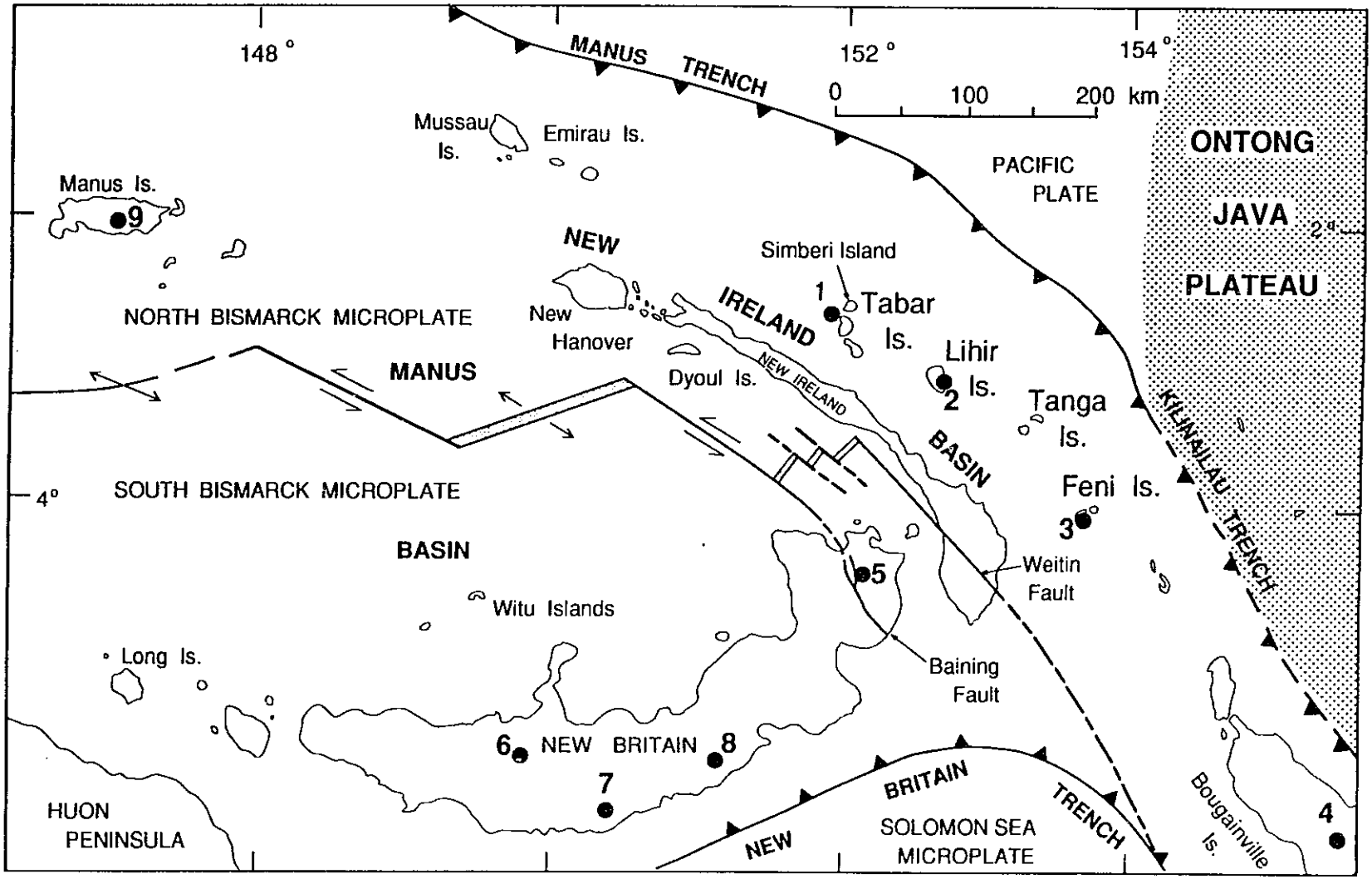
148 °
MANUS TRENCH
152 °
154 °
0
100
200 km
Mussau Is.
Emirau Is.
ONTONG JAVA PLATEAU
PACIFIC PLATE
Manus Is.
9
NEW IRELAND
Simberi Island
1
Tabar Is.
NORTH BISMARCK MICROPLATE
New Hanover
IRELAND
Lihir Is.
2
MANUS
Dyoul Is.
NEW IRELAND
Tanga Is.
KILINAILAU TRENCH
BASIN
4°
SOUTH BISMARCK MICROPLATE
Feni Is.
3
BASIN
5
Weitin Fault
Witu Islands
Long Is.
Baining Fault
6
NEW BRITAIN
8
7
HUON PENINSULA
NEW BRITAIN TRENCH
SOLOMON SEA MICROPLATE
Bougainville Is.
4

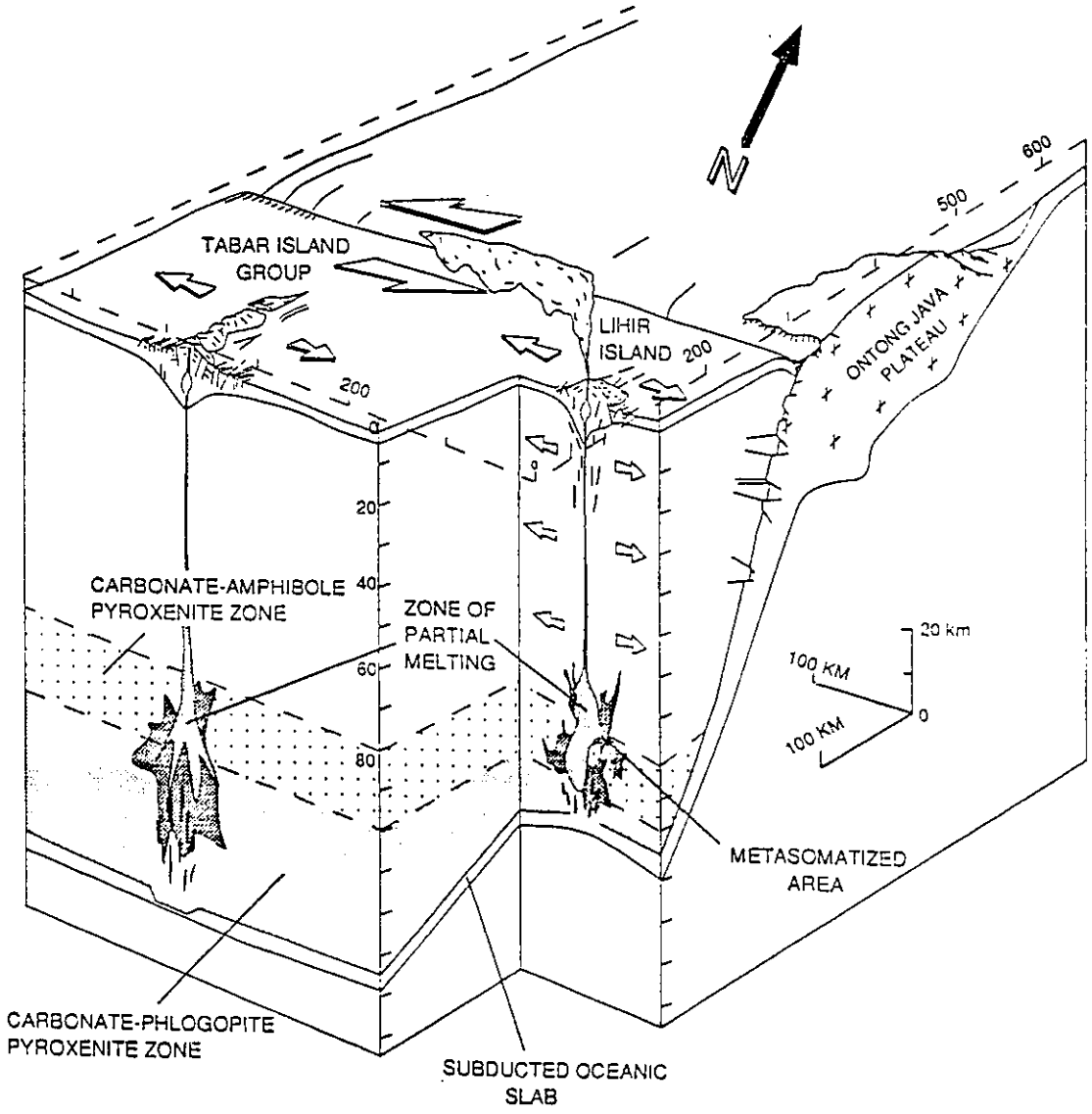
N
TABAR ISLAND GROUP
LIHIR ISLAND
ONTONG JAVA PLATEAU
200
0
20
40
60
80
500
600
CARBONATE-AMPHIBOLE PYROXENITE ZONE
ZONE OF PARTIAL MELTING
20 km
100 KM
100 KM
0
METASOMATIZED AREA
CARBONATE-PHLOGOPITE PYROXENITE ZONE
SUBDUCTED OCEANIC SLAB

Figure 2.

Figure 3.


457X 20KV WD:25MM S:00022 P:00012
100UM
sd
an
cc
Na
mg

Figure 4.

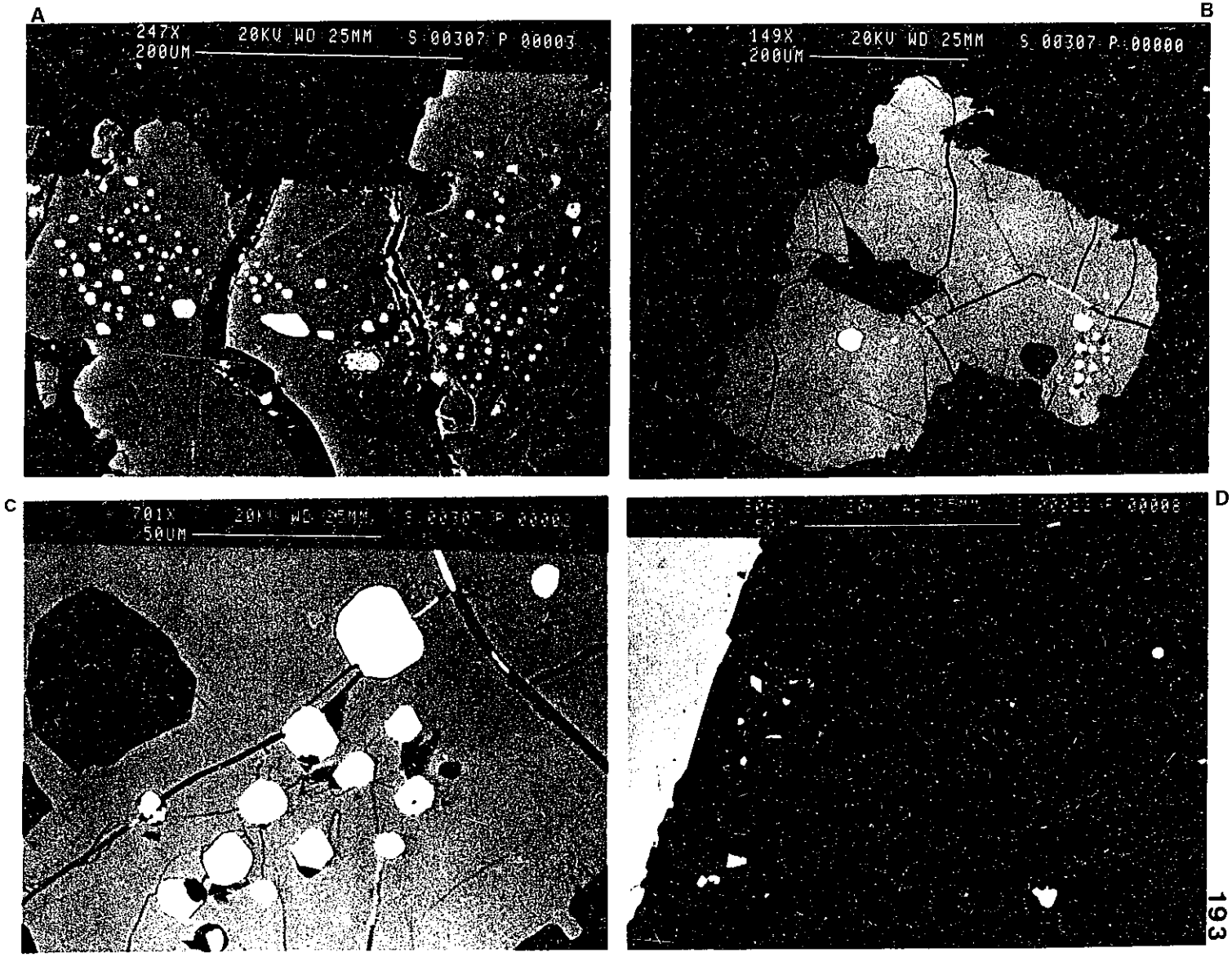
A
247X 20KV WD 25MM S 00307 P 00003
200UM
B
149X 20KV WD 25MM S 00307 P 00000
200UM
C
701X
50UM
D

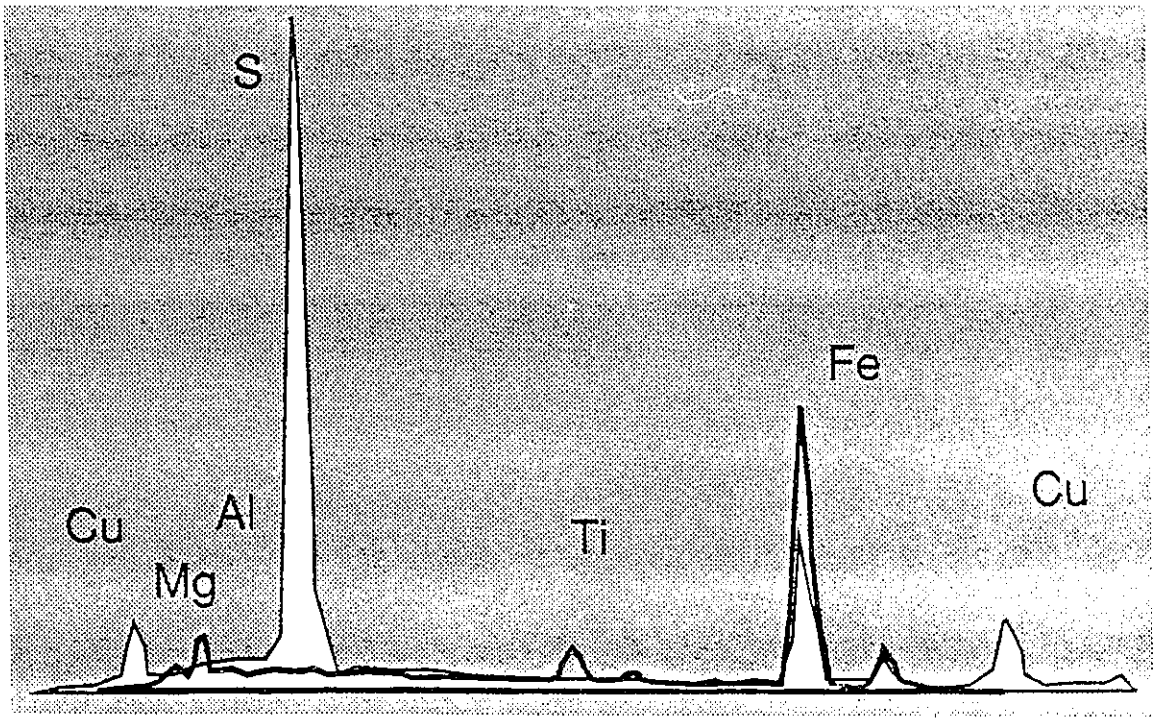

Figure 5.

Figure 6.

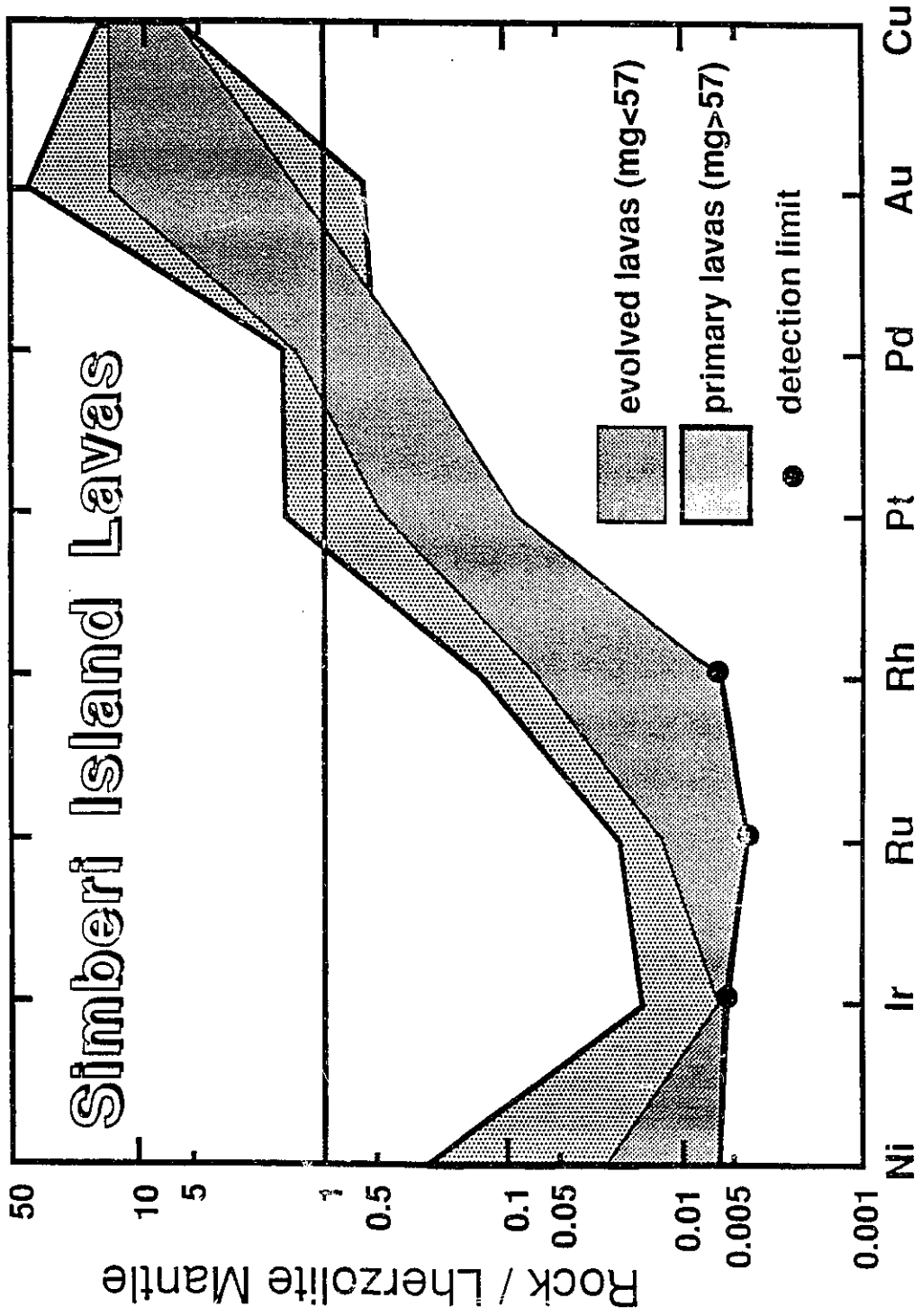
Simberi Island Lavas
Rock / Lherzolite Mantle
50
10
5
1
0.5
0.1
0.05
0.01
0.005
0.001
Ni
Ir
Ru
Rh
Pt
Pd
Au
Cu
evolved lavas (mg<57)
primary lavas (mg>57)
detection limit

Figure 7.

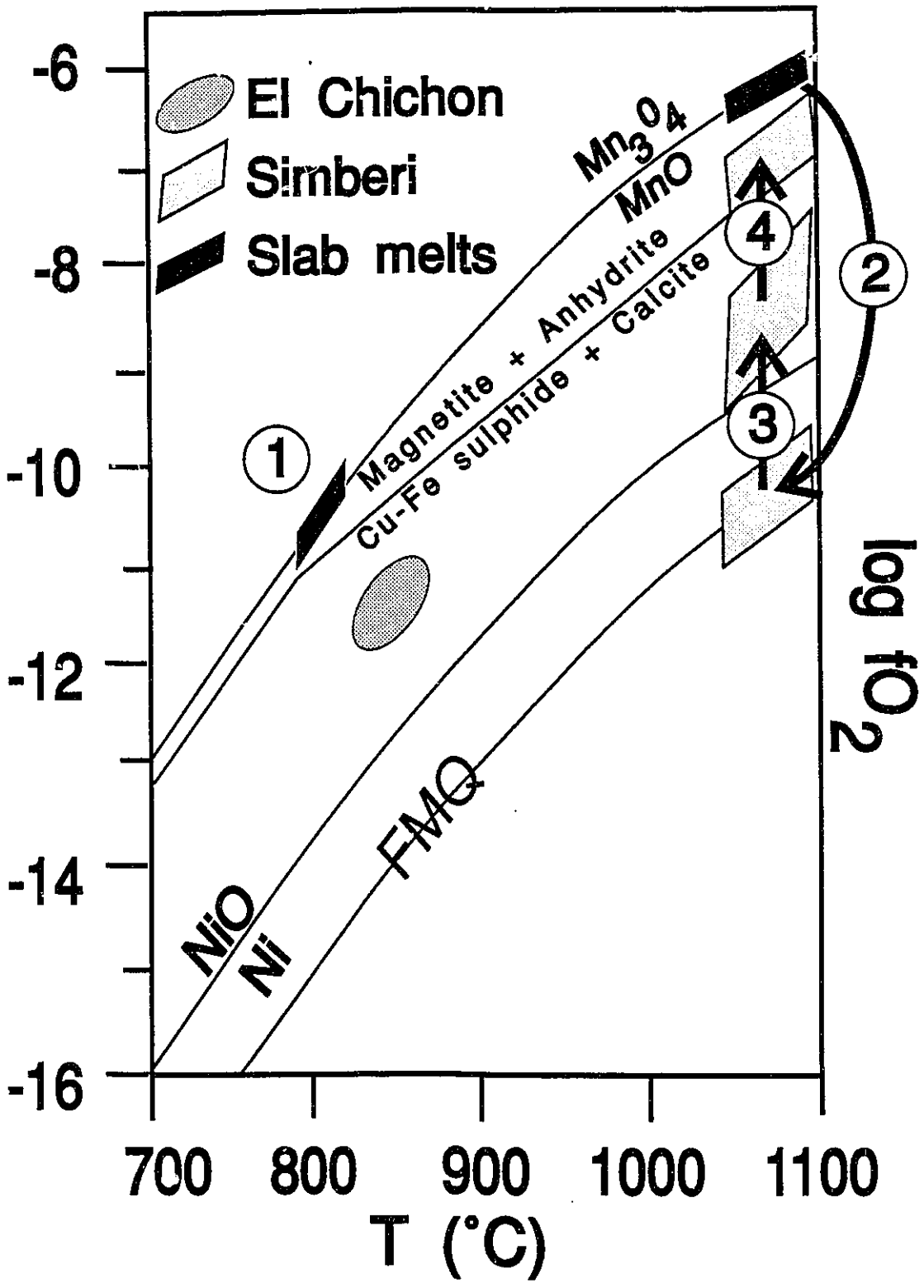
El Chichon
Simberi
Slab melts
Mn_3O_4
MnO
Magnetite + Anhydrite
Cu-Fe sulphide + Calcite
NiO
Ni
FMQ
1
2
3
4
-6
-8
-10
-12
-14
-16
700
800
900
1000
1100
T (°C)
log fO_2

Table 1. Geochemical Data for Simberi Island Lavas

n	Element	Range	Mean (1σ)	Median	Mantle Abundance*
32	Ni (ppm)	13-450	110 (140)	27	2000[2]
15	Ir (ppb)	<0.05-0.07	---	---	3.6[1]
15	Ru (ppb)	<0.05-0.13	---	---	5.6[2]
15	Rh (ppb)	<0.02-0.20	---	---	1.6[2]
15	Pt (ppb)	0.7-32.9	5.4 (8)	2.9	8.3[2]
15	Pd (ppb)	1.6-6.7	3.8 (1.7)	3.7	4.0[1]
32	Au (ppb)	0.1-24.4	5.9 (6.5)	5	0.6[1]
32	Cu (ppm)	65-170	106 (30)	110	10[1]

--- values below the limit of detection; 1σ=standard deviation

*References: 1, Mitchell and Keays (1981) and references therein, spinel lherzolite mantle; 2, Barnes et al. (1988) and references therein, primitive mantle lherzolite

Table 2. Geochemical data (ppb) for magnetite separates

Sample	Pt	Pd	Ru	Ir	Rh	Au
310	8.5	8.8	3.1	1.4	<0.5	nd
311	105	59	17.4	7.2	<0.5	nd
312	17.4	24.4	7.6	4.7	<0.5	nd
nd: no data due to sample preparation problems which precluded accurate determination of Au						

CONCLUSIONS

The results of this research can be summarized as follows:

1. Tectonic setting

Volcanism on Simberi Island (and in the Tabar-Lihir-Tanga-Feni arc) occurred in a transtensional tectonic regime, and coincided with the initiation of backarc spreading in the Manus basin at approximately 3.5 Ma. Transposition of the island of New Britain to the southeast caused "localized" perturbation of the lithosphere in the New Ireland and TLTF region, and resulted in the propagation of volcanism from the Tabar to Feni Island Groups.

2. Magma series

Volcanic rocks on Simberi Island include basanites, alkali olivine basalts, trachybasalts and trachyandesites. These rocks are silica-undersaturated, yet can best be described as belonging to the high-K calc-alkaline magma series. These magmas formed as a result of partial melting by adiabatic decompression of subduction-modified asthenospheric mantle following lithosphere extension. Production of silica-undersaturated magmas may be related to the presence of carbonate (as a source for CO_2) in the mantle wedge. The high Fe_2O_3/FeO ratio of 1 and the presence of a sulphate-bearing feldspathoidal mineral (haüyne) in Tabar-Lihir-Tanga-Feni lavas indicates that the mantle source region is oxidized.

3. Age dating

K-Ar and Ar-Ar methods have been used to determine the volcanic history of

Simberi Island. Alkali olivine basalts range in age from 3.6 to 3.1 Ma, whereas trachybasalts and trachyandesites appear to be younger, ranging from 3.1 to 2.3 Ma. Gold deposits are spatially and temporally associated with the stabilization and crystallization of trachyandesite domes. Extremely high $^{40}Ar/^{36}Ar$ ratios are recorded in mantle xenocrysts from a basanite intrusion. This "excess argon" is possibly hosted in melt inclusions containing phonolitic glass, anhydrite and calcite.

4. Melt inclusions

Hosted within xenocrysts of sodian diopside and forsteritic olivine are alkali-rich aluminosilicate glasses which contain daughter minerals of calcite, anhydrite, sodalite and fluorapatite. These glasses are the quenched equivalents of a sulphate-, carbonate-, H_2O-, alkali-rich aluminosilicate magma (SCHARM). SCHARM is not in equilibrium with mantle assemblages, and therefore acts as a metasomatic agent, reacting with mantle olivine to produce titanian phlogopite and titanomagnetite at $P > 30$ kbar. SCHARM is highly oxidized ($fO_2 \approx FMQ + 4$), and contains substantial dissolved F, Cl, Sr and Ba.

5. Mantle nodule

Between 21 and 30 kbars amphibole is formed rather than phlogopite, as evidenced by the discovery of a calcite-magnesiochromite-aluminous diopside-amphibole nodule discovered in a trachybasalt dyke near the South Samat diatreme complex. $\delta^{18}O$ and $\delta^{13}C$ ratios of the calcite are not consistent with "mantle values" and are similar to calcite veins within seawater altered basalts. $^{87}Sr/^{86}Sr$ values of the calcite are similar to the host trachybasalt and preclude surficial contamination by

reef material. The high $\delta^{18}O$ values of the calcite may be primary feature of carbonated silicate melts derived during the melting of seawater-altered basalt under high pressure and temperature conditions. This requires that carbonate and silicate ions do not readily exchange oxygen, an hypothesis which must be tested by experimentation.

6. Trace and rare earth elements

Simberi volcanic rocks are enriched in large ion lithophile (Sr, Ba, K) and depleted in high field strength elements (Ti, Ta, Nb), similar to other high-K calc-alkaline volcanic rocks. Chondrite-normalized rare earth element plots show a minor negative Ce and a strong positive Eu anomaly, combined with an overall depletion in the heavy rare earth elements. The trace and rare earth element data are evidence that SCHARM is derived during the melting of a feldspathic phase in subducted, seawater-altered oceanic basalt at the *basalt-eclogite transition* in the mantle.

7. Oxidation of the mantle wedge and Au-Cu metallogenesis

The Tabar-Lihir-Tanga-Feni island arc contains numerous volcanic-hosted gold deposits, including the world class Ladolam deposit on Lihir Island. The presence of sulphate and carbonate in melt inclusions indicates that slab melts derived from seawater-altered basalt have a high intrinsic oxygen fugacity ($fO_2 \approx FMQ+4$). These high fO_2 melts are in disequilibrium with mantle sulphide assemblages and cause them to be destabilized, liberating the chalcophile elements Cu and Au. Subsequent partial melting of mantle regions which have undergone oxidative

metasomatism may allow Au and Cu to be transported to crustal regions by halogen-rich magmas, where they release high temperature, metalliferous, volatile-rich fluids. These fluids may be discharged directly into the atmosphere during volcanic activity or, react with an overlying water column causing the deposition of metals in porphyry Cu-Au systems at high temperature and auriferous magmatic-hydrothermal acid-sulphate systems at lower temperature ($<400°C$), which are the predominant ore deposit-types found in volcano-plutonic arc complexes.

REFERENCES

Allègre, C.J., Treuil, M., Minster, J.H.F., Minster, B. and Albarède, F. 1977. Systematic use of trace elements in igneous process. *Contrib. Mineral. Petrol.* 60, 57-75.

Allègre, C.J., Staudacher, T., Sarda, P., and Kurz, M. 1983. Constraints on evolution of Earth's mantle from rare gas systematics. *Nature* 303, 762-766.

Albarède, F. and Michard, A. 1986. Transfer of continental Mg, S, O and U to the mantle through hydrothermal alteration of the oceanic crust. *Chem. Geology* 57, 1-15.

Amossé, J., Allibert, M., Fischer, W., and Piboule, M. 1990. Experimental study of the solubility of platinum and iridium in basic silicate melts-implications for the differentiation of platinum-group elements during magmatic processes. *Chem. Geology* 81, 45-53.

Amundsen, H.E.F. 1987. Evidence for liquid immiscibility in the upper mantle. *Nature* 327, 692-695.

Andersen, T., Griffin, W., and O'Reilly, S. 1987. Primary sulphide melt inclusions in mantle-derived megacrysts and pyroxenites. *Lithos* 20, 279-295.

Andersen, T., O'Reilly., S. and Griffin, W. 1984. The trapped fluid phase in upper mantle xenoliths from Victoria, Australia: implications for upper mantle metasomatism. *Contrib. Mineral. Petrol.* 88, 72-85.

Anderson, R.N., Delong, S.E. and Schwarz, W.M. 1980. Dehydration, asthenospheric convection and seismicity in subduction zones. *J. Geol.* 88, 445-451.

Aoki, K. and Shiba, I. 1973. Pyroxenes from lherzolite inclusions of Itinome-gata, Japan. *Lithos* 6, 41-51.

Arculus, R.J., Johnson, R.W. and Perfit, M.R. 1978. Alkaline volcanic rocks from the Tabar-to-Feni Islands, Papua New Guinea: oceanic or island-arc magmas?: Abstracts of the International Geodynamics Conference, Tokyo, 1978, 200-201.

Arculus, R.J. and Johnson, R.W. 1981. Island-arc magmas sources: a geochemical assessment of the roles of slab-derived components and crustal contamination. *Geochem. J.* 15, 109-133.

Arculus, R.J., Johnson, R.W., Chappell, B.W., McKee, C.O., and Sakai, H. 1983. Ophiolite-contaminated andesites, trachybasalts, and cognate inclusions of Mount Lamington, Papua New Guinea: anhydrite-amphibole-bearing lavas and the 1951 cumulodome. *Jour. Volcanol. Geotherm. Res.* 18, no. 1/4, 215-248.

Arima, M. and Edgar, A.D. 1981. Substitution mechanism and solubility of titanium in phlogopites from rocks of probable mantle origin. *Contrib. Mineral. Petrol.* 77, 288-295.

Arima, M. and Kerrich, R. 1988. Jurassic kimberlites from Picton and Varty Lake, Ontario: Geochemical and stable isotpic characteristics. *Contrib. Mineral. Petrol.* 99, 385-

391.

Armstrong, R.L. 1981. Radiogenic isotopes: the case for crustal recycling on a near steady state in continental growth. *Phil. Trans. R. Soc. London*, Ser. A 301, 443-472.

Babkine, J., Conquéré, F. and Vilmonot, J.C. 1968. Les caractères particuliers du volcanisme au nord de Montpellier; l'absarokite du Pouget; la ferrisalite sodique de Grabels. *Bull. Soc. Fr. Mineral. Cristallogr.* 91, 141-150.

Bailey, D.K. 1989. Carbonate melt from the mantle in the volcanoes of south-east Zambia. *Nature* 338, p. 415-418.

Bailey, D.K. 1987. Mantle metasomatism-perspective and prospect *in* Fitton, J.G. and Upton, B.G.J. (eds.) *Alkaline Igneous Rocks*, Geological Society Special Publication No. 30, pp. 1-13.

Baker, M.B. and Wyllie, P.J. 1990. Liquid immiscibility in a nephelinite-carbonate system at 25 kbar and implications for carbonatite origin. *Nature* 346, 168-170.

Ballhaus, C., Berry, R.F., and Green D.H. 1990. Oxygen fugacity controls in the Earth's upper mantle. *Nature* 348, 437-440.

Barnes, S-J., Boyd, R., Korneliussen, A., Nilsson, L-P., Often, M., Pederson, R.B., and Robins, B. 1988. The use of mantle normalization and metal ratios in discriminating between the effects of partial melting, crystal fractionation and sulphide segregation on platinum-group elements, gold, nickel and copper: examples from Norway, *in* Prichard, H.M., Potts, P.J., Bowles, J.F.W., and Cribb, S. (eds.). *Geo-platinum 87*, Elsevier, Barking, pp. 113-143.

Basaltic Volcanism Study Project 1981. *Basaltic volcanism on the terrestrial planets*. Pergamon Press, New York, 1286 pp.

Beakhouse, G.P. and Heaman, L.M. 1980. The chemical separation of Rb and Sr for mass spectrometric analysis. McMaster Univ. Tech. Memo 80-6.

Bédard, J., Francis, D.M. and Ludden, J. 1988. Petrology and pyroxene chemistry of Monteregian dykes: the origin of concentric zoning and green cores in clinopyroxenes from alkali basalts and lamprophyres. *Can. J. Earth Sci.* 25, 2041-2058.

Bencini, A., Ciurli, C., Tanelli, G. and Verrucchi, C. 1990. Distribution of gold in some magmatic rocks from Central Italy. *Mineralium Deposita* 25, 582-585.

Berg, G.W. 1986. Evidence for carbonate in the mantle. *Nature* 324, p. 50-51.

Berger, G.W., and York, D. 1981. Geothermometry from $^{40}Ar/^{39}Ar$ dating experiments. *Geochim. Cosmochim. Acta* 45, 795-811.

Blake, D.H. and Miezitis, Y. 1967. Geology of Bougainville and Buka Island, New Guinea. *Bull. Bur. Mineral. Resour. Geol. Geophys. Aust.*, 93 p.

Bogoch, R., Magaritz, M., and Michard, A. 1986. Dolomite of possible mantle origin, southeast Sinai. *Chem. Geol.* 56, p. 281-288.

Boyd, F.R., and Gurney, J.J. 1982. Low calcium garnets: Keys to craton structure and diamond crystallization: *Carnegie Institution of Washington Year Book*, v. 81, 261-266.

Brey, G.P., and Green, D.H. 1975. The role of CO_2 in the genesis of olivine melilitite: *Contrib. Mineral. Petrol.* 49, 93-103.

Brooker, R.A. and Hamilton, D.L. 1990. Three-liquid immiscibility and the origin of carbonatites. *Nature* 346, 459-462.

Brooks, C.K. and Prinzlau, I. 1978. Magma mixing in mafic alkaline volcanic rocks: the evidence from relict phenocryst phases and other inclusions. *J. Volcanol. Geotherm. Res.* 4, 315-331.

Brown, C.M. 1982. Kavieng, Papua New Guinea-1:250,000 Geological Series. Geological Survey of Papua New Guinea Explanatory Notes, SA/56-9.

Buat-Menard, P. and Arnold, M. 1978. The heavy metal chemistry of atmospheric particulate matter emitted by Mount Etna Volcano. *Geophys. Res. Letters* 5, 245-248.

Bulanova, G.P. 1986. Compositional evolution of syngenetic inclusions of ultrabasic association in Yakution diamond: *Geological Society of Australia Abstract Series*, v. 1G, p. 371-373.

Burnham, C.W., 1979, Magmas and Hydrothermal Fluids, *in* H.L. Barnes, ed., *Geochemistry of Hydrothermal Ore Deposits*: John Wiley and Sons, New York, p. 76-136.

Cameron, K.L., Carman, M.F., and Butler, J.C. 1970. Rhönite from Big Bend National Park, Texas. *Am. Mineral.* 55, 864-874.

Canil, D. 1990. Experimental study bearing on the absence of carbonate in mantle-derived xenoliths. *Geology* 18, p. 1011-1013.

Carroll, M.R., and Rutherford, M.J., 1987, The stability of igneous anhydrite: Experimental results and implications for sulfur behavior in the 1982 El Chichon trachyandesite and other evolved magmas. *J. Petrol.* 28, p. 781-801.

Carroll, M.R., and Rutherford, M.J. 1985. Sulfide and sulfate saturation in hydrous silicate melts: Proc. 15th Lunar Planet. Sci. Conf., *J. geophys. Res.* 90, C601-612.

Carroll, M.R. and Stolper, E.M. 1991. Argon solubility and diffusion in silica glass: Implications for the solution behavior of molecular gases. *Geochim. Cosmochim. Acta*, 55, 211-225.

Cavarretta, G., and Lombardi, G. 1990. Origin of sulphur in the Quarternary perpotassic melts of Italy: Evidence from hauyne sulphur isotope data. *Chemical Geology* 82, 15-20.

Cawthorn, R.G., and O'Hara, M.J. 1976. Amphibole fractionation in calcalkaline magma genesis. *Am. J. Sci.* 276, 309-329.

Chase, C.G. 1981. Ocean island Pb: two-stage histories and mantle evolution. *Earth Planet. Sci. Lett.* 52, 277-284.

Chayes, F. 1963. Relative abundance of intermediate members of the oceanic basalt-trachyte association. *J. geophys. Res.* 68(5), 1519-34.

Chayes, F. 1977. The oceanic basalt-trachyte relation in general and in the Canary Islands. *Am. Mineral.* 62, 666-71.

Clayton, R.N. and Mayeda, T.K. 1963. The use of bromine pentafluoride in the extraction of oxygen from oxides and silicates for isotopic analysis. *Geochim. Cosmochim. Acta* 72, 43-52.

Clemens, J.D. and Wall, V.J. 1981. Origin and crystallization of some peraluminous (S-Type) granitic magmas. *Can. Mineral.* 19, 111-131.

Cocker, J.D., Griffin, B.J. and Muehlenbachs, K. 1982. Oxygen and carbon isotope evidence for sea-water-hydrothermal alteration of the Macquarie Island ophiolite. *Earth Planet. Sci. Lett.* 61, 112-122.

Cole, D.R., and Ohmoto, H. 1986. Kinetics of isotopic exchange at elevated temperatures and pressures, in Valley, J.W., Taylor, H.P., Jr., O'Neill, J.R. (eds), *Stable Isotopes in High Temperature Geological Processes*, Reviews in Mineralogy, v. 16, 41-90.

Coleman, P.J. and Packham, G.H. 1976. The Melanesian borderlands and India-Pacific plates' boundary. *Earth Science Reviews* 12, 197-233.

Coleman, P.J. and Kroenke, L.W. 1981. Subduction without volcanism in the Solomon Islands arc. *Geo-marine Letters* 1, no. 2, 129-134.

Connelly, J.B. 1976. Tectonic development of the Bismarck Sea based on gravity and magnetic modelling. *Geophys. J.R. Astron. Soc.* 47, 23-40.

Conway, C.M. and Taylor, H.P. 1969. $^{18}O/^{16}O$ and $^{13}C/^{12}C$ ratios of coexisting minerals in the Oka and Magnet Cove carbonatite bodies. *J. Geology* 77, 616-626.

Cooper, P. and Taylor, B. 1987. Seismotectonics of New Guinea: A model for arc reversal following arc-continent collision. *Tectonics* 6, no. 1, 53-67.

Corfu, F. and Andrews, A.J., 1987. Geochronological constraints on the timing of magmatism, deformation and gold mineralization in the Red Lake greenstone belt, northwestern Ontario. *Can. J. Earth Sci.* 24, 1302-1320.

Curtis, J.W. 1973. Plate tectonics of the Papua New Guinea-Solomon Islands region. *Geological Society of Australia-Journal* 20, 1-19.

D'Addario, G.W., Dow, D.B., and Swoboda, R. 1976. Geology of Papua New Guinea, 1:2,500,000 scale geological map. Bureau of Mineral Resources, Canberra.

Daly, R.A. 1925. The geology of Ascension Island. *Proc. Am. Acad. Arts Sci.* 60, 1-80.

Daly, R.A. 1927. The geology of St. Helena Island. *Proc. Am. Acad. Arts Sci.* 62, 31-92.

Dasch, E.J. 1969. Strontium isotopes in weathering profiles, deep-sea sediments, and sedimentary rocks. *Geochim. Cosmochim. Acta* 33, 1521-1552.

Dasch, E.J., Hedge, C.E. and Dymond, J. 1973. Effect of sea water interaction on strontium isotope composition of deep-sea basalts. *Earth Planet. Sci. Lett.* 19, 177-183.

Davidson, J.P. 1987. Crustal contamination versus subduction zone enrichment: examples from the Lesser Antilles and implications for mantle source compositions of island arc volcanic rocks. *Geochim. Cosmochim. Acta* 51, 2185-2198.

Davies, R.M. and Ballantyne, G.H. 1987, Geology of the Ladolam Gold Deposit, Lihir Island, Papua New Guinea. *In* Pacific Rim Congress '87, p. 943-949. Australas. Inst. Min. Metall., Parkville.

Davies, H.L. and Smith, I.E. 1971. Geology of eastern Papua. *Geol. Soc. America-Bulletin* 82, 3299-3312.

Davies, H.L., and Jaques, A.L. 1984. Emplacement of ophiolite in Papua New Guinea, *Spec. Publ. Geol. Soc. London* 13, 341-349.

Davies, H.L. and Price, R.C. 1987. Basalts from the Solomon and Bismarck Seas. *Geo-Marine Letters*, 6: 193-202.

Dawson, J.B. 1980. *Kimberlites and their xenoliths*. 252 pp., Springer-Verlag, Berlin.

Deer, W.A., Howie, R.A. and Zussman, J., 1966. An introduction to the rock-forming minerals. Longman Group Ltd., London, 528 pp.

Deines, P. 1970. The carbon and oxygen isotopic compositio of carbonates from the Oka carbonatite, Quebec, Canada. *Geochim. Cosmochim. Acta* 34, 1199-1225.

Deines, P. and Gold, D.P. 1973. The isotopic composition of carbonatites and kimberlite carbonates and their bearing on the isotopic composition of deep-seated carbon. *Geochim. Cosmochim. Acta* 37, 1709-1733.

Deines, P. 1989. Stable isotope variations in carbonatites, in Bell, K. (ed.), *Carbonatites: Genesis and Evolution,* Unwin Hyman, 301-359.

Denham, D. 1973. Seismicity, focal mechanisms and the boundaries of the Indian-Australian plate, in *The Western Pacific: Island Arcs, Marginal seas, Geochemistry,* edited by Coleman PJ, pp. 35-53, University of Western Australia Press, Perth.

Devine, J.D., Sigurdsson, H., and Davis, A.N. 1984. Estimates of sulfur and chlorine yield to the atmosphere from volcanic eruptions and potential climatic effects. *J. Geophys. Res.* 89, 6309-6325.

DePaolo, D.J. and Wasserburg, G.J. 1977. The sources of island arcs as indicated by Nd and Sr isotopic studies. *Geophys. Res. Lett.* 4, 465-468.

Dixon, T.H. and Batiza, R. 1979. Petrology and chemistry of recent lavas in the northern Marianas: Implications for the origin of island arc basalts. *Contrib. Mineral. Petrol.* 70, 167-181.

Duda, A., Schmincke, H.U. 1985. Polybaric differentiation of alkali basaltic magmas: evidence from green-core clinopyroxenes (Eifel FRG). *Contrib. Mineral. Petrol.* 91, 340-353.

Dunkley, P.N. 1983. Volcanism and the evolution of the ensimatic Solomon Islands arc. in Shimozuru, D. and Yokoyama, I. (eds.), *Arc Volcanism: Physics and Tectonics*, Terra Sci. Pub. Co., Tokyo, 225-241.

Eastoe, C.J. 1978. A fluid inclusion study of the Panguna porphyry copper deposit, Bougainville, Papua New Guinea. *Econ. Geol.* 73, 721-748.

Eby, G.N. 1975. Abundance and distribution of the rare-earth elements and yttrium in the rocks of the Oka carbonatite complex, Quebec. *Geochim. Cosmochim. Acta* 39, 597-620.

Eby, G.N. 1980. Minor and trace element partitioning between immiscible ocelli-matrix pairs from lamprophyre dykes and sills, Monteregian Hills petrographic province, Quebec. *Contrib. Mineral. Petrol.* 75, 269-278.

Edgar, A.D. 1987. The genesis of alkaline magmas with emphasis on their source regions: inferences from experimental studies *in* Fitton, J.G. and Upton, B.G.J. (eds.) *Alkaline Igneous Rocks*, Geological Society Special Publication No. 30, pp. 1-13.

Eggler, D.H. 1974. Effects of CO_2 on the melting of peridotite. *Yearb. Carnegie Inst. Washington* 73, 215-224.

Eggler, D.H. 1978. The effect of CO_2 upon partial melting of peridotite in the system Na_2O-CaO-Al_2O_3-MgO-H_2O-CO_2 to 35 kb, with an analysis of melting in a peridotite-H_2O-CO_2 system. *Amer. J. Sci.* 278, 305-343.

Eggler, DH, 1978. Stability of dolomite in a hydrous mantle, with implications for the mantle solidus. *Geology* 6: 397-400.

Eggler, D.H. 1987. Discussion of recent papers on carbonated peridotite, bearing on mantle metasomatism and magmatism: an alternative. *Earth Planet. Sci. Lett.* 82, 398-400.

Eggler, D.H. 1989. Kimberlites: How do they form?, in Ross, J., ed., *Kimberlites and related rocks.* Volume 1: Geological Society of Australia Special Publication 14, 489-504.

Eggler, D.H. and Rosenhauer, M. 1978. Carbon dioxide in silicate melts. 2. Solubilities of CO_2 and H_2O in $CaMgSi_2O_6$ (diopside) liquids and vapors at pressures to 40 Kb. *Am. J. Sci.* 278, 64-94.

Elderfield, H., Hawkesworth, C.J., Greaves, M.J. and Calvert, S.E. 1981. Rare earth

element geochemistry of oceanic ferro-manganese nodules and associated sediments. *Geochim. Cosmochim. Acta* 45, 513-528.

Elderfield, H. and Greaves, M.J. 1982. The rare earth elements in seawater. *Nature* 296, 214-219.

Elson, C.M., and Chatt, A. 1983. Determination of gold in silicate rocks and ores by coprecipitation with tellurium and neutron activation spectrometry: *Anal. Chim. Acta* 155, 305-310.

Exon, N.F., Stewart, W.D., Sandy, M.J., and Tiffin, D.L. 1986. Geology and offshore petroleum prospects of the eastern New Ireland Basin, northeastern Papua New Guinea. *BMR Jour. of Australian Geol. Geophys.* 10, 39-51.

Fabriès, J., Bodinier, J-L., Dupuy, C., Lorand, J-P., and Benkerrou, C. 1989. Evidence for modal metasomatism in the orogenic spinel lherzolite body from Caussou (Northeastern Pyrenees, France). *J. Petrol.* 30, 199-228.

Falloon, T.J. and Green, D.H. 1990. Solidus of carbonated fertile peridotite under fluid-saturated conditions. *Geology* 18, 195-199.

Faure, G. 1986. *Principles of Isotope Geology*, 2nd Edition. John Wiley and Sons, New York.

Fine, G., and Stolper, E. 1985. The speciation of carbon dioxide in sodium aluminosilicate glasses. *Contr. Miner. Petrol.* 91, 105-121.

Finlayson, D.M. and Cull, J.P. 1973. Structural profiles in the New Britain-New Ireland region. *J. geol. Soc. Aust.* 20, 37-48.

Fisher, D.E. 1981. Quantitative retention of argon in a glassy basalt. *Nature* 290, 42-43.

Fisher, R.U. and Schmincke, H.-U. 1984. Pyroclastic Rocks, Springer-Verlag, New York.

Foden, J.D. 1983. The petrology of the calc-alkaline lavas of Rindjani volcano, East Sunda arc: a model for island arc petrogenesis. *J. Petrol.* 24, 98-130.

Foley, S.F. 1989. Experimental constraints on phlogopite chemistry in lamproites. 1. The effect of water activity and oxygen fugacity. *European Journal of Mineralogy* 1, 411-426.

Francis, D.M. 1976. The origin of amphibole in lherzolite xenoliths from Nunivak Island, Alaska. *J. Petrol.* 17, 357-378.

Francis, G. 1988. Stratigraphy of Manus Island, western New Ireland Basin, Papua New Guinea, in Marlow, M.S., Dadisman, S.V., and Exon, N.F., (eds.), *Geology and offshore resources of Pacific island arcs-New Ireland and Manus region, Papua New Guinea*, Circum-Pacific Council for Energy and Mineral Resources Earth Science Series, v. 9: Houston, Texas, Circum-Pacific Council for Energy and Mineral Resources, 31-40.

Fraser, D.G., Rammensee, W. and Hones, R. 1983) The mixing properties of melts in the system $NaAlSi_2O_6$-$KAlSi_2O_6$ determined by Knudsen Cell Mass Spectrometry. *Bull. Mineral.* 106, 111-117.

Freer, R. and Dennis, P.F. 1982. Oxygen diffusion studies. I. A preliminary ion microprobe investigation of oxygen diffusion in some rock-forming minerals. *Mineral. Mag.* 45, 179-192.

Frey, F.A. and Green, D.H. 1974. The mineralogy and origin of lherzolite inclusions in Victorian basanites. *Geochim. Cosmochim. Acta* 38, 1023-1059.

Friedman, I., and O'Neil, J.R. 1977. Compilation of stable isotope fractionation factors of geochemical interest., in *Data of Geochemistry*, 6th Ed. M. Fleischer, ed., U.S. Gov. Printing Office, Washington, D.C.

Friedman, I. and Long, W. 1984. Volcanic glasses, their origins and alteration processes. *Journal of Non-Crystalline Solids* 67, 127-133.

Fudali, R.F. 1963. Experimental studies bearing on the origin of pseudoleucite and associated problems of alkalic rock genesis. *Bull. Geol. Soc. Am.* 74, 1101-1126.

Furomoto, A.S., Webb, J.P., Odegard, M.E. and Hussong, D.M. 1976. Seismic studies on the Ontong Java Plateau, 1970. *Tectonophysics* 34, 71-90.

Garlick, G.D., MacGregor, I.D. and Vogel, D.E. 1971. Oxygen isotope ratios in eclogites from kimberlites. *Science* 172, 1025-1027.

Gemmel, J.B. 1987. Geochemistry of metallic trace elements in fumarolic condensates from Nicaraguan and Costa Rican volcanoes. *Journal of Volcanol. Geotherm. Res.* 33, 161-181.

Gianetti, B. and Luhr, J.F. 1990. Phlogopite-clinopyroxenite nodules from high-K magmas, Roccamonfina Volcano, Italy: evidence for a low-pressure metasomatic origin. *Earth Planet. Sci. Lett.* 101, 404-424.

Gill, J.B. 1970. Geochemistry of Viti Levu, Fiji, and its evolution as an island arc. *Contrib. Mineral. Petrol.* 27, 179-201.

Glaessner, R. 1915. Beitrage zur Kenntnis der Eruptivgesteine des Bismarck-Archipelo und der Salomon Inseln. *Beitrage Geologische Entforschung Deutchen Schutzgebiete* 10, 1-85.

Goldsmith, J.R. 1976. Scapolites, granulites, and volatiles in the lower crust. *Bull. Geol. Soc. Am.* 87, 161-168.

Goldsmith, J.R. and Newton, R.C. 1977. Scapolite-plagioclase stability relations at high pressures and temperatures in the system $NaAlSi_3O_8$-$CaAl_2Si_2O_8$-$CaCO_3$-$CaSO_4$. *Am. Mineral.* 62, 1063-1081.

Green, D.H. 1973. Experimental melting studies on a model upper mantle composition at high pressure under water-saturated and water-undersaturated conditions. *Earth*

Planet. Sci. Lett. 19, 37-53.

Green, D.H. and Wallace, M.E. 1988. Mantle metasomatism by ephemeral carbonatite melts. *Nature* 336, 459-462.

Green, T.H. and Ringwood, A.E. 1972. Crystallization of garnet-bearing rhyodacite under high pressure hydrous conditions. *J. Geol. Soc. Aust.* 19, 203-212.

Green, T.H. and Pearson, N.J. 1986. Ti-rich accessory phase saturation in hydrous mafic-felsic compositions at high P, T. *Chem Geol* 54, 185-201.

Green, T.H. and Pearson, N.J. 1987. An experimental study of Nb and Ta partitioning between Ti-rich minrals and silicate liquids at high pressure and temperature. *Geochim. Cosmochim. Acta* 51, 55-62.

Green, T.H., and Watson, E.B. 1982. Crystallization of apatite in natural magmas under high pressure, hydrous conditions, with particular reference to 'orogenic' rock series. *Contrib. Mineral. Petrol.* 79, 96-105.

Gregoire, D.C., 1988, Determination of platinum, palladium and iridium in geological materials by inductively coupled plasma mass spectrometry with sample introduction by electrothermal vaporization, *J. Anal. At. Spectrocs.* 3, 309-314.

Gregory, R.T. and Taylor, H.P., Jr. 1981. An oxygen isotope profile in a section of Cretaceous oceanic crust, Samail ophiolite, Oman: Evidence for $\delta^{18}O$ buffering of the oceans by deep (>5 km) seawater-hydrothermal circulation at mid-ocean ridges. *J. Geophys. Res.* 86, 2737-2755.

Gulf Research and Development. 1973. Regional marine geophysical reconnaissance of Papua New Guinea. Gulf Research and Development Company and Australian Gulf Oil Company, Sydney.

Hamilton, W. 1979. Tectonics of the Indonesian region. *USGS - Professional Paper*, 1078.

Hamlyn, P.R., Keays, R.R., Cameron, W.E., Crawford, A.J., and Waldron, H.M. 1985. Precious metals in magnesian low-Ti lavas: Implications for metallogenesis and sulfur saturation in primary magmas. *Geochim. Cosmochim. Acta* 49, 1797-1811.

Hanson, G.N. 1978. The application of trace elements to the petrogenesis of igneous rocks of granitic composition. *Earth Planet. Sci. Lett.* 38, 26-43.

Hanson, G.N. 1980. Rare earth elements in petrogenetic studies of igneous systems. *Ann. Rev. Earth Planet. Sci.* 8, 371-406.

Hart, S.R., Erlank, A.J. and Kable, E.J.D. 1974. Sea floor basalt alteration: some chemical and Sr isotopic effects. *Contrib. Mineral. Petrol.* 44, 219-230.

Hawkesworth, C.J., and Powell, M. 1980. Magma genesis in the Lesser Antilles island arc. *Earth Planet. Sci. Lett.* 51, 297-308.

Hawkesworth, C.J., Rogers, N.W., van Calsteren, P.W.C., and Menzies, M. 1984. Mantle

enrichment processes. *Nature* 311, 331-335.

Hay, R.L. and O'Neil, J.R. 1983. Carbonatite tuffs in the Laetolil beds of Tanzania and the Kaiserstuhl in Germany. *Contrib. Mineral. Petrol.* 82, 403-406.

Hedenquist, J.W. 1986. Mineralization associated with volcanic-related hydrothermal systems in the circum-Pacific basin., in Horn, M.K. (ed.), Transactions of the Fourth Circum-Pacific Energy and Mineral Resources Conference, Singapore, 513-524.

Hellman, P.L., Green, T.H. 1979. The role of sphene as an accessory phase in the high-pressure partial melting of hydrous mafic compositions. *Earth Planet. Sci. Lett.* 42, 191-201.

Heming, R.F. 1979. Undersaturated lavas from Ambitle Island, Papua New Guinea. *Lithos* 12, 173-186.

Heming, R.F. and Rankin, P.C. 1979. Ce-anomalous lavas from Rabaul caldera, Papua New Guinea. *Geochim. Cosmochim. Acta*, 43, 1351-1355.

Henderson, P. 1982. *Inorganic geochemistry*. Pergamon Press, Oxford, 353 p.

Henley, R.W. 1971. Geochemistry and genesis of Precambrian gold deposits: Unpublished Ph.D. dissertation, Victoria University of Manchester, 97p.

Henley, R.W., and McNabb, A. 1978. Magmatic vapor plumes and ground-water interaction in porphyry copper emplacement. *Econ. Geol.* 73, 1-20.

Henley, R.W. 1986. The geothermal framework of epithermal deposits, in *Geology and Geochemistry of Epithermal Systems* (B.R. Berger and P.M. Bethke, eds.), Reviews in Economic Geology, v. 2., Society of Economic Geologists, p. 1-21.

Henry, D.J., MacKinnon, D.R., Chan, I. and Navrotsky, A. 1983. Subliquidus glass-glass immiscibility along the albite-diopside join. *Geochim. Cosmochim. Acta* 47, 277-282.

Hickey, R.L. and Frey, F.A. 1982. Geochemical characteristics of boninite series volcanics: implications for their source. *Geochim. Cosmochim. Acta* 46, 2099-2115.

Hoffman, A.W. and White, M.W. 1982. Mantle plumes from ancient oceanic crust. *Earth Planet. Sci. Lett.* 57, 421- 436.

Hohnen, P.D. 1978. The geology of New Ireland. Bureau of Mineral Resources Australia, Bulletin 176, 39p.

Hole, M.J., Saunders, A.D., Marriner, G.F. and Tarney, J. 1984. Subduction of pelagic sediments: Implications for the origin of Ce-anomalous basalts from the Mariana Islands. *J. Geol. Soc. London* 141, 453-472.

Honza, E., Davies, H.L., Keene, J.B. and Tiffin D.L. 1987. Plate boundaries and evolution of the Solomon Sea Region. *Geo-Marine Letters* 7, 161-168.

Huang, W.L., Wyllie, P.J. and Nehru, C.E. 1980. Subsolidus and liquidus phase

relationships in the system $CaO-SiO_2-CO_2$ to 30 kbar with geological applications. *Am. Mineral.* 65, 285-301.

Hubberten, H-W., Katz-Lehnert, K., and Keller, J. 1988. Carbon and oxygen isotope investigations in carbonatites and related rocks from the Kaiserstuhl, Germany. *Chem. Geol.* 70, 257-274.

Huckenholz, H.G., Kunzmann, T. and Spicker, G. 1988. Stability of titanian magnesiohastingsite and its breakdown to rhonite bearing assemblages.(abs.) *TERRA cognita* 8, 66.

Hughes, G.W. and Turner, C.C. 1977. Upraised Pacific seafloor, southern Malaita, Solomon Islands. *Geol. Soc. Am. Bull.* 88, 412-414.

Hunter, R.H. and McKenzie, D. 1989. The equilibrium geometry of carbonate melts in rocks of mantle composition. *Earth Planet. Sci. Lett.* 92, 347-356.

Irvine, T.N. and Baragar, W.R.A. 1971. A guide to the chemical classification of common volcanic rocks. *Can. J. Earth Sci.* 8, 523-548.

Irving, A.J. and Frey, F.A. 1984. Trace element abundances in megacrysts and their host basalts: Constraints on partition coefficients and megacryst genesis. *Geochim. Cosmochim. Acta* 48, 1201-1221.

Ito, E., Harris, D.M. and Anderson, A.T. 1983. Alteration of oceanic crust and geological cycling of chlorine and water. *Geochim. Cosmochim. Acta* 47, 1613-1624.

Ito, E., and Stern, R.J. 1985. Oxygen and strontium isotopic investigations of subduction zone volcanism: the case of the Volcano Arc and the Marianas Island Arc. *Earth Planet. Sci. Lett.* 76, 312-320.

Ito, M. 1988. Kimberlites and their ultramafic xenoliths from western Kenya. *Tschermaks. Min. Pet. Mitt.* 35, 193-216.

Jakes, P. and Gill, J. 1970. Rare earth elements and the island arc tholeiite series. *Earth Planet. Sci. Lett.* 9, 17-28.

James, D.E., 1981. The combined use of oxygen and radiogenic isotopes as indicators of crustal contamination. *Ann. Rev. Earth. Planet. Sci.* 9, 311-344.

Jaques, A.L. and Robinson, G.P. 1977. The continent/island-arc collision in northern Papua New Guinea. *BMR Jour. Australian Geol. and Geophys.* 2, 289-303.

Javoy, M., Pineau, F. and Iiyama, I. 1978. Experimental determination of the isotopic fractionation between gaseous CO_2 and carbon dissolved in tholeiitic magma. *Contrib. Mineral. Petrol.* 67, 35-39.

Javoy, M., Pineau, F. and Allegre, C.J. 1982. Carbon geodynamic cycle. *Nature* 300, 171-173.

Johns, R.J., 1972. Vegetation. In *Encyclopedia of Papua New Guinea*. Ed. P. Ryan. Vol. 2.

Melbourne University Press, p. 1163-1170.

Johnson, R.W., Perfit, M.R., Chappell, B.W., Jaques, A.L., Shuster, R.D. and Ridley, W.I. 1988. Volcanism in the New Ireland Basin and Manus Island region: Notes on the geochemistry and petrology of some dredged volcanic rocks from a rifted-arc region in Marlow, M.S., Dadisman S.V., and Exon, N.F. (eds), Geology and offshore resources of Pacific island arcs-New Ireland and Manus region, Papua New Guinea, Circum-Pacific Council for Energy and Mineral Resources Earth Science Series, v.9, p.113-130.

Johnson, R.W., Wallace, D.A. and Ellis, D.J. 1976. Feldspathoid-bearing potassic rocks and associated tyypes from volcanic islands off the coast of New Ireland, Papua New Guinea: a preliminary account of geology and petrology. *In* Johnson, RW (Ed.), Volcanism in Australasia, 297-316. Elsevier, Amsterdam.

Johnson, R.W., McKenzie, D.E. and Smith, I.E.M. 1978. Volcanic rock association at convergent plate boundaries: reappraisal of the concept using case histories from Papua New Guinea. *Geol. Soc. Am. Bull.* 89, 96-106.

Johnson, R.W. 1979. Geotectonics and volcanism in Papua New Guinea: a review of the late Cenozoic. *BMR Journal of Australian Geology & Geophysics* 4, 181-207.

Johnston, A.D., and Stout, J.H. 1984. A highly oxidized ferrian salite-, kennedyite-, forsterite- and rhönite-bearing alkali gabbro from Kauai, Hawaii and its mantle xenoliths. *Am. Mineral.* 69, 57-68.

Johnston, A.D., Stout, J.H., and Murthy, V.R. 1985. Geochemistry and origin of some unusually oxidized alkaline rocks from Kauai, Hawaii. *Jour. Volcanol. Geotherm. Res.* 25, 225-248.

Joplin, G. 1968. Shoshonites. *Geol. Soc. Aust. Journal*, 15 (2), 275-294.

Kagiyama, T. 1983. Thermal activities of volcanoes in the Japan Arc; in **Arc Volcanism: Physic and Tectonics**, (D. Shimozuru and I. Yokoyama, eds.), Terra Scientific Pub. Co., Tokyo, pp. 13-27.

Kapustin, Yu. L. 1985. A differentiated analcime basalt sill with segregated calcite. *International Geology Review* 28, 1031-1044.

Katsura, T., and Nagashima, S. 1974. Solubility of sulfur in magmas. *Geochim. Cosmochim. Acta* 38, 517-531.

Kay, R.W., and Gast, P.W. 1973. The rare earth content and origin of alkali-rich basalts. *J. Geology* 81, 653-682.

Kelemen, P.B., Johnson, K.T.M., Kinzler, R.J. and Irving, A.J. 1990. High-field-strength element depletions in arc basalts due to mantle-magma interaction. *Nature* 345, 521-524.

Kennedy, A.K., Hart, S.R., and Frey, F.A. 1990a. Composition and isotopic constraints on the petrogenesis of alkaline arc lavas: Lihir Island, Papua New Guinea. *J. geophys.*

Res. 95, No. B5, 6929-6942.

Kennedy, A.K., Grove, T.L., and Johnson, R.W. 1990b. Experimental and major element constraints on the evolution of lavas from Lihir Island, Papua New Guinea. *Contrib. Mineral. Petrol.* 104, 722-734.

Kjarsgaard, B.A. and Hamilton, D.L. 1989. The genesis of carbonatites by immiscibility., in Bell, K. (ed.), *Carbonatites: Genesis and Evolution,* Unwin Hyman, 388-404.

Kleeman, J.D., Green, D.H. and Lovering, J.F. 1969. Uranium distribution in ultramafic inclusions from Victorian basalts. *Earth Planet. Sci. Lett.* 5(7), 449-458.

Kobelskii, B.J., Gold, D.P., and Deines, P. 1979. Variations in stable isotope compositions for carbon and oxygen in some South African and Lesothan kimberlites, in Boyd F.R., Meyer H.O.A. (eds) *Kimberlites, diatremes, and diamonds; Their geology, petrology, and geochemistry.* American Geophysical Union, Washington DC, pp. 252-271.

Koster van Groos, A.F. and Wyllie, P.J. 1973. Liquid immiscibility in the join $NaAlSi_3O_8$-$CaAlSi_2O_8$-Na_2CO_3-H_2O. *Am. J. Sci.*, 273, 465-487.

Krauskopf, K.B. 1964. The possible role of volatile metal compounds in ore genesis. *Econ. Geol.* 59, 22-45.

Kroenke, L.W. 1972. Geology of the Ontong Java Plateau. *Rept. Hawaii Inst. Geophys.* HIG-72-5, 119 pages.

Kroenke, L.W. 1984. Cenozoic tectonic development of the southwest Pacific: Committee for Co-ordination of Joint Prospecting in South Pacific Offshore Areas, United Nations Economic and Social Commission for Asia and the Pacific, *Tech. Bull. 6,* 122 p.

Kushiro, I. 1960. Si-Al relation in clinopyroxenes from igneous rocks. *Am. J. Sci.* 258, 548-554.

Kyser, T.K., O'Neil, J.R. and Carmichael, I.S.E. 1981. Oxygen isotope thermometry of basic lavas and mantle nodules. *Contrib. Mineral. Petrol.* 77, 11-23.

Kyser, T.K., O'Neil, J.R. and Carmichael, I.S.E. 1982. Genetic relations among basic lavas and ultramafic nodules: evidence from oxygen isotope compositions. *Contrib. Mineral. Petrol.* 81, 88-102.

Kyser, T.K. 1986. Stable isotope variations in the mantle, in Valley, J.W., Taylor, H.P., Jr., O'Neill, J.R. (eds), *Stable Isotopes in High Temperature Geological Processes,* Reviews in Mineralogy, v. 16, 141-164.

Langshur, A., 1990. The geology, geochemistry and structure of the Mooshla Intrusion, Bousquet Mining Centre, Quebec. M.Sc. Thesis, University of Ottawa, 172 pp.

Lasaga, A.C. 1981. Transition state theory, in A.C. Lasaga and R.J. Kirkpatrick,eds. *Kinetics of Geochemical Processes,* Reviews in Mineralogy 8, 135-169.

Le Bas, M.J. 1962. The role of aluminum in igneous clinopyroxenes with relation to their parentage. *Am. J. Sci.* 260, 267-288.

Le Bas, M.J., Le Maitre, R.W., Streckeisen, A., and Zanettin, B. 1986. A chemical classification of volcanic rocks based on the total alkali-silica diagram. *J. Petrol.* 27, 745-750.

Le Bas, M.J. 1987. Nephelinites and carbonatites, in Fitton, JG and Upton, BGJ (eds) *Alkaline Igneous Rocks*, Geological Society Special Publication.

Le Cloarec, M.F., Allard, P., Sheppard, D.S. and Ardouin, B. 1989. Radioactive isotopes and trace elements in gaseous emissions from White Island., in IAVCEI Commission on the Chemistry of Volcanic Gases (ed. W.F. Giggenbach), Newsletter 4.

Licence, P.S., Terrill, J.E., and Fergusson, L.J. 1987. Epithermal gold mineralization, Ambitle Island, Papua New Guinea, in Pacific Rim Congress 87, Gold Coast, Queensland 1987, Proc.: Parkville, Australia, Australasian Inst. Mining Metallurgy, 273-278.

Longstaffe, F.J., 1977. The oxygen isotope and elemental geochemistry of Archean rocks from northern Ontario. Ph.D. Thesis, McMaster University, 564 pp.

Lowenstern, J.B., Mahood, G.A., Rivers, M.L. and Sutton, S.R. 1991. Evidence for extreme partitioning of copper into a magmatic vapor phase. *Science* 252, 1405-1409.

Ludden, J.N. and Thompson, G. 1979. An evaluation of the behavior of the rare earth elements during the weathering of sea-floor basalt. *Earth Planet. Sci. Lett.* 43, 85-92.

Macrae, N.E. 1979. Silicate glass and sulphides in ultramafic xenoliths, Newer Basalts. Victoria, Australia. *Contrib. Min. Pet.* 68, 275-280.

Margaritz, M., Whitford, D.J., James, D.E. 1978. Oxygen isotopes and the origin of high $^{87}Sr/^{86}Sr$ andesites. *Earth. Planet. Sci. Lett.* 40, 220-230.

Marty, B., Zashu, S. and Ozima, M. 1983. Two noble gas components in a Mid-Atlantic Ridge basalt. *Nature* 302, 238-240.

Mason, R.A., Smith, J.V., Dawson, J.B. and Treves, S.B. 1982. A reconnaissance of trace elements in anorthoclase megacrysts. *Mineral. Mag.* 46, 7-11.

McCrea, J.M. 1950. On the isotope chemistry of carbonates and a paleotemperature scale. *J. Chem. Phys.* 18, 849-857.

McCue, K.F. 1988. Earthquakes and crustal stress in the north Bismarck Sea., in Marlow, M.S., Dadisman, S.V., and Exon, N.F., (eds.), *Geology and offshore resources of Pacific island arcs-New Ireland and Manus region, Papua New Guinea*, Circum-Pacific Council for Energy and Mineral Resources Earth Science Series, v. 9: Houston, Texas, Circum-Pacific Council for Energy and Mineral Resources, p. 41-46.

McCulloch, M.T., Compston, W., Abbott, M., Chivas, A. 1983. Neodymium, strontium,

lead and oxygen isotopic and trace element constraints on magma genesis in the Banda island-arc, Wetar. *Geol. Soc. Aust. Abs.* 9, 152-153.

McGetchin, T.R. and Besancon, J.R. 1973. Carbonate inclusions in mantle-derived pyropes. *Earth Planet. Sci. Lett.* 18, 408-410.

McInnes, B.I.A., Evans, N.J., Cameron, E.M. and Gregoire, D.C. 1991. Gold-copper enrichment in island arcs by mantle oxidation: Evidence from mantle metasomatism in the Tabar-Lihir-Tanga-Feni island arc, Papua New Guinea., in Geological Association of Canada-Mineralogical Association of Canada Joint Annual Meeting with Society of Economic Geologists, Program with Abstracts, v. 16, A82.

McKenzie, D.P. 1978. Some remarks on the development of sedimentary basins. *Earth Planet. Sci. Lett.* 49, 25-32.

Meeker, K.A. 1988. The emission of gases and aerosols from Mount Erebus Volcano, Antarctica. Unpublished M.Sc. thesis, N.M. Inst. Mining and Tech., 172 pp.

Meeker, K.A., Chuan, R.L., Kyle, P.R. and Palais, J.M. 1991. Emission of Au particles from Mt. Erebus, Ross Island, Antarctica. *Geophysical Research Letters* 18, 1405-1408.

Meen, J.K. 1987. Mantle metasomatism and carbonatites; An experimental study of a complex relationship. *Geological Society of America Special Paper* 215, 91-100.

Menyailov, I.A. and Nikitina, L.P., 1980. Chemistry and metal contents of magmatic gases: The new Tolbachik volcanoes case (Kamchatka). *Bull. Volcanol.* 43, 197-205.

Menzies, M. 1983. Mantle ultramafic xenoliths in alkaline magmas; Evidence for mantle heterogeneity modified by magmatic activity, in Hawkesworth, C.J., and Norry, M.J. (eds.) *Continental basalts and mantle xenoliths*: Nantwich, U.K., Shiva Publishing, p. 92-110.

Menzies, M.A., and Murhty, V.R., 1980. Mantle metasomatism as a precursor to the genesis of alkaline magmas: Isotopic evidence. *Am. J. Sci.* 280-A, The Jackson Volume, 622-638.

Menzies, M.A. and Wass, S.Y. 1983. CO_2-rich and LREE-rich mantle below eastern Australia: A REE and isotopic study of alkaline magmas and apatite-rich mantle xenoliths from the southern highlands province, Australia. *Earth. Planet. Sci. Lett.* 56, 287-302.

Mitchell, A.H.G., and Garson, M.S., 1972. Relationship of porphyry copper and circum-Pacific tin deposits to palaeo-Benioff zones: *Institute of Mining and Metallurgy Transactions*, 81, B10-B25.

Mitchell, R.H. 1986. Kimberlites: Mineralogy, Geochemistry and Petrology: Plenum Press, New York, 442 p.

Mitchell, R.H. 1991. Coexisting glasses occurring as inclusions in leucite from lamproites: examples of silicate liquid immiscibility in ultrapotassic magmas. *Mineral. Mag.* 55, 197-202.

Mitchell, R.H. 1991. Kimberlites and lamproites: Primary sources of diamond. *Geoscience Canada*, 18, no. 1, 1-16.

Mitchell, R.H., and Bergman, S.C. 1991. Petrology of Lamproites: Plenum Press, New York, 456 p.

Mitchell, R.H., and Keays, R.R. 1981. Abundance and distribution of gold, palladium and iridium in some spinel and garnet lherzolites; Implications for the nature and origin of precious metal-rich intergranular components in the upper mantle. *Geochim. Cosmochim. Acta* 45, 2425-2442.

Moberiey, R, Jr. 1972. Origin of lithosphere behind island arcs, with reference to the western Pacific. *Geological Society of America Memoirs* 132, 35-55.

Morris, J. 1989. Subduction, volcanism and change in the earth. *Carnegie Institute of Washington Yearbook (1988)*, 111-117.

Morris, J.D., Leeman, W.P. and Tera, F. 1990. The subducted component in island arc lavas: constraints from Be isotopes and B-Be systematics. *Nature* 344, 31-36.

Morrison, G.W. 1980. Characteristics and tectonic setting of the shoshonite rock association. *Lithos* 13, 97-108.

Muehlenbachs, K. 1987. Oxygen isotope exchange during weathering and low temperature alteration, in Kyser, T.K. (ed)., *Stable Isotope Geochemistry of Low Temperature Fluids*, Mineralogical Association of Canada, Short Course v. 13, 162-186.

Muehlenbachs, K. 1986. Alteration of the oceanic crust and the ^{18}O history of seawater, in Valley, J.W., Taylor, H.P., Jr., O'Neill, J.R. (eds), *Stable Isotopes in High Temperature Geological Processes*, Reviews in Mineralogy, v. 16, 425-444.

Muehlenbachs, K. and Clayton, R. 1972. Oxygen isotope studies of fresh and weathered submarine basalts. *Can. J. Earth Sci.* 9, 172-184.

Mysen, B.O. and Virgo, D. 1980. Solubility mechanisms of carbon dioxide in silicate melts: A Raman spectroscopic study. *Am. Mineral.* 65, 885-899.

Neal, C.R. and Taylor, L.A. 1989. A negative Ce anomaly in a peridotite xenolith: Evidence for crustal recycling into the mantle or mantle metasomatism? *Geochim. Cosmochim. Acta* [illegible] 1035-1040.

Nelson, D.R., Chivas, A.R., Chappell, B.W. and McCulloch, M.T. 1988. Geochemical and isotopic systematics in carbonatites and implications for the evolution of ocean-island sources. *Geochim. Cosmochim. Acta* 52, 1-17.

Neuman, H., Mead, J. and Vitaliano, C.J. 1954. Trace element variations during fractional crystallization as calculated from the distribution law. *Geochim. Cosmochim. Acta* 6, 90.

Nicholls, I.A. and Ringwood, A.E. 1973. Effect of water on olivine stability in tholeiites and production of silica-saturated magmas in the island arc environment. *J. Geol.* 81,

285-300.

Nier, A.O. 1950. A redetermination of the relative abundances of the isotopes of carbon, nitrogen, oxygen, argon, and potassium. *Phys. Rev.* 77, 789-793.

Niugini Mining Ltd., 1988. Annual Report, 28 p.

Nixon, P.H. 1987. The Pacific plate and adjoining regions., in *Mantle Xenoliths,* Nixon, P.H. (ed.), 295-303, John Wiley & Sons Ltd.

Nriagu, J.O. 1989. A global assessment of natural sources of atmospheric trace metals. *Nature* 338, 47-49.

Olafsson, M. and Eggler, D.H. 1983. Phase relations of amphibole, amphibole-carbonate, and phlogopite-carbonate peridotite: petrologic constraints on the asthenosphere. *Earth Planet. Sci. Lett.* 64, 305-315.

Olmez, I., Finnegan, D.L., and Zoller, W.H. 1986. Iridium emissions from Kilauea Volcano. *J. geophys. Res.* 91, no. B1, 653-663.

Ozima, M., S. Zashu, and O. Nitosh. 1983. $^{3}He/^{4}He$ ratio, noble gas abundance and K-Ar dating of diamonds. An attempt to search for the records of early terrestrial history. *Geochim. Cosmochim. Acta* 47, 2217-2224.

Pearce, J.A. 1983. The role of sub-continental lithosphere in magma gensis at destructive plate margins, in *Continental basalts and mantle xenoliths,* C.J. Hawkesworth and M.J. Norry (eds), 230-249. Nantwich: Shiva.

Philpotts, A.R. 1972. Density, surface tension and viscosity of the immiscible phase in a basic alkaline magma. *Lithos* 5, 1-18.

Philpotts, A.R. 1976. Silicate liquid immiscibility-its probable extent and petrogenetic significance. *Am. J. Sci.* 276, 1147-1177.

Philpotts, A.R. 1989. *Petrography of Igneous and Metamorphic Rocks,* Prentice Hall, Englewood Cliffs, New Jersey, 178 p.

Pitari, G., Visconti, G., and Rizi, V. 1991. Sensitivity of stratospheric ozone to heterogeneous chemistry of sulfate aerosols. *Geophysical Research Letters* 18, 833-836.

Puchelt, H. and Emmerman, R. 1976. Bearing of rare earth patterns of apatites from igneous and metamorphic rocks. *Earth Planet. Sci. Lett.* 31, 279-286.

Ramsay, W.R.H., Crawford, A.J., and Foden, J.D. 1984. Field setting, mineralogy, chemistry, and genesis of arc picrites, New Georgia, Solomon Islands. *Contrib. Mineral. Petrol.* 88, 386-402.

Rayleigh, J.W.S. 1896. Theoretical considerations respecting the separation of gases by diffusion and similar processes. *Philos. Mag.* 42, 77.

Richards, J.P., 1990. Petrology and geochemistry of alkalic intrusives at the Porgera gold deposit, Papua New Guinea, in Hedenquist, J.W., White, N.C., and Siddley, G., eds., *Epithermal gold mineralization of the Circum-Pacific: Geology, geochemistry, origin and exploration*, I: *Jour. Geochem. Expl.* 35, 141-199.

Ringwood, A.E. and Green, D.H. 1966. An experimental investigation of the gabbro to eclogite transformation and some geophysical implications. *Tectonophysics* 3, 383-427.

Rock, N.M.S. 1987. The nature and origin of lamprophyres: an overview, in Fitton, J.G. and Upton, B.G.J. (eds), *Alkaline Igneous Rocks*, Geological Society Special Publication No. 30, 191-226.

Rock, N.M.S. and Groves, D.I. 1988a. Do lamprophyres carry gold as well as diamonds? *Nature* 332, 253-255.

Rock, N.M.S. and Groves, D.I. 1988b. Can lamprophyres resolve the genetic controversy over mesothermal gold deposits? *Geology* 16, 538-541.

Rock, N.M.S., Groves, D.I., Perring, C.S. and Golding, S.D. 1989. Gold, lamprophyres, and porphyries: What does their association mean? *Economic Geology Monograph 6*, 609-625.

Rock, N.M.S., and Finlayson, E.J. 1990. Petrological affinities of intrusive rocks associated with the giant mesothermal gold deposit at Porgera, Papua New Guinea. *Jour. Southeast Asian Earth Sciences*. 4(3), 247-257.

Roedder, R. 1979. Silicate liquid immiscibility in magmas., in *The Evolution of the Igneous Rocks* (Yoder, H.S., ed.), Princeton University Press, 15-57.

Rogers, N.W. and Hawkesworth, C.J. 1982. Proterozoic age and cumulate origin for granulite xenoliths, Lesotho. *Nature* 299, 409-413.

Roux, J. and Hamilton D.L. 1976. Primary igneous analcite-an experimental study. *J. Petrol.* 17, 244-257.

Rovetta, M.R. and Mathez, E.A. 1982. Magnesite and other minerals in fluid inclusions in a lherzolite xenolith from an alkali basalt (abs). *Terra Cognita*, v. 2, 229.

Ruxton, B.P., and McDougall, I., 1967. Denudation rates in northeast Papua from potassium-argon dating of lavas: *Am. Jour. Sci.* 265, 545-561.

Ryabchikow, I.D. and Green, D.H. 1978. The role of carbon dioxide in the petrogenesis of highly potassic magmas., in *Problems of the petrology of the Earthls crust and upper mantle.* Inst. Geol. Geofiz. Nauka, Novosibirsk, 403, 49-64.

Ryabchikov, I.D., Baranova, N.N., Zotov, A.V., and Orlova, G.P., 1985, The stability of $Au(OH)^{\circ}_{sol}$ in supercritical water and the metal contents of fluids in equilibrium with a granite magma. *Geokhimiya* 1985, 267-268.

Rye, R.O., Bethke, P.M., and Wasserman, M.D., 1991, The stable isotope geochemistry of

acid-sulfate alteration and vein forming alunite: USGS Open-File Report 91-257, 59 p.

Ryerson, F.J. and Hess, P.C. 1978. Implications of liquid-liquid distribution coefficients to mineral-liquid partitioning. *Geochim. Cosmochim. Acta* 42, 921-932.

Ryerson, F.J., and Watson, E.B., 1987. Rutile saturation in magmas: implications for Ti-Nb-Ta depletion in island-arc magmas. *Earth Planet. Sci. Lett.* 86, 225-229.

Sakai, H., Casadevall, T.J., and Moore, J.G. 1982. Chemistry and isotope ratios of sulfur in basalts and volcanic gases at Kilauea volcano, Hawaii: *Geochim. Cosmochim. Acta* 46, 729-738.

Sato, M. 1978. Oxygen fugacity of basaltic magmas and the role of gas-forming elements. *Geophys. Res. Lett.* 5, 447-449.

Saunders, A.D., Tarney, J., Marsh, N.G., and Wood, D.A. 1980a. Ophiolites as ocean crust or marginal basin crust: a geochemical approach. In *Proc. Int. Ophiolite Conf.* Nicosia, Cyprus, A. Panayiotou (ed.), 193-204.

Saunders, A.D., Tarney, J. and Weaver, S.D. 1980b. Transverse geochemical cariations across the Antarctic Peninsula: implications for the genesis of calc-alkaline magmas. *Earth Planet. Sci. Lett.* 46, 344-360.

Sawkins, F.J. 1972. Sulfide ore deposits in relation to plate tectonics. *J. Geology*, 80, 377-397.

Schilling, J.-G., Zajac, M., Evans, R., Johnston, T., White, W., Devine, J.D., and Kingsley, R. 1983. Petrologic and geochemical variations along the Mid-Atlantic Ridge from 27°N to 73°N. *Am. J. Sci.* 283, 510-586.

Schneider, M.E. and Eggler, D.H., 1986. Fluids in equilbrium with peridotite minerals: implications for mantle metasomatism. *Geochim. Cosmochim. Acta* 50, 711-724.

Schrieber, H.D., Lauer, H.V. and Thitinant, T. 1980. The redox state of cerium in basaltic magmas: An experimental study of iron-cerium interactions in silicate melts. *Geochim. Cosmochim. Acta* 44, 1599-1612.

Scott, P.W. 1980. Zoned pyroxenes and amphiboles from camptonite near Gran, Norway. *Mineralog. Mag.* 43, 913-917.

Sekine, T. and Wyllie, P.J. 1982a. Synthetic systems for modeling hybridization between hydrous siliceous magmas and peridotite in subduction zones. *J. Geology* 90, 734-741.

Sekine, T. and Wyllie, P.J. 1982b. Phase relationships in the system $KAlSiO_4$-Mg_2SiO_4-SiO_2-H_2O as a model for hybridization between hydrous siliceous melts and peridotite. *Contrib. Mineral. Petrol.* 79, 368-374.

Sen, G. 1987. Xenoliths associated with the Hawaiian Hot Spot, in *Mantle Xenoliths* (ed. Nixon, P.H.). John Wiley and Sons.

Seward, T.M. 1984. The transport and deposition of gold in hydrothermal systems, *in* Foster, R.P., ed., *Gold '82*, Rotterdam, A.A. Balkema Pub., 165-181.

Seward, T.M., 1989, The hydrothermal chemistry of gold and its implications for ore formation: Boiling and conductive cooling as examples. *Econ. Geol. Monograph 6*, 398-404.

Sharp, Z.D. 1990. A laser-based microanalytical method for the *in situ* determination of oxygen isotope ratios of silicates and oxides. *Geochim. Cosmochim. Acta* 54, 1353-1357.

Shaw, D.M. 1970. Trace element fractionation during anatexis. *Geochim. Cosmochim. Acta* 34, 237-243.

Shimizu, N. 1990. The oscillatory trace element zoning of augite phenocrysts. *Earth-Science Reviews* 29, 27-37.

Shimizu, N. 1975. Rare earth elements in garnets and clinopyroxenes from garnet lherzolite nodules in kimberlites. *Earth Planet. Sci. Lett.* 25, 26-32.

Sillitoe, R.H. 1972. A plate tectonic model for the origin of porphyry copper deposits. *Econ. Geol.* 67, 184-197.

Sillitoe, R.H. 1973. The tops and bottoms of porphyry copper deposits. *Econ. Geol.* 68, 799-815.

Sillitoe, R.H. 1983. Enargite-bearing massive sulfide deposits high in porphyry copper systems. *Econ. Geol.* 78, 348-352.

Sillitoe, R.H. 1985. Ore-related breccias in volcanoplutonic arcs. *Econ. Geol.* 80, 1467-1514.

Sillitoe, R.H. 1989. Gold deposits in western Pacific island arcs: The magmatic connection. *Econ. Geol. Monograph 6*, 274-291.

Simkin, T. and Smith, J.V. 1970. Minor-element distribution in olivine. *J. Geol.* 78, 304-325.

Solomon, M. 1990. Subduction, arc reversal, and the origin of porphyry copper-gold deposits in island arcs. *Geology* 18, 630-633.

Spera, F.J. 1984. Carbon dioxide in petrogenesis, III. Role of volatiles in the ascent of alkaline magma with special reference to xenolith-bearing mafic lavas. *Contrib. Mineral. Petrol.* 88, 217-232.

Spera, F.J. 1987. Dynamics of translithospheric migration of metasomatic fluid and alkaline magma., in *Mantle Metasomatism* (M.A. Menzies and C.J. Hawkesworth, eds.), Academic Press, London, 1-18.

Staudigel, H., Hart, S.R. and Richardson, S.H. 1981. Alteration of the oceanic crust: processes and timing. *Earth Planet. Sci. Lett.* 52, 311-327.

Staudigel, H., Muehlenbachs, K., Richardson, S.H. and Hart, S.R. 1981. Agents of low temperature ocean crust alteration. *Contrib. Mineral. Petrol.* 77, 150-157.

Stewart, D.C. 1975. Crystal clots in calc-alkaline andesites as breakdown products of high-Al amphiboles. *Contrib. Mineral. Petrol.* 53, 195-204.

Stewart, W.D., Francis, G., and Pederson, S.L., 1986. Hydrocarbon potential of the Bougainville and southeastern New Ireland Basins, Papua New Guinea. Geol. Surv. P.N.G. Report No. 86/11, 14 p.

Stewart, W.D. and Sandy, M.J. 1988. Geology of New Ireland and Djaul Islands, Northeastern Papua New Guinea. in Marlow, M.S., Dadisman, S.V., and Exon, N.F., (eds.), *Geology and offshore resources of Pacific island arcs-New Ireland and Manus region, Papua New Guinea*, Circum-Pacific Council for Energy and Mineral Resources Earth Science Series, v. 9: Houston, Texas, Circum-Pacific Council for Energy and Mineral Resources.

Stoiber, R.E. and Jepsen, A. 1973. Sulfur dioxide contributions to the atmosphere by volcanoes. *Science* 182, 577-578.

Stolper, E., Fine, G., Johnson, T., and Newman, S., 1987. Solubility of carbon dioxide in albitic melt. *American Mineralogist* 72, 1071-1085.

Tatsumi, Y. 1981. Melting experiments on a high-magnesian andesite. *Earth Planet. Sci. Lett.* 54, 357-365.

Taylor, B. 1979. Bismarck Sea: evolution of a back-arc basin. *Geology* 7, 171-174.

Taylor, H.P., Jr., Frechen, J., and Degens, E.T. 1967. Oxygen and carbon isotope studies of carbonatites from the Laacher See district, West Germany and the Alnö district, Sweden. *Geochim. Cosmochim. Acta* 31, 407-430.

Taylor, H.P., Jr. 1986. Igneous rocks: II. Isotopic case studies of CircumPacific magmatism, in Valley, J.W., Taylor, H.P., Jr., O'Neill, J.R. (eds), *Stable Isotopes in High Temperature Geological Processes*, Reviews in Mineralogy, v. 16, 273-316.

Taylor, H.P., Jr., and Sheppard, S.M.F. 1986. Igneous rocks: I. Processes of isotope fractionation and isotope systematics, in Valley, J.W., Taylor, H.P., Jr., O'Neill, J.R. (eds), *Stable Isotopes in High Temperature Geological Processes*, Reviews in Mineralogy, v. 16, 227-272.

Taylor, HP, Jr., Gregory, RT, and Turi, B. 1987. $^{18}O/^{16}O$ evidence for fluid-rock interaction in the upper mantle: Data from ultramafic nodules and K-rich volcanic rocks in Italy, in Helgeson, HC (ed.), *Chemical Transport in Metasomatic Processes*, NATO ASI Series C: Vol. 218, 1-37, D. Reidel Publishing Co.

Taylor, L.A. and Neal C.R. 1989. Eclogites with oceanic crustal and mantle signatures from the Bellsbank Kimerilte, South Africa. Part I: Mineralogy, petrography and whole rock chemistry. *J. Geology* 97, 551-567.

Thompson, A.B.J. and Thompson, J.F.H. 1988. Geological evaluation of the Sorowar and

Botlu South prospects, Simberi Island, Papua New Guinea. Unpublished private report to Kennecott Exploration, 31 p.

Thornton, C.P., and Tuttle, O.F., 1960. Chemistry of igneous rocks: pt. I, Differentiation Index, *Am. J. Sci.* 258, 664-684.

Thorpe, R.S., Potts, P.K., and Prancis, P.W. 1976. Rare earth data and petrogenesis of andesite from the North Chilean Andes. *Contrib. Mineral. Petrol.* 54, 65-78.

Tomita, T. 1934. On kaersutite from Dogo, Oki Islands, Japan, and its magmatic alteration and resorption. *Shonghai Sci. Inst. J. Sect.* 2, 1, 99-136.

Turner, F.J. 1981. Metamorphic petrology: Mineralogical, field and tectonic aspects. McGraw-Hill, New York, 524p.

Twyman, J.D. and Gittins J. 1987. Alkalic carbonatite magmas: parental or derivative? in Fitton JG & Upton BGJ (eds), *Alkaline Igneous Rocks*, Geological Society Special Publication No. 30, pp. 85-94.

Ueda, A. and Sakai, H. 1984. Sulfur isotope study of quaternary volcanic ricks from the Japanese Island Arc. *Geochim. Cosmochim. Acta* 48, 1837-1848.

Venturelli, G., Capedri, S., Barbieri, M., Toscani, L., Salvioli Marian, E., and Zerbi, M. 1991. The Jumilla lamproite revisited: a petrological oddity. *Eur. J. Mineral.* 3, 123-145.

Villa, I.M. 1990. $^{40}Ar/^{39}Ar$ dating of amphiboles from Zabargad Island (Red Sea) is precluded by interaction with fluids. *Tectonophysics* 180, 369-373.

Vinogradov, V.I., Krasnov, A.A., Kuleshov, V.N., and Sulerzhitskiy, L.D. 1978. $^{13}C/^{12}C$, $^{18}O/^{16}O$, and ^{14}C concentrations in the carbonatites of the Kalyango Volcano (East Africa) (in Russian). *Izv Akad Nauk SSSR*, Ser Geol, 6, 33-41.

Wallace, D.A., Johnson, R.W., Chappell, B.W., Arculus, R.J., Perfit, M.R., Crick, I.H. 1983. Cainozoic volcanism of the Tabar, Lihir Tanga and Feni Islands, Papua New Guinea. *Rep. BMR Geol. and Geophys.* (Aust) 243.

Wallace, E.W. and Green, D.H. 1988. An experimental determination of primary carbonatite magma composition. *Nature* 335, 343-346.

Walsh, P.R., Duce, R.A., and Fashing, J.L. 1979. Considerations of the enrichment, sources, and flux of arsenic in the troposphere. *J. geophys. Res.* 84, 1719-1726.

Weissel, J.K. 1981. Magnetic lineations in marginal basins of the western Pacific. *Phil. Trans. R. Soc. Lond.* A 300, 217-442.

Weissel J.K., Taylor, B. and Karner, G.D. 1982. The opening of the Woodlark Basin, subduction of the Woodlark spreading system and the evolution of northern Melanesia since mid-Pliocene time. *Tectonophysics* 87, 253-277.

Wendlandt, R. and Eggler, D.H. 1980. Stability of phlogopite in natural spinel lherzolite and in the system $KalSiO_4$-MgO-SiO_2-H_2O-CO_2 at high pressures and high temperatures.

Am. J. Sci. 280, 421-458.

White, W.M. and Patchett, J. 1984. Hf-Nd-Sr isotopes and incompatible element abundances in island arcs: Implications for magma origins and crust-mantle relationships. *Earth Planet. Sci. Lett.* 67, 167-185.

Wilson, M. 1989. Igneous petrogenesis: A global tectonic approach. Unwin Hyman, London, 466 p.

Winkler, H.G.F. 1979. Petrogenesis of metamorphic rocks. Fifth Edition, Springer-Verlag, New York, 348 p.

Woodcock, N.H. 1986. The role of strike-slip systems at plate boundaries. *Phil. Trans. R. Soc. Lond.* A 317, 13-29.

Wyllie, P.J. 1977. Mantle fluid compositions buffered by carbonates in peridotite-CO_2-H_2O. *J. Geology* 85, 187-207.

Wyllie, P.J. 1981. Plate tectonics and magma genesis. *Geol. Rundsch.* 70, 128-153.

Wyllie, P.J. 1987. Discussion of recent papers on carbonated peridotite, bearing on mantle metasomatism and magmatism. *Earth Planet. Sci. Lett.* 82, 391-397.

Wyllie, P.J. and Huang, W.L. 1976. Carbonation and melting reactions in the system CaO-MgO-SiO_2-CO_2 at mantle pressures with geophysical and petrological applications. *Contrib. Min. Petrol.* 54, 79-107.

Wyllie, P.J., Huang, W.L., Otto, J., and Byrnes, A.P. 1983. Carbonation of peridotite and decarbonation of siliceous dolomites represented in the system CaO-MgO-SiO_2-CO_2 to 30 kbar. *Tectonophysics* 100, 359-388.

Wyllie, P.J. and Sekine, T. 1982. The formation of mantle phlogopite in subduction zone hybridization. *Contrib. Min. Petrol.* 79, 375-380.

Wyman, D., and Kerrich, R. 1988. Alkaline magmatism, major structures, and gold deposits: Implications for greenstone belt gold metallogeny. *Econ. Geol.* 83, 454-461.

Wyman, D., and Kerrich, R. 1989. Archean shoshonitic lamprophyres associated with Superior Province gold deposits: Distribution, tectonic setting, noble metal abundances, and significance for gold mineralization. *Econ. Geol. Monograph 6*, 651-667.

Yoder, H.S. Jr. (1973) Contemporaneous basaltic and rhyolitic magmas. *Am. Mineral.* 58, 153-171.

Zachariasen, W.H. 1932. The atomic arrangement in glasses. *J. Am. Chem. Soc.* 54, 3841-3851.

Zoller, W.H., Parrington, J.R., and Phelan Kotra, J.M. 1983. Iridium enrichment in airborne particles from Kilauea Volcano: January, 1983. *Science* 222, 1118-1121.

Appendix A. Rock and Mineral Geochemistry

A.1 Whole rock sample preparation

Samples were collected on two separate trips to Simberi Island from May to July 1988 and from June to August, 1989. Weathered surfaces were sawn off and hand samples described on site before shipment to Canada. Sample preparation at the University of Ottawa included crushing and homogenization using a steel plate jaw crusher, a ceramic pulverizer and a tungsten carbide shatterbox. Thorough cleaning and pre-contamination of the equipment was conducted before each crushing run. Samples were sieved over nylon mesh and the -200 mesh fraction was collected for major, trace and isotopic analysis. Whole rock powders for isotopic analysis were acid washed to remove traces of secondary carbonate.

Mineral separates for isotopic analysis were obtained from the -80 mesh fraction. Magnetite separates were collected by hand magnet. Olivine and clinopyroxene was separated using a Franz electromagnetic separator. All mineral separates were purified by hand picking under a binocular microscope.

A.2 X-ray fluorescence (XRF) spectroscopy

Rock powders (1.5 gm) were fused with 0.433 gm Li_2CO_3 and 3.9 gm $Li_2B_4O_7$ in a platinum crucible. The resulting glass disks were analyzed for major and selected trace elements (Cr, Ni, Zn, Rb, Sr, Zr, Ba and V) by XRF at the University of Ottawa using a Phillips PW1410-80 model. Calibration of the XRF spectrometer using the routine of LaChance and Traill (1966) was conducted by R.

Hartree.

The following are estimates of the analytical precision of the XRF method at the time of analysis, expressed as relative errors (± standard deviation/mean), extracted from Langshur (1990): SiO_2 ±1.02%; TiO_2 ±1.9%; Al_2O_3 ±1.8%; MgO ±8.0%; CaO ±1.1%; Na_2O ±7.9%; K_2O ±1.2%; P_2O_5 ±18%; MnO ±0%; Fe_2O_3 ±2.5%; Ba ±10%. For all other trace elements, the error is estimated at ±50% for values between 10 and 30 ppm, and ±10% for values exceeding 30 ppm.

Detection limits for the trace elements analyzed by XRF are 10 ppm. Values less than 10 ppm are reported as zero. For the Simberi suite all Nb values are less than 10 ppm.

Accuracy was estimated by Langshur (1990) based on 8 analyses of the internal diorite standard DR-N. All major element oxides were within 1% of accepted values (Abbey, 1983) except for MgO, TiO_2 and P_2O_5 which were within 4%. The trace elements Ba, Cr, V and Zn were within 15%. Nickel values for DR-N (16 ppm) are close to the limit of detection by XRF and therefore the reported accuracy of Ni was only 40%.

A.3 Loss on ignition and FeO/Fe_2O_3 determination

H_2O (total), CO_2 (total) and S (total) were determined via combustion/infrared detection and ferric/ferrous iron by the Pratt Method in the laboratories of the Geological Survey of Canada (GSC). Estimates of the validity of results are ±0.2%

+ 5% of the total concentration for FeO and Fe_2O_3 , ±0.1% + 5% of the total concentration for H_2O and CO_2, and ±0.04 + 5% of the total concentration of sulphur.

A.4 Instrumental Neutron Activation Analysis (INAA)

A suite of trace elements was analyzed on whole rock powders via INAA by the Ottawa laboratories of Bondar-Clegg. The Simberi samples contained the following elements above the limit of detection for this method (detection limit; ± estimated relative errors based on limited duplicate analysis): Sc (0.2 ppm; <5%), Co (5 ppm; <5%), As (0.5 ppm; <10%), W (1 ppm; <50%), Au (1 ppb; <5%), U (0.2 ppm; <20%), Th (0.2 ppm; <20%), Cs (0.5 ppm; <100%), Hf (1 ppm; <10%) and Ta (0.5 ppm; <60%). INAA was also able to determine the maximum concentration of the following elements which were all reported as below the limit of detection: Se (5 ppm), Ag (2 ppm), Cd (5 ppm), Sn (100 ppm) and Te (10 ppm). Analysis of the rare earth elements (REE) La (2 ppm), Ce (5 ppm), Sm (0.1 ppm), Eu (1 ppm), Tb (0.5 ppm), Yb (2 ppm) and Lu (0.2 ppm) by INAA is reported for several samples in Appendix A.8, however INAA is less sensitive, precise and accurate for REE than induced coupled plasma-mass spectrometry (ICP-MS) techniques.

A.5 Induced Coupled Plasma-Emission and Mass Spectrometry Analysis (ICP-ES and MS)

A suite of samples was selected for precise platinum-group element (PGE), gold and REE analysis using advanced mass spectrometry techniques at the GSC.

Analysts for PGE + Au were N.J. Evans and D.C. Gregoire and for REE, N. Bertrand.

Platinum (Pt), palladium (Pd), ruthenium (Ru) and iridium (Ir) were measured by isotope dilution induced coupled plasma mass spectrometry (ICP-MS), whereas rhodium (Rh) and gold (Au) were determined by external calibration ICP-MS. Total PGE contents were determined using an hydrofluoric acid and aqua regia digestion procedure (Gregoire, 1988), but with spike solutions added to solid material at the start of the procedure. Prior to analysis by ICP-MS, Te co-precipitation was used to pre-concentrate and separate analyte from matrix components (Elson and Chatt, 1983). Detection limits using a 5 g sample for Pt, Pd were 0.1 ppb, Ru and Ir were 0.05 ppb, Rh (0.02 ppb) and Au 0.2 ppb. The average of four determinations of USGS standard W-1 by this method, in ppb, are: Pt, 11.5 (13); Pd, 13.1 (14); Ru, 0.17 (0.2); Ir, 0.30 (0.3); Rh, 0.042 (no data); Au, 4.0 (4.3). Data in parentheses are accepted values. Precision was determined to be 13% (Pt), 7% (Pd), 6% (Ru), 7% (Ir), 21% (Rh) and 16% (Au).

Cu and Be were determined by ICP-ES following acid (10% HCl) dissolution and fusion of the remaining residue of a 1 g sample. The estimated validity of the results are ± 10 ppm + 5% of total concentration for Cu, and ±0.5 ppm + 5% of total concentration for Be.

The entire suite of REE from La to Lu were analyzed along with Y by ICP-MS. REE were determined on the remaining solution used for Cu and Be determination

after 10x pre-concentration and separation of major elements using an ion exchange resin. The detection limit for REE is about 20 ppb (D.C. Gregoire, 1991, pers. comm.). Repeated analysis of rock standard PCR-1 allowed precision measurements of ±5% for all the REE.

A.6 Isotopic Analysis of Whole Rock and Mineral Separates

A.6.1 Silicate Rocks and Minerals

Six fresh whole rock samples were washed in hydrochloric acid, rinsed in distilled water and sent to F. Ghazban at McMaster University for oxygen and strontium isotope analysis.

For strontium isotope analysis of whole rock samples, the samples were dissolved and strontium separated by wet chemical techniques (adapted from Beakhouse and Heaman, 1980). The $^{87}Sr/^{86}Sr$ was determined on a VG 354 five-collector solid-source mass spectrometer with computer controlled magnetic field switching and data processing capabilities. The error reported in the $^{87}Sr/^{86}Sr$ ratio is ±0.00002 at the 2σ level based on the rock standard NBS 987, which returned a $^{87}Sr/^{86}Sr$ ratio of 0.71024.

For oxygen isotope analysis of silicate rocks and minerals, samples were reacted with BrF_6 to produce O_2, which was reacted with a carbon rod at 550°C to produce CO_2, following the method of Longstaffe (1977), modified from Clayton and Mayeda (1963). All $\delta^{18}O$ values are reported relative to standard mean ocean water (SMOW). Duplicate analysis of standard NBS 28 returned $\delta^{18}O$ (SMOW) of

9.58 and 9.59 ‰. Duplicate analysis of Simberi rock sample SORD PLUT returned $\delta^{18}O$ values of 11.03 and 10.86 ‰. Nine mineral separates of olivine, clinopyroxene and magnetite were also determined as above. Duplicate analysis of an olivine separate returned $\delta^{18}O$ values of 4.94 and 5.00 ‰.

A.6.2 Carbonate minerals

Carbonate in the carbonate-amphibole-magnesiochromite, in the amphibole nodule and in vesicular lavas was sampled via micro-drilling and subsequently analyzed for $\delta^{13}C$, $\delta^{18}O$ and $^{87}Sr/^{86}Sr$. The oxygen and carbon isotope compositions were determined at the University of Ottawa by G. St.-Jean and M. McLaren using the method of McCrea (1950), where calcite is dissolved in 100% H_3PO_4 and the degassed CO_2 analyzed by mass spectrometry.

Strontium isotopic analyses of four of the carbonate separates from the massive carbonate portion of the carbonate-amphibole-magnesiochromite nodule was conducted by Krueger Enterprises Inc. of Cambridge, Massachusetts. The samples were digested briefly in cold weak HCl, and immediately centrifuged, to avoid leaching any Sr from silicate mineral impurities which may have been present. During the analysis procedure, three determinations of the $SrCO_3$ standard E&A gave a $^{87}Sr/^{86}Sr$ ratio of 0.70802 ± 0.00002 (2σ error).

A.7 Microprobe Analysis

Microanalysis of mineral and glass phases via electron probe was conducted using a Cameca MB-1 unit at McGill University, a Cameca SX-50 unit at the

Geological Survey of Canada and a JEOL 733 Superprobe unit at the Mineral Sciences Division of the Canadian Museum of Nature (CMON). Each probe was calibrated using natural and synthetic mineral standards (ZAF data reduction). Beam width varied from spot analyses (approximately 2 μm) for non-volatile mineral phases to a defocussed beam of approximately 10 to 15 μm diameter width for volatile and alkali-bearing minerals, glass and carbonate. The wide beam width was necessary to minimize Na and K mobility, particularly from glass phases which often yield apparent concentrations less than the true value. Small diameter (ca. <20 μm) melt inclusions and glass phases required spot analyses, and K and Na loss under these circumstances is a distinct possibility.

All elements were determined by wavelength dispersive techniques. Accuracy of determination for major elements is $\pm 1\%$ and $\pm 10\%$ for trace elements relative to standards. The McGill probe was operated using an 8nA beam current, 15 kV accelerating voltage and counting times were a maximum of 25 seconds. Backgrounds were counted for 5 seconds. Data reduction was carried out using the ONQUANT resident software of Cameca. The CMON probe was operated under 20 nA beam current and 15 kV accelerating voltage conditions. Count times ranged from 5 to 50 seconds depending on the elemental concentration and background was counted for 5 seconds. Reduction of X-ray spectra was performed using full ZAF correction methods using Tracor Northern software. The GSC probe was operated under 10 and 30 nA beam current and 15 kV accelerating voltage. Count times ranged from 10 to 20 seconds depending on elemental concentration and background was counted for 5 seconds.

Recalculation of mineral analyses into cation units was accomplished following the methods of Deer *et al.* (1966) and assisted by the computer program MINFILE by A.M. Afifi and E.J. Essene of the University of Michigan. A complete listing of analysed mineral and glass phases is provided below along with their calculated cation units and CIPW norms:

(a) Olivine data are presented on pages 233-235,

(b) Pyroxenes data are presented on pages 236-241,

(c) Phlogopite data are presented on page 242,

(d) Amphibole data are presented on page 243 and

(e) Glass data are presented on pages 244-245.

Olivine data

310.olx1	phenox core
310.olx2	phenox core
310.olx3	phenox core
310.4	phenox core
310.6a	phenox core
310.6a	phenox core
310.6a	phenox rim
310.olx4	phenox core
310.olx5	phenox core
310.olx6	megax core
310.olx7	megax core
310.olx8	ol core near 2dary inclusions
310.olx9	ol gn rim near 2dary incs
311d.3a	phenox core
311d.3a	duplicate of 311d.3a
311d.3ar	phenox rim
311d.4	core
311d.1d	small phenox in glass
311d.olx1	small phenox
311d.olx2	small-med gd ol phenox
311d.olx3	med-crse ol phenox
10.2K	OLIVINE ADJACENT TO MELT INCLUSION
10.2	OLIVINE CORE NEAR MELT INCLUSION
10.12M	OLIVINE CORE ADJACENT TO MELT INCLUSION
10.2P	OLIVINE ADJACENT TO PHLOGOPITE IN MELT INC
10.2H	OLIVINE ADJACENT TO PHLOGOPITE IN MELT INCLUSION
10.14A	OLIVINE CORE ADJACENT TO PHLOGOPITE IN MELT INCLUSION
10.5A	TWINNED OLIVINE CORE
10.5B	INNER PORTION OF REMOVED RIM OF TWINNED OLIVINE
10.5C	OUTERMOST PORTION OF REMOVED RIM OF TWINNED OLIVINE
10.6A	OLIVINE MEGAX CORE
10.6B	OUTER RIM OF OLIVINE MEGAX
10.12A	OLIVINE ADJACENT TO PHLOGOPITE 10.12B

Olivine data

	0.olx1	0.olx2	0.olx3	310.4	310.6a	310.6a	310.6a	0.olx4	0.olx5	0.olx6
FeO	10.46	11.84	7.79	7.92	10.74	11.10	14.17	12.13	14.34	9.20
MnO	0.25	0.35	0.10	0.14	0.26	0.29	0.55	0.35	0.57	0.19
SiO2	40.98	40.83	41.49	41.30	40.81	40.73	40.32	40.47	40.27	41.24
MgO	48.20	46.61	52.12	51.37	47.70	47.00	44.83	47.77	44.77	49.32
CaO	0.09	0.10	0.09	0.07	0.09	0.08	0.23	0.14	0.25	0.11
TiO2	-	0.02	0.01	-	-	0.02	0.01	-	0.01	0.01
NiO	0.24	0.24	0.33	0.35	0.25	0.27	0.11	0.23	0.09	0.26
TOTAL	100.22	99.99	101.93	101.15	99.85	99.49	100.22	101.09	100.30	100.33
	-	-	-	-	-	-	-	-	-	-
#Fe+2	0.21	0.25	0.16	0.16	0.22	0.23	0.30	0.25	0.30	0.19
#Mn+2	0.01	0.01	0.00	0.00	0.01	0.01	0.01	0.01	0.01	0.00
#Si+4	1.01	1.01	0.99	0.99	1.01	1.01	1.01	0.99	1.01	1.00
#Mg+2	1.76	1.72	1.85	1.84	1.75	1.74	1.67	1.75	1.67	1.79
#Ca+2	0.00	0.00	0.00	0.00	0.00	0.00	0.01	0.00	0.01	0.00
#Ni+2	0.00	0.00	0.01	0.01	0.00	0.01	0.00	0.00	0.00	0.01
#TOTAL	2.99	2.99	3.01	3.01	2.99	2.99	2.99	3.01	2.99	3.00
#O-2	4.00	4.00	4.00	4.00	4.00	4.00	4.00	4.00	4.00	4.00

	0.olx7	0.olx8	0.olx9	11d.3a	11d.3a	1d.3ar	311d.4	11d.1d	d.olx1	d.olx2
FeO	10.66	13.88	13.48	8.28	8.33	18.18	9.48	18.80	19.99	19.38
MnO	0.23	0.45	0.42	0.13	0.13	0.67	0.11	0.85	0.87	0.75
SiO2	40.97	40.36	40.49	41.44	41.62	39.77	41.35	39.42	39.24	39.30
MgO	47.42	45.37	45.99	50.05	50.34	41.94	49.56	40.55	39.76	40.12
CaO	0.08	0.21	0.19	0.10	0.09	0.28	0.07	0.26	0.33	0.32
TiO2	0.02	-	-	0.01	-	0.01	0.02	0.02	-	0.03
NiO	0.27	0.14	0.16	0.31	0.32	0.08	0.32	0.07	0.02	0.05
TOTAL	99.65	100.41	100.73	100.32	100.83	100.93	100.91	99.97	100.21	99.95
	-	-	-	-	-	-	-	-	-	-
#Fe+2	0.22	0.29	0.28	0.17	0.17	0.38	0.19	0.40	0.43	0.42
#Mn+2	0.00	0.01	0.01	0.00	0.00	0.01	0.00	0.02	0.02	0.02
#Si+4	1.01	1.00	1.00	1.01	1.00	1.01	1.00	1.01	1.01	1.01
#Mg+2	1.75	1.68	1.70	1.81	1.81	1.58	1.79	1.55	1.52	1.54
#Ca+2	0.00	0.01	0.01	0.00	0.00	0.01	0.00	0.01	0.01	0.01
#Ni+2	0.01	0.00	0.00	0.01	0.01	0.00	0.01	0.00	0.00	0.00
#TOTAL	2.99	3.00	3.00	2.99	3.00	2.99	3.00	2.99	2.99	2.99
#O-2	4.00	4.00	4.00	4.00	4.00	4.00	4.00	4.00	4.00	4.00

Olivine data

	d.olx3	10.2K	10.2	10.12M	10.2P	10.2H	10.14A	10.5A	10.5B	10.5C
FeO	10.40	7.20	7.75	13.81	8.01	8.77	12.38	8.30	12.36	13.57
MnO	0.17	-	-	-	-	-	-	-	-	-
SiO2	41.08	40.64	40.17	39.36	39.66	41.09	41.37	40.24	39.66	40.80
MgO	48.43	50.56	50.11	45.80	51.37	50.67	48.05	52.20	47.99	46.90
CaO	0.28	0.09	0.11	0.23	0.12	0.16	0.19	0.10	0.13	0.17
TiO2	-	0.01	0.01	-	-	0.01	-	-	-	-
NiO	0.15	-	-	-	-	-	-	-	-	-
TOTAL	100.51	98.50	98.15	99.20	99.16	100.70	101.99	100.84	100.14	101.44
	-	-	-	-	-	-	-	-	-	-
#Fe+2	0.21	0.15	0.16	0.29	0.16	0.18	0.25	0.17	0.26	0.28
#Mn+2	0.00	-	-	-	-	-	-	-	-	-
#Si+4	1.00	1.00	0.99	0.99	0.97	0.99	1.00	0.97	0.98	1.00
#Mg+2	1.77	1.85	1.85	1.72	1.88	1.83	1.74	1.88	1.77	1.72
#Ca+2	0.01	0.00	0.00	0.01	0.00	0.00	0.00	0.00	0.00	0.00
#Ni+2	0.00	-	-	-	-	-	-	-	-	-
#TOTAL	3.00	3.00	3.01	3.01	3.03	3.01	3.00	3.03	3.02	3.00
#O-2	4.00	4.00	4.00	4.00	4.00	4.00	4.00	4.00	4.00	4.00

	10.6A	10.6B	10.12A
FeO	7.19	12.37	13.76
MnO	-	-	-
SiO2	40.80	40.10	40.17
MgO	51.83	47.94	46.40
CaO	0.10	0.14	0.25
TiO2	-	-	-
NiO	-	-	-
TOTAL	99.92	100.55	100.58
	-	-	-
#Fe+2	0.15	0.26	0.29
#Mn+2	-	-	-
#Si+4	0.99	0.99	1.00
#Mg+2	1.87	1.76	1.72
#Ca+2	0.00	0.00	0.01
#Ni+2	-	-	-
#TOTAL	3.01	3.01	3.00
#O-2	4.00	4.00	4.00

Clinopyroxene data

310.8X	BROWN ROD
310.8	MASSIVE GN
310.8	CPX INTGN W FSPAR
310.8	TI-AL RCH AUGIT
310.8	cpx in met hb
310.1A	CPX CORE NR SPINEL
310.2A	GRN CORE CPX
310.2A	CPX CLEAR RIM
310.2A	CPX GREEN CORE
310.2A	CPX GREEN CORE
310.3a	cpx core
310.5	GROUNDMASS CPX
310.6b	cpx rplc ol
310.6b	cp rplc ol2
310.7b	cpx core
310.7b	px rim
22C	CPX RIM OF CARB XEN
22C.1A	PX GMASS
22C.3	BRN ROD IN HB GHOST
22C.3	PX ROD IN HB GHOST
22C.3	CRSE GRN ROD
22C.4	CPX CORE
22C.5A	OL GRN CPX CORE
22C.5B	DRK OL GN CPX MIDDLE
22C.5C	LIGHT CPX RIM
22C.7C	PX CORE SURR AMPH
22C.7C	GREEN CPX SUR AMPH
22C.9A	LRG CPX NR CALCITE
22C10D	CPX SURR BY AMPH
45B.2A	CPX BNG RP BY HB
45B.3B	CPX MEGAX CORE
45B.3B	MD GRN ZONE IN CPX
45B.3B	CLEAR CPX RIM
45B.4A	CPX
311D.1A	GROUNDMASS CPX CORE
311d1b	CPX RIM ADJACENT TO GLASS
311d1b	CPX RIM ADJACENT TO GLASS
311d2a	GMASS CPX CORE
311d2b	GMASS CPX RIM ADJACENT TO GLASS
311dx	CLEAR CORE OF GMASS CPX
311dx	GREEN GROWTH ZONE IN GMASS CPX
305.1a	GROUNDMASS CPX CORE
305.4A	GROUNDMASS CPX CORE
305.4B	GROUNDMASS CPX RIM
22.7px	
10.2g	melt inclusion daughter cpx

Clinopyroxene data

	310.8X	310.8	310.8	310.8	310.8	310.1A	310.2A	310.2A	310.2A	310.2A
SiO2	44.11	45.88	45.02	42.74	49.83	51.13	51.65	50.55	51.13	51.91
TiO2	2.06	1.91	2.16	2.11	0.61	0.39	0.15	0.51	0.33	0.46
Al2O3	10.23	8.82	8.41	10.90	4.95	3.32	0.88	3.88	1.39	1.66
Cr2O3	-	-	-	-	0.05	-	-	-	-	-
Fe2O3	6.68	5.41	6.41	10.44	3.05	3.68	5.84	2.80	6.78	5.78
FeO	2.29	1.87	1.51	0.66	3.69	2.22	6.87	3.59	6.75	7.68
MnO	0.04	0.09	0.13	0.09	0.14	0.11	0.80	0.08	0.68	0.69
NiO	-	-	-	-	-	-	-	-	-	-
MgO	11.37	12.60	12.32	12.64	14.17	15.39	10.39	14.64	9.99	9.59
CaO	22.32	22.34	22.40	20.65	22.70	23.57	20.38	23.34	19.56	18.97
Na2O	0.71	0.75	0.73	0.69	0.41	0.33	2.06	0.26	2.40	2.74
K2O	0.04	0.02	0.03	0.02	0.02	-	0.01	0.01	-	-
Total	99.85	99.69	99.12	100.95	99.62	100.14	99.04	99.66	99.01	99.48
#Si IV	1.65	1.71	1.69	1.58	1.85	1.88	1.97	1.87	1.95	1.97
#Al IV	0.35	0.29	0.31	0.42	0.15	0.12	0.03	0.13	0.05	0.03
T site	2.00	2.00	2.00	2.00	2.00	2.00	2.00	2.00	2.00	2.00
#Al VI	0.10	0.09	0.06	0.06	0.06	0.02	0.01	0.04	0.01	0.04
#Ti	0.06	0.05	0.06	0.06	0.02	0.01	0.00	0.01	0.01	0.01
#Cr	-	-	-	-	0.00	-	-	-	-	-
#Fe +3	0.19	0.15	0.18	0.29	0.08	0.10	0.17	0.08	0.19	0.16
#Fe +2	0.07	0.06	0.05	0.02	0.11	0.07	0.22	0.11	0.22	0.24
#Mn +2	0.00	0.00	0.00	0.00	0.00	0.00	0.03	0.00	0.02	0.02
#Ni	-	-	-	-	-	-	-	-	-	-
#Mg	0.63	0.70	0.69	0.70	0.78	0.84	0.59	0.81	0.57	0.54
#Ca	0.89	0.89	0.90	0.82	0.90	0.93	0.83	0.93	0.80	0.77
#Na	0.05	0.05	0.05	0.05	0.03	0.02	0.15	0.02	0.18	0.20
#K	0.00	0.00	0.00	0.00	0.00	-	0.00	0.00	-	-
M1,M2	2.00	2.00	2.00	2.00	2.00	2.00	2.00	2.00	2.00	2.00
#O	6.00	6.00	6.00	6.00	6.00	6.00	6.00	6.00	6.00	6.00
Charge	-	-1E-06	-	0.00	-	-	0.00	-	-	-

Clinopyroxene data

	310.3a	310.5	310.6b	310.6b	310.7b	310.7b	22C	22C.1A	22C.3	22C.3
SiO2	51.34	51.91	51.46	51.75	49.43	50.68	54.29	51.33	28.23	26.45
TiO2	0.39	0.31	0.35	0.20	0.69	0.43	-	0.41	3.19	3.99
Al2O3	3.54	3.07	3.48	2.93	4.47	3.07	0.68	3.14	16.21	17.64
Cr2O3	0.59	0.37	0.92	0.01	-	0.02	-	-	-	-
Fe2O3	1.10	1.42	1.91	1.64	3.95	3.95	0.76	3.06	37.88	40.20
FeO	3.40	3.30	2.72	5.04	3.73	7.31	3.73	3.62	-1E+01	-1E+01
MnO	0.06	0.07	0.07	0.21	0.17	0.69	0.37	0.13	0.18	0.16
NiO	-	0.06	-	-	-	-	-	-	-	-
MgO	15.44	15.81	15.74	15.18	13.64	11.07	18.03	15.45	14.84	14.98
CaO	22.97	23.20	23.23	22.15	22.12	21.57	21.04	22.79	11.60	11.27
Na2O	0.28	0.22	0.26	0.29	0.67	1.17	0.37	0.27	1.63	1.64
K2O	0.01	-	0.01	0.01	0.02	0.06	-	-	0.02	0.02
Total	99.12	99.73	100.15	99.40	98.90	100.03	99.28	100.21	101.28	102.60
#Si IV	1.90	1.91	1.89	1.92	1.85	1.91	1.99	1.89	1.07	0.99
#Al IV	0.10	0.09	0.11	0.08	0.15	0.09	0.01	0.11	0.72	0.78
T site	2.00	2.00	2.00	2.00	2.00	2.00	2.00	2.00	1.79	1.77
#Al VI	0.05	0.04	0.04	0.05	0.05	0.04	0.02	0.02	-	-
#Ti	0.01	0.01	0.01	0.01	0.02	0.01	-	0.01	0.09	0.11
#Cr	0.02	0.01	0.03	0.00	-	0.00	-	-	-	-
#Fe +3	0.03	0.04	0.05	0.05	0.11	0.11	0.02	0.08	1.08	1.13
#Fe +2	0.11	0.10	0.08	0.16	0.12	0.23	0.11	0.11	-4E-01	-4E-01
#Mn +2	0.00	0.00	0.00	0.01	0.01	0.02	0.01	0.00	0.01	0.01
#Ni	-	0.00	-	-	-	-	-	-	-	-
#Mg	0.85	0.87	0.86	0.84	0.76	0.62	0.98	0.85	0.84	0.84
#Ca	0.91	0.91	0.91	0.88	0.89	0.87	0.83	0.90	0.47	0.45
#Na	0.02	0.02	0.02	0.02	0.05	0.09	0.03	0.02	0.12	0.12
#K	0.00	-	0.00	0.00	0.00	0.00	-	-	0.00	0.00
M1,M2	2.00	2.00	2.00	2.00	2.00	2.00	2.00	2.00	2.21	2.23
#O	6.00	6.00	6.00	6.00	6.00	6.00	6.00	6.00	6.00	6.00
Charge	-	-	0.00	-1E-06	-	-	-	-	0.00	-

Clinopyroxene data

	22C.3	22C.4	22C.5A	22C.5B	22C.5C	22C.7C	22C.7C	22C.9A	22C10D	45B.2A
SiO2	48.03	52.59	51.92	51.18	49.73	48.52	46.10	54.99	55.46	51.92
TiO2	1.04	0.14	0.33	0.24	0.53	0.62	0.69	0.02	0.03	0.25
Al2O3	6.95	1.08	2.37	2.34	4.86	6.62	8.77	0.57	0.69	2.76
Cr2O3	-	-	-	-	-	-	-	-	-	-
Fe2O3	5.44	3.16	3.02	4.45	4.14	3.44	5.54	-	-	3.59
FeO	1.50	8.67	5.11	8.34	2.24	4.10	3.38	4.18	3.73	4.38
MnO	0.32	0.91	0.47	0.80	0.11	0.11	0.14	0.43	0.36	0.16
NiO	-	-	-	-	-	-	-	-	-	-
MgO	14.63	11.13	13.70	9.91	14.55	13.13	11.70	16.37	16.34	13.01
CaO	21.05	21.54	22.66	20.60	23.69	22.97	23.43	22.74	23.08	22.91
Na2O	0.74	1.27	0.72	1.77	0.28	0.33	0.29	0.59	0.61	1.12
K2O	0.02	0.03	-	-	-	-	-	-	0.01	0.01
Total	99.73	100.53	100.30	99.63	100.13	99.85	100.05	99.89	100.31	100.11
#Si IV	1.77	1.97	1.92	1.94	1.83	1.80	1.72	2.01	2.02	1.92
#Al IV	0.23	0.03	0.08	0.06	0.17	0.20	0.28	-	-	0.08
T site	2.00	2.00	2.00	2.00	2.00	2.00	2.00	2.01	2.02	2.00
#Al VI	0.07	0.02	0.03	0.05	0.04	0.09	0.11	0.02	0.03	0.04
#Ti	0.03	0.00	0.01	0.01	0.01	0.02	0.02	0.00	0.00	0.01
#Cr	-	-	-	-	-	-	-	-	-	-
#Fe +3	0.15	0.09	0.08	0.13	0.11	0.10	0.16	-	-	0.10
#Fe +2	0.05	0.27	0.16	0.26	0.07	0.13	0.11	0.13	0.11	0.14
#Mn +2	0.01	0.03	0.01	0.03	0.00	0.00	0.00	0.01	0.01	0.01
#Ni	-	-	-	-	-	-	-	-	-	-
#Mg	0.80	0.62	0.76	0.56	0.80	0.73	0.65	0.89	0.89	0.72
#Ca	0.83	0.87	0.90	0.84	0.94	0.91	0.94	0.89	0.90	0.91
#Na	0.05	0.09	0.05	0.13	0.02	0.02	0.02	0.04	0.04	0.08
#K	0.00	0.00	-	-	-	-	-	-	0.00	0.00
M1,M2	2.00	2.00	2.00	2.00	2.00	2.00	2.00	1.99	1.98	2.00
#O	6.00	6.00	6.00	6.00	6.00	6.00	6.00	6.00	6.01	6.00
Charge	-	-	-	-	-	-	-1E-06	0.00	0.02	-

Clinopyroxene data

	45B.3B	45B.3B	45B.3B	45B.4A	11D.1A	311d1b	311d1b	311d2a	311d2b	311dx
SiO2	48.88	45.29	49.52	48.95	46.41	49.76	49.81	46.98	52.67	51.12
TiO2	0.56	0.81	0.58	0.68	1.33	0.69	0.67	0.99	0.42	0.50
Al2O3	4.72	7.95	4.79	4.46	8.20	4.63	4.95	7.70	3.96	3.74
Cr2O3	-	-	-	-	0.02	0.03	-	0.08	0.15	0.22
Fe2O3	4.90	6.16	3.43	4.78	4.88	4.22	2.04	5.18	1.52	2.08
FeO	4.51	6.47	5.69	6.17	4.13	3.60	5.62	3.41	4.42	3.13
MnO	0.32	0.28	0.17	0.54	0.24	0.19	0.13	0.12	0.10	0.09
NiO	-	-	-	-	-	-	-	0.03	-	0.06
MgO	12.29	9.35	12.47	10.50	11.82	14.22	13.46	12.49	15.48	15.31
CaO	23.15	22.92	22.83	22.67	22.40	22.40	22.22	22.58	22.83	23.19
Na2O	0.55	0.44	0.51	1.00	0.55	0.48	0.42	0.50	0.43	0.28
K2O	-	0.02	0.01	0.01	-	0.02	-	-	-	-
Total	99.88	99.69	100.00	99.76	99.98	100.24	99.32	100.05	101.98	99.71
#Si IV	1.83	1.73	1.85	1.85	1.73	1.84	1.86	1.75	1.90	1.88
#Al IV	0.17	0.27	0.15	0.15	0.27	0.16	0.14	0.25	0.10	0.12
T site	2.00	2.00	2.00	2.00	2.00	2.00	2.00	2.00	2.00	2.00
#Al VI	0.04	0.08	0.06	0.05	0.09	0.04	0.08	0.09	0.06	0.05
#Ti	0.02	0.02	0.02	0.02	0.04	0.02	0.02	0.03	0.01	0.01
#Cr	-	-	-	-	0.00	0.00	-	0.00	0.00	0.01
#Fe +3	0.14	0.18	0.10	0.14	0.14	0.12	0.06	0.15	0.04	0.06
#Fe +2	0.14	0.21	0.18	0.19	0.13	0.11	0.18	0.11	0.13	0.10
#Mn +2	0.01	0.01	0.01	0.02	0.01	0.01	0.00	0.00	0.00	0.00
#Ni	-	-	-	-	-	-	-	0.00	-	0.00
#Mg	0.69	0.53	0.69	0.59	0.66	0.78	0.75	0.69	0.83	0.84
#Ca	0.93	0.94	0.91	0.92	0.90	0.89	0.89	0.90	0.88	0.92
#Na	0.04	0.03	0.04	0.07	0.04	0.03	0.03	0.04	0.03	0.02
#K	-	0.00	0.00	0.00	-	0.00	-	-	-	-
M1,M2	2.00	2.00	2.00	2.00	2.00	2.00	2.00	2.00	2.00	2.00
#O	6.00	6.00	6.00	6.00	6.00	6.00	6.00	6.00	6.00	6.00
Charge	-	-	-	-	-	0.00	-	-	-	-

Clinopyroxene data

	311dx	305.1a	305.4A	305.4B	22.7px	10.2g
SiO2	49.15	49.97	50.41	49.61	49.38	48.89
TiO2	0.79	0.69	0.58	0.67	0.78	1.76
Al2O3	5.43	5.10	4.59	4.96	5.75	5.60
Cr2O3	-	0.04	0.07	-	0.08	0.60
Fe2O3	3.14	1.98	1.99	2.87	4.38	5.63
FeO	4.69	5.37	5.28	5.05	2.61	-9E-01
MnO	0.16	0.20	0.09	0.19	0.10	-
NiO	0.02	-	-	0.02	0.07	-
MgO	13.49	13.54	14.36	13.78	14.46	14.47
CaO	22.25	22.16	22.20	21.90	23.43	22.48
Na2O	0.43	0.49	0.30	0.44	0.25	1.37
K2O	0.02	-	-	-	-	0.01
Total	99.57	99.54	99.87	99.49	101.30	99.87
#Si IV	1.83	1.86	1.87	1.85	1.80	1.79
#Al IV	0.17	0.14	0.13	0.15	0.20	0.21
T site	2.00	2.00	2.00	2.00	2.00	2.00
#Al VI	0.07	0.08	0.07	0.07	0.05	0.04
#Ti	0.02	0.02	0.02	0.02	0.02	0.05
#Cr	-	0.00	0.00	-	0.00	0.02
#Fe +3	0.09	0.06	0.06	0.08	0.12	0.16
#Fe +2	0.15	0.17	0.16	0.16	0.08	-3E-02
#Mn +2	0.01	0.01	0.00	0.01	0.00	-
#Ni	0.00	-	-	0.00	0.00	-
#Mg	0.75	0.75	0.79	0.77	0.79	0.79
#Ca	0.89	0.88	0.88	0.87	0.92	0.88
#Na	0.03	0.04	0.02	0.03	0.02	0.10
#K	0.00	-	-	-	-	0.00
M1,M2	2.00	2.00	2.00	2.00	2.00	2.00
#O	6.00	6.00	6.00	6.00	6.00	6.00
Charge	-	-	-	-	-1E-06	-

Phlogopite data

	10.2J	10.12B	310.1a	310.1a	310.2b	310.3a
SiO2	37.85	38.26	34.58	36.53	39.51	36.82
TiO2	7.41	4.16	8.01	7.35	4.73	8.06
Al2O3	13.12	13.69	14.72	14.72	13.03	14.33
Cr2O3	-	-	0.04	0.04	0.01	0.27
Fe2O3	0.00	-	-	0.00	0.00	0.00
FeO	5.37	7.04	9.07	8.99	7.05	10.09
MnO	-	-	0.06	0.06	0.15	-
MgO	20.40	20.72	16.07	17.09	21.18	16.29
Li2O	-	-	-	-	-	-
BaO	-	-	-	0.24	0.22	0.77
CaO	0.08	0.06	0.30	0.26	0.06	0.13
Na2O	1.20	0.95	0.34	0.33	0.56	0.59
K2O	9.47	9.60	9.95	9.71	10.13	9.46
Rb2O	-	-	-	-	-	-
Cs2O	-	-	-	-	-	-
H2O	3.49	3.44	3.47	3.36	2.82	3.77
F	1.38	1.45	1.20	1.50	2.74	0.55
Cl	0.04	0.04	0.06	0.05	0.05	0.14
O=F	0.58	0.61	0.50	0.63	1.15	0.23
O=Cl	0.01	0.01	0.01	0.01	0.01	0.03
Total	99.22	98.79	97.35	99.58	101.06	101.00
#Si IV	5.47	5.58	5.22	5.35	5.65	5.36
#Al IV	2.24	2.35	2.62	2.54	2.20	2.46
#Fe IV	0.00	-	-	0.00	0.00	0.00
#Ti IV	0.30	0.07	0.17	0.10	0.16	0.18
T site	8.00	8.00	8.00	8.00	8.00	8.00
#Al VI	-	-	-	-	-	-
#Ti VI	0.51	0.39	0.74	0.71	0.35	0.70
#Cr	-	-	0.00	0.00	0.00	0.03
#Fe +3	-	-	-	-	-	-
#Fe +2	0.65	0.86	1.14	1.10	0.84	1.23
#Mn +2	-	-	0.01	0.01	0.02	-
#Mg	4.39	4.50	3.61	3.73	4.51	3.53
#Li	-	-	-	-	-	-
O site	5.55	5.75	5.51	5.55	5.73	5.49
#Ba	-	-	-	0.01	0.01	0.04
#Ca	0.01	0.01	0.05	0.04	0.01	0.02
#Na	0.34	0.27	0.10	0.09	0.15	0.17
#K	1.75	1.79	1.91	1.82	1.85	1.76
#Rb	-	-	-	-	-	-
#Cs	-	-	-	-	-	-
A site	2.09	2.06	2.06	1.96	2.02	1.99
#O	20.00	20.00	20.00	20.00	20.00	20.00
#OH	3.36	3.32	3.41	3.29	2.75	3.71
#F	0.63	0.67	0.57	0.69	1.24	0.25
#Cl	0.01	0.01	0.02	0.01	0.01	0.03
Charge	0.00	0.00	0.00	-1E-06	-2E-06	0.00

Amphibole data

	22c.7j	22.8a	22.9	45b.2b	337.a3	313.4b
SiO2	39.95	40.50	41.39	40.45	40.57	42.50
TiO2	1.55	1.70	1.89	1.48	1.06	1.15
Al2O3	14.10	14.09	13.72	13.46	13.77	11.91
Cr2O3	-	-	-	-	-	-
Fe2O3	-	0.00	-	0.00	-	0.00
FeO	11.90	11.09	9.75	14.90	9.89	13.01
MnO	0.12	0.01	0.16	0.21	-	-
MgO	14.10	14.86	15.43	11.84	15.32	13.77
ZnO	-	-	-	-	-	-
CaO	12.50	12.29	12.19	11.66	12.06	11.16
Na2O	2.18	2.11	2.18	2.74	2.44	3.12
K2O	1.57	1.55	1.44	1.38	1.70	1.14
H2O	2.02	2.04	2.05	2.00	1.92	1.92
F	-	-	-	-	0.20	0.20
Cl	-	-	-	-	-	-
O=F	-	-	-	-	0.08	0.08
O=Cl	-	-	-	-	-	-
Total	99.99	100.24	100.20	100.12	98.85	99.80
#Si IV	5.94	5.97	6.05	6.07	6.04	6.31
#Al IV	2.06	2.03	1.95	1.93	1.96	1.69
#Fe +3	-	-	-	-	-	-
#Ti IV	-	-	-	-	-	-
T site	8.00	8.00	8.00	8.00	8.00	8.00
#Al VI	0.41	0.41	0.42	0.45	0.45	0.39
#Fe +3	-	0.00	-	0.00	-	0.00
#Ti	0.17	0.19	0.21	0.17	0.12	0.13
#Cr	-	-	-	-	-	-
#Mg	3.12	3.26	3.36	2.65	3.40	3.05
#Fe +2	1.29	1.13	1.01	1.73	1.03	1.43
#Zn	-	-	-	-	-	-
#Mn	-	-	-	-	-	-
#Ca	-	-	-	-	-	-
M1,2,3	5.00	5.00	5.00	5.00	5.00	5.00
#Mg	-	-	-	-	-	-
#Fe +2	0.18	0.23	0.18	0.14	0.20	0.19
#Zn	-	-	-	-	-	-
#Mn	0.02	0.00	0.02	0.03	-	-
#Ca	1.80	1.77	1.80	1.83	1.80	1.78
#Na	-	-	-	-	-	0.04
M4 site	2.00	2.00	2.00	2.00	2.00	2.00
#Ca	0.19	0.17	0.11	0.04	0.12	-
#Na	0.63	0.60	0.62	0.80	0.70	0.86
#K	0.30	0.29	0.27	0.26	0.32	0.22
A site	1.12	1.07	1.00	1.10	1.15	1.08
#O	22.00	22.00	22.00	22.00	22.00	22.00
#OH	2.00	2.00	2.00	2.00	1.91	1.91
#F	-	-	-	-	0.09	0.09
#Cl	-	-	-	-	-	-
Charge	0.00	-	0.00	-	-3E-06	-7E-07

SAMPLE	310.2F	310.1C	10.20	10.2CiA	307.3D	10.2Q	10.2CiB	10.12D	307.1Aii	307.1Ai	307.1Aiii	313.4E	310.3B	22C.7F	10.7G	10.12C	22C.7D	22C.7K
TYPE	K	K	K	K	K	K	K	K	K	MAFIC	NA	NA	NA	NA	NA	NA	NA	NA
SIO2	60.34	64.21	61.13	65.29	63.02	60.77	64.02	58.94	61.22	47.94	59.94	57.30	48.30	49.42	51.45	62.25	53.81	53.27
NA2O	0.74	2.06	5.20	1.20	1.93	3.51	5.31	1.18	1.67	0.80	6.38	17.04	10.14	22.06	15.68	7.60	8.77	9.11
K2O	13.59	13.99	12.10	12.85	13.68	11.25	11.93	12.80	12.03	0.79	0.38	0.03	0.26	0.04	0.14	2.62	1.09	0.72
AL2O3	19.23	19.38	19.29	20.44	19.19	18.70	20.01	21.39	19.75	7.35	24.78	25.63	27.07	21.95	29.36	22.09	22.32	22.78
TIO2	0.88	0.13	0.03	0.10	0.08	0.27	0.17	0.02	0.05	1.56	0.07	0.00	0.00	0.11	0.00	0.14	0.46	0.58
MGO	0.04	0.01	0.00	0.07	0.00	0.38	0.01	0.29	0.11	10.85	0.04	0.01	0.01	0.01	0.00	0.01	1.26	1.06
FEO	0.61	0.18	0.31	0.16	0.24	0.33	0.18	0.31	0.63	6.84	0.53	0.07	0.12	0.13	0.20	0.39	3.39	2.49
CAO	3.30	0.47	0.98	0.48	0.29	0.66	1.05	2.19	0.70	19.44	0.47	0.27	6.84	0.04	4.11	3.04	2.01	2.21
P2O5	0.03	0.07	0.22	0.00	0.02	0.05	0.03	0.05	0.09	1.19	0.03	0.00	0.00	0.02	0.07	0.06	0.12	0.18
MNO	0.02	0.07	0.00	0.00	0.00	0.00	0.00	0.00	0.00	0.20	0.00	0.00	0.05	0.00	0.00	0.00	0.05	0.00
CL	0.01	0.02	0.02	0.00	0.02	0.02	0.02	0.02	0.04	0.03	0.01	0.00	0.03	0.02	0.02	0.02	0.02	0.03
BAO	0.00	0.21	0.00	ND	0.00	0.00	0.00	0.00	0.00	0.00	0.00	0.00	0.00	0.03	0.00	0.00	0.02	0.18
F	0.00	0.00	0.04	0.00	0.00	0.08	0.05	0.02	0.14	0.23	0.13	0.00	0.00	0.00	0.05	0.00	0.00	0.09
CR2O3	0.00	0.05	0.00	0.00	0.00	0.00	0.00	0.00	0.00	0.00	0.00	0.00	0.02	0.02	0.00	0.00	0.05	0.06
NIO	0.04	0.00	ND	ND	ND	ND	ND	0.00	ND	0.00	ND	ND	0.00	0.03	ND	0.00	0.00	0.03
ZNO	0.00	0.00	ND	ND	ND	ND	ND		ND	ND	ND	ND	0.00	0.24	ND	ND	0.00	0.00
SRO	0.61	0.31	0.21	1.27	0.20	0.47	0.29	2.00	0.20	0.08	0.11	0.14	0.05	0.07	0.07	0.35	0.07	0.05
V2O3	0.00	0.00	ND	ND	ND	ND	ND		ND	ND	ND	ND	0.00	0.02	ND	ND	0.02	0.00
SO3	0.00	0.04	ND	ND	ND	ND	ND		ND	ND	ND	ND	0.00	0.10	ND	ND	0.07	0.04
TOTAL	99.48	101.20	99.54	101.85	98.67	96.49	103.08	99.21	96.64	97.30	92.88	100.59	92.88	94.30	101.16	98.58	93.49	92.88

CIPW NORMS CALCULATED ON SELECTED ANALYSES ONLY, ASSUMING FEO/FEOtotal = 0.1

AP	0.03	0.07	0.24		0.02					1.14				0.02	0.07	0.06		
IL	0.08	0.14	0.03	0.02	0.07					1				0.01		0.04		
OR	59.56	60.4	52.68	55.36	60.33					3.1		0.13	1.2	0.18	0.6	11.23		
AB	7.06	10.33	17.94	11.25	11.22					3.44		78.11	55.85	54.47	52.92	65.57		
AN	2.42			2.92						7.02								
DI	0.37	0.09								72.97		0.1	0.26		0.03	0.09		
HY				0.3														
OL										5.41				0.03				
NE										1.79		4.75	23.56	13.26	25.47			
AC		0.2	0.35		0.28							0.08	0.14	0.15	0.22	0.43		
C				0.37														
Q	22.26	25.62	19.32	29.64	25.69											13.81		
HM	0.24			0.06						2.39								
TN	1.77	0.09	0.02		0.09											0.24		
PV										1.75				0.14				
RU				0.08										0.04				
NS		2.05	7.21		1.63							16.21	0.53	31.7	10.5	1.13		
WO	6.2	1	2.2		0.67							0.62	18.45		10.19	7.4		

Glass analyses

SAMPLE	22C.7L	22A.GLA	22C.7D	31D.5B	31D.1C	10.2N	10.2Ci	10.7I	10.12	10.12	10.13C	10.13A	310.1D
TYPE	NA	NA		NA	NA	NA	NA	NA	NA	NA	NA	NA	NA
SIO2	53.39	49.59	58.47	61.85	62.00	49.54	59.12	55.68	56.22	45.47	57.14	55.00	55.82
NA2O	7.45	19.61	2.54	3.57	3.31	9.75	4.89	8.01	5.94	9.15	9.10	10.92	8.28
K2O	0.85	0.04	0.65	0.04	0.12	0.17	0.15	0.06	1.98	2.03	1.03	0.78	0.15
AL2O3	22.47	24.26	22.57	23.64	23.26	25.79	25.04	28.28	23.28	29.07	26.99	25.14	24.51
TIO2	0.53	0.02	0.57	0.05	0.02	0.01	0.08	0.01	0.04	0.04	0.07	0.07	0.00
MGO	1.21	0.02	0.89	0.01	0.01	0.01	0.01	0.00	0.14	2.02	0.02	0.02	0.00
FEO	2.78	0.07	2.50	0.34	0.29	0.08	0.26	0.29	0.28	0.53	0.60	0.47	0.03
CAO	1.99	0.10	1.93	0.68	0.88	2.98	0.26	1.22	2.21	2.96	7.94	6.03	1.90
P2O5	0.01	0.00	0.00	0.00	0.00	0.04	0.03	0.02	0.09	0.33	0.09	0.07	0.00
MNO	0.18	0.07	0.05	0.01	0.02	0.00	0.00	0.00	0.00	0.00	0.00	0.00	0.00
CL	0.01	0.00	0.00	0.00	0.00	0.03	0.00	0.04	0.03	3.53	0.01	0.02	0.00
BAO	0.06	0.13	0.00	0.00	0.00	0.00	0.00	0.00	0.00	0.00	0.00	0.00	0.00
F	0.00	0.00	0.00	0.00	0.00	0.11	0.13	0.04	0.00	0.06	0.06	0.00	0.00
CR2O3	0.00	0.00	0.00	0.02	0.00	0.00	0.00	0.00	0.00	0.00	0.00	0.00	0.01
NIO	0.02	0.04	0.00	0.03	0.01	0.00	ND	ND	0.00	ND	ND	ND	0.00
ZNO	0.35	0.30	0.00	0.00	0.00	ND	ND	ND	ND	ND	ND	ND	0.00
SRO	0.09	0.04	0.00	0.00	0.00	0.09	0.06	0.02	0.29	0.29	0.67	0.63	0.03
V2O3	0.00	0.00	0.00	0.00	0.00	ND	ND	ND	ND	ND	ND	ND	0.07
SO3	0.00	0.02	0.00	0.00	0.00	ND	ND	ND	ND	ND	ND	ND	0.03
TOTAL	91.38	94.01	90.16	90.23	89.93	88.59	90.02	93.67	90.49	95.46	103.71	99.15	90.83

A.8 Whole Rock Analyses

The following pages contain analytical data for major elements, trace elements and Sr and O isotopic ratios for the Simberi volcanic rocks. Samples are grouped into compositional categories according to the IUGS chemical classification system. The first two rows are grid location descriptors in metres based on the Kennecott Exploration (Australia) Ltd. detailed survey grid system. Major elements are expressed in wt.%; trace elements in parts per million (ppm), unless otherwise indicated as parts per billion (ppb). Elements which were not determined or below the level of detection are noted by the abbreviations ND and BLD, respectively. The ferric/ferrous ratio was not determined on two rock samples, 326 and 332, and the iron is reported as total Fe_2O_3.

Also included in the data table are rock samples collected on Simberi Island and reported by Johnson *et al.* (1975) and Wallace *et al.* (1983).

SAMPLE #	22	301	303	306	311	312	313xe	320	326
mE	9525	10090	9790	13030	8090	11300	10230	9875	10080
mN	7135	8175	7945	8920	9790	8560	7950	8350	8320
	Hawaiite	Mugearite	Hawaiite	AOB	AOB	AOB	Mugearite	Mugearite	Mugearite
SiO2	49.73	50.50	49.56	49.66	46.94	46.13	55.30	49.79	49.75
TiO2	0.70	0.62	0.87	0.86	0.78	0.95	0.41	0.63	0.64
Al2O3	17.06	18.61	16.42	19.87	12.79	15.90	19.78	18.40	18.24
Fe2O3 (t)	3.98	4.86	6.42	5.30	4.97	4.50	3.76	4.76	8.24
FeO	3.03	2.44	4.17	1.59	4.36	5.96	1.62	3.55	nd
MnO	0.16	0.22	0.21	0.10	0.17	0.18	0.17	0.20	0.21
MgO	4.10	2.79	4.67	3.76	10.53	6.74	1.33	3.30	3.04
CaO	11.35	9.05	8.18	9.28	13.42	13.09	6.19	8.63	8.06
Na2O	3.83	4.72	3.83	2.70	3.17	2.53	5.36	5.35	4.18
K2O	1.99	2.77	2.81	1.77	0.42	1.42	3.21	2.00	3.25
P2O5	0.38	0.51	0.12	0.49	0.29	0.40	0.26	0.42	0.57
S	0.01	0.02	0.01	0.01	0.00	0.00	0.01	0.16	0.04
H2O	2.20	1.90	2.90	4.20	2.40	1.80	1.20	2.30	2.20
CO2	1.30	1.50	0.00	0.00	0.10	1.10	0.70	0.10	1.30
Total	99.82	100.51	100.17	99.59	100.34	100.70	99.30	99.59	99.72
100Mg/(Mg+Fe")	70.69	67.08	66.62	80.82	81.15	66.84	59.41	62.36	ND
100Mg/(Mg+Fe"total	52.50	42.19	45.56	51.31	68.00	54.55	32.15	42.89	42.22
87Sr/86Sr	0.70372	ND	ND	ND	0.70354	ND	ND	ND	ND
18O/16O	12.38	ND	ND	ND	11.35	ND	ND	ND	ND
Trace Elements (ppm unless indicated otherwise)									
Sc	16	7	20	17	27	32	4	13	8
Cr	197	43	32	114	397	149	8	16	19
Co	44	31	30	23	43	41	20	30	31
Ni	289	24	19	52	149	124	27	13	12
V	332	296	462	353	240	430	223	345	306
Rb	45	45	35	18	23	15	32	29	50
Sr	2889	2473	1359	2270	1516	1583	2837	2227	2505
Zr	68	84	58	71	57	41	43	67	84
Ba	613	323	238	317	102	166	357	281	518
Cs	18.00	4.90	BLD	0.80	5.40	BLD	2.40	2.70	15.00
Th	2.00	2.90	1.40	2.20	0.80	1.10	2.70	2.60	3.10
U	2.10	3.10	1.50	1.50	0.90	0.80	1.70	2.70	3.20
Be	1.40	2.00	1.30	1.50	1.20	1.10	1.80	1.60	1.90
Y	21.00	24.00	18.00	25.00	19.00	19.00	23.00	19.00	24.00
Hf	BLD	2.00	1.00	3.00	1.00	2.00	1.00	2.00	BLD
Ta	1.10	0.70	0.50	BLD	0.50	0.60	1.10	0.70	0.50
Nb	BLD	BLD	BLD	BLD	BLD	BLD	BLD	BLD	BLD
La	23	37	20	34	18	21	34	29	38
Ce	45	66	36	59	39	44	69	52	70
Pr	6.30	8.60	5.00	8.50	5.60	6.20	9.00	6.90	9.20
Nd	25	35	22	36	25	27	36	30	37
Sm	5.80	6.60	4.90	7.20	5.40	5.60	6.80	6.20	7.20
Eu	2.30	2.50	1.70	2.40	2.40	2.50	2.40	2.30	2.60
Gd	4.80	5.10	4.20	5.80	4.90	5.40	5.90	5.80	6.10
Tb	0.62	0.72	0.56	0.79	0.60	0.70	0.72	0.78	0.81
Dy	3.30	3.80	3.00	3.90	3.30	3.70	3.60	3.40	4.00
Ho	0.65	0.76	0.57	0.74	0.65	0.68	0.65	0.65	0.77
Er	1.75	2.04	1.47	2.02	1.58	1.73	1.95	1.80	2.33
Tm	0.23	0.30	0.22	0.27	0.22	0.25	0.27	0.26	0.33
Yb	1.60	2.10	1.50	1.90	1.50	1.60	1.70	1.70	2.30
Lu	0.28	0.36	0.25	0.34	0.26	0.28	0.32	0.31	0.38
Cu	110	120	140	64	94	170	85	120	120
Zn	65	90	83	82	60	120	63	140	90
As	2.30	2.50	2.80	3.30	BLD	BLD	8.20	1.90	5.40
W	129	70	45	17	51	59	62	64	54
Au (ppb)	5.60	3.60	6.90	0.33	2.20	4.10	0.10	6.80	1.00
Ir (ppb)	BLD	BLD	BLD	BLD	0.05	BLD	BLD	BLD	ND
Ru (ppb)	BLD	0.07	0.05	BLD	0.05	0.12	0.06	BLD	ND
Rh (ppb)	0.03	BLD	BLD	BLD	0.02	BLD	BLD	BLD	ND
Pt (ppb)	2.10	1.90	32.90	12.60	2.90	3.10	0.70	2.90	ND
Pd (ppb)	3.80	1.30	4.10	2.10	3.60	3.70	2.30	2.80	ND
	BLD = below limit detection; ND = not determined								
CIPW Norm									
Ap	0.87	1.16	0.27	1.18	0.65	0.90	0.59	0.97	1.29
Il	1.38	1.22	1.70	1.72	1.52	1.85	0.80	1.26	0.46
Mt	6.00	7.00	9.59	3.11	7.37	6.68	4.72	7.28	
Or	12.20	16.85	17.06	10.97	2.53	8.57	19.47	12.43	19.71
Ab	25.68	29.19	28.30	23.96	16.97	13.87	44.87	26.85	31.91
An	24.37	22.05	19.84	38.67	19.84	28.49	20.98	21.34	21.98
Di	24.92	15.48	16.62	4.78	36.47	28.32	6.88	16.60	10.78
Hy				7.59					
Ol	0.26		3.91		9.01	7.02	0.16	2.00	1.96
Ne	4.31	6.47	2.71		5.64	4.29	0.92	11.25	2.38
C									
Q				4.61					
Hm				3.43			0.61		8.48

SAMPLE #	332	335	337	347	SORD PLUTBOTSOR-1		310	45A	302
mE	9710	9300	9735	10170	10000	8100	8110	10265	9940
mN	9540	7780	7685	7380	9820	9800	9800	8000	8120
	BenmoreitMugeariteHawaiite			AOB	Mugearite	AOB	AOB	MugeariteMugearite	
SiO2	53.45	53.02	48.06	48.39	55.00	46.00	45.70	49.34	54.78
TiO2	0.43	0.47	0.70	0.77	0.42	0.66	0.65	0.61	0.51
Al2O3	19.29	19.60	17.24	16.89	19.20	12.50	12.43	18.35	20.27
Fe2O3 (t)	6.11	3.74	5.89	5.30	3.80	5.10	4.53	5.05	3.78
FeO	nd	1.88	6.28	3.28	1.70	4.40	4.74	2.67	1.09
MnO	0.20	0.19	0.33	0.18	0.17	0.16	0.17	0.20	0.11
MgO	1.87	2.36	3.36	5.26	1.92	13.50	13.73	2.70	1.23
CaO	5.26	7.44	7.13	11.02	6.42	10.90	10.57	8.75	4.75
Na2O	4.12	4.62	3.31	3.00	5.30	3.30	3.19	4.64	4.25
K2O	5.57	3.21	2.99	2.52	3.63	1.20	1.03	3.21	3.63
P2O5	0.31	0.38	0.35	0.36	0.28	0.40	0.38	0.42	0.37
S	0.08	0.00	0.01	0.02	0.01	0.00	0.00	0.01	0.00
H2O	1.50	2.80	2.10	2.20	1.50	2.00	1.90	2.30	3.50
CO2	1.90	0.20	2.40	0.20	1.30	0.20	0.10	1.80	0.30
Total	100.09	99.91	100.15	99.39	100.65	100.32	99.12	100.05	98.57
100Mg/(Mg+Fe")	ND	69.11	48.81	74.08	66.81	84.54	83.77	64.32	66.79
100Mg/(Mg+Fe"total	37.74	44.51	34.09	53.81	40.07	72.80	73.52	40.02	32.80
87Sr/86Sr	ND	ND	ND	ND	0.70391	0.70370	0.70362	0.70400	ND
18O/16O	ND	ND	ND	ND	10.94	10.89	10.05	12.33	ND
Trace Elements (pp									
Sc	5	5	17	23	6	32	19	9	5
Cr	18	10	32	71	16	830	637	9	18
Co	17	15	65	37	42	130	52	35	18
Ni	19	19	48	34	18	400	449	10	9
V	225	207	363	352	150	230	307	299	227
Rb	113	50	46	36	57	38	32	57	59
Sr	2077	2592	1700	2505	2100	1500	1480	2325	2043
Zr	104	80	52	67	80	50	56	77	100
Ba	708	349	277	360	420	160	144	294	361
Cs	11.00	BLD	4.40	5.20	12.00	BLD	BLD	42.00	5.20
Th	4.00	3.20	1.70	1.70	5.00	1.40	1.30	2.50	3.60
U	3.90	3.20	1.70	2.00	4.60	1.20	1.10	2.50	3.40
Be	2.20	1.80	1.90	1.40	2.10	1.40	ND	ND	ND
Y	18.00	22.00	25.00	20.00	18.00	42.00	15.00	27.00	17.00
Hf	2.00	3.00	1.00	2.00	BLD	BLD	2.00	BLD	2.00
Ta	BLD	0.50	BLD	1.20	1.20	2.20	0.60	0.70	0.80
Nb	BLD	BLD	BLD	BLD	19.00	17.00	BLD	BLD	BLD
La	33	35	22	23	33	20	15	17	26
Ce	58	61	40	43	58	39	39	51	52
Pr	7.50	8.10	5.60	6.10	7.30	ND	ND	ND	ND
Nd	29	34	25	26	28	ND	ND	ND	ND
Sm	5.80	6.50	5.70	5.60	5.30	ND	5.40	6.80	6.10
Eu	2.30	2.40	2.20	2.30	2.00	6.90	1.00	1.00	1.00
Gd	4.20	5.30	5.80	5.30	4.60	BLD	ND	ND	ND
Tb	0.60	0.77	0.69	0.68	0.64	ND	0.80	1.00	0.80
Dy	3.00	3.40	3.70	3.40	2.80	1.00	ND	ND	ND
Ho	0.58	0.67	0.72	0.65	0.55	ND	ND	ND	ND
Er	1.74	1.86	1.95	1.67	1.60	ND	ND	ND	ND
Tm	0.25	0.28	0.28	0.26	0.24	ND	ND	ND	ND
Yb	1.60	1.90	2.00	1.60	1.60	ND	BLD	BLD	BLD
Lu	0.29	0.32	0.33	0.28	0.31	BLD	BLD	BLD	BLD
Cu	70	65	140	110	85	110	15	27	17
Zn	87	70	260	70	190	170	73	89	81
As	4.00	2.20	2.40	1.00	2.30	BLD	0.60	20.00	13.00
W	52	30	23	79	187	502	69	70	26
Au (ppb)	2.70	2.40	1.30	1.00	9.30	24.40	6.00	BLD	BLD
Ir (ppb)	BLD	BLD	BLD	BLD	BLD	BLD	0.07	ND	ND
Ru (ppb)	BLD	BLD	BLD	BLD	BLD	0.12	0.13	ND	ND
Rh (ppb)	BLD	BLD	BLD	BLD	BLD	0.02	0.05	ND	ND
Pt (ppb)	2.10	2.60	3.80	1.60	2.40	3.40	5.50	ND	ND
Pd (ppb)	1.90	5.50	3.10	6.30	3.10	6.30	6.70	ND	ND
CIPW Norm									
Ap	0.73	0.86	0.81	0.82	0.63	0.96	0.86	0.96	0.86
Il	0.88	0.92	1.39	1.51	0.82	1.28	1.27	1.21	1.03
Mt	0.25	5.50	8.95	7.94	4.93	7.54	6.77	7.65	2.53
Or	35.39	19.57	18.47	15.34	21.92	7.22	6.26	19.76	22.64
Ab	28.58	36.82	29.28	20.65	39.57	13.19	14.39	24.88	37.96
An	19.03	24.01	24.41	25.95	18.27	16.03	17.03	20.60	22.32
Di	5.65	8.99	8.35	21.96	9.69	28.48	27.15	15.35	
Hy			0.88						3.22
Ol	4.65	1.34	7.47	2.84	0.29	17.04	19.02		
Ne	4.83	1.90		2.99	3.39	8.25	7.24	8.69	
C									1.69
Q									5.49
Hm		0.08			0.49				2.26

SAMPLE #	305	307	308A	308B	309	321	325	328	85-32
mE	13030	10650	10430	10430	10775	10050	10000	9730	11180
mN	8680	9040	9210	9215	9115	8500	9930	7180	8788
	AOB	AOB	AOB	AOB	AOB	MugeariteMugeariteHawaiite			AOB
SiO2	44.74	48.21	46.65	49.66	48.79	52.23	53.25	46.62	49.01
TiO2	0.86	0.87	0.88	0.92	0.76	0.55	0.41	0.66	0.81
Al2O3	17.65	17.40	17.75	18.19	17.00	18.31	18.76	17.04	18.71
Fe2O3 (t)	8.13	6.06	6.19	7.42	6.88	5.41	4.29	3.92	6.29
FeO	2.55	3.04	3.45	3.33	2.32	1.54	1.87	3.96	1.94
MnO	0.09	0.12	0.16	0.11	0.18	0.18	0.22	0.20	0.12
MgO	3.84	4.61	4.82	4.27	5.28	3.03	1.97	3.82	4.22
CaO	10.77	10.50	10.77	8.88	11.04	5.91	6.01	8.34	9.76
Na2O	1.79	3.37	3.42	2.49	3.09	3.68	4.89	3.59	2.84
K2O	1.33	1.94	1.57	2.51	2.53	4.35	3.81	3.02	2.01
P2O5	0.43	0.48	0.48	0.36	0.36	0.39	0.31	0.48	0.43
S	0.00	0.04	0.00	0.01	0.01	0.01	0.01	0.16	0.00
H2O	5.10	2.30	2.40	3.10	4.00	1.90	2.10	3.10	3.80
CO2	0.40	1.10	0.50	0.10	0.50	1.30	1.90	4.80	0.20
Total	97.68	100.04	99.04	101.35	102.74	98.79	99.80	99.71	100.14
100Mg/(Mg+Fe")	72.86	72.99	71.35	69.56	80.22	77.81	65.25	63.23	79.50
100Mg/(Mg+Fe"total	40.96	49.17	48.78	43.20	52.51	45.74	38.00	47.63	49.74
87Sr/86Sr	ND	ND	ND	ND	ND	ND	ND	ND	ND
18O/16O	ND	ND	ND	ND	ND	ND	ND	ND	ND
Trace Elements (pp									
Sc	25	23	22	22	23	11	5	15	18
Cr	101	40	22	19	80	21	21	25	114
Co	28	27	30	31	24	22	25	21	25
Ni	24	22	31	18	35	21	15	21	42
V	397	424	433	426	346	272	205	323	356
Rb	9	50	15	35	37	73	72	46	14
Sr	1504	1850	1850	1748	2508	2015	1990	1430	2040
Zr	43	68	59	69	72	85	99	73	64
Ba	228	284	201	222	336	518	435	245	316
Cs	BLD	23.00	21.00	50.00	16.00	1.50	52.80	1.50	1.30
Th	1.00	2.20	1.90	1.80	2.10	3.20	4.10	2.30	1.90
U	0.70	1.70	1.20	1.70	1.70	3.10	4.30	2.30	1.60
Be	ND	ND	ND	ND	ND	ND	ND	ND	ND
Y	21.00	22.00	48.00	44.00	42.00	45.00	33.00	21.00	21.00
Hf	2.00	BLD	BLD	BLD	2.00	2.00	BLD	2.00	2.00
Ta	BLD	0.60	0.60	0.60	BLD	0.60	BLD	BLD	BLD
Nb	BLD	BLD	BLD	BLD	BLD	BLD	BLD	BLD	BLD
La	17	19	19	19	17	24	31	21	22
Ce	37	43	48	44	42	42	57	44	46
Pr	ND	ND	ND	ND	ND	ND	ND	ND	ND
Nd	ND	ND	ND	ND	ND	ND	ND	ND	ND
Sm	5.10	5.90	6.60	6.60	5.80	5.70	6.60	5.90	5.80
Eu	BLD	BLD	1.00	BLD	BLD	1.00	1.00	1.00	BLD
Gd	ND	ND	ND	ND	ND	ND	ND	ND	ND
Tb	0.50	0.90	1.10	0.90	0.90	0.80	1.00	0.60	1.00
Dy	ND	ND	ND	ND	ND	ND	ND	ND	ND
Ho	ND	ND	ND	ND	ND	ND	ND	ND	ND
Er	ND	ND	ND	ND	ND	ND	ND	ND	ND
Tm	ND	ND	ND	ND	ND	ND	ND	ND	ND
Yb	BLD	BLD	BLD	3.00	2.00	2.00	3.00	BLD	BLD
Lu	BLD	BLD	BLD	BLD	BLD	BLD	BLD	BLD	BLD
Cu	17	20	22	11	19	43	33	17	18
Zn	85	110	97	99	93	110	79	102	81
As	0.80	12.00	4.30	4.00	3.70	2.60	2.60	1.50	3.30
W	22	25	31	30	15	32	49	16	13
Au (ppb)	3.00	4.00	11.00	10.00	17.00	4.00	BLD	BLD	3.00
Ir (ppb)	ND	ND	ND	ND	ND	ND	ND	ND	ND
Ru (ppb)	ND	ND	ND	ND	ND	ND	ND	ND	ND
Rh (ppb)	ND	ND	ND	ND	ND	ND	ND	ND	ND
Pt (ppb)	ND	ND	ND	ND	ND	ND	ND	ND	ND
Pd (ppb)	ND	ND	ND	ND	ND	ND	ND	ND	ND
CIPW Norm									
Ap	1.03	1.09	1.10	0.81	0.81	0.90	0.71	1.16	0.98
Il	1.78	1.71	1.74	1.79	1.47	1.10	0.81	1.38	1.60
Mt	6.55	7.95	9.35	9.61	5.98	4.15	5.81	6.24	4.48
Or	8.52	11.86	9.64	15.11	15.21	26.89	23.50	19.54	12.35
Ab	16.43	27.28	25.05	21.47	21.08	32.59	38.21	24.53	25.00
An	39.27	27.55	29.58	31.64	25.48	21.55	18.78	24.88	33.67
Di	12.21	18.04	17.75	8.48	21.74	5.05	7.99	13.58	10.75
Hy	4.72			6.90		3.56			5.95
Ol		2.49	3.05		2.34	1.40	1.00	5.37	
Ne		1.21	2.73		2.99		2.70	3.33	
C									
Q	5.17			3.57					1.74
Hm	4.33	0.80		1.64	2.89	2.81	0.48		3.47

SAMPLE #	85-34	85-39	P17-231	SO11-228	P12-108
mE	10160	Tatau	9480	9193	9548
mN	10972	Table 1	8885	10290	8700
	AOB	Hawaiite	Mugearit	Mugearite	Mugearite
SiO2	47.62	47.43	50.36	50.70	51.80
TiO2	0.86	0.74	0.48	0.51	0.50
Al2O3	15.90	18.55	17.87	18.70	19.00
Fe2O3 (t)	4.01	5.95	3.33	3.80	5.50
FeO	5.61	3.12	2.32	2.90	4.50
MnO	0.18	0.[illegible]	0.20	0.21	0.65
MgO	7.39	3.79	3.60	2.30	1.71
CaO	12.15	8.80	6.12	6.55	2.95
Na2O	2.80	4.47	4.41	4.50	3.70
K2O	1.55	2.28	3.79	4.52	5.37
P2O5	0.34	0.43	0.40	0.40	0.40
S	0.00	0.02	0.01	0.06	0.02
H2O	1.40	4.10	3.40	1.90	1.90
CO2	0.00	0.20	3.40	3.60	2.20
Total	99.81	100.11	99.69	100.65	100.20
100Mg/(Mg+Fe")	70.13	68.41	73.45	58.57	40.38
100Mg/(Mg+Fe"total	58.83	44.36	54.69	39.35	24.39
87Sr/86Sr	ND	ND	ND	ND	ND
180/160	ND	ND	ND	ND	ND
Trace Elements (pp					
Sc	28	15	7	7	9
Cr	180	17	19	16	17
Co	42	29	14	28	47
Ni	51	11	44	12	27
V	386	359	246	180	200
Rb	16	33	64	75	88
Sr	1580	1450	1719	1700	2000
Zr	45	66	101	240	250
Ba	170	402	312	350	370
Cs	BLD	1.00	7.90	0.90	3.90
Th	1.30	1.40	3.30	4.80	4.40
U	0.90	1.20	3.50	4.10	3.90
Be	ND	ND	ND	2.10	2.80
Y	22.00	25.00	19.00	62.00	30.00
Hf	2.00	2.00	2.00	3.00	3.00
Ta	0.70	BLD	BLD	0.60	0.60
Nb	BLD	BLD	BLD	24.00	12.00
La	17	19	24	31	29
Ce	34	44	46	70	72
Pr	ND	ND	ND	ND	ND
Nd	ND	ND	ND	ND	ND
Sm	5.40	6.30	5.60	8.00	7.10
Eu	1.00	BLD	1.00	1.00	1.00
Gd	ND	ND	ND	ND	ND
Tb	0.80	0.90	BLD	1.00	0.80
Dy	ND	ND	ND	ND	ND
Ho	ND	ND	ND	ND	ND
Er	ND	ND	ND	ND	ND
Tm	ND	ND	ND	ND	ND
Yb	BLD	2.00	BLD	3.00	3.00
Lu	BLD	BLD	BLD	BLD	BLD
Cu	18	22	ND	81	75
Zn	78	95	92	220	190
As	0.60	2.10	2.10	1.80	8.50
W	65	50	23	75	56
Au (ppb)	5.00	3.00	6.00	9.00	8.00
Ir (ppb)	ND	ND	ND	ND	ND
Ru (ppb)	ND	ND	ND	ND	ND
Rh (ppb)	ND	ND	ND	ND	ND
Pt (ppb)	ND	ND	ND	ND	ND
Pd (ppb)	ND	ND	ND	ND	ND
CIPW Norm					
Ap	0.76	0.99	0.95	0.92	0.92
Il	1.66	1.47	0.97	1.02	1.10
Mt	5.92	9.03	5.25	5.94	4.15
Or	9.30	14.06	24.23	28.06	26.89
Ab	17.21	25.97	32.00	25.26	32.59
An	26.65	24.86	21.72	18.36	21.55
Di	25.93	13.88	6.48	10.44	5.05
Hy					3.56
Ol	8.86	2.43	5.60	2.01	1.40
Ne	3.71	7.31	2.75	7.99	
C					
Q					
Hm					2.81

SAMPLE #	74400037	74400033	74400032	69400377	69400387	76400028	74400031	nMORB
mE					9000	Boulder E	Tiripats	Schilling et
mN					8430	of Tiripats	Caldera	al. 1983
	AOB	AOB	AOB	AOB	Benmoreite	Q-trachyte	Q-trachyte	
SiO2	46.60	45.00	48.70	48.20	56.20	67.95	68.50	48.77
TiO2	0.75	1.07	0.87	0.81	0.51	0.23	0.30	1.15
Al2O3	12.90	15.10	16.80	17.10	19.50	17.20	16.30	15.90
Fe2O3 (t)	3.95	5.30	4.60	5.55	4.30	1.44	1.46	1.33
FeO	5.10	5.30	4.10	3.75	1.15	0.40	0.46	8.62
MnO	0.18	0.19	0.14	0.19	0.17	0.04	0.04	0.17
MgO	11.00	6.70	5.90	5.50	1.20	0.44	0.42	9.67
CaO	12.30	13.50	10.80	10.20	4.25	0.74	0.55	11.16
Na2O	2.70	2.75	3.20	3.65	4.80	6.76	5.95	2.43
K2O	1.60	0.65	1.62	2.00	4.40	4.18	4.85	0.08
P2O5	0.38	0.41	0.33	0.37	0.33	0.01	0.01	0.09
S	0.03	0.01	0.02	0.06	0.02	0.03	0.02	
H2O	2.14	2.40	2.68	2.08	2.68	0.72	0.62	0.30
CO2	0.25	1.35	0.20	0.05	0.02	0.01	0.10	
Total	99.88	99.73	99.96	99.51	99.53	100.34	99.57	
100Mg/(Mg+Fe")	79.36	69.26	71.95	72.33	65.03	66.22	61.94	66.66
100Mg/(Mg+Fe"total	69.38	54.26	56.07	52.86	29.88	ERR	ERR	63.71
87Sr/86Sr	Samples 74400037, 74400033, 74400032, 69400377 and 69400387							
18O/16O	are from Johnson et al. (1976) and Wallace et al. (1983).							
Trace Elements (pp								
Sc						3		
Cr						8		
Co						4		
Ni						5		
V						70		
Rb						68		
Sr						910		
Zr						164		
Ba						340		
Cs								
Th								
U								
Be								
Y						8		
Hf								
Ta								
Nb						7.5		
La						7		
Ce						12		
Pr								
Nd						9		
Sm								
Eu								
Gd								
Tb								
Dy								
Ho								
Er								
Tm								
Yb								
Lu								
Cu						12		
Zn						20		
As								
W								
Au (ppb)								
Ir (ppb)								
Ru (ppb)								
Rh (ppb)								
Pt (ppb)								
Pd (ppb)								
CIPW Norm								
Ap	0.86	0.94	0.75	0.84	0.75		0.02	
Il	1.46	2.12	1.71	1.58	1.00		0.58	
Mt	5.89	8.02	6.88	8.28	2.88		0.75	
Or	9.69	4.00	9.86	12.14	26.86		28.99	
Ab	10.99	17.16	26.46	24.27	41.97		50.91	
An	18.82	28.05	27.49	25.03	19.29		2.69	
Di	32.74	31.03	20.21	19.28	0.21			
Hy					2.98		1.06	
Ol	12.83	4.85	5.87	4.54				
Ne	6.73	3.83	0.77	4.04				
C							0.29	
Q					1.59		13.74	
Hm					2.47		0.96	

Appendix B. $^{40}Ar/^{39}Ar$ dating results for minerals separated from Simberi Island volcanics

Lab#	Sample	Mineral	40/39	37/39	36/39	40*/39	% Rad	^{40}Ar	Age	±
Parameters: J=0.0001937; Analysed Feb/90										
4	Sord Plut	Pl	146.95	2.62	0.48	6.51	4.4	9.95	2.28	0.82
5a			315.03	2.88	1.06	2.08	0.7	3.97	0.73	1.31
5b			22.54	3.92	0.07	1.62	7.2	0.24	0.57	0.91
6			55.76	3.35	0.15	12.15	21.7	0.9	4.24	0.48
Most probable age			**0.6 - 4.2 ± ?**							
1	Sord Plut	Hb	27.75	3.09	0.06	9.41	33.8	1.24	3.29	0.36
2			19.27	3.34	0.04	7.50	38.8	1.36	2.62	0.23
3			28.63	3.55	0.07	9.06	31.6	2.21	3.16	0.27
4			19.13	3.52	0.04	8.34	43.5	1.73	2.91	0.16
5			15.23	4.06	0.03	8.00	52.3	1.83	2.79	0.15
6			17.65	3.48	0.03	8.18	46.2	2.44	2.86	0.16
Most probable age			**2.94 ± 0.25**							
1	Botsor Hill	Cpx	13.71	0.87	0.03	5.49	40	0.77	1.92	0.27
2			549.82	1.01	0.02	545.1	99.1	53.48	*181.1*	*1.90*
3			422.59	0.81	0.03	412.8	97.6	54.06	*138.8*	*1.34*
4			438.62	1.18	0.04	428.5	97.6	60.77	*143.9*	*1.62*
5			157.93	0.89	0.02	151.3	95.7	14.21	*52.1*	*0.53*
6			2063.3	0.93	0.04	2052	99.4	135.1	*603.8*	*5.96*
Most probable age			**1.92 ± 0.27?**							

Lab#	Sample	Mineral	40/39	37/39	36/39	40*/39	% Rad	^{40}Ar	Age	±
Parameters: J=0.000187; Analysed Jun/91										
1	22XEN	M-h	90.46	2.40	0.27	10.98	12.1	2.69	*3.70*	*3.35*
2			47.15	4.51	0.14	5.22	11.0	1.75	*1.76*	*1.57*
3			29.85	3.06	0.08	7.40	24.7	1.20	2.49	0.80
4			23.75	4.05	0.05	10.04	42.2	0.94	3.38	0.63
Most probable age						**2.9 ± 0.6**				
1	337	Hb	11.87	3.25	0.01	9.42	79.2	0.52	3.17	0.26
2			15.92	3.12	0.02	9.38	58.8	1.00	3.16	0.26
3			30.25	2.49	0.10	0.89	2.90	0.34	*0.30*	*1.33*
4			11.37	3.40	0.01	9.09	79.8	0.70	3.07	0.13
Most probable age						**3.13 ± 0.06**				
1	347	Hb	68.27	18.3	0.21	6.65	9.6	1.53	*2.24*	*1.95*
2			13.68	3.37	0.02	7.79	56.8	0.66	2.63	0.15
3			52.12	14.5	0.14	11.96	22.7	0.97	4.03	0.71
4			36.16	13.8	0.08	12.30	33.7	0.99	4.14	0.70
Most probable age						**3.6 ± 0.8**				

Numbers in italics were not included in the calculation of the most probable age.
Most probable age = Mean ± 1 standard deviation on the mean age.
Abbreviations: Pl = plagioclase, Hb = hornblende, M-h = magnesio-hastingsite, Cpx = clinopyroxene